DEPARTAMENTO DE ASTROFISICA

Universidad de La Laguna

The transfer of resonance line polarization with partial frequency redistribution in the presence of arbitrary magnetic fields

Memoria que presenta
D. Ernest Alsina Ballester
para optar al grado de
Doctor en Ciencias Físicas.

Directores:
Prof. Javier Trujillo Bueno y Dr. Luca Belluzzi

INSTITUTO Đ ASTROFISICA Đ CANARIAS
Diciembre de 2017

Examination date: January, 2017
Thesis supervisors: Prof. Javier Trujillo Bueno and Dr. Luca Belluzzi

ISBN: xx-xxx-xxxx-x
Depósito legal: TF-xxxx/2017
Part of the material included in this document has been already published in three papers in *The Astrophysical Journal*.

Agradecimientos

Quiero agradecer a mis directores, Javier Trujillo Bueno (IAC) y Luca Belluzzi (IRSOL), la gran labor que han hecho guiándome durante el desarrollo de esta tesis. Ha sido un placer trabajar con ellos, y no podría haber pedido unos directores mejores, tanto a nivel científico como personal.

Estoy muy agradecido a Tanausú del Pino Alemán (HAO) y a Jiří Štěpán (ASCR) por discusiones que fueron de gran ayuda para mi trabajo. Asimismo, me siento muy afortunado de haber tenido la oportunidad de tener valiosas discusiones científicas con Egidio Landi Degl'Innocenti.

Me es grato agradecerle a Michele Bianda, a Renzo Ramelli y a todo el equipo del Istituto Ricerche Solari Locarno (IRSOL) su hospitalidad durante mis estancias, que hicieron todavía más agradable esta experiencia.

Valoro mucho la inestimable ayuda de Lourdes González y de Eva Bejarano durante mi tiempo en el IAC. También estoy agradecido a toda la gente del CAU, que me echaron una mano siempre que hizo falta. Agradezco la buena disposición de Cristina Arce, Sonia de León y Laura Hernández, que me facilitaron muchísimo los trámites relacionados con la tesis estos últimos meses.

Doy gracias a todos los compañeros del Instituto de Astrofísica de Canarias con los que he pasado grandes momentos durante estos años. He conocido a mucha gente maravillosa, y todos ellos tienen un lugar especial en mi corazón. También doy gracias de seguir en contacto con mis amigos de la UAB, muchos de los cuales me alegraron con sus visitas.

Por supuesto, no hubiese llegado aquí sin el cariño y apoyo de mi madre, Aurora, mi padre, Àlex, y mi hermano, Jan. A pesar de la distancia, han estado a mi lado en los buenos y malos momentos. Soy consciente de la gran suerte que tengo de tener una familia como ellos.

Por último, quiero agradecer al IAC la concesión de la beca de Astrofísico Residente "La Caixa"-Severo Ochoa, financiada por la Fundación la Caixa. También agradezco a la Acción COST titulada "Polarization as a Tool to Study the Solar System and Beyond" la financiación concedida para realizar varias estancias de trabajo en IRSOL.

Resumen

La intensidad y polarización de las líneas espectrales contienen una gran riqueza de información sobre las propiedades termodinámicas, magnéticas y dinámicas de la atmósfera solar. En esta tesis hemos considerado el complejo problema de modelizar, en condiciones fuera del equilibrio termodinámico local (no-LTE), los parámetros de Stokes de líneas resonantes fuertes en las que los fenómenos de redistribución parcial en frecuencias (PRD) son importantes, prestando atención especial al impacto de los campos magnéticos de fuerza arbitraria, tanto deterministas como microestructurados. Existen varios mecanismos físicos que pueden generar o modificar la polarización de las líneas espectrales. La dispersión de la radiación anisótropa es uno de ellos, cuyo efecto más notable es que polariza linealmente la radiación dispersada. Dicha polarización por dispersión puede ser modificada por los campos magnéticos del plasma mediante la acción conjunta de los efectos Hanle y Zeeman, y ambos son importantes en presencia de los campos débiles típicos de las regiones del Sol en calma. Además, los efectos de PRD, los cuales afectan de forma apreciable los perfiles de Stokes de líneas resonantes fuertes fuera del núcleo de la línea, tienen una importancia clave en esta investigación. Consideramos un modelo atómico de dos niveles con el nivel inferior no polarizado e infinitamente delgado, el cual permite modelizar de forma adecuada varias líneas resonantes (e.g., Sr I 4607 Å, Ca I 4227 Å, la región espectral correspondiente al núcleo de la línea k del Mg II, etc.). Debido a la complejidad del problema de la generación y transporte de polarización en líneas resonantes teniendo en cuenta fenómenos de PRD y la acción conjunta de los efectos Hanle y Zeeman, la investigación realizada en esta tesis se ha centrado en modelos atmosféricos unidimensionales.

Para realizar dichas investigaciones, hemos formulado y resuelto el problema de transporte radiativo, aplicando una teoría cuántica rigurosa para la generación y transporte de radiación polarizada. En concreto, hemos considerado una teoría que permite considerar la acción conjunta de los mecanismos físicos previamente mencionados (véase Bommier 1997b), utilizando el formalismo de las matrices de redistribución. Hemos desarrollado un código de transporte radiativo para resolver de forma eficiente tales problemas, el cual resuelve iterativamente las ecuaciones de transporte del vector de Stokes, teniendo en cuenta que los coeficientes de emisión dependen del campo de radiación incidente. Para ello, hemos desarrollado un es-

quema iterativo basado en el trabajo de Trujillo Bueno y Manso Sainz (1999) y de Belluzzi y Trujillo Bueno (2014). Dicho método iterativo mejora de forma considerable el ritmo de convergencia respecto a la iteración Lambda, para campos magnéticos de fuerzas tales que el desdoblamiento Zeeman es mucho menor que la anchura Doppler de la línea. También hemos desarrollado un método iterativo modificado, que requiere considerablemente más tiempo por iteración, pero con el cual el ritmo de convergencia es menos sensible a la fuerza del campo magnético.

Hemos aplicado dicho código de transporte radiativo primero al caso no magnético, con vistas a investigar la sensibilidad de los perfiles de intensidad y polarización de las líneas espectrales Sr I 4607 Å y Sr II 4078 Å al modelo atmosférico. Además, hemos analizado el impacto de las colisiones elásticas, poniendo especial atención en sus efectos de redistribución y de depolarización. Hemos considerado el impacto de tales colisiones tanto en líneas espectrales que se originan en la fotosfera (para las que los efectos de PRD tienen un impacto despreciable) y en líneas que se originan en la cromosfera (para las que los efectos de PRD son generalmente importantes).

El resto de los problemas de investigación que hemos considerado, que representan el grueso del trabajo realizado en esta tesis, se centran en entender la influencia del campo magnético en la polarización de las líneas resonantes. Una conclusión importante es que, en las líneas espectrales fuertes para las que los efectos de PRD dan lugar a perfiles de polarización lineales anchos con alas extensas, es crucial tener en cuenta la acción conjunta de la polarización por dispersión y los efectos Hanle y Zeeman para modelizar correctamente sus perfiles de Stokes. En efecto, mostramos que para tales líneas se tiene una sensibilidad magnética artificial en las alas de los perfiles de Q/I y U/I cuando se desprecia el efecto Zeeman, incluso cuando el campo magnético es lo bastante débil como para que el desdoblamiento por el efecto Zeeman sea mucho menor que la anchura Doppler de la línea.

Además de estudiar el impacto de campos magnéticos deterministas en las líneas espectrales, también hemos considerado campos microestructurados, es decir, campos cuya orientación cambia a escalas menores que el recorrido libre medio de los fotones de la línea. Para campos microestructurados distribuidos de forma isótropa, hemos investigado el impacto de despreciar los efectos Zeeman y de PRD en la polarización en el núcleo de la línea, para líneas fotosféricas tales como Sr I 4607 Å. Esta investigación fue motivada por el hecho de que tales efectos se habían despreciado en investigaciones anteriores, en las que se modelizaron obervaciones de dicha línea para inferir la fuerza de campos magnéticos no resueltos. También se ha estudiado el impacto de campos isótropos fuertes en la polarización de la radiación dispersada, poniendo particular atención en el caso en que las colisiones elásticas son tan eficientes que se obtiene el límite de CRD y se destruye la polarización atómica del nivel superior.

Quizás la contribución más importante de esta tesis esté relacionada con los efectos magneto-ópticos, es decir, los acoplamientos, inducidos por el campo magnético, entre distintos estados de polarización de la radiación que se propaga por el medio. En el marco de esta tesis, hemos descubierto que dichos efectos magneto-ópticos dan

lugar a una sensibilidad magnética observable en las alas de los perfiles de polarización lineal de líneas resonantes fuertes, donde los efectos de PRD producen señales de Q/I de gran amplitud. Hemos llevado a cabo una investigación detallada sobre el impacto de los efectos magneto-ópticos para varias geometrías y fuerzas del campo magnético, y hemos presentado argumentos teóricos para entender el hecho de que operan principalmente en las alas de la línea, incluso para fuerzas del campo típicas del Sol en calma. Hemos argumentado que dichos efectos extienden el potencial de diagnóstico de líneas que se originan en las regiones externas de la atmósfera solar ya que, gracias a ellos, las señales de polarización en las alas contienen información sobre la actividad magnética en regiones atmosféricas más profundas. El descubrimiento teórico de tal sensibilidad magnética supone una motivación adicional para desarrollar instrumentos capaces de tomar medidas espectropolarimétricas de alta precisión en líneas resonantes fuertes de la cromosfera y región de transición, como aquellas de los experimentos CLASP con cohetes sonda (Ly-α y Mg II h y k). También sugerimos que las sorprendentes señales en las alas de U/I y la variación espacial observada en las alas de los perfiles de Q/I y U/I para la línea cromosférica del Ca I a 4227 Å se pueden explicar mediante tales efectos. Finalmente, hemos investigado también las situaciones en las cuales los efectos magneto-ópticos pueden provocar una reducción neta de la fracción de polarización lineal en la líneas espectrales.

Los resultados de esta tesis motivan el desarrollo de nuevos trabajos para lograr más avances en esta línea de investigación. Un paso de gran interés actual es desarrollar un código de transporte radiativo que, teniendo en cuenta los mismos mecanismos físicos investigados en esta tesis, sea capaz de realizar inversiones a partir de observaciones de líneas cromosféricas en los cuatro parámetros de Stokes. Otros futuros desarrollos consisten en incluir modelos atómicos más complejos, y resolver el problema del transporte radiativo en modelos atmosféricos tridimensionales (3D), teniendo en cuenta todos los mecanismos físicos estudiados en esta tesis. Todos estos avances servirán para alcanzar un conocimiento más profundo del magnetismo solar, mediante la modelización de observaciones espectropolarimétricas.

x

Abstract

The intensity and polarization of spectral lines encodes a wealth of information on the thermodynamic, magnetic, and dynamic properties of the solar atmosphere. In this thesis we have considered the complex radiative transfer problem of modeling, in conditions far from local thermodynamic equilibrium (non-LTE), the Stokes profiles in strong resonance lines for which partial frequency redistribution (PRD) phenomena are important, placing particular focus on the role played by magnetic fields of arbitrary strength, both deterministic and micro-structured. There are several physical mechanisms that can generate or modify the polarization of spectral lines. The scattering of anisotropic radiation is one such mechanism, which most notably causes the scattered radiation to be linearly polarized. Such scattering polarization can be further modified by magnetic fields through the joint action of the Hanle and Zeeman effects, both of which are shown to be relevant for the weak fields typical of quiet solar regions. Moreover, PRD effects, which are well known to appreciably impact the Stokes profiles of strong resonance lines outside the Doppler core, also feature prominently in this investigation. We have considered a two-level model atom with an unpolarized and infinitely sharp lower level, which is suitable for modeling several resonance lines (e.g., Sr I 4607 Å, Ca I 4227 Å, the line core region of the Mg II k line, etc.). Given the complexity of the problem of the generation and transfer of resonance line polarization taking into account PRD phenomena and the joint action of the Hanle and Zeeman effects, the investigation in this thesis has been restricted to one-dimensional atmospheric models.

We have formulated the radiative transfer problem, applying a rigorous quantum theory for the generation and transfer of polarized radiation. In particular, we have considered a theory which allows for the inclusion of all the aforementioned physical mechanisms (see Bommier 1997b), using the redistribution matrix formalism. A radiative transfer code has been developed to efficiently solve such problems, which iteratively solves the Stokes-vector transfer equation, taking into account that the emission coefficients depend on the intensity and polarization of the incident radiation field. To this end, we have developed a suitable iterative scheme based on the work of Trujillo Bueno & Manso Sainz (1999) and Belluzzi & Trujillo Bueno (2014). Such iterative method greatly improves the convergence rate with respect to Lambda iteration, for field strengths such that the Zeeman splitting is much smaller than the

line's Doppler width. We have also developed a modified iterative method, which requires significantly more time per iteration, but for which the convergence rate is not as sensitive to the magnetic field strength.

The aforementioned radiative transfer code has first been applied to the unmagnetized case, in order to investigate the dependence of the intensity and polarization of the Sr I 4607 Å and Sr II 4078 Å spectral lines on the atmospheric model. Another point of interest has been to analyze the impact of elastic collisions on different spectral lines, focusing both on their frequency redistribution effect and their depolarizing effect. We have considered the impact of such collisions both for spectral lines originating in the photosphere (for which PRD effects have a neglible impact), and for lines originating in chromosphere (for which PRD effects are especially apparent in the wings).

The rest of the research problems considered, which represent the bulk of the work of this thesis, focus on the influence of the magnetic field on the polarization of resonance lines. An important conclusion is that, for strong spectral lines in which PRD effects produce broad polarization profiles that extend into the line wings, it is crucial to take into account the joint action of scattering polarization and the Hanle and Zeeman effects in order to suitably model their Stokes profiles. Indeed, we have shown that for such lines an artificial magnetic sensitivity is found in the wings of the Q/I and U/I profiles when the Zeeman effect is neglected, even when the magnetic field is weak enough that the Zeeman splitting is much smaller than the Doppler width.

Aside from studying the impact of deterministic magnetic fields on spectral lines, we have also considered micro-structured fields, i.e., fields whose orientation changes over scales smaller than the mean free path of the line photons. For isotropically distributed micro-structured fields, the impact of neglecting the Zeeman effect and PRD effects on the line core polarization, in photospheric lines such as Sr I 4607 Å, has been investigated. This was motivated by the fact that such effects had been neglected in previous investigations, in which observations of such lines were modeled in order to infer the strength of unresolved magnetic fields. We have also studied the impact of strong isotropic magnetic fields on the line scattering polarization, placing particular attention on the case in which elastic collisions are efficient enough to completely destroy atomic level polarization.

Perhaps, the main contribution of this work is the theoretical discovery that the magneto-optical effects, i.e., the magnetically-induced couplings between different polarization states of the radiation propagating through the medium, produce an observable magnetic sensitivity in the wings of the linear polarization profiles of strong resonance lines, where large Q/I amplitudes are produced by PRD effects. We have performed a detailed investigation on the impact of the magneto-optical effects for different geometries and strengths of the magnetic field, also providing theoretical arguments for the fact that they operate mainly in the line wings, and for field strengths that are typical of the quiet Sun. We have pointed out that the magneto-optical effects enhance the diagnostic capabilities of lines forming in the outer layers

of the solar atmosphere since, through them, the polarization signals in the wings encode information on the magnetic activity in deeper atmospheric regions. We have emphasized that this novel magnetic sensitivity further motivates the development of instruments capable of making high-precision spectropolarimetric observations of strong resonance lines of the chromosphere and transition region, such as those of the CLASP sounding rocket experiments (Ly-α and Mg II h & k). We have also proposed that the surprising U/I wing signals and the spatial variation found in the wings of the Q/I and U/I profiles of the Ca I 4227 Å chromospheric line can be explained by such effects. Finally, we have also investigated the physical situations in which the magneto-optical effects can produce a net decrease in the polarization fraction of spectral line radiation.

The results of this thesis strongly motivate further developments in this line of research. A step of interest is to develop a radiative transfer code that, taking into account the same physical mechanisms investigated in this work, is capable of performing inversions from Stokes-vector observations in chromospheric lines. Additional key developments will be to include more complex atomic models, and to solve the problem of three-dimensional (3D) radiative transfer taking into account all the physical mechanisms studied in this thesis. All of these breakthroughs will lead to a deeper understanding of solar magnetism through the modeling of spectropolarimetric observations.

Contents

1

Introduction

The magnetic field plays a fundamental role in the physics of the Sun, and it is strongly involved in phenomena such as the variability of solar irradiance and the solar cycle, which is driven by global dynamo effects. Many observable features of the solar atmosphere, such as sunspots (e.g., Solanki 2003), coronal loops (e.g., Zaitsev & Stepanov 2008; Reale 2014), filaments (e.g., Mackay et al. 2010), spicules (e.g., Beckers 1968; Sterling 2000; Centeno et al. 2010; Martínez-Sykora et al. 2017), and solar flares and coronal mass ejections (CMEs; e.g., Low 2001; Chen 2011) cannot be explained without the influence of magnetic fields. In order to understand the underlying physics of such phenomena in depth, and to be able to address open questions such as the acceleration of the solar wind, or the long-standing coronal heating problem, it is crucial to have a more detailed knowledge of the strength and topology of solar magnetic fields. This is especially true for the magnetic fields present in the chromosphere, transition region, and corona, about which little is known, compared to those present in the photosphere. Unfortunately, *in-situ* measurements of magnetic fields cannot be performed in the solar atmosphere. Thus, the magnetic fields present therein must instead be remotely measured.

The observable quantity which encodes the vast majority of information about the physical properties of the solar atmosphere is the emergent radiation. The intensity spectrum provides a great deal of information on the composition, structure and dynamics of the solar atmosphere. Indeed, since the application of spectroscopy to astronomical research - commonly considered to be the birth of modern astrophysics - an unprecedented understanding has been gained regarding the nature of the atmosphere of the Sun and its interior. By studying the different spectral lines of the solar spectrum, windows are opened into a variety of physical properties in different regions of the solar atmosphere. Ongoing investigations are painting an increasingly detailed picture of the nature of the Sun, as well as of other stars.

However, precise measurements of solar magnetic fields cannot be obtained from

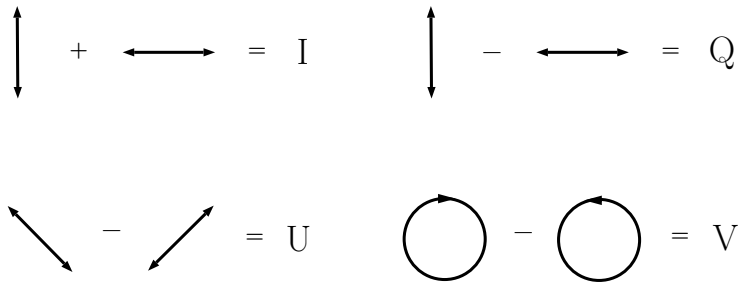

FIGURE 1.1— Schematic definition of the four Stokes parameters, for which the vertical direction has been taken as the direction for positive Stokes Q. The observer is assumed to be facing the radiation source. Figure adapted from Landi Degl'Innocenti & Landolfi (2004).

the intensity spectrum alone. Information on the geometry and strength of magnetic fields present in the region from which the observered radiation is emitted is mainly encoded in its polarization states. The polarization properties of a radiation beam, propagating in a given direction with a given frequency, are fully determined by its four Stokes parameters (see Chandrasekhar 1960; also Born & Wolf 1980), whose definition is schematically shown in Fig. 1.1. Stokes I represents the specific intensity of the beam. The Stokes Q parameter quantifies the difference between the specific intensities of the linear polarization states of a given radiation beam measured along two orthogonal axes in the plane perpendicular to the direction of propagation. The first axis is commonly referred to as the reference axis, which determines the positive contribution to Stokes Q. Together with Stokes U, quantifying the difference between the specific intensities for the linear polarization states measured along orthogonal axes rotated 45° counter-clockwise with respect to those defining Stokes Q, the linear polarization properties of the radiation beam are fully quantified. For a given radiation beam, the specific intensity of the linearly polarized component along a given axis can be measured by means of a polarizer, i.e., an optical device that allows the component of the electric field that oscillates along a given direction (the transmission axis) to pass unhindered, while the component oscillating in the perpendicular direction is filtered out. Stokes V quantifies the difference between the specific intensities of the right-handed and left-handed circular polarization states of the beam. Circular polarization can be measured by using a retarder, i.e., an optical device that modifies the relative phase between two orthogonal components of the electric field, together with a polarizer (e.g., Hauge 1976). In practice, the measurement of the Stokes parameters requires sophisticated devices and methods. The description of such methods is beyond the scope of this work, but the interested reader can find information of such methods for instance in Orrall (1971), Baur et al. (1980), Stenflo (1994), and del Toro Iniesta (2007).

Polarized radiation diagnostics were first used to study solar magnetic fields by Hale (1908), who observed circular polarization signals in sunspots, and concluded that their origin was the Zeeman effect produced by intense magnetic fields in such regions. Thereafter, instruments capable of measuring magnetic fields based on the Zeeman effect have been greatly improved (e.g., Hale et al. 1933, Kiepenheuer 1953, Babcock 1953). During the last decades, a number of diagnostic techniques that rely on this effect have been developed, through which a more profound understanding of solar magnetism has been gained, especially in the solar photosphere (e.g., Solanki 1993; Bellot Rubio 2006).

The Zeeman effect is not the only physical mechanism that impacts the polarization of spectral line radiation. Indeed, it is well known that the polarization emerging from quiet regions close to the limb is linearly polarized, both in the continuum and in spectral lines. This linear polarization is produced by scattering processes in which atoms and molecules are illuminated by an anisotropic radiation field. The amplitude of such polarization signals is typically small, being at the most a few percent of the intensity signal. In recent years, the development of instruments with high polarimetric sensitivity, such as the Zürich IMaging POLarimeter (ZIMPOL; see Povel 1995), the Advanced Stokes Polarimeter (ASP; see Elmore et al. 1992), or the Tenerife Infrared Polarimeter (TIP; see Martínez Pillet et al. 1999; also Collados et al. 2007), has made it possible to study the linearly polarized spectrum of the solar limb radiation with unprecedented accuracy. Such spectrum has revealed an astounding variety of features (see Stenflo & Keller 1997; Stenflo et al. 2000; Gandorfer 2000, 2002, 2005), with a complexity comparable to the ordinary intensity spectrum, and for this reason it has been given the name of "Second Solar Spectrum" (see Ivanov 1991). Many of its features are sensitive to the relatively weak magnetic fields present in the quiet Sun, endowing them with considerable diagnostic capabilities. The theoretical modeling of the Second Solar Spectrum has led to a great deal of advances, useful for the investigation of the solar atmosphere, and of the physical processes that leave their fingerprints on such polarization signals (e.g., Trujillo Bueno & Landi Degl'Innocenti 1997; Landi Degl'Innocenti 1998; Trujillo Bueno 1999; Trujillo Bueno et al. 2002; Manso Sainz & Trujillo Bueno 2003; Manso Sainz & Landi Degl'Innocenti 2003; Trujillo Bueno et al. 2004; Manso Sainz et al. 2004; Asensio Ramos & Trujillo Bueno 2005; Belluzzi et al. 2007, 2009, 2015; Casini et al. 2009; Štěpán & Trujillo Bueno 2010).

In order to extract information on solar magnetic fields from spectropolarimetric measurements, it is very important to have a profound and detailed understanding on how magnetic fields influence the generation and transfer of polarized radiation in the solar atmosphere. This is the ultimate goal of the theoretical investigations that have been conducted in this work, in which the impact of the magnetic field on the intensity and polarization of various spectral lines of diagnostic interest has been studied, accounting for both the Hanle and Zeeman effects. In the outer layers of the solar atmosphere, where conditions are far from local thermodynamic equilibrium (LTE), the forward modeling problem of calculating the Stokes profiles of the spectral

line radiation that emerges from a model atmosphere is very complex. Before this thesis, such radiative transfer problem had generally been solved either in the weak field regime, in which the impact of the Zeeman effect is neglected (e.g., Manso Sainz & Trujillo Bueno 2003; Anusha & Nagendra 2011; Štěpán & Trujillo Bueno 2013), or in the strong field regime, in which the Zeeman effect is taken into account but the impact on polarization due to scattering of anisotropic radiation and the Hanle effect is neglected (e.g., Socas-Navarro et al. 2000; Uitenbroek 2001). In this thesis, both the Hanle and Zeeman effects are taken into account, although we have considered the case of a two-level atomic model with an infinitely sharp lower level. We note that this assumption is suitable for modeling many resonance lines whose lower level has a very long lifetime, such as the Sr I line at 4607 Å, the Ca I line at 4227 Å, or the core region of the Mg II k line.

In our investigation, we have also accounted for partial frequency redistribution (PRD) in scattering, i.e., the frequency correlation between the incoming and scattered radiation. By considering all the aforementioned physical ingredients, we have discovered that the linear polarization signals in the line wings present a significant sensitivity to relatively weak magnetic fields through the so-called magneto-optical (MO) effects (see Alsina Ballester et al. 2016, 2017a, 2017b). Magneto-optical effects are the couplings between different polarization states of the radiation propagating through a medium, induced by the presence of a magnetic field. This result enhances the diagnostic potential of chromospheric lines that present such sensitivity, since it allows one to probe the magnetic activity in deeper regions of the solar atmosphere, where the line wings originate.

The success of the CLASP mission[1], together with the results of the theoretical investigation of Belluzzi & Trujillo Bueno (2012), have motivated the CLASP international team to propose a second mission to observe the four Stokes profiles in the spectral region that includes the Mg II h & k lines, scheduled for launch in 2019. Belluzzi & Trujillo Bueno (2012) modeled the linear polarization signals of these lines acoounting for scattering processes, and the circular polarization signals accounting for the Zeeman effect. The finding that the linear polarization signals are sensitive to the magnetic field through the MO effects (see Alsina Ballester et al. 2016; see also del Pino Alemán et al. 2016) further motivates the scientific interest of this mission. Moreover, motivated by the enigmatic spectropolarimetric observations of the Ca I 4227 Å resonance line by Bianda et al. (2003), characterized by surprising U/I wing signals and spatial variability in the wings of both the Q/I and U/I profiles, we have carried out a detailed radiative transfer investigation of this chromospheric line. Such investigation has shown that the joint action of PRD and MO effects can produce Q/I and U/I profiles with a remarkable qualitative similarity to the observations.

[1]The Chromospheric Lyman-Alpha Spectro-Polarimeter is a suborbital rocket experiment that provided the first successful measurement of the Q/I and U/I profiles of the Ly-α line in quiet regions of the solar disk (see Kano et al. 2017).

1.1 The Hanle and Zeeman effects

It is now instructive to provide a more detailed explanation on the physical processes through which the polarization in spectral lines is sensitive to the presence of a magnetic field, particularly the Hanle and Zeeman effects. They are best illustrated through a discussion on the modification of radiation in line scattering processes, i.e., those in which a photon interacts with an atom or molecule via bound-bound transitions, and a photon is emitted at the end of the process (for an in-depth review, see Trujillo Bueno 2001). Let us consider for simplicity an atomic model with two levels characterized by their total angular momentum J. Such levels are composed of $2J+1$ magnetic sublevels, each one characterized by a quantum number M, associated to the component of total angular momentum measured along a given direction, or quantization axis. The electronic transitions between the various $M-$levels of the lower and upper level are mediated by photons whose polarization states are determined by $\Delta M = M_u - M_\ell$. In the absence of a magnetic field, the magnetic sublevels that belong to the same level are degenerate, and all possible transitions have the same frequency. We further simplify the scenario by considering a normal Zeeman triplet, in which $J_u = 1$ for the upper level and $J_\ell = 0$ for the lower level. In addition to being relatively simple to model, the normal Zeeman triplet can be treated with a classical approach. Consider a statistical ensemble of such atoms, being illuminated by an isotropic and unpolarized radiation field, so that the various $M-$levels of the upper level are equally populated. In the absence of a magnetic field, the relative strength of the three possible transitions is such that their polarization signals cancel each other (see Landi Degl'Innocenti & Landolfi 2004; hereafter LL04), and the overall emitted radiation will be unpolarized.

Now consider the same situation in the presence of a magnetic field. Due to the coupling of the magnetic field to the atom's orbital angular momentum and to the electronic spin (see Condon & Shortley 1935), the degeneracy of the $M-$levels of the upper $J-$level is broken. This shift in energies of the magnetic sublevels is known as the Zeeman effect, and as a result the π ($\Delta M = M_u - M_\ell = 0$) and $\sigma_\pm$ ($\Delta M = \pm 1$) transitions will have different frequencies. Let us again consider an ensemble of such atoms illuminated by an isotropic and unpolarized radiation field. Due to such frequency shifts, the polarization states of the radiation emitted via the various transitions no longer cancel each other and instead the emitted radiation presents a spectrally structured polarization profile. Through the Zeeman effect, a magnetic field that is parallel to the observer's line of sight (LOS) produces circular polarization signals, whose amplitude, for not too strong fields, scales as the ratio R between the Zeeman splitting and the width of the spectral line[2]. Although such polarization signatures have widely been used to measure the LOS component of solar magnetic fields, they present the drawback that, when observing radiation emerging from spatially unresolved regions in which magnetic fields of opposite polarities are present, the various contributions can cancel each other, and thus the magnetic flux

[2] $R \sim \frac{\lambda B}{T}$, where B is the magnetic field strength, λ is the wavelength, and T is the temperature.

present in the region is underestimated. On the other hand, a magnetic field that is perpendicular to the LOS gives rise to linear polarization signals, whose amplitudes scale as R^2. In consequence, they are rarely observable outside active regions of the Sun. Furthermore, also these signals are susceptible to cancellations when they are emitted from a spatially unresolved region with tangled magnetic fields.

If the illuminating radiation field is anisotropic, the probabilities of absorption processes involving the different M-levels change. For example, if the radiation field is axially symmetric around the local vertical, and most of the radiation is propagating along this direction, the probability of absorption through σ transitions will increase, while those for a π transition will decrease. As a result, the various magnetic sublevels will be differently populated. This phenomenon is commonly referred to as optical pumping, and "atomic level polarization" is extensively used in the literature to refer to the population differences that may be present between magnetic sublevels belonging to the same level, and to the possible quantum interferences between them. One can distinguish between atomic alignment, in which magnetic sublevels with different $|M|$ quantum numbers are differently occupied, and atomic orientation, in which magnetic sublevels with quantum numbers M and $-M$ are differently occupied. Throughout this thesis we will assume that the lower level has no atomic level polarization, which for $J_\ell = 0$ is satisfied by definition. It is also a reasonable assumption for $J_\ell = 1/2$, since the level cannot carry atomic alignment, although orientation could be produced if the incident radiation field has net circular polarization. However, atomic orientation is typically negligible in quiet regions where $I \gg V$. Upon deexcitation, the transitions from differently populated sublevels into the lower level produce a non-zero net polarization profile, even in the absence of a magnetic field. In summary, an anisotropic radiation field can give rise to atomic level polarization, which in turn causes the emitted radiation to be polarized. Herafter, we refer to the polarized radiation produced by the interaction of atoms with a pumping radiation field as scattering polarization. Note that this is the basic physical mechanism at the origin of the Second Solar Spectrum.

Scattering polarization can be further modified by a magnetic field through the so-called Hanle effect (Hanle 1924), which can be defined as the modification of the atomic level polarization due to the action of a magnetic field. For a more intuitive explanation, based on a classical description, see Trujillo Bueno (2001) and LL04. Typically, the Hanle effect produces a reduction of the linear polarization of scattered radiation, and it can cause a rotation of its plane of linear polarization. Line scattering polarization signals are sensitive to the Hanle effect for magnetic field strengths between approximately $0.2\,B_{\rm H}$ and $5\,B_{\rm H}$, where $B_{\rm H}$ is the Hanle critical field[3]. For stronger magnetic fields, the Hanle effect is said to saturate, and a further increase in field strength no longer impacts the polarization amplitude of the line, although it is sensitive to the orientation of such field. In contrast to

[3]For a two-level atom with an unpolarized lower level, $B_{\rm H} = 1.137 \cdot 10^{-7} A_{u\ell}/g_u$, where $A_{u\ell}$ is the Einstein coefficient for spontaneous emission of the transition and g_u is the Landé factor of the upper level.

the signatures produced by the Zeeman effect, if the radiation originates from an atmospheric region where the magnetic field's orientation changes over spatial scales smaller than the resolution element, the Hanle effect still leaves its fingerprints on the scattered radiation through a net depolarization. Because of this, the Hanle effect has proved to be very useful for exploring magnetic fields present at sub-resolution scales (e.g., Stenflo 1982; Faurobert-Scholl et al. 1995; Trujillo Bueno et al. 2004). Furthermore, the Hanle effect's impact on the amplitude of linear polarization signals is independent of the line's width, and thus of the temperature of the region where it originates. This makes its signatures especially suited to investigate the magnetism in the outer regions of the solar atmosphere such as the chromosphere (e.g., Bianda et al. 1999; Manso Sainz & Trujillo Bueno 2010) or the transition region (e.g., Trujillo Bueno et al. 2011; 2012), and also in prominences (e.g., Leroy et al. 1977; Merenda et al. 2006; Orozco Suárez et al. 2014; Martínez González et al. 2015) and spicules (e.g., Trujillo Bueno et al. 2005; Centeno et al. 2010; Orozco Suárez et al. 2015).

1.2 The generation and transfer of polarized radiation

Our current theoretical knowlegde of the physics of the generation and transfer of polarized radiation in the solar atmosphere is sophisticated enough to achieve reliable inferences of solar magnetic fields in the photosphere, but less so in the outer atmospheric regions (chromosphere, transition region, and corona). One of the difficulties in modeling scattering polarization and the Hanle effect in the strong resonance lines that are used to diagnose the magnetic activity in the solar chromosphere and the transition region is the necessity to suitably account for the strong impact of PRD effects (e.g., Milkey & Mihalas 1973; Shine et al. 1975; Faurobert 1987; Holzreuter et al. 2005; Sampoorna et al. 2010; Belluzzi & Trujillo Bueno 2012). Hereafter, by PRD we will generally refer to the intermediate regime between fully coherent scattering (CS), in which the incoming and scattered photons have the same frequency in the atomic rest frame, and complete redistribution in frequencies (CRD), in which there is no correlation between the frequencies of incoming and scattered photons.

LL04 developed a theory for the generation and transfer of polarized radiation, based on a first-order perturbative expansion of the atom-radiation interaction. Within the framework of this theory, scattering, which is intrinsically a second-order processes, is treated as a succession of statistically independent absorption and reemission processes, which is known as the CRD approximation. This approach is strictly correct in two cases: when collisions are efficient enough to relax any frequency correlation between the incoming and scattered radiation, and when the incident radiation field is spectrally flat (e.g., Casini & Landi Degl'Innocenti 2007). The theory presented in LL04 is based on this second assumption, and requires the incident radiation to be spectrally flat across a frequency interval larger than (a) the inverse lifetime of each level and (b) the Bohr frequencies connecting the different magnetic sublevels, between which quantum interference is taken into account. Although, as stated, this theory cannot account for frequency correlations between

incoming and scattered photons, it allows for the treatment of very complex atomic models, such as those with multiple levels or terms, also accounting for hyperfine structure, and accounting for the possiblity of atomic level polarization in all levels that are taken into account. This theory has been used to develop numerical RT codes capable of calculating the polarization of spectral lines using multilevel atomic models, accounting for the Hanle and Zeeman effect (see Manso Sainz & Trujillo Bueno 2003, Štěpán & Trujillo Bueno 2013, del Pino Alemán & Trujillo Bueno 2017). Line scattering processes are treated in these codes by first determining the influence of the radiation field on the atomic state via the statistical equilibrium equations. From them, the RT coefficients, which quantify the emission, absorption, dichroism (the selective absorption of specific polarization states) and anomalous dispersion (the coupling between different polarization states) of the medium, can be calculated.

As previously pointed out, scattering is intrinsically a second-order atom-radiation interaction process, and frequency correlations can exist between the incoming and scattered photons. Thus, theories capable of accounting for such effects must go beyond a first-order perturbative expansion. A particularly useful way to describe PRD phenomena is through the redistribution matrix formalism (see Hummer 1962), in which each element of the redistribution matrix quantifies the probability that a photon of a given frequency, propagating in a given direction with a given polarization state will be scattered, with the emitted photon having another specific frequency, direction and polarization state. Note, however, that such formalism can only be applied if a closed analytical solution exists for the statistical equilibrium equations, as is the case for a two-level atom with an unpolarized lower level. When considering an atom with an infinitely sharp lower level, the redistribution matrix can be decomposed into an $\mathcal{R}_{\rm II}$ matrix, which quantifies scattering processes that are coherent in frequency in the atomic reference frame, and an $\mathcal{R}_{\rm III}$ matrix, which quantifies CRD scattering processes. We note that the frequency redistribution effects due to collisional processes are, by definition, included in $\mathcal{R}_{\rm III}$. The other main mechanism responsible for frequency redistribution, the Doppler effect, can be accounted for in the redistribution matrices by applying the suitable transformations from the atomic rest frame into the observer's reference frame. The well-known Kramers-Heisenberg scattering formula (e.g., Landi Degl'Innocenti 2014) can be used to derive the CS contribution to the redistribution matrix. Indeed, in recent years it has been used to obtain the $\mathcal{R}_{\rm II}$ matrix for increasingly complex atomic models (e.g., Smitha et al. 2011, Smitha et al. 2012, Sowmya et al. 2014, Sowmya et al. 2015), which account for the influence of both the Hanle effect and the magnetically-induced shifts in atomic energy levels. The heuristic theory of metalevels (see Landi Degl'Innocenti et al. 1997) also allows for the derivation of the $\mathcal{R}_{\rm II}$ matrix for the same atomic models (e.g., Belluzzi & Trujillo Bueno 2012; Belluzzi & Trujillo Bueno 2014; Belluzzi et al. 2015). Quantifying the impact of collisional processes in such frameworks has represented a significant theoretical challenge, and it is still under investigation. Bommier (1997a,b) proposed a PRD theoretical approach, also

based on a perturbative expansion of atom-radiation interaction, that accounts for collisional redistribution using the impact approximation. Redistribution matrices were derived using such approach, suitable for a two-level atom with an unpolarized lower level in the presence of an arbitrary magnetic field, and they are our starting point for the problem's formulation and the methods of solution of the RT problems presented in this thesis.

More recently, Casini et al. (2014) proposed a quantum-mechanical approach capable of considering higher-order processes to describe the time evolution of the atomic system and of the radiation field in terms of propagators, which relies on a representation of atom-radiation interaction based on Feynman diagrams. In this approach, scattering processes were described in the collisionless regime for a two-term model atom, which was subsequently extended to a three-term Λ-type atom (see Casini and Manso Sainz 2016). Further developments by Casini et al. (2017) have yielded an expression for the emissivity in which collisional rates are included in the branching ratios between its CRD and partial redistribution contributions, also for a Λ-type multiterm atom. Likewise, Bommier (2017) has presented expressions for the PRD redistribution matrix, for a two-term atom, that accounts for an arbitrary magnetic field and the role played by collisions, also allowing for the inclusion of hyperfine structure.

1.3 The non-LTE problem of the second kind

Under non-LTE conditions, the local values of the RT coefficients depend on the local radiation field. Of course, the radiation is sensitive to the physical properties at all spatial points of the model atmosphere, which makes the problem non-local. When polarization phenomena are neglected, the non-LTE problem consists in obtaining self-consistent values, at each spatial point, for the atomic level populations and the intensity of the radiation field. In order to perform calculations for the Sun's polarized spectrum, a much more complicated non-LTE problem must be solved (see Landi Degl'Innocenti 1987). This so-called non-LTE problem of the second kind presents a greater degree of complexity since it requires solving the statistical equilibrium equations accounting for the populations of each magnetic sublevel and quantum interference that may be present between pairs of them, while calculating the radiation field via the RT equations, taking into account its intensity, polarization, and angular dependence.

These problems can, in full generality, be written as a set of coupled equations, in which an operator $\hat{A}$, which contains all information on collisional and radiative rates, multiplies an unknown vector $\vec{u}$, related to the atomic state, giving a known vector $\vec{b}$. When a two-level atom with an unpolarized lower level is considered, and stimulated emission is neglected, the problem becomes linear, i.e., $\hat{A}$ is independent of $\vec{u}$. In this case, the problem can be solved by building and inverting a large matrix (e.g., Faurobert-Scholl 1991; Bommier & Landi Degl'Innocenti 1996), but the computional cost and time invested is often very large. In the past decades, iterative methods that use approximate $\hat{A}$ operators have gained a great deal of

popularity. The Lambda iteration method (e.g., Mihalas 1978), although conceptually simple, generally requires a very large number of iterative steps before reaching a reliable solution in optically thick plasmas. Olson et al. (1986) proposed an accelerated Lambda iteration (ALI) method based on Jacobi's iterative scheme (see Jacobi 1845), which greatly reduced the number of iterations required while only slightly increasing the computation time per iteration, and it was intially applied to unpolarized RT problems. Even faster iterative schemes, such as Gauss-Seidel and successive overrelaxation (SOR) iteration were developed by Trujillo Bueno & Fabiani Bendicho (1995). ALI methods including radiation polarization were introduced shortly thereafter (see Trujillo Bueno & Landi Degl'Innocenti 1996; Faurobert-Scholl et al. 1997; Trujillo Bueno & Manso Sainz 1999), which were extended in order to allow for a PRD treatment of scattering (see Paletou & Faurobert-Scholl 1997), and also to account for the influence of the magnetic field via the Hanle effect (see Nagendra et al. 1998; Manso Sainz & Trujillo Bueno 1999). Uitenbroek (2001) developed a multilevel accelerated lambda iteration (MALI) code in which polarized line transfer including PRD scattering effects was accounted for, but considering the impact of the magnetic field only through the Zeeman effect.

Our goal in this thesis is to formulate and solve the problem of the generation and transfer of resonance line polarization, under non-LTE conditions, taking into account PRD phenomena and the joint action of the Hanle and Zeeman effects. The atmospheric model is plane-parallel, i.e., its properties are constant over any given horizontal plane and depend only on the atmospheric height. A two-level atomic model with an infinitely sharp and unpolarized lower level is considered, and stimulated emission is neglected. The novelty of this investigation is that the full polarized RT problem is solved in optically thick media, accounting for the joint action of scattering of anisotropic radiation (fully taking into account PRD effects) and the magnetic fields, via both the Hanle and Zeeman effects. Building on the work of Trujillo Bueno & Manso Sainz (1999) and Belluzzi & Trujillo Bueno (2014), a suitable ALI method is formulated and a novel radiative transfer code is developed and applied.

1.4 Structure of the thesis

In Chapter 2 of this thesis, the theoretical framework used in this work is discussed, and we present the relevant equations for solving the RT problem, including the expressions for the emissivity in terms of redistribution matrices. We stress the importance of Doppler redistribution and discuss in detail the transformations for the various RT coefficients when going from the atomic reference frame into the observer's reference frame. We also introduce the transformations required in order to consider reference frames other than the one in which the quantization axis for total angular momentum is taken parallel to the magnetic field. Based on them, the expressions for the RT coefficients are presented also for the case of a microstructured magnetic field, i.e., one whose orientation changes over scales smaller than the line photon's mean free path. Finally, numerical methods, including the formal solution

of the RT equation and the iterative scheme developed in this thesis, are also detailed.

In the following chapters, numerical applications are performed using the abovementioned RT code, focusing on different physical mechanisms that influence the generation and transfer of polarized radiation in resonance spectral lines. In Chapter 3, after discussing the spectral lines on which we focus throughout the thesis, we study a number of physical mechanisms that control the polarization in the unmagnetized case. The role of elastic collisions, i.e., collisional processes that do not induce transitions between different atomic levels, is considered, and we focus both on their influence on frequency redistribution effects, and their depolarizing effect. This investigation is of particular interest for spectral lines which, due to PRD effects, present extended linear polarization signals in the wings, whose amplitudes are dependent on the elastic collisonal rates at its formation region. The apparent insensitivity of the wings to the depolarizing effect of collisions is also discussed. Also in this chapter, we investigate the sensitivity of the intensity and linear polarization profiles to the atmospheric model under consideration, due to the specific height variation of the physical properties of the atmosphere. Finally, numerical aspects of the calculations performed in the aforementioned RT code are studied, namely the dependence of the convergence rate of the iterative calculation on the opacity of the atmosphere and on the strength of the magnetic field, and the sensitivity of the synthesized Stokes profiles on the formal solution method of the RT equation, especially for lines originating close to the transition region, such as the Mg II k line.

In the rest of this work, the impact of the magnetic field on the Stokes profiles of spectral lines is studied in great detail. In particular, Chapter 4 focuses on the influence of the magnetic field on the line contribution to scattering emissivity. The approximation of neglecting the Zeeman splitting in the emission and absorption profiles when calculating the RT coefficients, i.e., the weak field approximation, has often been used in the past (e.g, Landi Degl'Innocenti et al. 1990, Manso Sainz & Trujillo Bueno 2003, Anusha et al. 2011) when considering magnetic fields weak enough that the Zeeman splitting is much smaller than the Doppler width. We confirm the validity of such approximation in resonance lines originating in the photosphere, but contrast this with stronger spectral lines in which PRD effects are significant in the wings, where it is found to be unreliable. Although the role played by the Hanle effect in forward scattering and 90° scattering is well known, its impact on the polarization signals of radiation that emerges at intermediate inclinations is often overlooked, and we present analytical calculations describing such situations. The influence of micro-structured magnetic fields on the emergent radiation is also studied, accounting for it through both the Hanle and Zeeman effects. A particularly striking result is found considering the situation in which the magnetic field is isotropically distributed, and elastic collisions are so efficient that the CRD limit is obtained and atomic level polarization is completely destroyed. Although, in principle, one may not expect the linear polarization signal to be influenced by the line scattering emissivity, we justify, through both numerical and analytical calculations, that such signatures can be produced in the presence of a

strong magnetic field, provided that the radiation field is spectrally structured and breaks the symmetry of the problem.

Trujillo Bueno et al. (2004) theoretically interpreted observational data of the center-to-limb variation (CLV) of Q/I signals of the Sr I line at 4607 Å in order to estimate the strength of spatially unresolved magnetic fields present in the quiet solar photosphere. By performing 3D RT calculations, assuming a volume-filling micro-structured and isotropic magnetic field of constant strength, the best fit to the observations was found for a field strength of 60 G. In such calculations, (a) PRD effects were neglected and (b) the magnetic field was taken into account via the Hanle effect, neglecting the possible impact of the Zeeman effect on the linear polarization profiles. Also in Chapter 4, 1D calculations are performed in order to estimate the error incurred by making such assumptions, which is found to be negligible even for field strengths up to 200 G.

Chapter 5 is dedicated to the investigation of the impact of MO effects on the polarization of spectral lines of diagnostic interest. Numerical calculations are presented in order to emphasize that the signatures of such effects can be found in the wings of lines that originate at high altitudes in the solar atmosphere in the presence of relatively weak magnetic fields. We show that such magnetic sensitivity is mainly produced by Faraday rotation, i.e., the MO effects that produce a rotation of the plane of linear polarization. Although Faraday rotation is produced by the longitudinal component of the magentic field along the direction of propagation of the radiation, we show that observable signatures can be produced even when they are perpendicular to the LOS. Through analytical arguments, the fact that Faraday rotation operates mainly in the wings of the line, and in the presence of magnetic field strengths comparable to the Hanle critical field, is justified. We also show that Faraday rotation can produce a net reduction of the total fractional linear polarization, and an explanation for such depolarization is presented.

Our theoretical discovery that the joint action of PRD and MO effects give rise to an observable magnetic sensitivity in the Q/I and U/I wings enhances the diagnostic potential of the spectral lines in which such effects operate, since the line wings encode information on the magnetic fields that are present in the lower atmospheric regions where the wing photons originate. Moreover, we argue that signals whose origin was currently unclear, such as the spatial variation in the Q/I and U/I wings of the Ca I line at 4227 Å, can be explained by such MO effects. Spectral lines that present extended linear polarization signals in the wings, and thus are sensitive to the MO effects, generally originate in the outer layers of the solar atmosphere. They are typically found in the blue and ultraviolet regions of the solar spectrum, which further motivates the development of instruments capable of making high-precision spectropolarimetric observations from ground, balloon, and space telescopes.

Finally, the main conclusions of this work are presented in Chapter 6.

2

Theoretical approach and numerical methods

In this chapter, we present the detailed theory and mathematical formalism through which the radiative transfer problem in non-LTE conditions has been treated. The case of a two-level atom with an infinitely sharp and unpolarized lower level is considered, taking into account frequency correlations between incoming and scattered photons, in the presence of an arbitrary magnetic field. The radiative transfer and statistical equilibrium equations are presented, as well as the redistribution matrices. Transformations between different reference systems are also presented and discussed. Then the case of a magnetic field whose orientation changes over very small spatial scales is treated in the same theoretical framework. We conclude this chapter discussing the numerical solutions of the radiative transfer equations, and the iterative schemes which have been used to solve the non-LTE radiative transfer problem.

2.1 Introduction

In this chapter we discuss the theory that is used in this work to model the intensity and polarization profiles of a variety of spectral lines, taking the effects of partial frequency redistribution (PRD), i.e., frequency correlations between the photons involved in the scattering processes, into account. The radiative transfer (RT) equation, which describes the propagation of polarized radiation through the stellar medium, is presented and numerical methods for its solution are discussed. The coefficients appearing in the RT equations depend on the state of the atoms, which, in non-LTE conditions, needs to be calculated by solving the so-called statistical equilibrium (SE) equations. These equations describe the temporal evolution of the atomic system due to its interaction with the radiation field (radiative processes), other particles (collisional processes), and the magnetic field. In the particular case in which a closed analytical solution for the SEE is available, the problem can be

formulated within the framework of the redistribution matrix formalism.

In this work, we will consider the case of a two-level atom with an infinitely sharp and unpolarized lower level. The starting equations are written in the atomic reference frame, taking the quantization axis for total angular momentum directed along the magnetic field. We also present their transformations into the observer's frame, accounting for the Doppler shift due to the velocity distributions of the atoms. Furthermore, by rotating the quantization axis for total angular momentum, one can work in a reference frame in which the radiation field has clearer symmetry properties. Such transformations also allow us consider, in a consistent manner, the case of a microstructured magnetic field, i.e., one whose orientation changes at scales smaller than the line photon's mean free path, within the formalism used in this work. This chapter concludes with the description of numerical methods which we have developed in order to rapidly and efficiently solve the non-LTE RT problem.

2.2 The radiative transfer equation

As a radiation beam propagates across a stellar medium in a specific direction, its intensity is attenuated by absorption and scattering processes, which can also modify the beam's polarization state. Furthermore, both collisional and radiative processes occuring in the medium add polarized radiation to the beam. Here we present the general RT equations for polarized radiation (see Landi Degl'Innocenti 1983), which are as follows

$$\frac{\mathrm{d}}{\mathrm{d}s}\begin{pmatrix} I \\ Q \\ U \\ V \end{pmatrix} = \begin{pmatrix} \varepsilon_I \\ \varepsilon_Q \\ \varepsilon_U \\ \varepsilon_V \end{pmatrix} - \begin{pmatrix} \eta_I & \eta_Q & \eta_U & \eta_V \\ \eta_Q & \eta_I & \rho_V & -\rho_U \\ \eta_U & -\rho_V & \eta_I & \rho_Q \\ \eta_V & \rho_U & -\rho_Q & \eta_I \end{pmatrix} \begin{pmatrix} I \\ Q \\ U \\ V \end{pmatrix} . \qquad (2.1)$$

This differential equation describes the evolution of the intensity and polarization properties of a monochromatic and unidirectional beam, with frequency ν and direction $\vec{\Omega}$, as it progates along a path, at spatial coordinate s. In RT calculations it is often useful to treat the four Stokes parameters of the beam as the four components $I_i(\nu, \vec{\Omega}, s)$ of the so-called Stokes-vector (with $i = 0, 1, 2$ and 3 standing for Stokes I, Q, U, and V, respectively). We recall that the four Stokes parameters are linear combinations of measurements of specific intensity for which only particular polarization states have been selected. The specific intensity is defined as the amount of energy passing through a unit area normal to the beam, per unit time, into a unit solid angle, per unit frequency interval. Thus, the Stokes parameters are given in units of $\mathrm{erg\,cm^{-2}\,s^{-1}\,sr^{-1}\,Hz^{-1}}$. The emissivities, or emission coefficients, ε_i quantify the specific intensity, in each of the I_i Stokes components, added to the beam as it propagates along the path in the spatial interval between s and $s + \mathrm{d}s$, with units of $\mathrm{erg\,cm^{-3}\,s^{-1}\,sr^{-1}\,Hz^{-1}}$. We note that in the applications considered in this work, the spectral dependence is shown in wavelength rather than frequency. Thus, hereafter, the specific intensities are given per wavelength unit instead of per

frequency unit, and since

$$I_i(\nu,\vec{\Omega})\big|\mathrm{d}\nu\big| = I_i(\lambda,\vec{\Omega})\big|\mathrm{d}\lambda\big|\,, \tag{2.2}$$

the intensity in the four Stokes parameters can be given in wavelength units after multiplying by the factor $|\mathrm{d}\nu/\mathrm{d}\lambda| = c/\lambda^2$. The specific intensity will be given in units of $N_\gamma\,\mathrm{s}^{-1}\mathrm{cm}^{-2}\mathring{\mathrm{A}}^{-1}\mathrm{sr}^{-1}$, for which the aforementioned conversion factor has been applied. $N_\gamma = \lambda\,E_\lambda/(hc)$ is the number of photons and E_λ is the energy of the radiation beam at wavelength λ. The same conversion is of course applied in order to write the emission coefficients in terms of wavelength.

The 4×4 matrix that appears on the right hand side Eq., (2.1), which couples the four Stokes parameters in this differential equation, is known as the propagation matrix, and all of its elements have units of inverse length. The $\eta_I(\nu,\vec{\Omega},s)$ appearing in the propagation matrix is the absorption coefficient, which quantifies the attenuation of the radiation's intensity (in the four Stokes parameters) as it propagates along the path in the spatial interval between s and $s+\mathrm{d}s$, for a given direction and frequency. The η_Q, η_U, and η_V coefficients - which also have a dependence on the frequency, direction, and the s coordinate along the path - are the so-called dichroism terms, which quantify the differential attenuation of Stokes parameters Q, U, and V, respectively, as the ray propagates along the same path element. The anomalous dispersion terms ρ_Q, ρ_U, and ρ_V quantify the modification of the radiation beam's polarization state as it propagates through the path element due to couplings between Stokes Q, U, and V.

A wide variety of physical mechanisms are involved in the generation and transfer of polarized radiation. The emission and absorption of photons due to the bound-bound processes of the chemical species present in the atmosphere give rise to the spectral lines found in the emergent radiation and contribute, respectively, to the emission coefficients and to the coefficients of the propagation matrix. On the other hand, free-free, bound-free and free-bound processes all play a role in absorption and emission of continuum photons. Thus, the emissivity can be divided into the two following terms

$$\varepsilon_i(\nu,\vec{\Omega},s) = \varepsilon_i^{\ell}(\nu,\vec{\Omega},s) + \varepsilon_i^{c}(\nu,\vec{\Omega},s)\,, \tag{2.3}$$

where the ℓ and c labels refer to the spectral line and continuum processes, respectively. Furthermore, for both contributions we can distinguish between a purely radiative scattering part, and a thermal part in which the energy of the emitted photon is extracted from the kinetic energy of the particles in the solar atmosphere via an interaction such as a collision. The spectral line emissivity is induced by thermal processes including, but not limited to, collisional excitations and collisional recombinations, followed by radiative relaxation, and by scattering processes through bound-bound atomic transitions. On the other hand, the main mechanisms which contribute to the continuum thermal emissivity are bremsstrahlung and radiative recombination, while the continuum (free-free) scattering processes include Thomson and Rayleigh scattering. For the absorption coefficient one can also distinguish

between line and continuum contributions, so

$$\eta_I(\nu,\vec{\Omega},s) = \eta_I^\ell(\nu,\vec{\Omega},s) + \eta_I^c(\nu,\vec{\Omega},s)\,. \tag{2.4}$$

We note that, aside from thermal (or "true") absorption processes in which the energy of the absorbed photon is transferred to the velocity distribution of the particles in the solar atmosphere, the absorption coefficient also accounts for scattering processes, in which the direction of the photon is changed and so it is "lost" to the beam. The line absorption coefficient has contributions from bound-bound scattering processes and thermal contributions, e.g., from photoexcitations followed by collisional deexcitations or collisional ionizations. The continuum absorption coefficient also has both a scattering and a thermal contribution

$$\eta_I^c(\nu,\vec{\Omega},s) = \sigma_c(\nu,s) + \kappa_c(\nu,s)\,, \tag{2.5}$$

where $\sigma_c(\nu,s)$ is the continuum scattering cross section, which accounts for Thomson scattering due to free electrons and for Rayleigh scattering due to hydrogen and helium atoms. $\kappa_c(\nu,s)$ quantifies the extinction due to thermal continuum processes, which include photoinization and free-free absorption.

Furthermore, the RT equation shown in Eq. (2.1) can also be written in a more notationally compact form in terms of its Stokes-vector

$$\frac{\mathrm{d}}{\mathrm{d}s}\vec{I} = \vec{\varepsilon} - \hat{K}\vec{I}\,, \tag{2.6}$$

where $\vec{I} = (I,Q,U,V)$, $\vec{\varepsilon} = (\varepsilon_I,\varepsilon_Q,\varepsilon_U,\varepsilon_V)$, and $\hat{K}$ is the propagation matrix.

2.2.1 The two-level atom

In this work we focus on the relatively simple case in which the atomic transition that gives rise to the spectral line under consideration is modeled assuming a two-level atom, whose lower level is assumed to be infinitely sharp (which is a reasonable assumption for ground or metastable levels with very a long lifetime), and to have no atomic level polarization. Given that the radiation field in the solar atmosphere is weak enough that the average number of photons per mode is much smaller than one, we have also taken the simplifying assumption of neglecting stimulated emission. The upper level is specified by quantum numbers (α_u, J_u), where α_u is a set of quantum numbers of the level. In particular, for an atom whose levels are described in the Russel-Saunders coupling scheme, α_u could represent a set of quantum numbers (β_u, L_u, S_u), which describe the electronic configuration, the orbital angular momentum, and electronic spin, respectively. J_u describes the level's total angular momentum. Likewise, the lower level is specified by the quantum numbers (α_ℓ, J_ℓ). The resonance frequency for the bound-bound transition $|\alpha_u J_u\rangle \rightarrow |\alpha_\ell J_\ell\rangle$ is

$$\nu_0 = \frac{E_u - E_\ell}{h}\,, \tag{2.7}$$

where h is the Planck constant, and E_u and E_ℓ are the unperturbed energies of the upper and lower levels, respectively. Each J-level is composed of $(2J+1)$ magnetic sublevels characterized by quantum number $M = [-J, -J+1, \cdots, J-1, J]$, also known as M-levels. In the absence of magnetic fields, the various magnetic sublevels are degenerate. When a magnetic field is present, the coupling between the magnetic field and both the orbital angular momentum and electronic spin in the magnetic Hamiltonian (see Condon & Shortley 1935) induces an energy shift between the different magnetic sublevels, breaking their degeneracy. Assuming the magnetic field is not strong enough to produces shifts in such M-levels comparable to the energy separation between different J-levels, the energy of each M-level is

$$E(M) = E_0 + \mu_0\, g\, BM\,, \tag{2.8}$$

where E_0 is the unperturbed energy, μ_0 is the Bohr magneton, B is the magnetic field strength, and g is the Landé factor for the level under consideration. Thus, the transition between two given sublevels of the upper and lower level M_u and M_ℓ

$$\nu_{M_u,M_\ell} = \frac{E(M_u) - E(M_\ell)}{h} = \nu_0 + \nu_L\left(g_u M_u - g_\ell M_\ell\right), \tag{2.9}$$

where $\nu_L = \frac{\mu_0 B}{h} = 1.3996 \cdot 10^6\, B$ is the Larmor frequency, and the field strength B given in gauss. When the energy levels are described by the aforementioned coupling scheme, the Landé factor of each level is given by

$$g = 1 + \frac{1}{2}\frac{J(J+1) + S(S+1) - L(L+1)}{J(J+1)}\,. \tag{2.10}$$

2.2.2 Elements of the propagation matrix

In the solar atmosphere, the presence of a magnetic field does not alter the frequency dependence of the continuum absorption coefficient which, moreover, is isotropic. Likewise, the magnetic field does not introduce dichroism or anomalous dispersion effects for the continuum (see LL04). Thus, the continuum contributions to the elements of the propagation matrix are

$$\eta_i^c(\nu, \vec{\Omega}) = \delta_{i,0}\, \eta_I^c(\nu)\,, \tag{2.11a}$$

$$\rho_i^c(\nu, \vec{\Omega}) = 0\,. \tag{2.11b}$$

Here we have used the notation that η_i with $i = [0, 1, 2, 3]$ refers to η_I, η_Q, η_U, and η_V, respectively. The anomalous dispersion terms ρ_i with $i = [1, 2, 3]$ similarly refer to ρ_Q, ρ_U, ρ_V, respectively. For simplicity, the spatial dependence of the quantities presented in the remainder of this work will not be shown explicitly, unless otherwise noted. The line contributions for the case of a two-level atom with an unpolarized lower level are given by (see Chapter 7 of LL04)

$$\eta_i^\ell(\nu, \vec{\Omega}) = k_L \sum_K \Phi_0^{0,K}(J_\ell, J_u; \nu)\mathcal{T}_0^K(i, \vec{\Omega})\,, \tag{2.12a}$$

$$\rho_i^\ell(\nu, \vec{\Omega}) = k_L \sum_K \Psi_0^{0,K}(J_\ell, J_u; \nu)\mathcal{T}_0^K(i, \vec{\Omega})\,. \tag{2.12b}$$

The previous equations are written using the powerful formalism of the irreducible spherical tensors. The polarization tensor $\mathcal{T}^K_Q(i,\vec{\Omega})$ is an irreducible spherical tensor introduced by Landi Degl'Innocenti (1983), which contains all the geometric information of the problem in a very compact manner. k_L is the frequency-integrated absorption coefficient, which is given by

$$k_L = \frac{h\nu_0}{4\pi}\mathcal{N}_\ell B(\alpha_\ell J_\ell \rightarrow \alpha_u J_u)\,, \tag{2.13}$$

where $B(\alpha_\ell J_\ell \rightarrow \alpha_u J_u)$ is the Einstein coefficient for absorption from level $|\alpha_\ell J_\ell\rangle$ to $|\alpha_u J_u\rangle$, and $\mathcal{N}_\ell$ is the number of atoms in the lower level per unit volume. The quantities $\Phi^{K,K'}_Q(J_\ell,J_u;\nu)$ and $\Psi^{K,K'}_Q(J_\ell,J_u;\nu)$ are the generalized profile and generalized dispersion profile, respectively, defined in Appendix 13 of LL04 as

$$\begin{aligned}\Phi^{KK'}_Q(J_\ell,J_u;\nu) = \sqrt{3(2J_u+1)(2K+1)(2K'+1)} \sum_{M_u M_u' M_\ell q q'} (-1)^{1+J_u-M_u+q'} \\ \times \begin{pmatrix} J_u & J_\ell & 1 \\ -M_u & M_\ell & -q \end{pmatrix} \begin{pmatrix} J_u & J_\ell & 1 \\ -M_u' & M_\ell & -q' \end{pmatrix} \begin{pmatrix} J_u & J_u & K \\ M_u' & -M_u & -Q \end{pmatrix} \\ \times \begin{pmatrix} 1 & 1 & K' \\ q & -q' & -Q \end{pmatrix} \frac{1}{2}\Big[\Phi(\nu_{M_u,M_\ell}-\nu) + \Phi(\nu_{M_u',M_\ell}-\nu)^*\Big]\,,\end{aligned} \tag{2.14}$$

and

$$\begin{aligned}\Psi^{KK'}_Q(J_\ell,J_u;\nu) = \sqrt{3(2J_u+1)(2K+1)(2K'+1)} \sum_{M_u M_u' M_\ell q q'} (-1)^{1+J_u-M_u+q'} \\ \times \begin{pmatrix} J_u & J_\ell & 1 \\ -M_u & M_\ell & -q \end{pmatrix} \begin{pmatrix} J_u & J_\ell & 1 \\ -M_u' & M_\ell & -q' \end{pmatrix} \begin{pmatrix} J_u & J_u & K \\ M_u' & -M_u & -Q \end{pmatrix} \\ \times \begin{pmatrix} 1 & 1 & K' \\ q & -q' & -Q \end{pmatrix} \frac{(-\mathrm{i})}{2}\Big[\Phi(\nu_{M_u,M_\ell}-\nu) - \Phi(\nu_{M_u',M_\ell}-\nu)^*\Big]\,,\end{aligned} \tag{2.15}$$

in which the quantities in brackets are the so-called $3j$ coefficients, which characterize the coupling between two total angular momenta (e.g., LL04; Racah 1942). The profiles are of the form

$$\Phi(\nu_0-\nu) = \phi(\nu_0-\nu) + \mathrm{i}\,\psi(\nu_0-\nu)\,, \tag{2.16}$$

and its complex conjugate is

$$\Phi(\nu_0-\nu)^* = \phi(\nu_0-\nu) - \mathrm{i}\,\psi(\nu_0-\nu)\,. \tag{2.17}$$

In the atomic rest frame, $\phi(\nu_0-\nu)$ and $\psi(\nu_0-\nu)$ are the Lorentzian and associated dispersion profiles, respectively

$$\phi(\nu_0-\nu) = \frac{1}{\pi}\frac{\Gamma/4\pi}{(\nu_0-\nu)^2+\left(\Gamma/4\pi\right)^2}\,; \tag{2.18a}$$

$$\psi(\nu_0-\nu) = \frac{1}{\pi}\frac{(\nu_0-\nu)}{(\nu_0-\nu)^2+\left(\Gamma/4\pi\right)^2}\,. \tag{2.18b}$$

Γ is the line broadening parameter, which accounts for the finite width of the upper level (we recall that we are assuming that the lower level is infinitely sharp), and it has three contributions

$$\Gamma = \Gamma_R + \Gamma_I + \Gamma_E \,. \tag{2.19}$$

Γ_R is the natural (or radiative) broadening of the level. Let us consider a radiative transition occuring through spontaneous emission from the upper level for which, due to the time-energy uncertainly principle, the upper level does not have a uniquely determined energy E_u, but rather it is a superposition of states with some energy spread around E_u. Morevoer, the effect of collisions with particles in the solar atmosphere also leads to a spread of the emitted frequencies (e.g., Mihalas 1978). Γ_I is the line broadening due to the effect of inelastic collisions, i.e., the collisions that induce transitions between level $|\alpha JM\rangle$ and another level $|\alpha' J' M'\rangle$, with the difference in energy being transferred to or from the particle responsible for the collision. Such collisions can be exciting or deexciting. Exciting collisions are those in which the final state has a higher energy than the state prior to the collision, and in the case of a two-level atom this corresponds to collisions which induce a transition from the lower J-level to the upper J-level. In deexciting collisions, the energy of the final state is lower than that of the initial state, which for the two-level atom corresponds to transitions from the upper J-level to the lower J-level. Γ_E is the line broadening due to elastic collisions, which are those that induce transitions between level $|\alpha JM\rangle$ and level $|\alpha JM'\rangle$, i.e., between M-levels (or magnetic sublevels) of the same J-level.

The spectral line's frequency dependence is further modified when one considers the observer's reference frame, since the random motions of the atoms which give rise to the line induce a Doppler shift in the observed frequency. Thus, the resulting spectral line is broadened by a Doppler width $\Delta\nu_D$ and, assuming that the atomic velocities follow a Maxwellian distribution, one must convolve the Lorentzian profile and its associated dispersion profile over a Gaussian function in order to account for such broadening. In this case, the expressions for $\phi(\nu_0 - \nu)$ and $\psi(\nu_0 - \nu)$ are the Voigt profile $H(x, a)$ and its associated dispersion profile $L(x, a)$. They can be written (see LL04) as

$$H(x,a) = \frac{a}{\pi}\int_{-\infty}^{\infty} \mathrm{e}^{-y^2} \frac{1}{(x-y)^2 + a^2}\,\mathrm{d}y\,; \tag{2.20a}$$

$$L(x,a) = \frac{1}{\pi}\int_{-\infty}^{\infty} \mathrm{e}^{-y^2} \frac{x-y}{(x-y)^2 + a^2}\,\mathrm{d}y\,, \tag{2.20b}$$

where $x = (\nu_0 - \nu)/\Delta\nu_D$ is the reduced frequency, $a = \Gamma/4\pi\Delta\nu_D$ is the damping parameter.

2.3 The emission coefficient

In the previous section we have presented the RT equation and the expressions for the elements of the propagation matrix. Here, the expressions for the emission coefficients are presented. As shown in Fluri & Stenflo (1999), the continuum contribution

can be divided into a thermal, or LTE, component, and a scattering component as follows

$$\varepsilon_i^c(\nu,\vec{\Omega}) = \kappa_c(\nu)\, B_\nu(T)\delta_{i,0} + \varepsilon_i^{c,\mathrm{sc}}(\nu,\vec{\Omega})\,. \tag{2.21}$$

Here, $B_\nu(T)$ is the well-known Planck function, for which the Wien approximation has been taken, which is valid when $h\nu \gg k_B T$. $\varepsilon_i^{c,\mathrm{sc}}(\nu,\vec{\Omega})$ is the contribution to continuum emission associated to scattering, which we treat as coherent in the observer's frame. This term accounts for Thomson and Rayleigh scattering through $\sigma_c(\nu)$, and it is directly related to the incoming radiation field. The scattering component of the continuum emissivity is given by

$$\varepsilon_i^{c,\mathrm{sc}}(\nu,\vec{\Omega}) = \sigma_c(\nu) \sum_{KQ} \mathcal{T}_Q^K(i,\vec{\Omega})(-1)^Q J^K_{-Q}(\nu)\,, \tag{2.22}$$

where the radiation field tensor is defined (e.g., Landi Degl'Innocenti 1983; LL04) as

$$J^K_Q(\nu) = \sum_{j=0}^{3} \oint \frac{\mathrm{d}\vec{\Omega}'}{4\pi} \mathcal{T}_Q^K(j,\vec{\Omega}') I_j(\nu,\vec{\Omega}')\,. \tag{2.23}$$

2.3.1 Density matrix and rate equations

We begin the discussion on the line part of the emission coefficient using the CRD theory presented in of LL04. For a two-level atom, the polarized emission coefficient is given by (e.g., Chapter 7 of LL04)

$$\begin{aligned}\varepsilon_i(\nu,\vec{\Omega}) = {} & \frac{h\nu}{4\pi}\mathcal{N}\sqrt{2J_u+1}\, A(\alpha_u J_u \to \alpha_\ell J_\ell) \\ & \times \sum_{KK'Q} \mathcal{T}_Q^{K'}(i,\vec{\Omega}) \rho^K_Q(\alpha_u J_u) \Phi_Q^{KK'}(J_\ell, J_u; \nu)\,.\end{aligned} \tag{2.24}$$

The quantity $\mathcal{N}$ gives the atomic number density. $A(\alpha_u J_u \to \alpha_\ell J_\ell)$ is the Einstein coefficient for spontaneous emission from level $|\alpha_u J_u\rangle$ to $|\alpha_\ell J_\ell\rangle$. Here, ρ^K_Q, i.e., the density matrix elements in their spherical statistical tensor representation have been introduced for the J-level with quantum numbers $(\alpha_u J_u)$. Now discuss them in greater depth. The atoms in a state characterized by quantum numbers (αJ) belong to a statistical ensemble of various quantum states (M-levels), which can be described by the density matrix elements (see Fano 1949)

$$\rho(\alpha JM, \alpha JM') = \left\langle \alpha JM \left| \hat{\rho} \right| \alpha JM' \right\rangle \tag{2.25}$$

where $\hat{\rho}$ is the density operator. The diagonal elements $\rho(\alpha JM, \alpha JM)$ represent the population of state $|\alpha JM\rangle$, while the off-diagional elements $\rho(\alpha JM, \alpha JM')$ represent quantum coherences between two different M-levels. In this work, we do not consider the possibility of quantum interferences between different J-levels. For our purposes, it will often be more convenient to introduce the irreducible spherical components of the density matrix, which offer a clearer view of the symmetry properties

of the atomic system. The multipole moments of the density matrix for a given atomic level can be found as

$$\rho^K_Q(\alpha J) = \sum_{MM'} (-1)^{J-M} \sqrt{2K+1} \begin{pmatrix} J & J & K \\ M & -M' & -Q \end{pmatrix} \rho(\alpha JM, \alpha JM') \,. \tag{2.26}$$

By definition, if a given J-level characterized by (αJ) has no atomic level polarization, only the $\rho^0_0(\alpha J)$ component will be nonzero. Using the impact approximation hypothesis (e.g., Trujillo Bueno & Manso Sainz 1999), the atomic state's temporal evolution is simply the sum of the radiative and collisional rate equations

$$\frac{\mathrm{d}}{\mathrm{d}t}\rho^K_Q(\alpha J) = \frac{\mathrm{d}}{\mathrm{d}t}\rho^K_Q(\alpha J)\bigg|_{\mathrm{rad}} + \frac{\mathrm{d}}{\mathrm{d}t}\rho^K_Q(\alpha J)\bigg|_{\mathrm{coll}} \,. \tag{2.27}$$

The collisional rate equations obviously have contributions from inelastic collisions, which induce transitions to and from the (αJ) level, but also from elastic collisions. By definition, elastic collsions do not induce such transitions. They do, however, relax the frequency coherence in the scattering process, broaden the spectral line profile (through Γ_E), and relax atomic level polarization, since they equalize the populations of the various magnetic sublevels, and relax coherences between them. For the particular case of a two-level atom with an unpolarized lower level, the collsional rate equation is given by (see LL04)

$$\begin{aligned} \frac{\mathrm{d}}{\mathrm{d}t}\rho^K_Q(\alpha_u J_u) =& \sqrt{\frac{2J_\ell+1}{2J_u+1}} C^{(0)}_I(\alpha_u J_u, \alpha_\ell J_\ell)\, \delta_{K0}\, \delta_{Q0}\, \rho^0_0(\alpha_\ell J_\ell) \\ & - \left[C^{(0)}_S(\alpha_\ell J_\ell, \alpha_u J_u) + D^{(K)}(\alpha_u J_u) \right] \rho^K_Q(\alpha_u J_u) \,, \end{aligned} \tag{2.28}$$

where $C^{(K)}_I(\alpha_u J_u, \alpha_\ell J_\ell)$ and $C^{(K)}_S(\alpha_\ell J_\ell, \alpha_u J_u)$ are the K-multipole components for the exciting and deexciting collisions, respectively[1]. The K-multipole components of the depolarizing collision rates $D^{(K)}(\alpha J)$ give the rate of relaxation of $\rho^K_Q(\alpha J)$ due to elastic collisions. Since such collisions do not change the population of a given J-level, it does not affect the $\rho^0_0(\alpha_u J_u)$ component, and so the $K = 0$ components are zero by definition. This expression can be somewhat simplified by using the Einstein-Milne relation

$$C^{(0)}_I(\alpha_u J_u, \alpha_\ell J_\ell) = \frac{2J_u+1}{2J_\ell+1} \exp\left[\frac{E_{\alpha_\ell J_\ell} - E_{\alpha_u J_u}}{k_B T} \right] C^{(0)}_S(\alpha_\ell J_\ell, \alpha_u J_u) \,. \tag{2.29}$$

The radiative rate equations are derived in LL04 from first principles of Quantum Mechanics. In the particular case of a two-level atom with an unpolarized lower

[1] The line broadening due to inelastic collsions Γ_I coincides with the $C^{(0)}_S(\alpha_\ell J_\ell, \alpha_u J_u)$ component of the deexciting collisional rate.

level they are given by

$$\frac{\mathrm{d}}{\mathrm{d}t}\rho^K_Q(\alpha_u J_u) = -2\pi \mathrm{i}\nu_L\, Q\, g_u\, \rho^K_Q(\alpha_u J_u) + \rho^0_0(\alpha_\ell J_\ell)\mathbb{T}_A(\alpha_u J_u KQ, \alpha_\ell J_\ell 00) - \sum_{K'Q'} \rho^{K'}_{Q'}(\alpha_u J_u)\mathbb{R}_E(\alpha_u J_u KQK'Q')\,, \tag{2.30}$$

The first term on the right hand side represents the rate at which the coherence between magnetic sublevels are relaxed due to the energy splitting produced by the presence of a magnetic field (i.e., the Hanle depolarization term). $\mathbb{R}_E(\alpha_u J_u KQK'Q')$ is the relaxation rate due to spontaneous emission

$$\mathbb{R}_E(\alpha_u J_u KQK'Q') = \delta_{KK'}\,\delta_{QQ'}\,A(\alpha_u J_u \rightarrow \alpha_\ell J_\ell)\,, \tag{2.31}$$

where $\mathbb{T}_A(\alpha_u J_u KQ, \alpha_\ell J_\ell 00)$ is the transfer rate due to absorption

$$\mathbb{T}_A(\alpha_u J_u KQ,\alpha_\ell J_\ell 00) = \sqrt{3(2J_\ell+1)}B(\alpha_\ell J_\ell \rightarrow \alpha_u J_u)(-1)^{1+J_\ell+J_u} \times \begin{Bmatrix} 1 & 1 & K \\ J_u & J_u & J_\ell \end{Bmatrix} (-1)^Q J^K_{-Q}(\nu_0)\,, \tag{2.32}$$

in which the $6j$ symbol has been introduced (see LL04). We remind the reader that this theory is based on the flat-spectrum approximation.

$$(2J_\ell+1)B(\alpha_\ell J_\ell \rightarrow \alpha_u J_u) = (2J_u+1)B(\alpha_u J_u \rightarrow \alpha_\ell J_\ell) \tag{2.33}$$

and defining the following quantity

$$w^{(K)}_{J_1J_2} = (-1)^{1+J_1+J_2}\sqrt{3(2J_u+1)}\begin{Bmatrix} 1 & 1 & K \\ J_1 & J_1 & J_2 \end{Bmatrix}. \tag{2.34}$$

then Eq. (2.30) can be rewritten

$$\frac{\mathrm{d}}{\mathrm{d}t}\rho^K_Q(\alpha_u J_u) = -2\pi \mathrm{i}\nu_L g_u Q \rho^K_Q(\alpha_u J_u) + \rho^0_0(\alpha_\ell J_\ell)\sqrt{\frac{2J_u+1}{2J_\ell+1}}B(\alpha_u J_u \rightarrow \alpha_\ell J_\ell)w^{(K)}_{J_uJ_\ell}(-1)^Q J^K_{-Q}(\nu_0) - \rho^K_Q(\alpha_u J_u)A(\alpha_u J_u \rightarrow \alpha_\ell J_\ell)\,. \tag{2.35}$$

By imposing the statistical equilibrium condition, i.e., $\mathrm{d}\rho^K_Q/\mathrm{d}t = 0$, together with Eq. (2.27), we reach the statistical equilbrium (SE) equations for the upper level

$$\left[2\pi \mathrm{i}\nu_L g_u Q + A(\alpha_u J_u \rightarrow \alpha_\ell J_\ell) + C^{(0)}_S(\alpha_\ell J_\ell, \alpha_u J_u) + D^{(K)}(\alpha_u J_u)\right]\rho^K_Q(\alpha_u J_u) = = \left[\sqrt{\frac{2J_u+1}{2J_\ell+1}}B(\alpha_u J_u \rightarrow \alpha_\ell J_\ell)w^{(K)}_{J_uJ_\ell}(-1)^Q J^K_{-Q}(\nu_0) + + \sqrt{\frac{2J_u+1}{2J_\ell+1}}\exp\left(\frac{E_{\alpha_\ell J_\ell} - E_{\alpha_u J_u}}{k_B T}\right)C^{(0)}_S(\alpha_\ell J_\ell, \alpha_u J_u)\right]\rho^0_0(\alpha_\ell J_\ell). \tag{2.36}$$

Using the definition for the Planck function in the Wien limit

$$B_{\nu_0}(T) = \frac{2h\nu_0^3}{c^2} \mathrm{e}^{-\frac{h\nu_0}{k_B T}}\,, \tag{2.37}$$

and the relation between Einstein coefficients

$$A(\alpha_u J_u \to \alpha_\ell J_\ell) = \frac{2h\nu_0^3}{c^2} B(\alpha_u J_u \to \alpha_\ell J_\ell)\,, \tag{2.38}$$

the SE equations become

$$\begin{aligned}\left[2\pi \mathrm{i}\nu_L g_u Q + A_{u\ell} + C_{u\ell} + D^{(K)}(\alpha_u J_u)\right]\left(\frac{2h\nu_0^3}{c^2}\right)\rho^K_Q(\alpha_u J_u) = \\ = \left[\sqrt{\frac{2J_u+1}{2J_\ell+1}}\, A_{u\ell}\, w^{(K)}_{J_u J_\ell} (-1)^Q J^K_{-Q}(\nu_{\alpha_u J_u, \alpha_\ell J_\ell}) + \right. \\ \left. + \sqrt{\frac{2J_u+1}{2J_\ell+1}}\, \delta_{K0}\, \delta_{Q0}\, B_{\nu_0}(T) C_{u\ell}\right] \rho^0_0(\alpha_\ell J_\ell)\,.\end{aligned} \tag{2.39}$$

Here we have used the notation $A_{u\ell} = A(\alpha_u J_u \to \alpha_\ell J_\ell)$ and $C_{u\ell} = C_S^{(0)}(\alpha_\ell J_\ell, \alpha_u J_u)$. Using this expression for the upper level's spherical statistical tensors in terms of the (unpolarized) lower level in Eq. (2.24), and using the definition for k_L in Eq. (2.13), one obtains

$$\begin{aligned}\varepsilon_i(\nu,\vec{\Omega}) = k_L \left\{ \sum_{KK'Q} \Phi^{KK'}_Q(J_\ell, J_u; \nu) \mathcal{T}^K_Q(i,\vec{\Omega}) \frac{w^{(K')}_{J_u,J_\ell}}{1 + \mathrm{i}H_u Q + \epsilon' + \delta^{(K')}} (-1)^Q \right. \\ \left. \times J^{K'}_{-Q}(\nu_0) + \frac{\epsilon'}{1+\epsilon'} B_{\nu_0}(T) \sum_K \Phi^{0,K}_0(J_\ell, J_u; \nu) \mathcal{T}^K_0(i,\vec{\Omega}) \right\},\end{aligned} \tag{2.40}$$

where $\epsilon' = C_{u\ell}/A_{u\ell}$, $\delta^{(K)} = D^{(K)}/A_{u\ell}$, and $H_u = 2\pi\, \nu_L\, g_u/A_{u\ell}$ have been introduced.

2.4 The redistribution matrix

When a closed analytical solution for the SE equations is available, the emission coefficient can be written in terms of the pumping radiation field, as in the case shown in the previous section. Then, the emission coefficients can be written as

$$\varepsilon^\ell_i(\nu,\vec{\Omega}) = k_L \int \mathrm{d}\nu' \oint \frac{\mathrm{d}\vec{\Omega}'}{4\pi} \sum_{j=0}^{3} \mathcal{R}(\nu',\vec{\Omega}',\nu,\vec{\Omega})_{ij} I_j(\nu',\vec{\Omega}') + \varepsilon^{\ell,\mathrm{coll}}_i(\nu,\vec{\Omega})\,, \tag{2.41}$$

where we have introduced the redistribution matrix, for which each $\mathcal{R}(\nu',\vec{\Omega}',\nu,\vec{\Omega})_{ij}$ element quantifies the probability that a photon with frequency ν' and propagating in direction $\vec{\Omega}'$ is scattered into a photon with frequency ν and direction $\vec{\Omega}$ (see Fig. 2.1). The i,j labels indicate the coupling between Stokes component j of

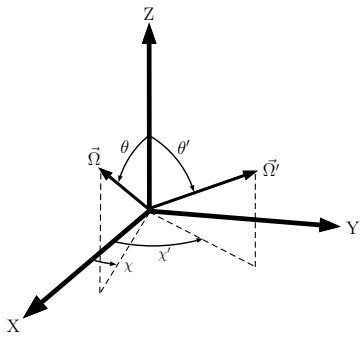

FIGURE 2.1— Scattering geometry in a right-handed Cartesian coordinate system where the Z-axis (quantization axis for the angular momentum) is along the local vertical. The direction of the scattered photon is characterized by $\vec{\Omega}$, with inclination with respect to the local vertical θ and azimuth χ, such that it is zero if the projection of $\vec{\Omega}$ onto the XY plane coincides with the X-axis. The direction of the incoming photon is characterized by $\vec{\Omega}'$, with inclination θ' and azimuth χ'.

the incoming photon and component i of the scattered photon. The redistribution matrix is an extension to the polarized case of the redistribution functions introduced in Hummer (1962). For a two-level atom the collisional term in Eq. (2.41) has the form

$$\varepsilon_i^{\ell,\mathrm{coll}}(\nu,\vec{\Omega}) = k_L \frac{\epsilon'}{1+\epsilon'} B_{\nu_0}(T) \sum_K \Phi_0^{0,K}(J_\ell, J_u; \nu) \mathcal{T}_0^K(i,\vec{\Omega})\,. \tag{2.42}$$

2.4.1 Redistribution matrices for a two-level atom with a magnetic field of arbitrary strength

We now consider the redistribution matrices derived by Bommier (1997b). These matrices were obtained from a higher-order perturbative quantum-mechanical approach which, given that scattering is instrinsically a second-order process, is required to treat atom-radiation interaction in a rigorous manner. In this theory, scattering polarization is taken into account, as well as the impact of the magnetic field (through both the Hanle and Zeeman effects). It can be shown that the redistribution matrix for a two-level atom with an infinitely sharp lower level can be given, in full generality, by

$$\left[\mathcal{R}(\nu',\vec{\Omega}',\nu,\vec{\Omega})\right]_{ij} = \left[\mathcal{R}_{\mathrm{II}}(\nu',\vec{\Omega}',\nu,\vec{\Omega})\right]_{ij} + \left[\mathcal{R}_{\mathrm{III}}(\nu',\vec{\Omega}',\nu,\vec{\Omega})\right]_{ij} \tag{2.43}$$

where $\mathcal{R}_{\mathrm{II}}$ is the term which describes the limit of coherent scattering (CS), i.e., the case in which the incoming and scattered photons have the same frequency in the atomic rest frame, and $\mathcal{R}_{\mathrm{III}}$ describes the limit of CRD in the atomic rest frame, meaning that the frequencies ν' and ν are uncorrelated. In the atomic rest frame, when the quantization axis for angular momentum is parallel to the direction of the

magnetic field, the $\mathcal{R}_{\rm II}$ redistribution matrix is given by (see Eq. (51) of Bommier 1997b)

$$\begin{aligned}\left[\mathcal{R}_{\rm II}(\nu',\vec{\Omega}',\nu,\vec{\Omega})\right]_{ij} &= \sum_{K'K''Q}\sum_{\substack{M_uM_u'M_\ell M_\ell'\\ pp'p''p'''}}\mathcal{C}_{K'K''QM_uM_u'M_\ell M_\ell'pp'p''p'''}\\ &\times\frac{\Gamma_R}{\Gamma_R+\Gamma_I+\Gamma_E+2\pi{\rm i}\nu_Lg_uQ}\\ &\times(-1)^Q\,\mathcal{T}^{K''}_{Q}(i,\vec{\Omega})\,\mathcal{T}^{K'}_{-Q}(j,\vec{\Omega}')\,\delta(\nu-\nu'-\nu_{M_\ell,M_\ell'})\\ &\times\frac{1}{2}\left[\Phi(\nu_{M_u',M_\ell}-\nu')+\Phi(\nu_{M_u,M_\ell}-\nu')^*\right].\end{aligned}\tag{2.44}$$

We remind the reader that the line broadening parameters

$$\Gamma_R=A_{u\ell}\,,\quad \Gamma_I=C_{u\ell}\,,\quad \Gamma_E=Q_{\rm el},\tag{2.45}$$

where $Q_{\rm el}$ is the elastic collisional rate. The $\mathcal{C}_{K'K''QM_uM_u'M_\ell M_\ell'pp'p''p'''}$ depends on the various quantum numbers involved. It is a real number given by (see Bommier 1997b)

$$\begin{aligned}&\mathcal{C}_{K'K''QM_uM_u'M_\ell M_\ell'pp'p''p'''}=3(2J_u+1)\sqrt{2K'+1}\sqrt{2K''+1}\,(-1)^{2J_u-M_\ell-M_\ell'}\\ &\times\begin{pmatrix}J_u&J_\ell&1\\M_u&-M_\ell&-p\end{pmatrix}\begin{pmatrix}J_u&J_\ell&1\\M_u'&-M_\ell&-p'\end{pmatrix}\begin{pmatrix}J_u&J_\ell&1\\M_u&-M_\ell'&-p''\end{pmatrix}\\ &\times\begin{pmatrix}J_u&J_\ell&1\\M_u'&-M_\ell'&-p'''\end{pmatrix}\begin{pmatrix}1&1&K'\\-p&p'&Q\end{pmatrix}\begin{pmatrix}1&1&K''\\-p''&p'''&Q\end{pmatrix}.\end{aligned}\tag{2.46}$$

The $\mathcal{R}_{\rm III}$ redistribution matrix is given by (see Eq. 49 of Bommier 1997b)

$$\begin{aligned}&\left[\mathcal{R}_{\rm III}(\nu',\vec{\Omega}',\nu,\vec{\Omega})\right]_{ij}=\\ &\sum_{KK'K''Q}\left[\frac{\Gamma_R}{\Gamma_R+\Gamma_I+D^{(K)}+2\pi{\rm i}\nu_Lg_uQ}-\frac{\Gamma_R}{\Gamma_R+\Gamma_I+\Gamma_E+2\pi{\rm i}\nu_Lg_uQ}\right]\\ &\times(-1)^Q\,\mathcal{T}^{K''}_{Q}(i,\vec{\Omega})\,\mathcal{T}^{K'}_{-Q}(j,\vec{\Omega}')\,\Phi^{KK''}_{Q}(J_\ell,J_u;\nu)\,\Phi^{KK'}_{Q}(J_\ell,J_u;\nu').\end{aligned}\tag{2.47}$$

The quotients appearing in the second and first lines of the right hand side of Eqs. (2.44) and (2.47), respectively, contain the branching ratios of such redistribution matrices. They determine the fraction of photons that, once absorbed by the atom, are re-emitted by coherent and non-coherent scattering processes. Relatedly, we define the coherence fraction as

$$\alpha_c=\frac{\Gamma_R+\Gamma_I}{\Gamma_R+\Gamma_I+\Gamma_R}\,,\tag{2.48}$$

which quantifies the probability that, after absorption, a photon will be emitted from the same atomic level before the atom is perturbed by an elastic collision

- and so the scattering processes is described by $\mathcal{R}_{\rm II}$ - provided that relaxation occurs through a radiative process. Moreover, we point out that the aforementioned quotients appearing in the redistribution matrices also contain information on the impact of the magnetic field on line scattering processes due to the Hanle effect, which modifies scattering polarization. For example, in the absence of collisions, the depolarization produced by the Hanle effect in $\mathcal{R}_{\rm II}$ (see Eq. (2.44)) becomes

$$\frac{\Gamma_R}{\Gamma_R+\Gamma_E+\Gamma_I+2\pi{\rm i}\nu_L g_u Q}=\frac{1}{1+{\rm i}H_u Q}\,, \tag{2.49}$$

where $H_u=2\pi g_u\nu_L/A_{u\ell}$ gives an indication of the efficiency of the Hanle effect in reducing scattering polarization. We point out that the Hanle effect only plays a role on the upper level, since we are considering a two-level atom with an unpolarized lower level. We take the Hanle critical field, i.e., the magnetic field strength that characterizes the onset of the Hanle effect, to be the field strength at which $H_u=1$. It can be written

$$B_c=\frac{1.137\cdot 10^{-7}A_{u\ell}}{g_u}\,. \tag{2.50}$$

At field strengths significantly below the Hanle critical field, the modification of scattering polarization introduced by the term containing H_u in Eq. (2.49) is small. On the other hand, when $H_u\gg 1$, further increases in field strength have very little impact on the scattering polarization, and the Hanle effect is said to have saturated. Note that the depolarization produced by the Hanle effect is independent of the Doppler width, and thus it is insensitive to the temperature of the medium and the wavelength of the line. Interestingly, the depolarizing efficiency of the Hanle effect is reduced when inelastic collisions, and the depolarizing effect of elastic collisions, are taken into account. This is known as the quenching of scattering polarization (see LL04).

2.5 Changing the reference frame

The expressions for $\mathcal{R}_{\rm II}$ and $\mathcal{R}_{\rm III}$ given in Eq. (2.44) and Eq. (2.47), respectively, are valid in the the atomic rest frame, in the case in which the quantization axis for angular momentum coincides with the direction of the magnetic field vector. In many cases, it is convenient to take the quantization axis in another direction, e.g., the vertical frame, in which the radiation field has much clearer symmetry properties, or to apply a translation to the reference frame in order to account for the Doppler shift due to the atmospheric motion with respect to the observer.

We first address the instance in which the total angular momentum's quantization axis is changed by performing a rotation of the reference system so that the axis is moved from the direction into the magnetic field (which we will hereafter refer to as the magnetic reference frame) into the desired, arbitrary direction. Such transformations are described by the so-called rotation matrices, defined through

$$\mathcal{D}^J_{MN}(R)=\langle JM\,|\,D(R)\,|\,JN\rangle\,, \tag{2.51}$$

where here $|JM\rangle$ and $|JN\rangle$ are angular momentum states. $D(R)$ is the rotation operator which rotates the entire reference system and is composed of three Euler angles $R = (\alpha, \beta, \gamma)$. It can be proven (see LL04) that such transformation can be written in terms of rotations around the initial z- and y-axes

$$D(R) = D_z(\alpha)\, D_y(\beta)\, D_z(\gamma) = \mathrm{e}^{-\mathrm{i}\alpha J_z}\, \mathrm{e}^{-\mathrm{i}\beta J_y}\, \mathrm{e}^{-\mathrm{i}\gamma J_z}\,. \tag{2.52}$$

We can further write the rotation matrix as

$$\mathcal{D}^J_{MN}(R) = \mathrm{e}^{-\mathrm{i}\alpha M}\, d^J_{MN}(\beta)\, \mathrm{e}^{-\mathrm{i}\gamma N}\,, \tag{2.53}$$

where $d^J_{MN}(\beta)$ is the so-called reduced rotation matrix (see Chapter 2 of LL04).

An irreducible spherical tensor of rank k is a tensor whose $(2k+1)$ components transform under rotation as

$$T'^k_q = \sum_p T^k_p \mathcal{D}^k_{qp}(R)\,. \tag{2.54}$$

Its inverse relation, which transforms the tensor from the new reference back into the original one is given by

$$T^k_q = \sum_p T'^k_p \mathcal{D}^k_{pq}(R)^*\,. \tag{2.55}$$

The polarization tensors $\mathcal{T}^K_Q(i, \vec{\Omega})$ are examples of irreducible spherical tensors. On the other hand, from the definition of the density matrix elements shown in Eq. (2.25), their transformation into the new reference frame can be found

$$\rho(\alpha JM, \alpha JM')\Big|_{\text{new}} = \sum_{NN'} \mathcal{D}^J_{NM}(R)^*\, \mathcal{D}^J_{N'M'}(R)\, \rho(\alpha JN, \alpha JN')\Big|_{\text{old}}\,. \tag{2.56}$$

Using Eq. (2.26), the transformation of the spherical statistical tensors into the new reference frame becomes

$$\rho^K_Q(\alpha J)\Big|_{\text{new}} = \sum_{Q'} \rho^K_{Q'}(\alpha J)\Big|_{\text{old}}\, \mathcal{D}^K_{Q'Q}(R)^*\,. \tag{2.57}$$

Their transformations involve the complex conjugate of rotation matrices, instead of rotation matrices themselves, so strictly speaking they are not irreducible spherical tensors. With an alternative definition of the density matrix elements, one could easily obtain spherical statistical tensors which satisfy the transformation law for irreducible spherical tensors. We note, however, that this alternative definition would offer no advantages over the one presented here. The inverse transformation for the spherical statistical tensors is

$$\rho^K_Q(\alpha J)\Big|_{\text{old}} = \sum_{Q'} \rho^K_{Q'}(\alpha J)\Big|_{\text{new}}\, \mathcal{D}^K_{QQ'}(R)\,. \tag{2.58}$$

Given that the emission coefficient's dependence on the selection of the quantization axis is implicit in the spherical statistical tensors ρ^K_Q and the polarization tensors $\mathcal{T}^K_Q(i,\vec{\Omega})$, one can obtain the transformation law for $\varepsilon_i(\nu,\vec{\Omega})$ from those shown in Eqs. (2.54 - 2.58), as is discussed, e.g., in Sect 7.12 of LL04. Then, one can easily find the transformation law for the redistribution matrix through Eq. (2.41).

The redistribution matrix can be obtained by introducing the analytical solution of the SE equations into the expression of the emission coefficient. All the information on the geometry of the physical process is contained in the polarization tensor $\mathcal{T}^K_Q(i,\vec{\Omega})$. The transformation law of the redistribution matrix can thus be obtained simply by rotating the polarization tensor according to Eq. (2.54). Performing such transformations, we obtain

$$\begin{aligned}
&\left[\mathcal{R}_{\rm II}(\nu',\vec{\Omega}',\nu,\vec{\Omega})\right]_{ij} = \\
&\sum_{K'K''QQ'Q''}\sum_{\substack{M_u{}'M_uM_\ell M_\ell{}'\\ pp'p''p'''}} \mathcal{C}_{K'K''QM_uM_u{}'M_\ell M_\ell{}'pp'p''p'''}\frac{\Gamma_R}{\Gamma_R+\Gamma_I+\Gamma_E+2\pi{\rm i}\nu_L g_u Q}\\
&\times(-1)^{Q'}\,\mathcal{T}^{K''}_{Q''}(i,\vec{\Omega})\,\mathcal{T}^{K'}_{-Q'}(j,\vec{\Omega}')\mathcal{D}^{K'}_{QQ'}(R_B)\,\mathcal{D}^{K''}_{QQ''}(R_B)^*\\
&\times\delta(\nu-\nu'-\nu_{M_\ell,M_\ell{}'})\frac{1}{2}\left[\Phi(\nu_{M_u{}',M_\ell}-\nu')+\Phi(\nu_{M_u,M_\ell}-\nu')^*\right],
\end{aligned}\tag{2.59}$$

and

$$\begin{aligned}
&\left[\mathcal{R}_{\rm III}(\nu',\vec{\Omega},\nu,\vec{\Omega})\right]_{ij} = \\
&\sum_{KK'K''QQ'Q''}\left[\frac{\Gamma_R}{\Gamma_R+\Gamma_I+D^{(K)}+2\pi{\rm i}\nu_L g_u Q}-\frac{\Gamma_R}{\Gamma_R+\Gamma_I+\Gamma_E+2\pi{\rm i}\nu_L g_u Q}\right]\\
&\times(-1)^{Q'}\,\mathcal{T}^{K''}_{Q''}(i,\vec{\Omega})\,\mathcal{T}^{K'}_{-Q'}(j,\vec{\Omega}')\mathcal{D}^{K'}_{QQ'}(R_B)\,\mathcal{D}^{K''}_{QQ''}(R_B)^*\\
&\times\Phi^{KK''}_Q(J_\ell,J_u;\nu)\,\Phi^{KK'}_Q(J_\ell,J_u;\nu')\,.
\end{aligned}\tag{2.60}$$

Here, $R_B=(-\gamma_B,-\theta_B,-\chi_B)$ is the rotation that brings the system from the magnetic reference frame into an arbitrary reference frame. The collisional part of the line emission coefficient in the new reference frame, using the relation shown in Eq. (2.55), is

$$\varepsilon^{\ell,{\rm coll}}=k_L\frac{\epsilon'}{1+\epsilon'}B_{\nu_0}(T)\sum_K\Phi^{0,K}_0(J_\ell,J_u;\nu)\sum_Q\mathcal{T}^K_Q(i,\vec{\Omega})\mathcal{D}^K_{0Q}(R_B)^*\,.\tag{2.61}$$

Similarly, the line components of the propagation matrix elements can be written in the new frame

$$\eta^\ell_i(\nu,\vec{\Omega})=k_L\sum_K\Phi^{0K}_0(J_\ell,J_u;\nu)\sum_Q\mathcal{T}^K_Q(i,\vec{\Omega})\mathcal{D}^K_{0Q}(R_B)^*\,,\tag{2.62a}$$

$$\rho^\ell_i(\nu,\vec{\Omega})=k_L\sum_K\Phi^{0K}_0(J_\ell,J_u;\nu)\sum_Q\mathcal{T}^K_Q(i,\vec{\Omega})\mathcal{D}^K_{0Q}(R_B)^*\,.\tag{2.62b}$$

Note that all the transformations we have presented in this section are independent on the choice of the γ_B angle, which we will take to be zero.

Now we discuss the transformation from the atomic rest frame into the observer's frame, in which the atomic velocities must be accounted for. Only random small-scale atomic motions are considered, but not bulk velocities. In the atomic reference frame, the frequency and angular dependencies of the redistribution matrix can be factorized

$$\Big[\mathcal{R}_X(\nu',\vec{\Omega}',\nu,\vec{\Omega})\Big]_{ij} = \sum_{K'K''Q} \Big[R_X\Big]_Q^{K'K''}(\nu',\nu)\Big[\mathcal{P}_Q^{K'K''}(\vec{\Omega},\vec{\Omega}')\Big]_{ij}\,, \tag{2.63}$$

where $X = \big(\mathrm{II},\mathrm{III}\big)$. Note that the geometric dependence is the same for both $\mathcal{R}_{\mathrm{II}}$ and $\mathcal{R}_{\mathrm{III}}$. Therefore, it is immediate to realize that the full redistribution matrix shown in Eq. (2.43) allows for an analogous factorization with

$$R_Q^{K'K''}(\nu',\nu) = \Big[R_{\mathrm{II}}\Big]_Q^{K'K''}(\nu',\nu) + \Big[R_{\mathrm{III}}\Big]_Q^{K'K''}(\nu',\nu)\,. \tag{2.64}$$

In a reference frame where the quantization axis for total angular momentum is rotated into an arbitrary direction

$$\Big[\mathcal{P}_Q^{K'K''}(\vec{\Omega},\vec{\Omega}')\Big]_{ij} = \sum_{Q'Q''}(-1)^{Q'}\mathcal{T}_{Q''}^{K''}(i,\vec{\Omega})\mathcal{T}_{-Q'}^{K'}(j,\vec{\Omega}')\mathcal{D}_{QQ'}^{K'}(R_B)\mathcal{D}_{QQ''}^{K''}(R_B)^*\,. \tag{2.65}$$

Although $\mathcal{P}_Q^{K'K''}(\vec{\Omega},\vec{\Omega}')$ remains unchanged in the observer's reference frame, the Doppler effect modifies the frequency redistribution and so the components of R_X must be appropriately transformed. Let us consider an atom with velocity $\vec{v}$. If $|\vec{v}| \ll c$, and provided that the values of R_X are only significant when $\frac{|\nu-\nu_0|}{\nu} \ll 1$ and $\frac{|\nu'-\nu_0|}{\nu'} \ll 1$ then, to first order in ν_0/c, the frequencies transform into the observer's frame as

$$\nu \to \nu - \frac{\nu_0}{c}\vec{v}\cdot\vec{\Omega}\,; \tag{2.66a}$$

$$\nu' \to \nu' - \frac{\nu_0}{c}\vec{v}\cdot\vec{\Omega}'\,. \tag{2.66b}$$

If we construct a Cartesian coordinate system such that the scattering process is contained in the $x-y$ plane and the x-axis is defined so that it bisects the scattering angle Θ, these transformations can be rewritten

$$\nu \to \nu - \frac{\nu_0}{c}\Big[v_x\,\alpha - v_y\,\beta\Big]\,; \tag{2.67a}$$

$$\nu' \to \nu' - \frac{\nu_0}{c}\Big[v_x\,\alpha + v_y\,\beta\Big]\,, \tag{2.67b}$$

with $\alpha = \cos\frac{\Theta}{2}$ and $\beta = \sin\frac{\Theta}{2}$. The expression for $\big[R_X\big]_Q^{K'K''}(\nu',\nu)$ can be easily found from Eqs. (2.63) and (2.65), and for the coherent scattering redistribution

function we can further decompose it into

$$\Big[R_{\rm II}\Big]_Q^{K'K''}(\nu',\nu) = \sum_{\substack{M_u{}'M_uM_\ell M_\ell{}'\\ pp'p''p'''}} f(\nu')\,\delta(\nu-\nu'-\nu_{M_\ell,M_\ell{}'})\,. \tag{2.68}$$

For notational simplicity, we have not explicitly shown the dependence of function $f(\nu')$ on the magnetic quantum numbers and on the indices appearing in the sum. Accounting for the Doppler shift as shown in Eqs. (2.67), it can be written

$$\Big[R_{\rm II}\Big]_Q^{K'K''}(\nu',\nu) = \sum_{\substack{M_u{}'M_uM_\ell M_\ell{}'\\ pp'p''p'''}} f\Big(\nu'-\frac{\nu_0}{c}\Big[v_x\,\alpha\,+\,v_y\,\beta\Big]\Big)$$
$$\times\,\delta\big(\nu-\nu'-\nu_{M_\ell,M_\ell{}'}\,+2\,\frac{\nu_0}{c}v_y\,\beta\big)\,. \tag{2.69}$$

In order to account for the small-scale random atomic motions, we must integrate the redistribution function over a its velocity distribution. We take a Maxwellian distribution of the form

$$P(v_x,v_y,v_z) = \left(\frac{m}{2\pi k_BT}\right)^{3/2}\exp\left[-m\frac{v_x^2+v_y^2+v_z^2}{2k_BT}\right]\mathrm{d}v_x\,\mathrm{d}v_y\,\mathrm{d}v_z\,, \tag{2.70}$$

where m is the atom's mass. In this case, the Doppler width is

$$\Delta\nu_D = \frac{\nu_0}{c}\left(\frac{2k_BT}{m}\right)^{1/2}. \tag{2.71}$$

It is now convenient to introduce the reduced velocity, which a dimensionless parameter defined as

$$\vec{u} = \left(\frac{m}{2k_BT}\right)^{1/2}\vec{v}\,.$$

Integrating Eq. (2.69) over the reduced velocities, weighted with the Maxwellian distribution shown in Eq. (2.70) leads to

$$\Big[R_{\rm II}^{\rm obs}\Big]_Q^{K'K''}(\nu',\nu) = \frac{1}{\pi}\int\int \mathrm{d}u_x\,\mathrm{d}u_y\,\mathrm{e}^{-u_x^2}\,\mathrm{e}^{-u_y^2}$$
$$\times\,f\Big(\nu'-\frac{\nu_0}{c}\Big[v_x\,\alpha+v_y\,\beta\Big]\Big)\delta\Big(\nu-\nu'-\nu_{M_\ell,M_\ell{}'}+2\,\frac{\nu_0}{c}v_y\,\beta\Big)\,, \tag{2.72}$$

where the relation $\int_{-\infty}^{\infty}e^{-x^2}\,\mathrm{d}x=\sqrt{\pi}$ has been used. Then, using the properties of the Dirac delta,

$$\Big[R_{\rm II}^{\rm obs}\Big]_Q^{K'K''}(\nu',\nu) = \frac{1}{\pi}\sum_{\substack{M_u{}'M_uM_\ell M_\ell{}'\\ pp'p''p'''}}\frac{1}{2\Delta\nu_D\,\beta}\exp\left[-\Big(\frac{\nu-\nu'-\nu_{M_\ell,M_\ell{}'}}{2\Delta\nu_D\,\beta}\Big)^2\right]$$
$$\times\int_{-\infty}^{\infty}\mathrm{d}u_x\,e^{-u_x^2}f\Big(\frac{\nu+\nu'-\nu_{M_\ell,M_\ell{}'}}{2}-\Delta\nu_D\,\alpha u_x\Big)\,. \tag{2.73}$$

Now, using the $f(\nu)$ from Eq. (2.59), and defining

$$W(a,x) = H(a,x) + \mathrm{i}\,L(a,x)\,, \tag{2.74}$$

where H and L are the Voigt profile and associated dispersion profile shown in Eq. (2.20), the frequency-dependent components are found to be

$$\begin{aligned}\left[R_{\mathrm{II}}^{\mathrm{obs}}\right]_Q^{K'K''}(\nu',\nu) = &\frac{1}{\pi}\frac{1}{2\beta\Delta\nu_D}\frac{1}{\alpha\Delta\nu_D}\sum_{\substack{M_u{}'M_uM_\ell M_\ell'\\ pp'p''p'''}}\mathcal{C}_{K'K''QM_uM_u{}'M_\ell M_\ell' pp'p''p'''}\\ &\times\frac{\Gamma_R}{\Gamma_R+\Gamma_I+\Gamma_E+2\pi\mathrm{i}\nu_L g_{J_u}Q}\exp\left[-\left(\frac{\nu-\nu'-\nu_{M_\ell,M_\ell'}}{2\Delta\nu_D\beta}\right)^2\right]\\ &\times\frac{1}{2}\left[W\left(\frac{a}{\alpha},\frac{\nu_{M_u{}',M_\ell}+\nu_{M_u{}',M_\ell'}-\nu-\nu'}{2\alpha\Delta\nu_D}\right)+\right.\\ &\left.+\,W\left(\frac{a}{\alpha},\frac{\nu_{M_u,M_\ell}+\nu_{M_u,M_\ell'}-\nu-\nu'}{2\alpha\Delta\nu_D}\right)^*\right].\end{aligned} \tag{2.75}$$

Clearly, due to the Doppler shift, the R_X factors of Eq. (2.63) are no longer independent of the scattering angle. Thus, the frequency and angular dependencies are coupled to one another in the observer's reference frame. Nevertheless, this difficulty can be avoided using the angle-averaged approximation described in Rees & Saliba (1982). Averaging $R_{\mathrm{II}}^{\mathrm{obs}}$ over all possible directions $\vec{\Omega}$ and $\vec{\Omega}'$, we obtain

$$\begin{aligned}\left[R_{\mathrm{II\text{-}AA}}^{\mathrm{obs}}\right]_Q^{K'K''}(\nu',\nu;B) = &\sum_{\substack{M_uM_u{}'M_\ell M_\ell'\\ pp'p''p'''}}\mathcal{C}_{K'K''QM_uM_u{}'M_\ell M_\ell' pp'p''p'''}\\ &\frac{\Gamma_R}{\Gamma_R+\Gamma_I+\Gamma_E+\mathrm{i}\omega_L g_{J_u}Q}\frac{1}{2\pi\Delta\nu_D{}^2}\int_0^\pi \mathrm{d}\Theta\exp\left[-\left(\frac{\nu'-\nu+\nu_{M_\ell,M_\ell'}}{2\Delta\nu_D\sin(\Theta/2)}\right)^2\right]\\ &\times\frac{1}{2}\left[W\left(\frac{a}{\cos(\Theta/2)},\frac{x_{M_u{}'M_\ell}+x'_{M_u{}'M_\ell'}}{2\cos(\Theta/2)}\right)\right.\\ &\left.+\,W\left(\frac{a}{\cos(\Theta/2)},\frac{x_{M_uM_\ell}+x'_{M_uM_\ell'}}{2\cos(\Theta/2)}\right)^*\right],\end{aligned} \tag{2.76}$$

where the reduced frequencies, including Zeeman frequency shifts,

$$x_{M_uM_\ell} = \frac{\nu_{M_u,M_\ell}-\nu}{\Delta\nu_D},\; x'_{M_uM_\ell} = \frac{\nu_{M_u,M_\ell}-\nu'}{\Delta\nu_D}\,,$$

have been introduced.

In the calculations presented in the following chapters, such angle-average is performed numerically using a Gauss-Legendre quadrature for the scattering angle.

The number of quadrature points that are required in order to achieve accurate results depends on the parameter appearing in the exponential in Eq. (2.76)

$$b = \frac{\nu' - \nu + \nu_{M_\ell, M_{\ell'}}}{2\Delta\nu_D} \,. \tag{2.77}$$

When it is essentially zero (i.e, when $b \leq 10^{-20}$), the integrand in Eq. (2.76) is very sensitive to variations in Θ, and in the calculations presented in the following chapters, a large number of quadrature points are taken in this case (namely, 100). As b increases ($10^{-20} < b \leq 1.5$), the integrand's dependence on the scattering angle is not as sharp, and 45 quadrature points are taken instead. For larger values of b, the angular dependence of the integrand is very smooth, and so only 15 points are taken

An analogous expression can be found for the $\mathcal{R}_{\rm III}$ redistribution matrix in the observer's reference frame, but the resulting expression is even more involved. For this reason, we will make the assumption of CRD in the observer's frame. In this case, we convolve the absorption and emission profiles with a Gaussian function which accounts for the Doppler broadening due to the small-scale random atmospheric motions. The resulting redistribution matrix is formally identical to Eq. (2.60), having substituted the Lorentzian profiles and its associated dispersion profiles by Voigt profiles and *its* associated dispersion profiles, respectively.

As shown in Eq. (2.41), obtaining the emission coefficients requires an integration over incoming frequencies, weighted by the redistribution matrices. In the calculations presented in the following chapters, the frequency integration is performed numerically over a discrete spectral grid. For $R_{\rm III}$, the frequency grids considered in the calculations are fine enough that a trapezoidal quadrature is suitable. However, the $R_{\rm II}$ redistribution matrix presents peaked structures in the spectral region around $\nu' = \nu$ (see Gouttebroze 1986) and so it requires a more precise evaluation of the numerical integration. One approach is to use cardinal natural cubic splines (see Adams et al. 1971 for a discussion on the properties of such splines; see also Belluzzi & Trujillo Bueno 2014). Using spline interpolation to perform the numerical integration, accurate results can be obtained with a small number points. However, due to the frequency shifts induced by the Zeeman effect, the peaks of $R_{\rm II}$ located at $\nu' = \nu + \nu_{M_\ell, M_{\ell'}}$ (see Eq. 2.76) may not coincide with any of the spectral points on the grid. In this case, numerical noise may be produced. Instead, in the calculations presented in the following chapters, the integration is performed by using a trapezoidal quadrature, but subdividing the spectral grid so that the separation between points is smaller than $2 \cdot 10^{-2}\Delta\nu_D$. When calculating the emission coefficient, the radiation field is considered to vary linearly in the interval between two adjacent points in the unrefined spectral grid. Although refining the grid in this manner requires the evaluation of $R_{\rm II}$ at many spectral points, which may be time-consuming, their values are independent of the radiation field, and therefore they only need to be calculated once.

Furthermore, when considering a one-dimensional model atmosphere, the atmospheric motions cannot be accounted for in a consistent manner. As a consequence,

the Doppler width of the line would be underestimated. The random small-scale atomic motions are included in the calculations by introducing a so-called microturbulent velocity, so that the Doppler width is

$$\Delta\nu_D = \frac{\nu_0}{c}\left(\frac{2\pi k_B T}{m} + \xi^2\right)^{1/2} . \tag{2.78}$$

2.6 Microstructured magnetic fields

Up to now, only the case in which the magnetic field has a fixed strength and orientation at any given point in the atmosphere has been discussed. However, it is also interesting to study the case in which the magnetic field changes its orientation over distances smaller than the line photon's mean free path. Thus, for a discrete spatial grid, we can no longer consider that the magnetic field has a fixed direction at each height, but rather the field's orientation must be taken as an average of all possible field directions at every spatial element or grid point. Therefore, in the RT equation one must consider averages of all the quantities that depend on the orientation of the magnetic field

$$\frac{\mathrm{d}}{\mathrm{d}s}\begin{pmatrix} I \\ Q \\ U \\ V \end{pmatrix} = \begin{pmatrix} \langle\varepsilon_I\rangle \\ \langle\varepsilon_Q\rangle \\ \langle\varepsilon_U\rangle \\ \langle\varepsilon_V\rangle \end{pmatrix} - \begin{pmatrix} \langle\eta_I\rangle & \langle\eta_Q\rangle & \langle\eta_U\rangle & \langle\eta_V\rangle \\ \langle\eta_Q\rangle & \langle\eta_I\rangle & \langle\rho_V\rangle & -\langle\rho_U\rangle \\ \langle\eta_U\rangle & -\langle\rho_V\rangle & \langle\eta_I\rangle & \langle\rho_Q\rangle \\ \langle\eta_V\rangle & \langle\rho_U\rangle & -\langle\rho_Q\rangle & \langle\eta_I\rangle \end{pmatrix} \begin{pmatrix} I \\ Q \\ U \\ V \end{pmatrix} . \tag{2.79}$$

We note that the continuum components of all such quantities are independent of the strength and direction of the magnetic field. The dependence of the line components on the field direction is contained in the rotation matrices (see Eq. 2.62). We study two specific cases, (a) one in which any field inclination and azimuth is equally probable, and (b) one in which the inclination is fixed but there is no preferred azimuthal direction. For each of them, calculating the field averages only requires performing the averages over the factors composed of rotation matrices.

(a) Isotropic magnetic field case.

The average is performed over all inclinations (θ_B) and azimuths (χ_B) of the magnetic field

$$\frac{1}{4\pi}\int_0^{2\pi}\mathrm{d}\chi_B\int_0^{\pi}\mathrm{d}\theta_B\,\sin\theta_B \mathcal{D}^K_{0Q}(R_B)^* = \delta_{K0}\delta_{Q0}\,; \tag{2.80a}$$

$$\frac{1}{4\pi}\int_0^{2\pi}\mathrm{d}\chi_B\int_0^{\pi}\mathrm{d}\theta_B\,\sin\theta_B \mathcal{D}^{K'}_{QQ'}(R_B)\mathcal{D}^{K''}_{QQ''}(R_B)^* = \frac{1}{2K'+1}\delta_{K'K''}\delta_{Q'Q''}\,. \tag{2.80b}$$

The second relation has been obtained by making use of the Weyl theorem (see LL04). For an isotropic magnetic field, which is of course spherically symmetric, it can easily be seen from Eqs. (2.62) that the propagation matrix is diagonal and its

absorption coefficient is

$$\langle \eta_I \rangle^\ell (\nu, \vec{\Omega}) = k_L \sum_{M_\ell M_u q} \begin{pmatrix} J_u & J_\ell & 1 \\ -M_u & M_\ell & q \end{pmatrix}^2 \phi(\nu_{M_u, M_\ell} - \nu) \,. \tag{2.81}$$

The same field average can be used in the line part of the emissivity, using its expression in terms of the redistribution matrix in Eq. (2.41), the factorization in Eq. (2.63), and the expression for the radiation field tensor in Eq. (2.23)

$$\begin{aligned} \langle \varepsilon_i \rangle^\ell (\nu, \vec{\Omega}) = k_L \sum_{KQQ'} \frac{1}{2K+1} \mathcal{T}^K_Q(i, \vec{\Omega}) \int \mathrm{d}\nu' \, (-1)^Q J^K_{-Q}(\nu') \, R^{KK}_{Q'}(\nu', \nu) \\ + k_L \frac{\epsilon'}{1+\epsilon'} \Phi^{0,0}_0(J_\ell, J_u, \nu) B_{\nu_0}(T) \,. \end{aligned} \tag{2.82}$$

(b) Fixed inclination and random azimuth.
The inclination is kept fixed, while the average is performed over all azimuths

$$\frac{1}{2\pi} \int_0^{2\pi} \mathrm{d}\chi_B \, \mathcal{D}^K_{0Q}(R_B)^* = d^K_{00}(\theta_B) \, \delta_{Q0} \tag{2.83a}$$

$$\begin{aligned} &\frac{1}{2\pi} \int_0^{2\pi} \mathrm{d}\chi_B \, \mathcal{D}^{K'}_{QQ'}(R_B) \mathcal{D}^{K''}_{QQ''}(R_B)^* = \\ &= (-1)^{Q-Q'} \sum_\kappa (2\kappa+1) \begin{pmatrix} K' & K'' & \kappa \\ Q & -Q & 0 \end{pmatrix} \begin{pmatrix} K' & K'' & \kappa \\ Q' & -Q'' & 0 \end{pmatrix} d^\kappa_{00}(\theta_B) \,. \end{aligned} \tag{2.83b}$$

The expression for the elements of the propagation matrix, as well as for the emission coefficient in terms of the redistribution matrix, can be obtained in an analogous manner to the expressions for an isotropic magnetic field, but instead using the field averages shown in Eq. (2.83).

2.6.1 Numerical methods for the radiative transfer equation

Here we discuss the various numerical methods for solving the RT equation, implemented in the calculations shown in the following chapters. First, we introduce the optical depth scale as

$$\mathrm{d}\tau_\nu = -\eta_I(\nu, \vec{\Omega}, s) \, \mathrm{d}s \,. \tag{2.84}$$

Note that this scale depends on the frequency, but also on the direction of the line of sight (LOS). Using the optical depth scale, the equation shown in Eq. (2.6) can be reformulated as

$$\frac{\mathrm{d}}{\mathrm{d}\tau_\nu} \vec{I} = \hat{K}^* \vec{I} - \vec{S} \,, \tag{2.85}$$

In Eq. (2.85), we have introduced $\hat{K}^*(\nu, \vec{\Omega}) = \hat{K}(\nu, \vec{\Omega}) / \eta_I(\nu, \vec{\Omega})$ and the source function $\vec{S}(\nu, \vec{\Omega}) = \vec{\varepsilon}(\nu, \vec{\Omega}) / \eta_I(\nu, \vec{\Omega})$, for which its four components represent the source function in each of the Stokes parametres. The formal solutions of the RT equation that we consider in this thesis are all based on the concept of short-characteristics.

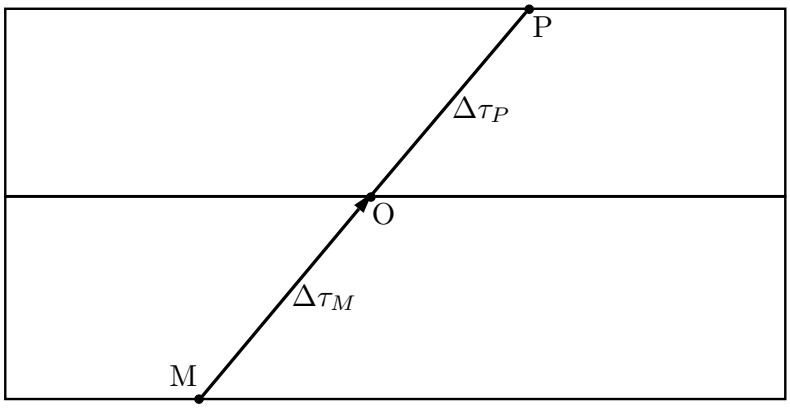

FIGURE 2.2— Ray propagating on a Cartesian grid, for a plane-parallel atmosphere, where O is the point under consideration, M is the upwind point and P is the downwind point. The optical distance between the M and O points (the short-characteristic) is $\Delta\tau_M$, and the optical distance between O and P is $\Delta\tau_P$. Such distances depend not only on the vertical separation between the points, but also on the inclination of the ray.

In order to better illustrate such short-characteristics methods, let us discretize a plane-parallel atmosphere, and consider a spatial point O. In short-characteristics methods, for a radiation beam propagating in a given direction, its intensity and polarization at point O can be obtained by interpolating in a specific interval, or short-characteristic, provided that such values are known at an upwind point M (see Fig. 2.2). First, we consider the simplified case in which the propagation matrix is diagonal. In this case, the equations for the four Stokes components are decoupled and the RT equation becomes

$$\frac{\mathrm{d}}{\mathrm{d}\tau_\nu} I_i = I_i - S_i \,. \tag{2.86}$$

In order to obtain the Stokes parameters at point O, we consider the adjacent grid points M (upwind) and P (downwind). For any frequency and direction

$$I_{i,O} = \mathrm{e}^{-\Delta\tau_M} I_{i,M} + \int_0^{\Delta\tau_M} S_i(t)\,\mathrm{d}t \tag{2.87}$$

where $\Delta\tau_M$ is the optical distance between points O and M, taken in absolute value. The solution of the integral of the source function depends on the exact short-characteristics method being used. As described in Kunasz & Auer (1988), it can be solved through parabolic interpolation by taking only the values at points

M, O, and P

$$\int_0^{\Delta\tau_M} S_i(t)\,\mathrm{d}t = \Psi_M S_{i,M} + \Psi_O S_{i,O} + \Psi_P S_{i,P}\,; \tag{2.88a}$$

$$\Psi_M = u_0(\Delta\tau_M) + \big[u_2(\Delta\tau_M) - (\Delta\tau_P + 2\Delta\tau_M) \times u_1(\Delta\tau_M)\big]/\big[\Delta\tau_M(\Delta\tau_M + \Delta\tau_P)\big]\,; \tag{2.88b}$$

$$\Psi_O = \big[(\Delta\tau_M + \Delta\tau_P)u_1(\Delta\tau_M) - u_2(\Delta\tau_M)\big]/(\Delta\tau_M\Delta\tau_P)\,; \tag{2.88c}$$

$$\Psi_P = \big[u_2(\Delta\tau_M) - \Delta\tau_M u_1(\Delta\tau_M)\big]/\big[\Delta\tau_P(\Delta\tau_M + \Delta\tau_P)\big]\,, \tag{2.88d}$$

where $\Delta\tau_P$ is the optical distance between spatial point O and P, and the factors

$$u_0(x) = 1 - \exp(-x)\,; \tag{2.89a}$$

$$u_1(x) = x - 1 + \exp(-x) = x - u_0(x)\,; \tag{2.89b}$$

$$u_2(x) = x^2 - 2x + 2 - 2\exp(-x) = x^2 - 2u_1(x)\,, \tag{2.89c}$$

are functions of the optical depth. We consider that there is no radation entering the upper boundary, and that the radiation entering the bottom boundary is assumed to be thermalized, i.e., its intensity is equal to the Planck function (e.g., Mihalas 1978). When considering the grid point on a boundary, such that its downwind point is outside the spatial grid, the P point cannot be considered, and so we must instead use linear interpolation

$$\int_0^{\Delta\tau_M} S_i(t)\,\mathrm{d}t = \Psi'_M S_{i,M} + \Psi'_O S_{i,O}\,; \tag{2.90a}$$

$$\Psi'_M = u_0(\Delta\tau_M) - u_1(\Delta\tau_M)/\Delta\tau_M\,; \tag{2.90b}$$

$$\Psi'_O = u_1(\Delta\tau_M)/\Delta\tau_M\,. \tag{2.90c}$$

DELO methods

In the case in which the propagation matrix is not diagonal, this short-characteristics method can be extended into the so-called DELO (Diagonal Element Lambda Operator) methods, first introduced by Rees et al. (1989). Given that the four Stokes parameters are coupled to one another, they must all be calculated simultaneously. The RT equation can be written

$$\frac{\mathrm{d}}{\mathrm{d}\tau}\vec{I} = \vec{I} - \vec{S}_{\mathrm{eff}} \tag{2.91}$$

where the effective source function $\vec{S}_{\mathrm{eff}} = \vec{S} - \hat{K}'\vec{I}$, and $\hat{K}' = \hat{K}^* - \mathbb{1}$. Thus, the Stokes parameter I_i can be found at point O through

$$I_{i,O} = \mathrm{e}^{-\Delta\tau_M} I_{i,M} + \int_0^{\Delta\tau_M} S_{i,\mathrm{eff}}(t)\,\mathrm{d}t\,. \tag{2.92}$$

Compared to the previous case, in which the propagation matrix is diagonal, there is a further difficulty; the effective source function, and thereby the Stokes parameters

at point O, are dependent on the Stokes parameters in the MOP spatial interval. When calculating the Stokes parameters at point O, the ones at point M have of course already been calculated, and $I_{i,O}$ can be used implicity. However, the values at the downwind point P will not be known, and so a parabolic interpolation cannot be used in this case. Instead, it is assumed that between points M and O the $\hat{K}'\vec{I}$ product changes linearly with t. This method is generally referred to as DELO-linear.

In the DELO-linear method, the source functions are assumed to depend linearly on τ_ν between points M and O, i.e., when solving the integral the entire $\vec{S}_{\text{eff}}$ is assumed to have a linear behavior in the interval between 0 and $\Delta\tau_M$. Its formal solution is

$$\left[\mathbb{1} + {\Psi'}_O\hat{K'}_O\right]\vec{I}_O = \left[\mathrm{e}^{-\Delta\tau_M}\mathbb{1} - {\Psi'}_M\hat{K'}_M\right]\vec{I}_M + {\Psi'}_M\vec{S}_M + {\Psi'}_M\vec{S}_O\,. \tag{2.93}$$

On the other hand, on can also treat $\hat{K}'\vec{I}$ as varying linearly, but instead interpolating $\vec{S}$ parabolically. At point O, this formal solution, which we will refer to as DELOPAR (see Trujillo Bueno 2003), is

$$\left[\mathbb{1} + {\Psi'}_O\hat{K'}_O\right]\vec{I}_O = \left[\mathrm{e}^{-\Delta\tau_M}\mathbb{1} - {\Psi'}_M\hat{K'}_M\right]\vec{I}_M + \Psi_M\vec{S}_M + \Psi_O\vec{S}_O + \Psi_M\vec{S}_P\,. \tag{2.94}$$

In certain model atmospheres, this method has been found to yield inaccurate results, due to overshoots in the parabolic interpolation of the source function. Such inaccuracies may introduce errors in the calculated emergent profiles, or may even cause the entire numerical system to diverge. Auer (2003) proposed a method of solution based on the use of piecewise monotonic Bézier splines for the interpolations. Elaborating on this method, Štepán & Trujillo Bueno (2013) developed the BESSER (BEzier Spline SolvER) algorithm, which imposes the condition that the first derivative of such splines must be continuous around central point O. Thus, overshoots which would be produced if the source functions were simply interpolated parabolically can be avoided, and so BESSER tends to give much better results for atmospheric models in which there are abrupt changes in parameters such as temperature or density, while the overall increase in computation time is very small. In the calculations presented in the following chapters, a BESSER formal solution has been used, except where otherwise stated. For other methods of formal solution based on short-characteristics that use Bézier splines, see Holzreuter & Solanki (2012) and de la Cruz Rodríguez & Piskunov (2013). For a detailed discussion on the accuracy and stability of the most important formal solvers of the DELO family, see Janett et al. (2017).

The evolution operator formalism

Alternatively, the RT equation can be formulated in full generality by considering an evolution operator (see Landi Degl'Innocenti & Landi Degl'Innocenti 1985). This operator, $\hat{O}(s, s')$, is a 4×4 matrix that gives the Stokes vector at point s due to a

Stokes vector propagating from point s'

$$\vec{I}(s) = \hat{O}(s,s')\vec{I}(s')\,, \tag{2.95}$$

and when considering a material with a certain emissivity, the solution of the non-homogenous RT equation

$$\vec{I}(s) = \hat{O}(s,s')\,\vec{I}(s') + \int_{s'}^{s} \mathrm{d}s''\,\vec{\varepsilon}(s'')\,. \tag{2.96}$$

This evolution operator is defined as

$$\hat{O}(s,s') = \mathbb{1} + \\ + \sum_{n=1}^{\infty} \frac{(-1)^n}{n!} \int_{s'}^{s} \mathrm{d}s_1 \int_{s'}^{s} \mathrm{d}s_2 \cdots \int_{s'}^{s} \mathrm{d}s_n\, \mathbb{P}\Big\{\hat{K}(s_1)\,\hat{K}(s_2)\cdots\hat{K}(s_n)\Big\}\,, \tag{2.97}$$

where $\mathbb{P}$ is the Dyson chronological product. In most cases, this expression for the evolution operator cannot be simplified further, which limits its usefulness in solving the RT equation. However, provided that the propagation matrices commute with each other for any two points s_A and s_B in the (s',s) interval, it can be proven that the evolution operator can be expressed as

$$\hat{O}(s,s') = \mathrm{e}^{-\int_{s'}^{s}\hat{K}(s'')\mathrm{d}s''}\,. \tag{2.98}$$

We will consider two specific scenarios in which such propagation matrices commute, which are relevant for the following chapters. We study the case in which the matrices are independent of s, and the case in which, no matter their spatial dependence, the only nonzero components of the matrix are η_I and ρ_V. In the first case the integral in Eq. (2.98) becomes

$$\hat{O}(s,s') = \mathrm{e}^{-(s-s')\hat{K}}\,, \tag{2.99}$$

which, using some algebra, can be rewritten as (see Landi Degl'Innocenti & Landi Degl'Innocenti 1985)

$$\begin{aligned}\hat{O}(s,s') = &\,\mathrm{e}^{-(s-s')\,\eta_I} \\ &\times \left\{\frac{1}{2}\Big[\cosh\big[(s-s')\Lambda_+(\vec{\eta},\vec{\rho})\big] + \cos\big[(s-s')\Lambda_-(\vec{\eta},\vec{\rho})\big]\Big]\hat{M}_1(\vec{\eta},\vec{\rho})\right. \\ &- \sin\big[(s-s')\Lambda_-(\vec{\eta},\vec{\rho})\big]\hat{M}_2(\vec{\eta},\vec{\rho}) - \sinh\big[(s-s')\Lambda_+(\vec{\eta},\vec{\rho})\big]\hat{M}_3(\vec{\eta},\vec{\rho}) \\ &\left. + \frac{1}{2}\Big[\cosh\big[(s-s')\Lambda_+(\vec{\eta},\vec{\rho})\big] - \cos\big[(s-s')\Lambda_-(\vec{\eta},\vec{\rho})\big]\Big]\hat{M}_4(\vec{\eta},\vec{\rho})\right\}, \end{aligned} \tag{2.100}$$

in which $\vec{\eta} = (\eta_Q, \eta_U, \eta_V)$ and $\vec{\rho} = (\rho_Q, \rho_U, \rho_V)$ have been introduced, as well as the variables

$$\Lambda_+(\vec{\eta},\vec{\rho}) = \sqrt{\sqrt{(\eta^2-\rho^2)^2/4 + (\vec{\eta}\cdot\vec{\rho})^2} + (\eta^2-\rho^2)/2}\,; \tag{2.101a}$$

$$\Lambda_-(\vec{\eta},\vec{\rho}) = \sqrt{\sqrt{(\eta^2-\rho^2)^2/4 + (\vec{\eta}\cdot\vec{\rho})^2} - (\eta^2-\rho^2)/2}\,. \tag{2.101b}$$

And the expressions for the $\hat{M}_i$ matrices can be found in Landi Degl'Innocenti & Landi Degl'Innocenti (1985).

Now let us consider the situation in which the only nonzero components of the propagation matrix are η_I and ρ_V, although their spatial dependence is unconstrained. Here, the propagation matrix can be written as (e.g, LL04)

$$\hat{K}(s) = \eta_I(s)\,\mathbb{1} + \frac{\mathrm{i}}{2}\rho_V(s)\,\hat{A}_3 - \frac{\mathrm{i}}{2}\rho_V(s)\,\hat{B}_3\,, \tag{2.102}$$

where

$$\hat{A}_3 = \hat{B}_3^* = \begin{pmatrix} 0 & 0 & 0 & 1 \\ 0 & 0 & -\mathrm{i} & 0 \\ 0 & \mathrm{i} & 0 & 0 \\ 1 & 0 & 0 & 0 \end{pmatrix} \tag{2.103}$$

and so $\hat{A}_3 \cdot \hat{B}_3 = \hat{B}_3 \cdot \hat{A}_3 = \mathbb{1}$ and

$$\hat{A}_3^2 = \hat{B}_2^2 = \begin{pmatrix} 1 & 0 & 0 & 0 \\ 0 & -1 & 0 & 0 \\ 0 & 0 & -1 & 0 \\ 0 & 0 & 0 & 1 \end{pmatrix}. \tag{2.104}$$

The evolution operator in this case becomes

$$\hat{O}(s,s') = \mathrm{e}^{-H_I \mathbb{1}}\,\mathrm{e}^{-\frac{\mathrm{i}}{2}R_V\hat{A}_3}\,\mathrm{e}^{\frac{\mathrm{i}}{2}R_V\hat{B}_3}\,, \tag{2.105}$$

with

$$H_I = \int_{s'}^{s} \eta_I(s'')\,\mathrm{d}s''\,, \quad R_V = \int_{s'}^{s} \rho_V(s'')\mathrm{d}s''\,, \tag{2.106}$$

from which we can obtain

$$\hat{O}(s,s') = \mathrm{e}^{-H_I} \begin{pmatrix} 1 & 0 & 0 & 0 \\ 0 & \cos R_V & -\sin R_V & 0 \\ 0 & \sin R_V & \cos R_V & 0 \\ 0 & 0 & 0 & 1 \end{pmatrix}. \tag{2.107}$$

If the spatial grid is discrete, and if one considers point O, whose adjacent upwind and downwing points are M and P, respectively, Eq. (2.96) can be rewritten in terms of optical distance

$$\vec{I}_O = \hat{O}(0,\Delta\tau_M)\vec{I}_M + \int_0^{\Delta\tau_M} \mathrm{d}t\,\hat{O}(t,\Delta\tau_M)\vec{S}(t)\,, \tag{2.108}$$

and, interpolating parabolically in analogy to Eq. (2.87), the Stokes vector at point O becomes

$$\vec{I}_O = \hat{O}(0,\Delta\tau_M)\,\vec{I}_M + \hat{\Psi}_M\,\vec{S}_M + \hat{\Psi}_O\,\vec{S}_O + \hat{\Psi}_P\,\vec{S}_P\,, \tag{2.109}$$

where the expressions for the interpolation factors are now 4×4 matrices of the form

$$\hat{\Psi}_M = \hat{u}_0(\Delta\tau_M) + \big[\hat{u}_2(\Delta\tau_M) - (\Delta\tau_P + 2\Delta\tau_M) \times \hat{u}_1(\Delta\tau_M)\big]/\big[\Delta\tau_M(\Delta\tau_M + \Delta\tau_P)\big]\,; \tag{2.110a}$$

$$\hat{\Psi}_O = \big[(\Delta\tau_M + \Delta\tau_P)\hat{u}_1(\Delta\tau_M) - \hat{u}_2(\Delta\tau_M)\big]/(\Delta\tau_M\Delta\tau_P)\,; \tag{2.110b}$$

$$\hat{\Psi}_P = \big[\hat{u}_2(\Delta\tau_M) - \Delta\tau_M\hat{u}_1(\Delta\tau_M)\big]/\big[\Delta\tau_P(\Delta\tau_M + \Delta\tau_P)\big]\,, \tag{2.110c}$$

and

$$\hat{u}_0(x) = \hat{K'}^{-1}\big[\mathbb{1} - \hat{O}(0,x)\big]\,; \tag{2.111a}$$

$$\hat{u}_1(x) = \hat{K'}^{-1}\big[x\mathbb{1} - \hat{u}_0(x)\big]\,; \tag{2.111b}$$

$$\hat{u}_2(x) = \hat{K'}^{-1}\big[x^2\mathbb{1} - \hat{u}_1(x)\big]\,. \tag{2.111c}$$

The assumption has been made that the elements of the propagation matrix are constant in the interval between gridpoints M and O, taking each element as the average of their values at the two points, for the direction under consideration. Such constraint can lead to significant errors in the calculation, unless a sufficiently fine spatial grid is considered.

2.7 Iterative methods

Due to the fact that the RT equations and the expressions for the emission coefficient, which in the formalism considered here involve the redistribution matrices, are coupled to one another, they cannot be solved independently. Furthermore, the radiation field at a specific point in the atmosphere is sensitive to the emissivity at other points in the atmosphere, and to the transfer properties of the material. Thus, when solving this non-LTE problem, one requires a self-consistent solution of the two sets of equations, which must be solved iteratively until the solution converges. The first difficulty in this problem is that of non-locality, which has been addressed by Olson et al. (1986) and Scharmer (1981), using operator splitting methods (e.g., Varga 1962). We now briefly discuss such methods, based on the description presented in Trujillo Bueno & Fabiani Bendicho (1995)

2.7.1 Operator splitting methods: general theory

Say that we have a system of algebraic equations of the form

$$\hat{A}\,\vec{u} = \vec{b}\,, \tag{2.112}$$

where $\vec{u}$ is the unknown (for example the source function at every height point), $\vec{b}$ is a known vector, while $\hat{A}$ is an operator. Now, say that we have an approximate solution $\vec{u}^{\,\mathrm{old}}$ which gives a residual of the form

$$\vec{r} = \vec{b} - \hat{A}\,\vec{u}^{\,\mathrm{old}} = \hat{A}\,\vec{e}\,, \tag{2.113}$$

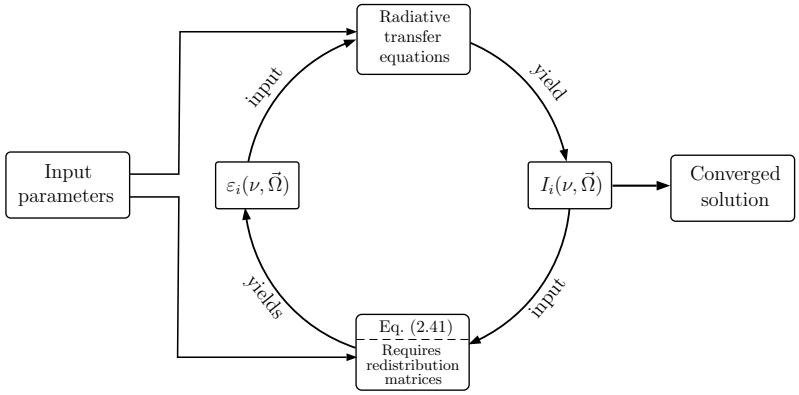

FIGURE 2.3— Schematic representation of the non-LTE problem of the second kind. In the following chapters, the problem is solved by iterating the radiative transfer (RT) equations and statistical equilibrium (SE) equations, in this case contained in the redistribution matrices, until a self-consistent solution is reached.

where $\vec{e}$ is the error, such that $\vec{u} = \vec{u}^{\,\mathrm{old}} + \vec{e}$. However, this equation has the same degree of complexity as the previous one. Instead, an approximate correction can be found as

$$\hat{A}^* \, \vec{e} = \vec{r} \, . \tag{2.114}$$

$\hat{A}^*$ is an approximate operator with a form that allows for a simpler calculation than when using $\hat{A}$. Given that the "true" value of $\vec{u}$ is unknown, we instead consider corrections of the form $\vec{\Delta u} = \vec{u}^{\,\mathrm{new}} - \vec{u}^{\,\mathrm{old}}$, leading to the system

$$\hat{A}^* \, \vec{\Delta u} = \vec{b} - \hat{A} \, \vec{u}^{\,\mathrm{old}} \, , \tag{2.115}$$

or

$$\vec{\Delta u} = \left[\hat{A}^*\right]^{-1} \left[\vec{b} - \hat{A} \, \vec{u}^{\,\mathrm{old}}\right] \tag{2.116}$$

By applying the previous equation iteratively, if a suitable $\hat{A}^*$ has been used, the $\vec{\Delta u}$ correction becomes progressively smaller, and we say the solution converges.

2.7.2 Operator splitting methods: Polarized case with frequency redistribution

In full generality, on a discrete spatial grid with N_P points, the i Stokes parameters for radiation at point n, propagating in direction Ω with frequency ν, can be written in terms of the source functions with the same frequencies and directions of propagation:

$$I_i(\nu,\vec{\Omega},n) = \sum_{j=0}^{3} \sum_{m=1}^{N_P} \Lambda_{\nu,\vec{\Omega}}(n,m)_{ij} S_j(\nu,\vec{\Omega},m) + T_i(\nu,\vec{\Omega},n) \, . \tag{2.117}$$

Here, j indicates the Stokes component of the source function, and m is any spatial grid point. $T_i(\nu,\vec{\Omega},n)$ is the radiation transmitted from the boundary into grid point n. $\hat{\Lambda}$ is the formal operator which contains all information on the transfer of radiation between points contained inside the grid. Each $\Lambda_{\nu,\vec{\Omega}}(n,m)_{ij}$ element indicates the contribution to $I_i(\nu,\vec{\Omega})$ at point n due to the Stokes component of the source function $S_j(\nu,\vec{\Omega})$ whose value is 1 at point m and 0 everywhere else. Its value is determined by the elements of the propagation matrix and the formal solution of the RT equation. The source function can be decomposed into a line and continuum part, so at each spatial point

$$S_i(\nu,\vec{\Omega},n) = rS_i^{\ell}(\nu,\vec{\Omega},n) + (1-r)S_i^{c}(\nu,\vec{\Omega},n) \tag{2.118}$$

with

$$S_i^{\ell}(\nu,\vec{\Omega},n) = \frac{\varepsilon_i^{\ell}(\nu,\vec{\Omega},n)}{\eta_I^{\ell}(\nu,\vec{\Omega},n)} \quad \text{and} \quad S_i^{c}(\nu,\vec{\Omega},n) = \frac{\varepsilon_i^{c}(\nu,\vec{\Omega},n)}{\eta_I^{c}(\nu,n)}\,.$$

Although the dependence on frequency, direction, and spatial position for the r parameter has not been shown explicity, it is defined as

$$r = \frac{\eta_I^{\ell}(\nu,\vec{\Omega},n)}{\eta_i^{\ell}(\nu,\vec{\Omega},n) + \eta_I^{c}(\nu,n)}\,.$$

The emission coefficient can be decomposed into multipolar components as

$$\varepsilon_i^{Y}(\nu,\vec{\Omega},n) = \sum_{KQ} \mathcal{T}_Q^K(i,\vec{\Omega},n)\mathcal{E}_Q^K(\nu,n)^Y\,, \tag{2.119}$$

where $Y=(\ell,c)$ corresponds to the line and continuum contributions, respectively. As shown in Eq. (2.3), the total emissivity is the sum of the line and continuum parts, which is also the case for each of the multipolar components separately, i.e., $\mathcal{E}_Q^K(\nu,n) = \mathcal{E}_Q^K(\nu,n)^{\ell} + \mathcal{E}_Q^K(\nu,n)^{c}$. Furthermore, the line components are given by

$$\mathcal{E}_Q^K(\nu,n)^{\ell} = \mathcal{J}_Q^K(\nu,n) + k_L\frac{\epsilon'}{1+\epsilon'}B_{\nu_0}(T)\Phi_0^{0K}(J_{\ell},J_u;\nu)\mathcal{D}_{0Q}^K(R_B)^* \tag{2.120}$$

where its scattering component, $\mathcal{J}_Q^K(\nu,m)$, is

$$\mathcal{J}_Q^K(\nu,n) = k_L\sum_{K'Q'Q''}\mathcal{D}_{Q''Q'}^{K'}(R_B)\mathcal{D}_{Q''Q}^{K}(R_B)^*\int \mathrm{d}\nu'\,R_{Q''}^{K'K}(\nu',\nu,n)(-1)^{Q'}J_{-Q'}^{K'}(\nu',n)\,. \tag{2.121}$$

Writing the radiation field tensor as in Eq. (2.23), and using the expression for the Stokes parameters in terms of source functions at other grid points as in Eq. (2.117),

we have

$$\mathcal{J}^K_Q(\nu,n) = k_L \sum_{K'Q'Q''} \mathcal{D}^{K'}_{Q''Q'}(R_B)\mathcal{D}^K_{Q''Q}(R_B)^* \int \mathrm{d}\nu'\, R^{K'K}_{Q''}(\nu',\nu,n) \times (-1)^{Q'} \oint \frac{\mathrm{d}\vec{\Omega}'}{4\pi} \sum_{i=0}^{3} \mathcal{T}^{K'}_{-Q'}(i,\vec{\Omega}') \left\{ \sum_{m=1}^{N_P} \sum_{j=0}^{3} \Lambda_{\nu',\vec{\Omega}'}(n,m)_{ij} \times \left[\frac{\sum_{K_PQ_P} \mathcal{T}^{K_P}_{Q_P}(j,\vec{\Omega}')\mathcal{E}^{K_P}_{Q_P}(\nu',m)}{\eta_I(\nu',\vec{\Omega}',m)} + T_i(\nu',\vec{\Omega}';n) \right] \right\}. \quad (2.122)$$

From the previous equation, one can develop the corresponding iterative scheme. Starting from an estimate of the emission coefficient at all points[2], the RT equation such as the one contained in Eq. (2.117) is used to find a "new" value for the radiation field, from which a "new" value of the emission coefficient can be found through Eqs. (2.120) and (2.121). Since $\vec{u}$ in Eq. (2.112) corresponds to the emission coefficients, this is the case in which the approximate operator $\hat{A}^*$ is taken to be identity, and is known as the Lambda iteration method which, although it is conceptually simple, proves to have a very slow convergence rate in optically thick media (see Trujillo Bueno & Fabiani Bendicho 1995; also Trujillo Bueno & Manso Sainz 1999).

The convergence rate can be accelerated if, when calculating the emission coefficient (for example through $\mathcal{J}^K_Q$ in Eq. 2.122) at a given spatial point, instead of using the old value of the emission coefficient $\mathcal{E}^{K_P}_{Q_P}(\nu')^{\mathrm{old}}$, the new value at this spatial point is used implicilty in the calculation, while at the rest of the points the old values are used. In this case the approximate operator is diagonal, i.e. only $\Lambda_{\nu',\vec{\Omega}'}(n,n)_{ij}$ are considered, and this iterative method is known as Jacobi iteration. For the line contribution to the emission coefficient, where the optical distances can be very large at certain frequencies, we will make use of the Jacobi iterative method, while for the continuum contribution it will be suitable to consider Lambda iteration. For notational simplicity, in the remainder of this chapter we will use $\mathcal{E}^K_Q(\nu)$ to refer to the line part of the multipolar components of the emissivity. Therefore, in Eq. (2.122) together with Eq. (2.120), for each spatial grid point n

$$\Delta\mathcal{E}^K_Q(\nu;n) = k_L \frac{\epsilon'}{1+\epsilon'} B_{\nu_0}(T)\, \Phi^{0K}_0(J_\ell,J_u;\nu)\mathcal{D}^K_{0Q}(R_B)^* + \left[\mathcal{J}^K_Q(\nu;n)\right]^{\mathrm{old}} - \left[\mathcal{E}^K_Q(\nu;n)\right]^{\mathrm{old}} + \int \mathrm{d}\nu' \sum_{K_PQ_P} \Lambda_{KQ,K_PQ_P}(\nu',\nu;n)\Delta\mathcal{E}^{K_P}_{Q_P}(\nu';n)\,, \quad (2.123)$$

[2]Such estimate can be calculated first from an estimate of the radiation field tensor.

where

$$\Lambda_{KQ,K_PQ_P}(\nu',\nu;n) = k_L \sum_{K'Q'Q''} \mathcal{D}^{K'}_{Q''Q'}(R_B)\mathcal{D}^{K}_{Q''Q}(R_B)^* \int \mathrm{d}\nu' R^{K'K}_{Q''}(\nu',\nu;n)$$
$$\times (-1)^{Q'} \oint \frac{\mathrm{d}\vec{\Omega}'}{4\pi} \frac{r}{\eta_I(\nu',\vec{\Omega}';n)^\ell} \sum_{i,j=0}^{3} \mathcal{T}^{K'}_{-Q'}(i,\vec{\Omega}')\Lambda_{\nu',\vec{\Omega}'}(n,n)_{ij}\mathcal{T}^{K_P}_{Q_P}(j,\vec{\Omega}')\,, \quad (2.124)$$

We remind the reader that quantities such as k_L, ϵ', or r carry a spatial dependence, although it is not shown explicitly. We note also that when Lambda iteration is considered, $\Lambda_{\nu',\vec{\Omega}'}(n,n)_{ij}$ are also taken to be zero and so all $\Lambda_{KQ,K_PQ_P}(\nu',\nu;n)$ are set to zero, which is of course equivalent to taking $\hat{A}^*$ equal to identity.

When considering Jacobi iteration, provided that the magnetic field is sufficiently weak and radiation anisotropy is small, then at all spatial points $I \gg Q, U, V$. Therefore, the multipolar component $\mathcal{E}^0_0(\nu,n)$ dominates over the others and so, similarly to what is discussed in Trujillo Bueno & Manso Sainz (1999), this iterative RT problem can be solved using only the physical information contained in $\Lambda_{00,00}(\nu',\nu,n)$. In other words, given that the J^K_Q components depend almost exclusively on Stokes I, which in turn is essentially given by $\mathcal{E}^0_0$, the convegence rate of all $\mathcal{E}^K_Q$ is driven by the convergence rate of the $\mathcal{E}^0_0$ component. In this situation, the Jacobi iteration method only needs to be used for this component, while Lambda iteration is applied to the others. This simplifies the problem to

$$\Delta\mathcal{E}^0_0(\nu;n) = k_L \frac{\epsilon'}{1+\epsilon'} B_{\nu_0}(T)\,\Phi^{00}_0(J_\ell,J_u;\nu) + \left[\mathcal{J}^0_0(\nu;n)\right]^{\mathrm{old}}$$
$$- \left[\mathcal{E}^0_0(\nu;n)\right]^{\mathrm{old}} + \int \mathrm{d}\nu' \Lambda_{00,00}(\nu',\nu;n)\,\Delta\mathcal{E}^0_0(\nu';n)\,. \quad (2.125)$$

It is obvious that in this iterative scheme there is a coupling between different frequencies, due to the redistribution functions. At a given spatial point n, if one considers a discrete array of frequencies, then Eq.(2.125) leads, in analogy to appendix E of Belluzzi & Trujillo Bueno (2014), to a system of equations for $\mathcal{E}^0_0$ in frequency space

$$\hat{M}\Delta\vec{\mathcal{E}}^0_0 = \vec{\mathcal{C}}\,, \quad (2.126)$$

where $\hat{M}$ is an $N_F \times N_F$ operator, with N_F the number of spectral grid points. Considering this approximation, the element for $\mathcal{C}$ at frequency point ν_i is

$$\mathcal{C}(\nu_i) = \left[\mathcal{J}^0_0(\nu_i)\right]^{\mathrm{old}} - \left[\mathcal{E}^0_0(\nu_i)\right]^{\mathrm{old}} + k_L \frac{\epsilon'}{1+\epsilon'} B_{\nu_0}(T)\,\Phi^{00}_0(J_\ell,J_u;\nu_i)\,. \quad (2.127)$$

In the calculations based on this method which are shown in the following chapters, these systems of equations have been solved numerically using a LU decomposition (see Press et al. 1986). Information on other methods for the transfer of spectral line polarization accounting for PRD effects can be found in Nagendra et al. (2002) and Sampoorna et al. (2008)

If a somewhat larger magnetic field is considered, and the polarization fraction becomes more significant, then the aforementioned approximation becomes increasingly inaccurate and the convergence rate begins to deteriorate, even producing instabilities. As a possible improvement for cases in which $\mathcal{E}_0^0$ still dominates over the other $\mathcal{E}_Q^K$ contributions, but nevertheless the others cannot be neglected, the iterative method can be applied as follows. Despite applying the Jacobi method only to $\mathcal{E}_0^0$, the "new" values of $\mathcal{E}_{Q_P}^{K_P}$ at the current iteration, found using Lambda iteration, are also used in its calculation

$$\Delta\mathcal{E}_0^0(\nu;n) = k_L \frac{\epsilon'}{1+\epsilon'} B_{\nu_0}(T)\,\Phi_0^{00}(J_\ell, J_u;\nu) + \left[\mathcal{J}_0^0(\nu;n)\right]^{\text{old}} - \left[\mathcal{E}_0^0(\nu;n)\right]^{\text{old}} + \int \mathrm{d}\nu' \sum_{K_P Q_P} \Lambda_{00,K_P Q_P}(\nu',\nu;n)\Delta\mathcal{E}_{Q_P}^{K_P}(\nu';n)\,. \quad (2.128)$$

In order to solve the iterative scheme in this case, one still solves a system of equations of the form shown in Eq. (2.126), but in this case $\vec{\mathcal{C}}$ has the following expression on a discrete frequency grid

$$\mathcal{C}(\nu_i) = \left[\mathcal{J}_0^0(\nu_i)\right]^{\text{old}} - \left[\mathcal{E}_0^0(\nu_i)\right]^{\text{old}} + k_L \frac{\epsilon'}{1+\epsilon'} B_{\nu_0}(T)\Phi_0^{00}(J_\ell, J_u;\nu_i) + \sum_{j=1}^{N_F} \sum_{K_P\neq 0} \sum_{Q_P} \Lambda_{00,K_P Q_P}(\nu_j,\nu_i;n)\Delta\mathcal{E}_{Q_P}^{K_P}(\nu_j;n)\,. \quad (2.129)$$

It should be noted that calculating this correction requires substantially more time per iteration than when only the contribution from the $\mathcal{E}_0^0$ components is considered. Furthermore, when the polarization fraction becomes large enough that other $\left|\mathcal{E}_Q^K\right|$ are comparable to $\left|\mathcal{E}_0^0\right|$, the previously mentioned simplifications to Eq. (2.123) are no longer valid, so Jacobi iteration must be considered for all components of the line emissivity. Thus, unlike in Eqs. (2.126), the system of equations that must be solved, all multipolar components at all frequency grid points may be coupled to one another. This is a formidable numerical problem that cannot be solved in a reasonable amount of time without resorting to suitable computational techniques. Such an approach, however, is outside of the scope of this thesis.

3

Numerical solutions of the non-LTE radiative transfer problem and illustrative applications

We present applications of the numerical radiative transfer code, developed based on the theory presented in the previous chapter. We have studied the convergence rate of the iterative method implemented in the code, focusing on its dependence on the magnetic field strength. We also show calculations that highlight the sensitivity of the emergent Stokes profiles to certain atmospheric parameters, as well as calculations that provide some insights into the physics of spectral line polarization, paying close attention to the effects of elastic collisions. Finally we show that, for spectral lines forming close to the transition region, the resulting polarization profiles are sensitive to the choice of formal solver.

3.1 Introduction

The forward modeling approach for the synthesis of the intensity and polarization profiles of the radiation emerging from a given model atmosphere, considering a given atomic model, has received a lot of attention over the years. Based on the line formation theory of Unno (1956), which accounted for the magnetic sensitivity of spectral line polarization via the Zeeman effect, Landi Degl'Innocenti (1976) developed MALIP, an RT code which makes the assumption of LTE and of CRD (see also Wittmann 1974). Trujillo Bueno & Manso Sainz (1999) numerically solved non-LTE polarized RT problems, taking into account scattering polarization in a two-level atomic model. Such calculations were based on the theoretical framework introduced by Landi Degl'Innocenti (1983), considering the powerful formalism of irreducible spherical tensors (e.g., Bommier & Sahal-Brechot 1978). Such formalism allows for a compact description of many physical processes that can produce or modify the polarization of spectral lines, such as the Hanle and Zeeman effects, dichroism

effects due to atomic polarization of the lower level of the transition, i.e., zero-field dichroism (see Trujillo Bueno & Landi Degl'Innocenti 1997, Landi Degl'Innocenti 1998), or collsional depolarization. In order to solve the problem numerically, iterative schemes based on the accelerated lambda iteration (ALI) methods of Olson et al. (1986), and on the Gauss-Seidel and successive over-relaxation (SOR) methods presented in Trujillo Bueno & Fabiani Bendicho (1995) were implemented. The same authors investigated a similar numerical problem in Manso Sainz & Trujillo Bueno (2003), also allowing for scattering polarization and the Hanle effect. The Ca II infrared triplet was modeled as a multilevel atom, and the critical role played by zero-field dichroism was identified. More recently, Štepán & Trujillo Bueno (2013) developed PORTA, an efficient multilevel RT code oriented towards massively parallel computers, which can solve polarized transfer problems, assuming CRD and taking the joint action of scattering polarization and the Hanle effect into account, in 3D atmospheric models.

Partial frequency redistribution (PRD) effects in scattering were already included in the numerical solution of RT problems by Milkey & Mihalas (1973), for the unpolarized case. Based on the Jacobi method of Olson et al. (1986), Faurobert-Scholl et al. (1997) developed PALI (Polarized Accelerated Lambda Iteration) methods for the forward modeling of spectral line polarization, including the effects of optical pumping. Such methods were extended in order to consider a PRD treatment of scattering (Paletou & Faurobert-Scholl 1997) and also the Hanle effect (see Nagendra et al. 1998 and Nagendra et al. 1999). Uitenbroek (2001) introduced a MALI (Multilevel Accelerated Lambda Iteration) method for polarized line transfer with PRD in scattering and developed the RH RT code, in which polarization is exclusively induced through the Zeeman effect, while the impact of anistropic illumination and of the Hanle effect was neglected. Based on the Kramers-Heisenberg formula for scattering amplitudes (e.g., Stenflo 1998), Sampoorna (2011) derived the redistribution matrix for a two-level atomic model, suitable for a PRD treatment of scattering, which accounted for the presence of a magnetic field of arbitrary strength, including both the Hanle and Zeeman effects. Numerical single-scattering experiments were performed using such redistribution matrix for a spectral line with $J_\ell = 1/2$ and $J_u = 3/2$. The Kramers-Heisenberg formula has since been used to derive the redistribution matrix for increasingly complex atomic models (e.g. Smitha et al. 2011, Sowmya et al. 2014).

As discussed in detail in Sect. 2.4.1, for the numerical RT calculations presented in this thesis, scattering processes are treated through the redistribution matrix presented in Bommier (1997b). Through such redistribution matrix, the impact on the polarization of spectral lines due to optical pumping, together with the Hanle and Zeeman effects due to an arbitrary magnetic field can be accounted for, as well as the effects of collisions. In the calculations presented in this work, the full polarized RT equation is solved at every iterative step, instead of taking the last scattering approximation.

The main advantage of such RT code, which we hereafter refer to as the HZ code,

is that it can quickly and efficiently solve the non-LTE problem in optically thick plasmas accounting for PRD effects, in the presence of a magnetic field of arbitrary strength. When considering spectral lines that form at various spatial regions in the solar atmosphere, such a forward modeling tool can be of great aid in isolating specific physical mechanisms which affect the emergent intensity and polarization. In this chapter, the stability and the convergence rate of the code's iterative scheme, and dependence on the magnetic field strength, has been investigated.

Before considering specific applications, certain geometrical aspects are discussed, including the choice of the coordinate system, which is common to most of the physical situations we will consider in this thesis. This chapter is mainly dedicated to studying specific physical processes involved in the generation and transfer of polarized radiation. Furthermore, the HZ code, as a forward modeling tool, should be able to provide realistic intensity and polarization profiles corresponding to the solar spectrum. In order to do this, it is important to consider suitable atomic models when performing non-LTE calculations. Thus, we provide a discussion on the nature of the spectral lines considered in this work, including the structure of the atoms which produce them, the field strength characterizing the onset of the Hanle effect, and the atmospheric regions from which most of the radiation of a given spectral line emerges (i.e., their formation regions).

In this chapter, little attention is paid to the impact of the magnetic field on the resulting spectral line polarization. Instead, we focus on the sensitivity of the intensity and polarization of various spectral lines to the thermodynamic properties of the solar atmosphere, by considering multiple atmospheric models which correspond to different solar regions. The impact of elastic collisions on the Stokes profiles of the emergent spectral lines, through their relaxation of the frequency coherence of scattering, is also studied. Relatedly, the validity of taking the CRD limit for such calculations is evaluated. The depolarizing effect of collisions is also studied. Finally, a numerical aspect of the problem has been considered, namely the influence of the choice of formal solver for the RT equation. It has been studied by comparing the resulting line profiles obtained with DELOPAR and BESSER formal solvers, as well as one that is based on the evolution operator formalism, using a short-characteristics method with parabolic interpolation.

3.2 Implementation

Here, we discuss relevant aspects of our RT code, such as the geometry of the problems considered in the following sections, its required inputs, and the criteria for convergence of the self-consistent solution.

3.2.1 Geometry

For the following RT problems, we consider plane-parallel model atmospheres, i.e., those whose parameters are vertically stratified and constant in all horizontal planes. The curvature of the atmosphere can be neglected because the solar radius ($R_\odot \sim 7 \cdot 10^5$ km) is much greater than the thickness of the atmosphere (which is of the

order of 10^3 km), although we point out that this assumption may be unsuitable when considering lines of sight (LOS) that are very close to the limb. Furthermore, we make the assumption of a static solar atmosphere, so the solution of the problem does not account for its macroscopic motions.

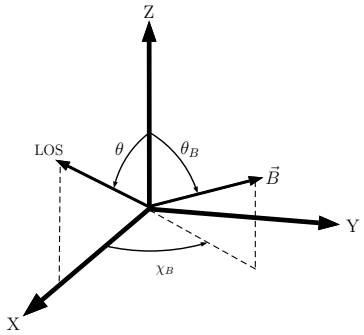

FIGURE 3.1— Geometry of the problem. We consider a right-handed Cartesian coordinate system where the Z-axis (quantization axis for the angular momentum) is along the local vertical, and the X-axis is directed so that the LOS lies in the X-Z plane, and therefore it is characterized only by its inclination $\mu = \cos\theta$. In this reference system, the direction of the magnetic field $\vec{B}$ is specified by its inclination with respect to the vertical (θ_B) and its azimuth (χ_B). The reference direction for positive Stokes Q is taken to be perpendicular to the local vertical or, if the LOS is along the local vertical, parallel to the Y-axis.

A right-handed Cartesian coordinate system is considered, in which the Z-axis is taken along the local vertical, which coincides with the symmetry axis for the radiation field, as shown in Fig. 3.1. The coordinate system is defined so that the line of sight (LOS) for the emergent radiation is always contained in the X-Z plane, so it is characterized solely by the parameter $\mu = \cos\theta$, where θ is the inclination with respect to the local vertical, or heliocentric angle. The magnetic field direction is specified by both its inclination with respect to the vertical axis, θ_B, and by its azimuth χ_B, which is the angle between the X-axis and the projection of the magnetic field onto the X-Y plane. The direction for positive Stokes Q is always defined along the Y axis. For LOS other than $\mu = 1$, this means the direction for positive Q is parallel to the limb.

When solving the RT problems considered in this thesis, we take an initial estimate of the radiation field which is axially symmetric around the Z axis, so all components of the radiation field tensor other than J^0_0 and J^2_0 are zero. Nevertheless, if the axial symmetry of the problem is broken, e.g., due to the presence of a magnetic field, it is necessary to account for the other tensorial components of the radiation field (see Eq. (2.23)). Thus, when calculating such components numerically, the radiation from different direction must be calculated from the RT equations, for multiple inclinations and azimuths. Indeed, for the applications presented in the re-

mainder of this chapter and in the following ones, a Gauss-Legendre quadrature (see Abramowitz & Stegun 1972) is used for the integration over inclination angles and, unless otherwise specified, 9 points have been taken in the $\theta' = \left[0°, 90°\right]$ interval and 9 more have been taken for $\left[90°, 180°\right]$. For the integration over azimuthal angles, a trapezoidal quadrature is used, considering a total of 8 points. We consider this selection of quadrature points to be suitable, since we have found calculations with an increased number of inclinations or azimuths not to produce appreciable changes in the resulting Stokes profiles. Unless otherwise noted, in the following applications the RT equations are calculated using the BESSER formal solver.

3.2.2 Required quantities

In order to model the emergent radiation of a given spectral line, the following physical quantities, used in the aforementioned RT code, must be provided as inputs.

- **The frequency grid**. The discrete spectral points, or wavelengths, considered when performing such RT calculations. The computation time required per iteration is highly sensitive to the number of spectral points.

- **Atmospheric parameters**. They quantify the thermodynamic properties of the atmosphere at all positions in the discrete spatial grid under consideration. Since plane-parallel atmospheric models are considered, such quantities vary only in terms of their atmospheric height. At each height point, the following input quantities are required: temperature, electron number density, neutral hydrogen number density, proton number density, the atmospheric microturbulent velocity, and the strength and direction of the magnetic field. The relative abundance of the atomic species that gives rise to the spectral line under consideration must also be provided.

- **Atomic parameters**. The two-level atomic model considered in this code requires the energy, total angular momentum, orbital angular momentum and electronic spin of both the upper and lower levels. The Einstein coefficent $A_{u\ell}$ for spontaneous emission is also required.

Many of the quantities required to obtain the Stokes profiles of the emergent radiation are calculated directly from such inputs by HZ. However, other quantities are obtained from them, but instead of being calculated in HZ, they are found by first performing an unpolarized RT calculation using the RH code presented in Uitenbroek (2001). In this code, the ionization balance of the chemical species that gives rise to the spectral line, and the population of each level are determined in non-LTE conditions. From such calculations, the number density of atoms in the lower level of the transition $\mathcal{N}_\ell$, the inelastic collisional rate $\mathcal{C}_{u\ell}$, the elastic collsional rate $Q_{\rm el}$ (see Anstee & O'Mara 1995 and Barklem & O'Mara 1997), the total continuum opacity η_I^c, the continuum scattering cross-section due to Thompson and Rayleigh scattering σ_c and the thermal continuum opacity given by κ_c are all obtained. Lastly, the

initial estimate for the J^0_0 and J^2_0 components of the radiation field tensor used in the HZ code is also taken from the self-consistent solution of RH.

The RH code itself uses more complex atomic models to perform the calculations. For each of the four spectral lines considered throughout this thesis, a specific atomic model is considered in order to obtain the previously mentioned quantities. In the next section, the number of levels and lines in each of them is detailed. Aside from the input atomic parameters required for the HZ code, the radiative rates (related to their Einstein coefficients) and the collisional rates (see van Regemorter 1962) between any two atomic levels must be provided, as well as collisional ionization and photoionization cross sections for each level.

Once the values of the required inputs are determined, they are introduced in the input files of the HZ code. `lambda.dat` stores the wavelengths considered in the frequency grid, `continuum.dat` stores the quantities related to the continuum, for each point in the spatial and spectral grid, `radfield.dat` stores the initial estimates for the radiation field tensors, for each point in the spatial and spectral grid, `magnetic.dat` stores the strength and orientation of the magnetic field at each point of the spatial grid, `isot2L.dat` stores the properties of the two-level atom considered by HZ, such as the total angular momentum, orbital angular momentum, and spin of both the upper and lower angular levels, and `atmosphere.dat` stores atmospheric parameters such as temperature, the lower level population, the damping constant for the Voigt function, or the collisional rates. Afterwards, the HZ code can be easily used to calculate the Stokes profiles of the emergent radiation.

3.2.3 Finding the self-consistent solution

As noted in Sect. 2.7, the non-LTE transfer problems considered in this work require the iterative solution of the RT equations and the equations for the evalutation of the emission coefficients (which involve the redistribution matrices). At each iterative step, the emission coefficients are calculated using the values for the radiation field tensors obtained from the previous solution of the RT equations and, in turn, the RT equations use the previously calculated emission coefficients as inputs. As more iterations are performed, the self-consistent solution is approached, i.e., the difference between the results obtained at a given iterative step and at the previous one begin to decrease.

For frequencies corresponding to the continuum, the optical thickness of the model atmospheres is not very large. In this case Lambda iteration is suitable for achieving a fast convergence for the multipolar components of the emissivity. However, in spectral regions where the line contribution is significant, Lambda iteration is found to give a very slow convergence rate, so we use the Jacobi iterative scheme discussed in Sect. 2.7. Thus, throughout this chapter, we will focus only on the convergence rate of the line contribution to emissivity. Dropping the ℓ label, the

maximum relative change for its various multipolar components is given by

$$R_c(\mathcal{E}_Q^K) = \max\left(\frac{\left|\mathcal{E}_Q^K(\nu;n)^{\rm new} - \mathcal{E}_Q^K(\nu;n)^{\rm old}\right|}{\left|\mathcal{E}_Q^K(\nu;n)^{\rm new}\right|}\right), \tag{3.1}$$

where the maximum is taken over all frequency and spatial points. Whether we have considered a Jacobi iterative scheme based on Eq. (2.127) or Eq. (2.129), the convergence rate of all multipolar components is driven by that of $\mathcal{E}_0^0$ (e.g., Trujillo Bueno & Manso Sainz 1999). Indeed, in the applications we discuss hereafter, the criterion for the converged solution is as follows. First of all, unless otherwise noted, 100 iterative steps are performed. This is done because the initial estimate for J_0^2 may differ significantly from the "true" or converged result, so the evolution (especially for the $\mathcal{E}_Q^2$ multipolar components of the line emissivity) may be very sharp at the first iterations. After such initial steps, the solution is considered to have converged when $R_c(\mathcal{E}_0^0)$ stops decreasing, at which point the maximum attainable accuracy has been reached. Taking this criterion, instead of establishing a threshold for convergence for all the $\mathcal{E}_Q^K$ based on their maximum relative change, is a suitable approach because the solution has been initialized using the solution of the unpolarized RT problem using RH. Therefore, the initial estimate of $\mathcal{E}_0^0$ will be close to the converged result, and furthermore its evolution will drive the convergence rate of the other multipolar components (see Trujillo Bueno & Manso Sainz 1999).

3.3 Spectral Lines

Here we introduce the main spectral lines which will be studied in the following sections. We discuss their suitability for being modeled using a two-level atom and their diagnostic potential. The atmospheric region from which most of the emergent radiation is emitted is also indicated. Although there are more realistic methods for determining such regions (see Uitenbroek 2006), for our purposes it will be suitable to take the estimate from the Eddington-Barbier relation, i.e., to take the atmospheric height at which the optical depth $\tau = 1$, for each specific frequency and inclination of the LOS. For each line, it is illustrative to also show the coherence fraction α_c at such heights, given in Eq. (2.48). We also provide the value of the Hanle critical field for each spectral line, i.e., the magnetic field strength for the onset of the Hanle effect, as shown in Eq. (2.50).

3.3.1 The Sr I line at 4607 Å

This line is produced by a transition between the lower level $^1\mathrm{S}_0$, corresponding to the ground level, and and upper level $^1\mathrm{P}_1$. As such, it corresponds to a normal Zeeman triplet, for which the results of a semi-classical treatment coincide with those of a quantum mechanical approach. Given that it is a resonance line, the coupling of the lower level with other levels of neutral strontium is not expected to play a major role in order to determine their populations. Furthermore, since the upper level of

the transition is not radiatively connected to any level of lower energy apart from the ground level, this line can be suitably modeled with a two-level atomic model.

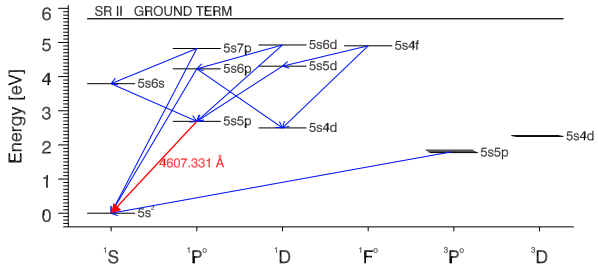

FIGURE 3.2— Grotrian diagram for the Sr I atomic model used in the execution of the RH code, showing all the atomic levels and radiative transitions which have been considered.

Performing calculations with the RH code, we have checked that, for atmospheric models corresponding to the quiet Sun, the vast majority of the Sr atoms present the solar atmosphere are found in its first ionized state (i.e., Sr II is the majority species), except at atmospheric heights which correspond to the transition region, where the number density of Sr III atoms is comparable to that of Sr II. When determining the ionization balance of Sr, it is therefore suitable, for the Sr I 4607 Å line, to consider only the neutral and the first ionized species. For the initial calculation with RH, an atomic model with 16 levels, including the ground level of Sr II, and 12 line transitions, has been considered (see Fig. 3.2). A frequency grid of 163 points, centered around the resonance frequency of the transition, has been taken. The points closest to the core are separated linearly, and the ones further in the wings are logarithmically separated.

Given that the number density of Sr I is relatively low, the opacity of the Sr I 4607 Å line is small. Therefore, it forms low in the solar atmosphere, at photospheric regions around 300 km above the $\tau_{5000} = 1$ height.

An estimate for the formation height of this line is shown in Fig. 3.3, obtained through the Eddington-Barbier relation for the FALC semi-empirical atmospheric model, which confirms that this line forms in the photosphere for all LOS considered. Even so, given that the Einstein coefficient for spontaneous emission of this transition is large, with $A_{u\ell} = 2 \cdot 10^8\,\mathrm{s}^{-1}$, radiative processes dominate over the ones driven by collisions ($\epsilon' \ll 1$). Together with the fact that the Hanle critical field for this line is $B_c \simeq 23$ G, this makes it an excellent candidate for inferring magnetic fields in the photosphere via the Hanle effect. Indeed, in the past the Sr I 4607 Å line has been used to infer the strength of unresolved magnetic fields in the photosphere

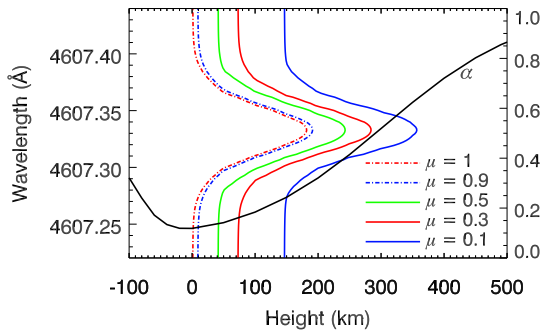

FIGURE 3.3— Estimates for the formation height of the Sr I 4607 Å line, found using the Eddington-Barbier relation, and considering the atomic number densities obtained from the RH code, for the FALC model atmosphere. Black solid curve: Coherence fraction (α_c) as a function of height. The colored curves show the heights at which $\tau = 1$, for various LOS (see legend in figure).

(e.g., Trujillo Bueno et al. 2004).

3.3.2 The Sr II line at 4078 Å

This spectral line is produced by a transtion with lower level $^2S_{1/2}$, corresponding to the ground level, and upper level $^2P_{3/2}$ of strontium in its first ionized state. The number density of Sr II is much greater than that of neutral Sr, both in the photosphere, and higher in the solar atmosphere. Therefore, when calculating the population per unit volume of the ground level of the Sr II, transitions to and from levels of neutral strontium can be safely negelected. The initial calculations with RH have been performed with an atomic model that considers 6 levels, including the ground level for Sr III, and the corresponding bound-free transitions, as well as 5 line transitions. This be seen in Fig. 3.4. For such calculations, we have taken a frequency grid with 251 points.

Since this ionized species has a larger number density than Sr I, the line forms higher in the atmosphere than the Sr I 4607 Å line. At such heights the coherence fraction is more significant and, therefore, the effects of PRD are expected be much more relevant in this case (see Fig. 3.5). This line has $A_{u\ell} = 1.41 \cdot 10^8\,\mathrm{s}^{-1}$, and so it is sensitive to the Hanle effect for weaker fields, with $B_c \simeq 12$ G.

As can be seen from Fig. 3.4, for this line the upper level of the transition is radiatively connected to metastable levels of lower energy (namely the $^2D_{3/2}$ and $^2D_{5/2}$ levels). Although the code developed in the framework of this thesis cannot account for such atomic levels, findings by Deb & Derouich (2014) suggest that the polarization of the Sr II 4078 Å line is sensitive to collisions with neutral hydrogen

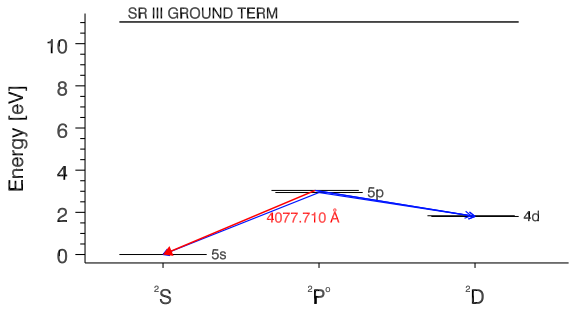

FIGURE 3.4— Grotrian diagram for the Sr II atomic model used in the execution of the RH code. The Sr I levels have not been included, given that the ionized species dominates over it at all atmospheric heights.

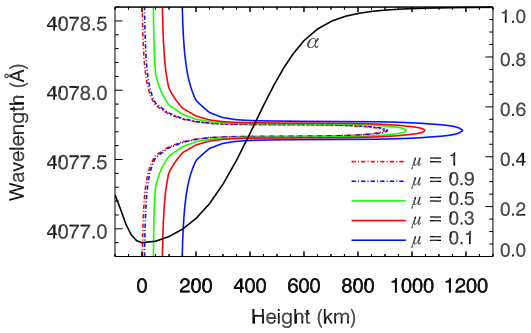

FIGURE 3.5— Estimates for the formation height of the Sr II 4078 Å line, found using the Eddington-Barbier relation, and considering the atomic number densities obtained from the RH code, for the FAL-C model atmosphere. Black solid curve: Coherence fraction (α_c) as a function of height. The colored curves show the heights at which $\tau = 1$, for various LOS (see legend in figure).

atoms, due to the collisional susceptibility of such metastable levels. However, PRD and transfer effects were neglected in such investigation. In the future, it would be of great interest to perform multi-level RT calculations of this line accounting for PRD effects, in order to suitably evaluate the influence of the aforementioned metastable levels on the line's emergent linear polarization (see the theory presented

in Casini et al. 2017). It also should be noted that, of the multiple existing isotopes of strontium, only ^{87}Sr, with a relative abundance of roughly 7%, has hyperfine structure. However, in the calculations presented in this thesis, hyperfine structure is neglected. Despite such limitations, the calculations presented in the thesis for this line still provide valuable insights into the generation and transfer of polarized radiation for spectral lines whose line core originates in the solar chromosphere.

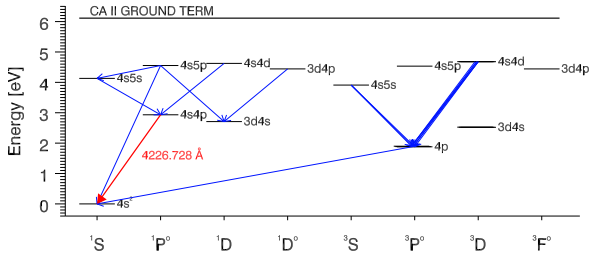

FIGURE 3.6— Grotrian diagram for the Ca I atomic model used in the execution of the RH code. Note that the upper Ca I 4227 Å line is not radiatively connected to any lower energy level besides the ground state.

3.3.3 The Ca I line at 4227 Å

This line is produced by a transition between the $^1S_0$ ground level and the $^1P_1$ upper level, with $A_{u\ell} = 2.18 \cdot 10^8\,\mathrm{s}^{-1}$ and a Hanle critical field of $B_c \simeq 25$ G. Much like in the case of strontium, the first ionized species (Ca II) is dominant in the solar atmosphere. However, since the relative abundance of calcium is much higher than that of strontium, the number densities of Ca I are also sizable, and so the opacity for this line is larger. Indeed, its core forms in the chromosphere, as shown in Fig. 3.6, and thus the effects of PRD to have a noticeable impact on the polarization signal of the emergent radiation.

The relative abundance of the Ca isotopes that have hyperfine structure is less than 1%, and approximately 97% all Ca atoms are in the form of ^{40} Ca. Also, unlike in the case of the Sr II 4078 Å line, the upper level is not radiatively connected to metastable levels of lower energy. Therefore this spectral line is an even more suitable candidate to be modeled considering a two-level atom. Spectropolarimetric observations of this line (e.g. Bianda et al. 2003; Sampoorna et al. 2009) have shown a spatial variation of the wing's linear polarization for which no physical mechanism has been conclusively determined. In Chapter 5, we suggest a satisfactory explanation for such phenomenon.

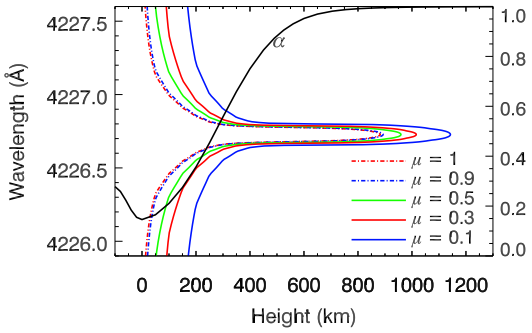

FIGURE 3.7— Estimates for the formation height of the Ca I 4227 Å line, found using the Eddington-Barbier relation, and considering the atomic number densities obtained from the RH code, for the FALC model atmosphere. Black solid curve: Coherence fraction (α_c) as a function of height. The colored curves show the heights at which $\tau = 1$, for various LOS (see legend in figure).

3.3.4 The Mg II k line at 2795 Å

The transition responsible for this very strong resonance line has a lower (ground) level $^2\mathrm{S}_{1/2}$ and upper level $^2\mathrm{P}^{\mathrm{o}}_{3/2}$, with $A_{u\ell} = 2.60 \cdot 10^8\ \mathrm{s}^{-1}$ and a Hanle critical field of $B_c \simeq 22$ G. The core of this line forms high in chromosphere, close to the solar transition region, so it has great potential for the exploration of magnetism in this atmospheric region (see Belluzzi & Trujillo Bueno 2012).

The Mg II k line belongs to a doublet; the other component, the Mg II h line, is less than 7 Å apart. The quantum interference between the upper levels of such lines plays an important role, and it must be properly taken into account for a correct modeling of the linear polarization pattern across this doublet. In general, a two-term model atom (which accounts for such interference) is therefore needed to model the Mg II h & k system. Nonetheless, a two-level model atom is a good approximation for the line-core region of these lines. This can be clearly seen from Fig. 3.8, where calculations considering a two-term model atom, both accounting for PRD effects and neglecting them, are compared to the calculation assuming a two-level model atom, in the PRD case. Such calculations were carried out using the RT code described in Belluzzi & Trujillo Bueno (2014). It can be seen that the polarization profile for the Mg II k line obtained when accounting for PRD, both assuming a two-level and a two-term atom, coincide very well in the spectral region comprised between 2795 and 2796 Å. Applications to this line using the (two-level) HZ code are presented in the following sections, focusing on the aforementioned spectral range.

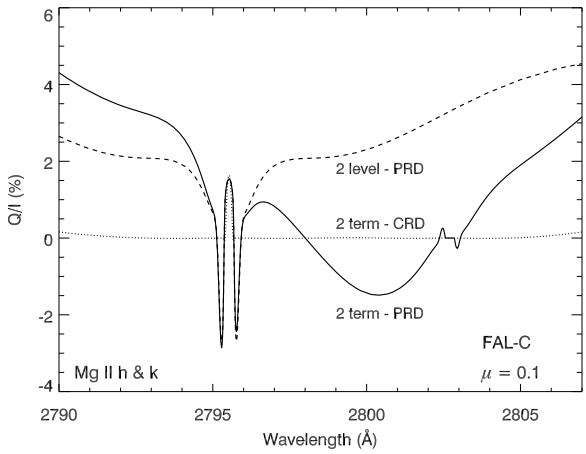

FIGURE 3.8— Scattering polarization Q/I pattern of the Mg II h & k lines calculated in the FALC semi-empirical model assuming CRD (dotted curve) and taking into account PRD effects (solid curve), in both cases including the effects of J-state interference. The dashed curve indicates the calculation considering PRD for a two-level atom for the Mg II k line. Note that the positive line-center peak and the two negative peaks located in the near wings of the Q/I profile coincide well with the ones obtained with the two-term PRD calculation. The reference direction for positive Stokes Q is the parallel to the closest limb. Figure adapted from Belluzzi & Trujillo Bueno (2012). Calculations courtesy of Dr. Luca Belluzzi.

3.4 Convergence rate

In the following sections of this chapter, we present illustrative applications of our RT code. Unless otherwise noted, the magnetic field strength and orientation is the same at all points in the spatial grid. Similarly, when a microstructured field is considered, its strength and distribution of orientations is taken to be the same at all spatial points. In this section, we study the convergence rate of such iterative calculations for the Sr I 4607 Å and the Sr II 4078 Å lines, showing their dependence on the field strength and the iterative scheme.

As a first application, we analyze the convergence rates of the multipolar components of the line contribution to emissivity $\mathcal{E}_0^0$ and $\mathcal{E}_0^2$ (see Eqs. (2.120) and (2.121)), in the absence of a magnetic field. Throughout this work, these quantities are calculated by taking the quantization axis of total angular momentum parallel to the local vertical. In this case, provided that the magnetic field is not strong, only these two $\mathcal{E}_Q^K$ components should be significant. The convergence rate has been found using Eq. (2.125), i.e., the correction to $\mathcal{E}_0^0$ at each iterative step has been calculated using the Jacobi method, accounting for the contribution from $\mathcal{E}_0^0$ only. The correction to

$\mathcal{E}^2_0$ is obtained using Lambda iteration. In Fig. 3.9, the dependence of the maximum

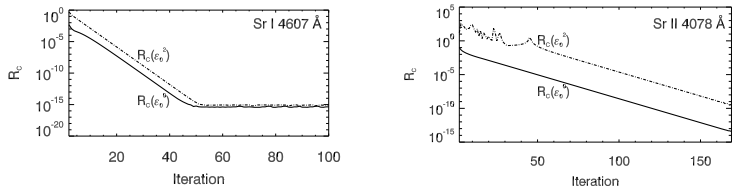

FIGURE 3.9— Change in $R_c(\mathcal{E}^0_0)$ (solid curves) and $R_c(\mathcal{E}^2_0)$ (dash-dotted curves) per iteration. The calculation has been performed using the HZ code, accounting for PRD, in the absence of magnetic fields. The frequency-by-frequency method has been used, considering $\Lambda_{00,00}$ as shown in Eq. (2.125). The left panel shows the calculations for the Sr I 4607 Å line and the right one shows the same for the Sr II 4078 Å line. The FAL-C atmospheric model has been used in the calculations.

relative change on the iterative step of both $\mathcal{E}^0_0$ and $\mathcal{E}^0_2$, for the Sr I 4607 Å and Sr II 4078 Å lines, is shown. The FAL-C model has been used in such calculations. Due to its lower opacity, the calculation for the emergent polarized radiation of the Sr I 4607 Å line converges much faster than it does for the Sr II 4078 Å line. In the first case, from around the fiftieth iteration onwards, the maximum relative change no longer decreases, since the numerical precision of the calculation has been reached. For the calculation for the Sr II 4078 Å line, $R_c(\mathcal{E}^2_0)$ experiences large fluctuations in the first iterative steps but at further iterations its evolution is driven by that of $R_c(\mathcal{E}^0_0)$, as described in Trujillo Bueno & Manso Sainz (1999), and it acquires a smoother behavior.

The presence of a magnetic field can produce a breaking of symmetry, and thus the values of the $\mathcal{E}^K_Q$ multipolar components are modified, and components other than $\mathcal{E}^0_0$ and $\mathcal{E}^2_0$ begin to appear. This happens because the magnetic field, via the Hanle and Zeeman effects, modifies the redistribution matrices (see Eqs. (2.44) and (2.47)), which in turn contribute to the $\mathcal{E}^K_Q$. Therefore, we have also investigated the impact of the magnetic field on the convergence rate and, as an example, we have considered a horizontal magnetic field that is perpendicular to the LOS (i.e., with $\chi_B = 90°$).

In Fig. 3.10 the convergence rates obtained using only the $\Lambda_{00,00}$ operator (see Eqs. 2.123 and 2.124), shown in the left panels, are compared to the ones obtained when all $\Lambda_{00,KQ}$ operators are included in the Jacobi iterative scheme, i.e., when the contributions from all multipolar components of the line emissivity are used to obtain the correction to $\mathcal{E}^0_0$, in the right panels. As the magnetic field increases, the $\mathcal{E}^K_Q$ components other than $\mathcal{E}^0_0$ tend to increase in magnitude, and so their contribution to the correction to $\mathcal{E}^0_0$ becomes more significant. As a result, the convergence rate calculated using only the $\Lambda_{00,00}$ operator is found to deteriorate already when considering magnetic fields strengths around 500 G, and at 800 G instabilities are

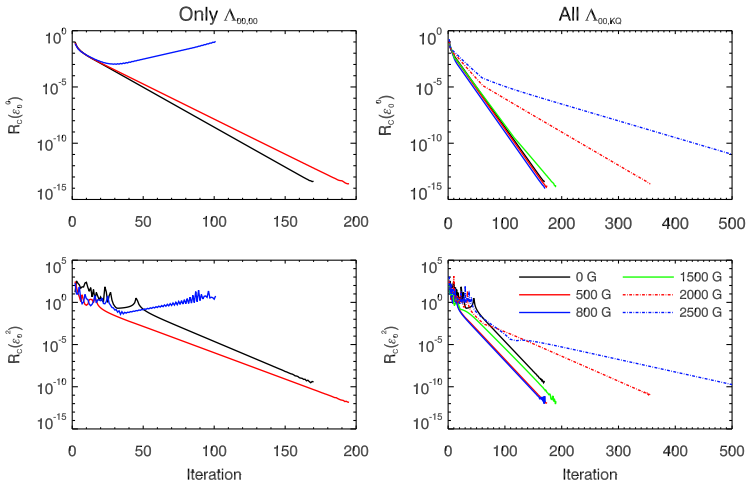

FIGURE 3.10— Change in $R_c(\mathcal{E}_0^0)$ (top panels) and $R_c(\mathcal{E}_0^2)$ (bottom panels) per iteration for the Sr II 4078 Å line. The calculation has been performed using the HZ code, accounting for PRD, in the presence of a horizontal ($\theta_B = 90°$) magnetic fields with azimuth $\chi_B = 90°$ and various field strengths (see legend in figure). The left panels show the convergence rates when only the $\Lambda_{00,00}$ operator is considered, i.e., only the contribution from $\mathcal{E}_0^0$ is used when calculating the correction to $\mathcal{E}_0^0$, and the right panels show the rates when all the $\Lambda_{00,KQ}$ operators are considered, i.e., calculating the correction to $\mathcal{E}_0^0$ using all $\mathcal{E}_Q^K$ components (see Sect. 2.7 and discussion therein).

encountered. Thus, the convergence rates for stronger fields are not shown in this case. On the other hand, when the correction to $\mathcal{E}_0^0$ accounts for contributions from all $\mathcal{E}_Q^K$ (see Eq. 2.128), its stability increases considerably, and the convergence rate of $R_c(\mathcal{E}_0^0)$ is barely affected by the magnetic field up to strengths of 1500 G. However, at 2500 G the rate has already deteriorated considerably and, for even stronger fields, the solution also fails to converge when considering all Λ_{00,K_PQ_P}. As is mentioned at the end of Sect. 2.7, in this case the iterative scheme of Eq. (2.124) requires using the Jacobi method, not only for the line part of $\mathcal{E}_0^0$, but for all line components simultaneously. In the two lower panels of Fig. 3.10, $R_c(\mathcal{E}_0^2)$ per iteration is shown for the same field strengths and iterative schemes. Again, its evolution is driven by that of $\mathcal{E}_0^0$ and, therefore, obviously has the same dependence on field strength.

3.5 The role of the atmospheric model

The intensity and polarization of the solar spectrum is sensitive to the atmospheric region from which the radiation originates, i.e., the region from where most of the observed radiation has been emitted. The Stokes parameters of the emergent radiation depend on the magnetic activity in such region, as well as on properties such as

temperature, density and, in general, on the dynamics of the atmospheric material (although in this work the atmosphere is assumed to be static). In order to provide some insight on the sensitivity of the polarization properties of various spectral lines to the thermodynamic properties of the solar regions from which they originate, we compare the synthesized profiles obtained from calculations using the various semiempirical atmospheric models presented in Fontenla et al. (1993) to each other. Such models include model A (hereafter FAL-A), representative of a faint region in the quiet Sun, model F (FAL-F), representative of a bright region of the quiet Sun, and model P (FAL-P), representative of a typical plage area. Model C is instead representative of an averaged region of the quiet Sun. Analogous calculations have been performed for the M_{CO} model, presented in Avrett (1995), which is also representative of a quiet Sun region but, at heights around 1000 km, its temperature and density are considerably lower than for the previous models for the quiet Sun.

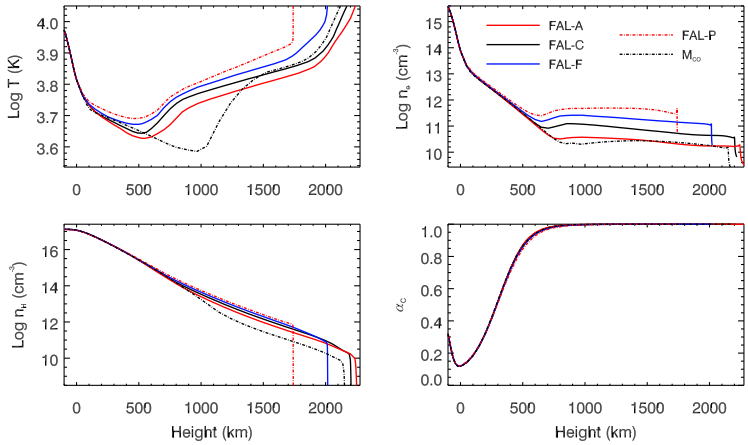

FIGURE 3.11— Plots of temperature (top left panel), electron number density (top right panel), neutral hydrogen number density (bottom left panel), and the coherence fraction for the Sr I 4607 Å line (bottom right panel) as a function of height, for the various atmospheric models considered, including FAL-A (solid red curve), FAL-C (solid black curve), FAL-F (solid blue curve), FAL-P (dashed-dotted red curve), and M_{CO} (dashed-dotted black curve).

In Fig. 3.11, the temperature T, the electron number density n_e, the neutral hydrogen number density n_H, and the coherence fraction α_c, obtained from calculations of the Sr I line at 4607 Å, are all shown as a function of atmospheric height for the five atmospheric models we have considered. We note that for models corresponding to more active regions such as FAL-P the transition region is deeper in the atmosphere. Moreover, at heights corresponding to the chromosphere and the upper photosphere, T, n_e, and n_H are all larger for such models. We also note that

at the same heights the atmospheric parameters in M_{CO} are stratified in a manner that is qualitatively different from the other models, which is especially apparent for T.

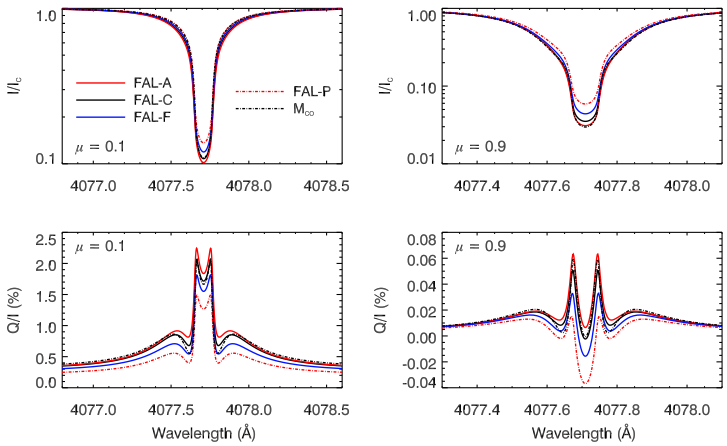

FIGURE 3.12— Emergent intensity, normalized to the continuum (top row) and Q/I (bottom row) for the Sr II line at 4078 Å. For the remainder of this chapter, calculations are performed using the HZ code, unless otherwise specified. The following atmospheric models have been used in the calculations: FAL-A (red solid curves), FAL-C (black solid curves), FAL-F (blue solid curves), FAL-P (red dashed-dotted curves), and M_{CO} (black dashed-dotted curves). We consider the radiation emerging at LOS with $\mu = 0.1$ (left column) and $\mu = 0.9$ (right column). The reference direction for positive Stokes Q is taken parallel to the limb.

In Fig. 3.12, the emergent intensity and Stokes Q/I profile is shown for the Sr II 4078 Å line, for an LOS close to the limb ($\mu = 0.1$) and another close to disk-center ($\mu = 0.9$). The emergent intensity is substantially larger when considering the FAL-P model, as expected since this model corresponds to a plage area. As such, for this model the temperature is higher throughout the atmosphere, including around the line core formation region (in the FAL-C atmospheric model, the formation region is found around 900 to 1200 km, depending on the LOS). The other atmospheric models correspond to quiet regions of the solar atmosphere, and their intensities are much closer to one another in the line core region. In descending order, they correspond to the FAL-F, M_{CO}, FAL-C and FAL-A models. This is in agreement with the findings of Supriya et al. (2014). In the line wings, the emergent intensities obtained in the four models presented by Fontenla et al. (1993) have the same relation to one another as in the line core. However, when going from the core into the wings, the intensity profile obtained with M_{CO} presents qualitative differences with respect to the others, as a consequence of the aforementioned qualitative differences in the

stratification of atmospheric parameters in this model.

As for the Q/I profile, the largest line core signal is found for the FAL-A model, while the smallest is found in FAL-P. The Q/I signal is indicative of the radiation anisotropy around the region where the emergent photons originates. This radiation anisotropy is strongly influenced by the gradient of the source function, and thus the Q/I signal is sensitive to the temperature gradient around the line's formation region. We note that, for the LOS with $\mu = 0.1$, the line core Q/I signal is positive for all calculations, while for the LOS with $\mu = 0.9$ it is negative for the calculations in certain atmospheric models, particularly for FAL-P. This is again related to the temperature gradients around the formation region at such LOS, causing the radiation anisotropy around this region to change its sign, going from negative to positive. Also for Q/I, the behavior obtained in the M_{CO} model is qualitatively different from the others when going from the core into the wings.

The synthesized spectral lines obtained with the same atmospheric models have also been compared for the Sr I 4607 Å line. Such calculations are shown in Fig. 3.13.

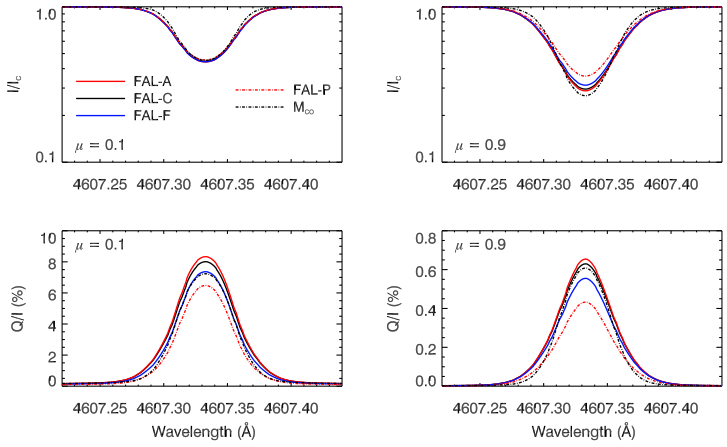

FIGURE 3.13— Emergent intensity, normalized to the continuum (top row) and Q/I (bottom row) for the Sr I line at 4607 Å. The following atmospheric models have been used in the calculations: FAL-A (red solid curves), FAL-C (black solid curves), FAL-F (blue solid curves), FAL-P (red dashed-dotted curves), and M_{CO} (black dashed-dotted curves). We consider the radiation emerging at LOS with $\mu = 0.1$ (left column) and $\mu = 0.9$ (right column). The reference direction for positive Stokes Q is taken parallel to the limb.

As for the intensity (normalized to the continuum), which is sensitive to the temperature at the lower photosphere, its profiles for the various models are quite similar to one another for the LOS with $\mu = 0.1$, although certain differences are found for $\mu = 0.9$. The line core Q/I, being sensitive to the temperature gradient at pho-

tospheric heights, is largest for calculations in the FAL-A model and smallest for calculations in the FAL-P model. We also point out that this photospheric line does not present linear polarization wing lobes with large amplitudes, as will be discussed in greater detail in following sections.

It is thus clear that the polarization profiles of the emergent radiation are very sensitive to the conditions of the atmospheric region where the line originates. Therefore, the local atmospheric parameters, such as temperature and density, must be well constrained - for example, from measurements of the spectral line intensity profiles - in order to accurately measure the magnetic field based on the spectral line's polarization. We remind the reader that the calculations presented in this section have been performed in the absence of a magnetic field. In the applications presented hereafter, the FAL-C atmospheric model will be used unless otherwise noted.

3.6 The impact of PRD

The complex RT problem considered in this work is simplified considerably under the assumption that the frequencies of the incoming and scattered photons are completely uncorrelated (CRD approximation). Therefore, it is very important to clarify when such approximation can be safely applied. As mentioned before, the hypothesis of CRD is generally suitable for treating weak spectral lines, and for estimating the polarization in the core region of strong lines. On the other hand, it is not suitable for modeling the extended wings of strong resonance lines. In order to illustrate this, we provide a detailed comparison between the results obtained through the full PRD calculation and in the limit of CRD, for the same lines discussed in the previous section, namely Sr I 4607 Å and Sr II 4078 Å.

Through the redistribution matrix formalism considered in this work, the detailed spectral structure of the incident radiation at each spatial point within the atmospheric model, and its impact on the scattered radiation, can be accounted for. In the atomic rest frame, frequency redistribution is produced only by the impact of elastic collisions, which is also included in the redistribution matrix. In the HZ code, the CRD limit is obtained by artificially increasing the value of Γ_E, so that the branching ratio for $\mathcal{R}_{\rm II}$ goes to zero and all scattering processes are described by the $\mathcal{R}_{\rm III}$ redistribution matrix. Although the depolarizing effect of elastic collisions must be included in order to provide a realistic treatment for many spectral lines, in this section such effect is neglected since we focus only on their frequency redistribution effects. In Fig. 3.14, the intensity and polarization patterns obtained for the Sr I 4607 Å and Sr II 4078 Å lines are presented, considering an LOS with $\mu = 0.1$. The reference direction for positive Q has been defined parallel to the limb; therefore, in the absence of a magnetic field, the resulting U/I signal is zero[1].

For both lines considered in the figure, the emergent intensity at line-center is

[1]It is worth noting that, when considering multi-dimensional atmospheric models, U/I signals can also be produced in the absence of a magnetic field, as a result of horizontal atmospheric inhomogeneities that break the axial symmetry of the problem. However, such effects cannot be included in the one-dimensional atmospheric models considered in this thesis.

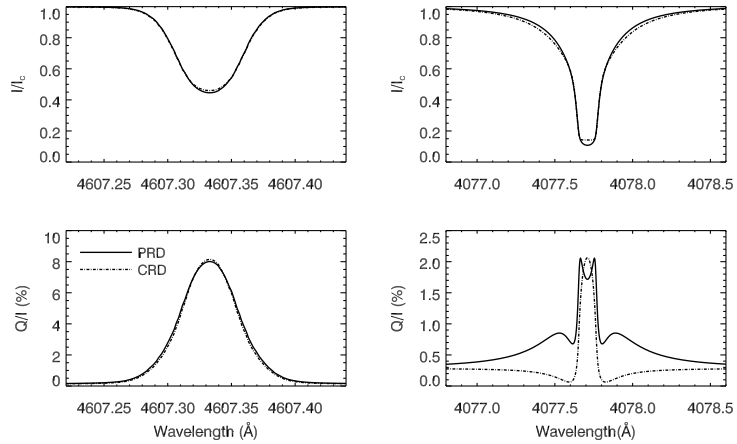

FIGURE 3.14— Emergent intensity normalized over the continuum (top row) and Stokes Q/I (bottom row), for the Sr I at 4607 Å (left column) and for Sr II at 4078 Å (right column). Caculations have been performed both considering PRD in the scattering process (solid curves), and in the CRD limit (dashed-dotted curves). The FAL-C atmospheric model has been used for the calculation. We consider the radiation emerging at an LOS with $\mu = 0.1$, and the direction for positive Q has been taken parallel to the limb.

slightly larger in the CRD limit than when the calculation accounts for PRD effects. This can be qualitatively understood as follows. In the limit of CRD, the radiation scattered at a given frequency depends on a frequency average of the incoming radiation over the whole line profile, weighted by an absorption profile which has its maximum at line center. On the other hand, in the coherent scattering (CS) limit the scattered radiation is related only to the incoming radiation with that same frequency (if Doppler redistribution is neglected). For an absorption line, the intensity of the radiation field increases when going from the core to the wings. Therefore, the intensity of the emergent radiation is larger in the core in the CRD limit, but at wing frequencies it is instead larger in the CS limit. When considering PRD effects, the coherence of scattering is only partially relaxed and so, similarly to the CS limit, the PRD intensity in the line core is also smaller than the one obtained in the CRD limit, and it is larger in the line wings.

The difference between the results obtained in the CRD limit and when accounting for PRD effects is clearly smaller for the Sr I 4607 Å line, and indeed we expect that, once the Stokes profiles are smeared in order to properly account for the effects of the atmosphere's large-scale turbulent motions and the finite spectral resolution of a typical instrument, the differences between the two calculations will be negligible, both for Stokes I and for the Q/I profiles (see Faurobert-Scholl 1993). This line

forms in the photosphere, where the density of neutral hydrogen (which is responsible for all elastic collisions) is rather high, with $Q_{\rm el}$ being comparible in magnitude to $A_{u\ell}$. At the height corresponding to $\tau = 1$ at the line-center frequency for $\mu = 0.1$ (around 350 km above the photospheric surface), the coherence fraction for the Sr I 4607 Å is $\alpha_c = 0.624$. Thus, the contribution from $\mathcal{R}_{\rm II}$ is still significant around this region. Nevertheless, as we have noted, the Stokes I and Q/I profiles obtained in the CRD limit and in the PRD case are in very good agreement. This is due to the fact that, when Doppler redistribution is taken into account, the contribution to the line emissivity from the $\mathcal{R}_{\rm II}$ and $\mathcal{R}_{\rm III}$ redistribution functions have a very similar behavior in the line core (see Faurobert 1987; also Thomas 1957).

The impact of PRD is however much clearer for the Sr II 4078 line, for which the deviation from the CRD results is apparent, especially in the wings of Q/I. The intensity profiles obtained in the two calculations do not present significant differences, either in the line core or in the wings. This is because the absorption coefficient, which plays a major role in the emergent intensity of absorption lines such as the ones considered here, is unchanged when PRD effects are accounted for. We point out that the radiation emerging at the line core region originates from heights around 1200 km, in the FAL-C atmospheric model for a LOS with $\mu = 0.1$, where the density of perturbers is low enough that the coherence fraction is close to 1. However, thanks to Doppler redistribution, the emission coefficients in the line core region do not change significantly when PRD effects are accounted for, which further explains the similarities between the line core Stokes I found in calculations accounting for PRD and in the CRD limit.

Also because of Doppler redistribution, the line core Q/I changes little when PRD effects are included, although for this line one also finds a double-peak structure in the core region of the PRD Q/I profile. This is characteristic of CS when the temperature, and therefore the Doppler width, changes significantly over the spatial regions which contribute to the emergent radiation in the line core (e.g., Faurobert-Scholl 1992). Outside the Doppler core, the PRD Q/I profile presents extended wing lobes while, in the CRD limit, no such lobes are found and in this case the Q/I outside the line core is mainly produced by continuum scattering. In the relatively deep regions where the wings originate, the elastic collisional rate is higher than in the regions where the line core is formed, and the branching ratio for $\mathcal{R}_{\rm III}$ is considerable. Unlike for the $\mathcal{R}_{\rm II}$ redistribution matrix, both the emission and absorption profiles contained in $\mathcal{R}_{\rm III}$ have their maxima around the ν_{M_u,M_ℓ} frequencies of the transition which, even for strong fields of the order of kG, fall within the Doppler core. Thus, the radiation absorbed in the line wings is re-emitted at nearby frequencies almost exclusively through coherent scattering. For an absorption line, the radiation field is larger in the wings than in the core and so, through the $\mathcal{R}_{\rm II}$ redistribution matrix, both ε_I/η_I and ε_Q/η_I present broader wings, i.e., more photons are scattered in the wing region, when scattering is coherent. This explains the extended wing Q/I signals that are produced only when the effects of PRD are accounted for.

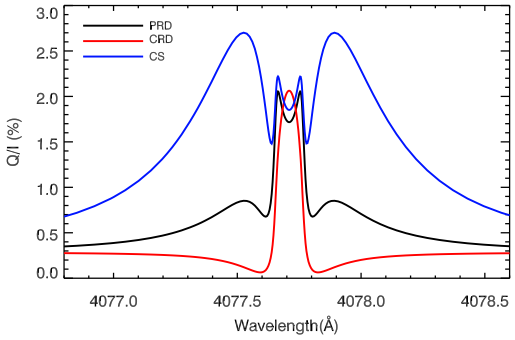

FIGURE 3.15— Stokes Q/I profiles of the emergent radiation for the Sr II 4078 Å line. The calculations have been performed considering PRD in the scattering processes (black curve), and in the CRD (red curve), and CS (blue curve) limits. The FAL-C atmospheric model has been used for the calculation. We consider the radiation emerging at an LOS with $\mu = 0.1$. The direction for positive Q has been taken parallel to the limb.

In order to further illustrate the contribution of CS to the wing polarization, in Fig. 3.15 the previous Q/I profiles are shown again, but in this case together with the calculation in the coherent scattering limit, which is obtained by artificially forcing the elastic collisional broadening Γ_E to be 0, so that all line scattering processes are described by $\mathcal{R}_{\rm II}$. The Q/I profile obtained in this limit is very similar to the PRD one in the line core region, but it is substantially larger in the wings. This increase in the wing polarization is due to the fact that, in the CS limit, the coherence fraction approaches 1, also in the spatial region from where the wing signals originate. Thus the branching ratio for the $\mathcal{R}_{\rm II}$ increases, and so does the resulting Q/I signal.

It is also interesting to note that, at line center, the fractional polarization is in fact lower in the PRD case than for either the CS or CRD limits. This happens when the ratio between the two Stokes parameters is considered, although not for each of them separately.

3.7 The impact of depolarizing collisions

Atomic level polarization can be relaxed not only by the presence of a magnetic field, but also by elastic collisions, which tend to equalize the populations amongst magnetic sublevels and reduce quantum coherences between them. In the previous section, we have already seen the role elastic collisions play on the frequency redistribution for the Sr I 4607 Å and the Sr II 4078 Å lines, through the branching ratios in the redistribution matrices. Here, we focus on how the depolarizing effects of such collisions modify the polarization of the emergent radiation. The depolarizing

effect of collisions is described through suitable rates that appear in the statistical equilibrium equations (see LL04). In this work, we assume that the $D^{(2)}$ multipolar component of the depolarizing collisional rate is given by

$$D^{(2)} = 0.5\,\Gamma_E\,. \tag{3.2}$$

The specific relation between the various $D^{(K)}$ rates depends on the type of interaction between the atom and the perturber (see LL04). For an interaction that can be described by a tensorial operator of rank 2, as is the case of a Van Der Waals potential, such relations are

$$\frac{D^{(1)}}{D^{(2)}} = \frac{1}{3}\,\frac{4J^2+4J-3}{4J^2+4J-7}\,, \qquad \text{where } J \neq 0, \frac{1}{2}, \tag{3.3a}$$

$$\frac{D^{(3)}}{D^{(2)}} = 2\,\frac{4J^2+4J-13}{4J^2+4J-7}\,, \qquad \text{where } J \geq \frac{3}{2}\,. \tag{3.3b}$$

We also recall that, by definition, $D^{(0)} = 0$.

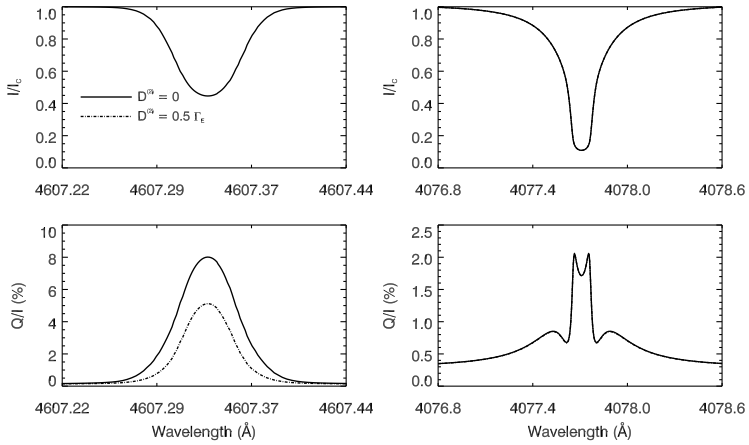

FIGURE 3.16— Emergent intensity normalized to the continuum (top row) and Q/I (bottom row) for the Sr I at 4607 Å (left column) and for Sr II at 4078 Å (right column). The calculations are performed without accounting for depolarizing collisions (solid curves), and taking the depolarizing collisional rate $D^{(2)} = 0.5\,\Gamma_E$ (dashed-dotted curves). The FAL-C atmospheric model has been used for the calculation. We consider the radiation emerging at an LOS with $\mu = 0.1$. The direction for positive Q has been taken parallel to the limb.

In Fig. 3.16 the same PRD calculations that were considered in the previous section are compared to calculations using aforementioned $D^{(K)}$ rates. We recall that the Γ_E rates are obtained from calculations using RH, which are based on the theory presented by Anstee & O'Mara (1995) and Barklem & O'Mara (1997).

For the Sr I 4607 Å line, the effect of elastic collisions on the Q/I signals of the emergent radiation is very clear; close to the limb, at $\mu = 0.1$, such modification of scattering polarization results in a line center Q/I signal of around 5% when $D^{(2)} = 0.5\,\Gamma_E$ is considered, instead of the 8% value which is obtained when it is neglected. This line's large sensitivity to depolarizing collisions is related to the fact that it forms in the photosphere, where the number density of the hydrogen atoms is large, and thus so are the Γ_E and $D^{(K)}$ rates. Nevertheless, we point out that the resulting intensity profile is not appreciably modified when such depolarizing rates are included in the calculation.

For the Sr II 4078 Å line, the effects of collisional depolarization are barely appreciable, given that its core forms at much greater altitudes in the solar atmosphere, where the density of perturbers is significantly lower. In order to illustrate this line's insensitivity to such effects, we have artificially enhanced the depolarizing collisional rates. Calculations, both taking $D^{(2)} = 0.5\,\Gamma_E$ and multiplying all $D^{(K)}$ rates by a factor 10, have been performed. However, in the calculations we have performed for this line, the impact of considering even the latter rates is barely appreciable, and so they are not shown in the figures. In the region where the line core forms, barely any of the scattering events are perturbed by a collision in the time interval between the absorption and the subsequent emission of a photon, which is why elastic collisions do not affect the polarization in the line core of the emergent radiation. This serves to emphasize that the same elastic collisions that relax the frequency coherence in scattering processes also play the role of relaxing atomic level polarization.

We also note that the collisional depolarization rates are contained in the expression for $\mathcal{R}_{\rm III}$ (see Eq. 2.47), but they are instead absent from $\mathcal{R}_{\rm II}$ (see Eq. 2.44). It can easily be seen from such expressions why also the wing polarization of the Sr II 4078 Å line is essentially unaffected by the $D^{(K)}$ rates; although its wings originate at atmospheric heights where elastic collisional rates are high, the polarized radiation scattered at such frequencies is mainly produced by processes described by $\mathcal{R}_{\rm II}$, as was discussed in the previous section. Such processes are not perturbed by elastic collisions, which therefore cannot play any role in reducing scattering polarization. Indeed, for the LOS with $\mu = 0.1$ considered in Fig. 3.16, there is no appreciable change in Q/I even between the calculation in which such depolarizing effects have been neglected and the case in which the $D^{(K)}$ rates are taken above any realistic upper boundary.

We remind the reader that the calculations presented in this work are based on the assumption of a two-level atom and, as pointed out by Deb & Derouich (2014), errors may be incurred for this line if the $^2\mathrm{D}_{3/2}$ and $^2\mathrm{D}_{5/2}$ metastable levels are not considered in the Sr II atomic model.

Aside from the collisional depolarization rates discussed in the previous paragraphs, other, more realistic, rates have been developed to model specific lines. In the previous calculations, the Γ_E rates are calculated in the RH code as described in Barklem & O'Mara (1997). In Fig. 3.17, we consider the Sr I line at 4607 Å, comparing results using the previously discussed rates to those obtained if the elastic

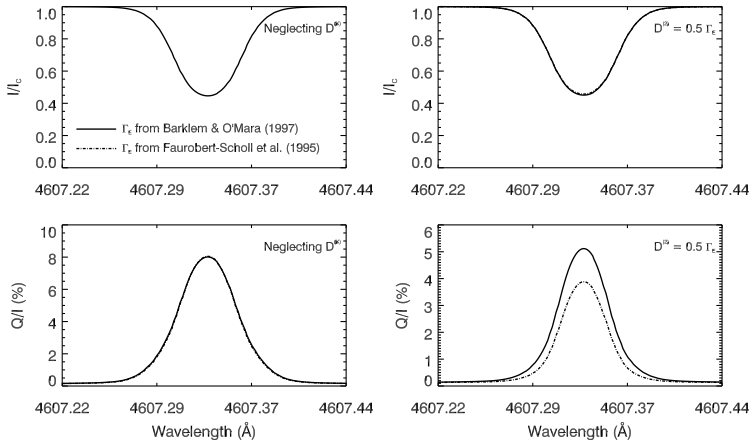

FIGURE 3.17— Emergent intensity normalized to the continuum (top row) and Q/I (bottom row) for Sr I 4607 Å.Calculations both neglecting the depolarizing effect of collisions (left column) and including the rates of Eqs. (3.2) and (3.3) (right column) are shown. The results using Γ_E as given by Barklem & O'Mara (1997) are plotted with solid curves and are compared to the results using Γ_E from Faurobert-Scholl et al. (1995), plotted with dashed-dotted curves. We consider the radiation emerging at an LOS with $\mu = 0.1$. The direction for positive Q has been taken parallel to the limb.

collisional rates are calculated as given in Faurobert-Scholl et al. (1995), i.e.,

$$\Gamma_E = 2.73 \cdot 10^{-8}\, n_H \left(T/5000\right)^{0.16}, \tag{3.4}$$

and for which the $D^{(K)}$ rates are likewise obtained from Eqs. (3.2) and (3.3). When the depolarizing effect of collisions is neglected and only the elastic collisional rate itself changes between the two calculations, the differences in their emergent Stokes profiles are not very significant. This is due to Doppler redistribution, through which the profiles become very similar in the line core, despite the fact that the branching ratios contained in $\mathcal{R}_{\rm II}$ and $\mathcal{R}_{\rm III}$ are slightly different. However, when the depolarizing rates are included, their impact on the emergent Q/I is clear; when using the rates shown in Eq. (3.4), its line-center value is slightly below 4% instead of being above 5%. Thus, when comparing photospheric spectral lines to observations it is of foremost importance to use realistic estimates for the elastic collisional broadening and the depolarizing collisional rates.

Finally, we point out that the impact of depolarizing collisions generally increases when considering LOS closer to disk center, both in the core and wing spectral regions. This is because, for LOS closer to $\mu = 1$, the radiation reaching the observer originates from deeper layers of the solar atmosphere, where the density of the perturbers that are responsible both for frequency redistribution and for a decrease

of scattering polarization are larger. However, for the Sr II 4078 Å line we have checked that, even when considering a LOS with $\mu = 0.9$, there is no appreciable impact of the depolarizing effect of collisions on its linear polarization signal when realistic estimates of elastic collisional rates and depolarizing collisional rates are taken.

3.8 The accuracy of the formal solver: DELOPAR and BESSER

Three formal solvers have been implemented in the HZ code, all of which are based on the concept of short-characteristics. The first of them, DELOPAR, separates the propagation matrix into its diagonal and off-diagonal components. The off-diagonal terms are interpolated linearly, while the source functions are interpolated parabolically. More details of this formal solver are shown in Sect. 2.6.1 and in the references presented there. The BESSER solver, introduced in Štěpán & Trujillo Bueno (2013), is based on the same principles, and differs in how the source functions are interpolated. Instead of parabolic interpolation, Bézier splines are used to interpolate the source functions in each spatial interval under consideration, which provides corrections to overshoots which may be produced in the DELOPAR formal solver, especially in regions where atmospheric parameters such as density or temperature have a sharp spatial dependence. Lastly, a formal solver based on the evolution operator has also been implemented. The evolution operators, described in Eq. (2.109), are obtained at every grid point, and the Stokes vector is obtained by parabolically interpolating the terms containing such operators and the source functions. More details are also given in Sect. 2.6.1. Unlike DELOPAR and BESSER, this formal solver does not impose the constraint that the $\hat{K}'\vec{I}$ product varies linearly between any two grid points. Note that in the absence of a magnetic field, the propagation matrix is diagonal (i.e., $\hat{K}' = 0$) and it becomes identical to DELOPAR.

In Fig. 3.18, the results of calculations for the Sr II 4078 Å line using the DELOPAR and BESSER formal solvers are compared to one another, for a LOS near the limb ($\mu = 0.1$) and another one close to disk center ($\mu = 0.9$). Since there is no magnetic field present, the propagation matrix is diagonal. There is no discernible change in the emergent intensity when selecting one formal solver or the other, for either of the LOS considered in the figure. On the other hand, for the Q/I signals of the emergent radiation there are some very small discrepancies in the core at $\mu = 0.1$, which are somewhat clearer - in relative value - for the $\mu = 0.9$, both in the core and in the wings. For this line, when considering atmospheric models that are representative of the quiet Sun such as FAL-C, whose parameters have a reasonably smooth spatial dependence, the few overshoots which occur when parabolically interpolating the source function do not introduce significant errors, either in the line core or in the wings.

This contrasts with the differences in the line core Q/I signal for the Mg II k line when comparing both formal solutions. As can be seen in Fig. 3.19, the overshoots that are produced when interpolating parabolically give rise to more significant discrepancies. The fact that they are greater in this case, both in absolute and

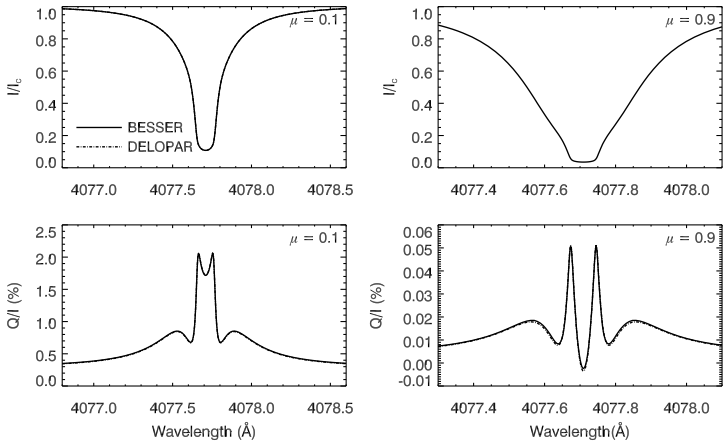

FIGURE 3.18— Stokes I (top row) and Q/I (bottom row) profiles for the Sr II line at 4078 Å. Calculations have been performed using the DELOPAR (dashed-dotted curves) and BESSER (solid curves) formal solver. The FAL-C atmospheric model has been used for the calculations. We consider the radiation emerging at an LOS with $\mu = 0.1$ (left column) and $\mu = 0.9$ (right column). Note that a smaller spectral range has been considered for the latter LOS. The reference direction for positive Q is taken parallel to the limb.

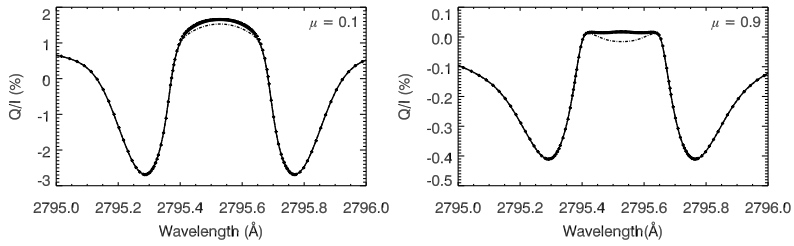

FIGURE 3.19— Stokes Q/I profiles for the Mg II k line at 2795 Å. The FAL-C atmospheric model has been used for the calculations. Such calculations have been performed using the DELOPAR (dash-dotted curves) and BESSER (solid curves) formal solver. The small crosses represent the results of a calculation using DELOPAR with a spatial grid where 12 additional points have been added around the line's formation region. We consider the radiation emerging at an LOS with $\mu = 0.1$ (left panel) and $\mu = 0.9$ (right panel). The direction for positive Stokes Q is taken parallel to the limb.

relative terms, is likely due to the fact that this line forms much higher in the chromosphere than the Ca I 4227 Å or Sr II 4078 Å lines. The radiation emerging at frequencies corresponding to the line core originates close to the transition region,

where the spatial variations of density and temperature are much steeper than at deeper atmospheric layers. Because of this, overshoots in this region produce larger errors and are more common.

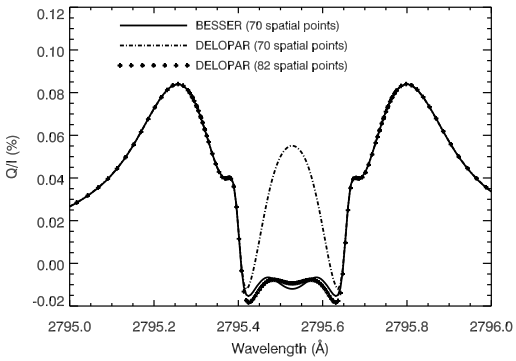

FIGURE 3.20— Stokes Q/I profile for the Mg II k line at 2795 Å. Calcuations have been performed in the presence of a horizontal ($\theta_B = 90^\circ$) magnetic field with azimuth $\chi_B = 0^\circ$ and $B = 20$ G. The FAL-C atmospheric model has been used for the calculations. Such calculations have been performed using the DELOPAR (dash-dotted curves) and BESSER (solid curves) formal solver. The small crosses represent the results of a calculation using DELOPAR with a spatial grid where 12 additional points have been added around the line's formation region. We consider the radiation emerging at an LOS with $\mu = 1$. The direction for positive Stokes Q is taken perpendicular to the magnetic field.

We have also performed a calculation using the DELOPAR formal solver in an atmospheric model with a finer spatial grid, which is obtained from the FAL-C atmospheric model and, around the formation region of the core of the Mg II k line, twelve additional points have been placed between the original ones, and the values of their atmospheric parameters have been found using linear interpolation. The resulting Q/I profile in this case approaches the result obtained using the BESSER formal solver, since refining the spatial grid tends reduce the occurence of overshoots and minimizes the error they introduce.

Discrepancies between the calculations obtained considering both formal solvers are also found in the forward scattering case; in Fig 3.20, the Q/I profile obtained in presence of a horizontal magnetic field of 20 G, is shown. In this case, the difference between the result obtained considering DELOPAR with a spatial grid with 70 points and both the results obtained using BESSER and when using DELOPAR with a refined spatial grid is especially striking. Not only are the differences in the line core Q/I signal very large in relative terms, but there is also a change in its sign. Thus, when performing calculations for the polarization of spectral lines that originate close to the transition region, it is important that the formal solver

considered in the calculation can suitably treat the sharp changes in the source function (or emissivity).

3.9 Conclusions

We introduce an RT code (HZ), based on the theory discussed in the previous chapter, which constitutes a novel forward modeling tool for solar and stellar spectropolarimetry. It considers a two-level atomic model with an unpolarized and infinitely sharp lower level, and it allows for the inclusion of the effects of PRD, as well as the joint action of the Hanle and Zeeman effects. This makes it suitable for the investigation of the magnetic sensitivity of resonance lines of diagnostic interest, such as the Sr II 4078 Å, Sr I 4607 Å, Ca I 4227 Å, and Mg II k.

In such non-LTE caculations, a Jacobi iterative scheme is considered for the $\mathcal{E}_0^0$ component of the line emissivity and Lambda iteration to the other $\mathcal{E}_Q^K$ components. We have first considered the iterative scheme in which the correction to $\mathcal{E}_0^0$ at each iterative step accounts only for the implicit contribution from $\mathcal{E}_0^0$. This yields a good convergence rate when weak magnetic fields are considered. However, in the presence of stronger magnetic fields, the other $\mathcal{E}_Q^K$ components begin to approach $\mathcal{E}_0^0$ in magnitude. In this case, it is no longer suitable to ignore their contributions in the Jacobi iterative scheme, and the convergence rate slows down, eventually producing instabilities as the magnetic field increases. When the contributions from such components are accounted for, i.e., when all $\Lambda_{00,KQ}$ operators are included in the iterative scheme, the convergence rate does not begin to deteriorate until much stronger magnetic fields are considered. For even stronger fields, such that even the latter approximation is unsuitable, it would be necessary to apply Jacobi iteration to all $\mathcal{E}_Q^K$ components, so that they are coupled to one another through the Λ_{KQ,K_PQ_P} operators, leading to a formidable numerical problem.

By considering various semi-empirical atmospheric models (see Fontenla et al. 1993 and Avrett 1995), we have found that the calculated I and Q/I profiles are are sensitive to the particular stratification of atmospheric parameters such as temperature and density. Thus, in order to perform accurate measurements of solar magnetic fields from observed polarization profiles, one must first have information on the thermodynamic properties of the solar atmosphere, e.g., from the intensity of the emergent radiation.

The impact of PRD phenomena on resonance lines has also been investigated. For Sr I 4607 Å, a photospheric line that does not present broad Q/I profiles with extended wings, we confirm that the CRD limit is a very good approximation for modeling the line intensity and polarization, in the absence of a magnetic field. On the other hand, for chromospheric resonance lines such as Sr II 4078 Å, the impact of PRD phenomena is very significant, especially in the near wings. The scattering polarization profiles of the emergent radiation present extended wings and complex multi-peak structures in the core. Such wing signals cannot be found in the limit of CRD which, however, represents a reasonably good approximation for modeling the intensity profile and the fractional linear polarization signal obtained in the line

core.

The impact of depolarizing collisions has also been studied for the two aforementioned spectral lines. For Sr I 4607 Å, the depolarizing effect of collisions on the Q/I profile of the emerging radiation is very clear. The reason is that the same elastic collisions that perturb collisional processes, causing them to be non-coherent in the atomic reference frame, also have the effect of noticeably decreasing scattering polarization. However, for Sr II 4078 Å, the impact of depolarizing collision is negligible in the core region and also in the wings since, despite the fact that the wing photons originate from spatial regions with large elastic collisional rates, the Q/I wings are produced mainly by coherent scattering processes that are unperturbed by such collisions.

The HZ code allows for the calculation of the RT equations using various formal solvers, although BESSER has been used for most of the applications presented in this work. In this chapter we have also used DELOPAR, which has been found to perform well except for the polarization profiles in the core of lines such as Mg II k, which originates in the transition region, where atmospheric parameters such as temperature and density change very sharply over small vertical distances. We also note that the results obtained with DELOPAR approach those obtained with BESSER if a spatial grid is refined around the formation region of the line core.

4

The impact of the magnetic field on the line scattering emissivity

The influence of the magnetic field on the scattered radiation and on the Stokes profiles of the emerging spectral lines is explored, for a variety of field strengths and configurations. The validity of the weak field approximation, i.e., neglecting the Zeeman splitting in the absorption and emission profiles of the RT coefficients, is studied in depth. We highlight that, even for weak fields, it is not suitable for modeling the wings of strong resonance lines for which the effects of PRD are important. An analytical study of the emitted intensity and polarization as a function of the magnetic field strength and the direction of emission, is also presented under such approximation. The case in which a magnetic field whose orientation changes over spatial scales smaller than the line photon's mean free path has also been considered, both for weak and for strong fields. The error incurred by considering the CRD limit and the weak field approximation when inferring the strength of an unresolved magnetic field has been studied. For lines in which the scattering process is mainly coherent, the appearance of circular polarization wing signatures of considerable amplitude is discussed.

4.1 Introduction

In the previous chapter we have presented some illustrative applications of the RT code developed in this thesis (HZ). This forward modeling tool allows us to study in depth a variety of physical mechanisms through which the Stokes profiles of the emergent radiation are sensitive to physical properties of the solar atmosphere. Thanks to such investigations, the diagnostic potential of the spectral line polarization is increased, and physical insights are gained on the generation and transfer of polarization in spectral lines. Nevertheless, in most of the applications presented up to now, the magnetic field has been disregarded, and the focus has instead been on physical elements such as the elastic collisions, and numerical aspects of the problem. In this chapter, we present applications in which the magnetic field, and its

influence on the generation and tranfer of polarized radiation, is the main object of study.

When studying solar magnetism via the interpretation of spectropolarimetric observations, a commonly used approximation in regions where the magnetic field is not strong, such as in the quiet Sun, is to neglect the Zeeman splitting in the absorption and emission profiles. This is known as the weak field approximation. In the following section, its validity will be studied in terms of both field strength and spectral range.

In Chapter 2, the case of a magnetic field whose orientation, instead of being fixed, changes over scales smaller than the line photon's mean free path, was introduced within the framework considered in this thesis. This model has been very useful for the interpretation of spectropolarimetric observations, especially for photospheric lines (e.g., Stenflo 1982; Faurobert-Scholl 1993; Trujillo Bueno et al. 2004; Shchukina & Trujillo Bueno 2011). In the following sections we apply the HZ code to investigate how such micro-structured fields, through the Hanle and Zeeman effects, modify the Stokes profiles of the emergent radiation. Our RT code is also used to study the reliability of inferences, based on the Hanle effect, of the strength of unresolved magnetic fields present in the quiet solar atmosphere, carried out in the CRD limit and assuming the weak field approximation.

We also discuss the circular polarization profiles produced when coherent scattering (CS) accounts for an substantial fraction of the scattering processes, in particular the features of Stokes V/I encountered in the wings of the Mg II k line.

4.2 The applicability of the weak field approximation

The aforementioned RT code allows us to investigate the effects of arbitrary magnetic fields on the polarization profiles of the emergent radiation. When the magnetic field is not very strong (e.g., outside of sunspots), the energy separation between magnetic sublevels induced by the Zeeman effect is generally much smaller than the Doppler width of the line. Under such conditions, a common approach is to neglect the Zeeman splitting of the magnetic sublevels in the emission and absorption profiles of the radiative transfer coefficients. In the formalism used in this work, such profiles appear in the redistribution matrices and in the coefficients of the propagation matrix. This is the so-called weak field approximation, which leads to a considerable simplification of the problem. In general, the Zeeman splitting does not appear only in such profiles, but it is also implicitly present in the Hanle depolarization factor (see the expressions in Eq. (2.44) and (2.47)), which is taken into account even when considering the weak field approximation.

We begin this section by analyzing the validity of the weak field approximation for the spectral lines considered in the previous chapter, by comparing the results both considering such approximation and relaxing it, accounting for the effects of PRD. Such approximation can be obtained by artificially setting the Landé factors of the upper and lower levels to zero in the absorption and emission profiles. In this case, the only nonzero element of the line contribution to the propagation matrix,

as shown in Eq. (2.12) becomes

$$\eta_I(\nu) = k_L\,\phi(\nu_0 - \nu)\,. \tag{4.1}$$

It is interesting to note that it has no angular dependence, unlike in the general case shown in Eq. (2.62a). Under the weak field approximation, the expressions for the redistribution matrices, in the atomic rest frame and having rotated the quantization axis for total angular momentum from the direction of the magnetic field into an arbitrary direction, are

$$\begin{aligned}\left[\mathcal{R}_{\rm II}\right]_{ij}(\nu',\vec{\Omega}',\nu,\vec{\Omega}) = &\sum_{KQ}\frac{\Gamma_R}{\Gamma_R+\Gamma_I+\Gamma_E+2\pi{\rm i}\nu_L g_u Q}\\ &\times W_K(J_\ell,J_u)\delta(\nu-\nu')\phi(\nu_0-\nu)\\ &\times\sum_{Q'Q''}\mathcal{T}^K_{Q''}(i,\vec{\Omega})(-1)^{Q'}\mathcal{T}^K_{-Q'}(j,\vec{\Omega}')\mathcal{D}^K_{QQ'}(R_B)\mathcal{D}^K_{QQ''}(R_B)^*\,,\end{aligned} \tag{4.2}$$

and

$$\begin{aligned}\left[\mathcal{R}_{\rm III}\right]_{ij}(\nu',\vec{\Omega}',\nu,\vec{\Omega}) = &\\ \sum_{KQ}&\left[\frac{\Gamma_R}{\Gamma_R+\Gamma_I+D^{(K)}+2\pi{\rm i}\nu_L g_u Q}-\frac{\Gamma_R}{\Gamma_R+\Gamma_I+\Gamma_E+2\pi{\rm i}\nu_L g_u Q}\right]\\ &\times W_K(J_\ell,J_u)\phi(\nu_0-\nu)\,\phi(\nu_0-\nu')\\ &\times\sum_{Q'Q''}\mathcal{T}^K_{Q}(i,\vec{\Omega})\,(-1)^{Q'}\,\mathcal{T}^K_{-Q}(j,\vec{\Omega}')\mathcal{D}^K_{QQ'}(R_B)\mathcal{D}^K_{QQ''}(R_B)^*\,.\end{aligned} \tag{4.3}$$

When considereing the observer's reference frame, these expressions must also be subjected to the transformations described in Sect. 2.5. Here we have introduced the polarizability factor $W_K(J_\ell,J_u)=\left[w^{(K)}_{J_uJ_\ell}\right]^2$. The iterative scheme, as presented in Sect. 2.7, and the formal solution for the RT equations, are greatly simplified in this case, which leads to an increase in computational speed per iteration, and we have checked that all results coincide with the ones obtained by setting the Landé factors to zero in the absorption and emission profiles.

Figure 4.1 shows the emergent polarization profiles of the Sr I line at 4607 Å for an LOS with $\mu = 0.1$, in the presence of magnetic field with strengths ranging from 0 to 200 G (which is roughly 10 times the Hanle critical field), calculated both in the weak field approximation and fully accounting for Zeeman splitting are presented. The magnetic fields are considered to be horizontal and contained in the plane defined by the LOS and the local vertical. For such geometry, the Hanle effect both reduces the linear polarization fraction of the scattered radiation and rotates the plane of linear polarization. Thus, as can be seen in the figure, the Q/I profiles decrease as the magnetic field strength increases until Hanle saturation is reached. For this LOS, one encounters a change of sign in Q/I as the magnetic field

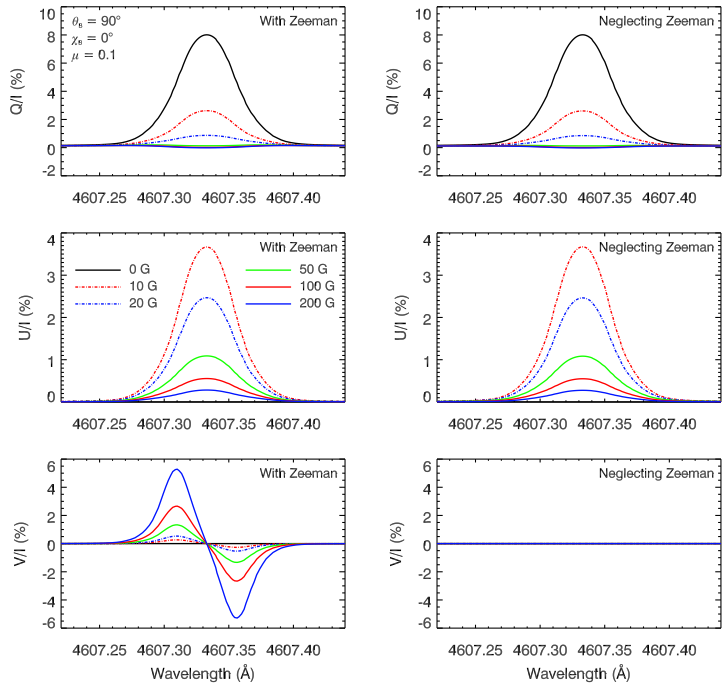

FIGURE 4.1— Stokes Q/I (top row), U/I (middle row), and V/I (bottom row) profiles for the Sr I 4607 Å line. For the remainder of this chapter, calculations are performed using the HZ code, unless otherwise specified. Here, the calculations have been performed in the presence of a horizontal ($\theta_B = 90°$) magnetic field with azimuth $\chi_B = 0°$, both taking into account (left column), and neglecting (right column) the Zeeman splitting in the absorption and emission profiles. Field strengths of 0 G (black solid curves), 10 G (red dashed-dotted curves), 20 G (blue dashed-dotted curves), 50 G (green solid curves), 100 G (red solid curves), and 200 G (blue solid curves) have been considered. The FAL-C atmospheric model has been used for the calculations. We consider the radiation emerging at an LOS with $\mu = 0.1$. The reference direction for positive Stokes Q has been taken parallel to the limb.

increases, which we will discuss later on in this section. Furthermore, a U/I signal is produced as a result of the Hanle effect, which rotates the plane of polarization of the scattered radiation. The amplitude of the signal increases for magnetic fields with strengths below the Hanle critical field, and then decreases as the field strength becomes even larger. For a more intuitive explanation on the impact of the Hanle effect on the polarization of spectral lines based on the classical theory, see Trujillo Bueno (2001).

As seen in Fig. 4.1 there is no appreciable difference between the linear polarization obtained when accounting for the Zeeman splitting and when neglecting it. This could be expected since, for the considered field strengths, the separation in frequency of the magnetic sublevels is considerably smaller than the line's Doppler width around its formation region. Using the atmospheric parameters of the FALC model, the Doppler width at a height of 300 km is $\Delta\nu_D \simeq 2.5 \cdot 10^9$ Hz, corresponding to $\Delta\lambda_D = 18$ mÅ, while the Larmor frequency, which is proportional to the magnetic splitting, is $\nu_L \simeq 2.8 \cdot 10^8$ Hz for a field strength of 200 G, which is about ten times smaller. For such field strengths, the Zeeman effect does not have any appreciable impact on the emergent intensity, which is therefore not shown in the figure. Furthermore, under the assumptions of a two-level atom in a plane-parallel atmosphere, circular polarization is produced only by the Zeeman effect, and so the V/I profile is zero for calculations considering the weak field approximation.

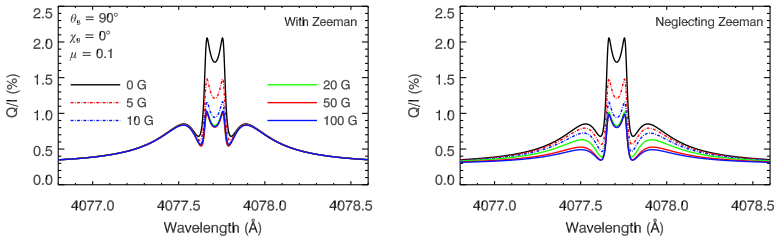

FIGURE 4.2— Stokes Q/I profiles for the Sr II 4078 Å line. The calculations have been performed in the presence of a horizontal ($\theta_B = 90°$) magnetic field with azimuth $\chi_B = 90°$, both when considering the Zeeman splitting in the absorption and emission profiles (left panel) and when neglecting it (right panel). Field strengths of 0 G (black solid curves), 5 G (red dashed-dotted curves), 10 G (blue dashed dotted curves), 20 G (green solid curves), 50 G (red solid curves), and 100 G (blue solid curves) have been considered. The FAL-C atmospheric model has been used for the calculation. We consider the radiation emerging at an LOS with $\mu = 0.1$. The reference direction for positive Stokes Q has been taken parallel to the limb.

We also analyze the impact of the weak field approximation on the calculated profiles when PRD phenomena have a significant impact on the scattering process, namely by considering the Sr II line at 4078 Å. In Fig. 4.2, a comparison between the calculations for Q/I, both making such approximation and relaxing it, is shown for a horizontal and transverse ($\theta_B = 90°$ and $\chi_B = 90°$) magnetic field. In this geometry the Hanle effect does not rotate the plane of linear polarization and the

magnetic field has no longitudinal component, so the U/I and V/I profiles are both zero and are thus not shown. The figure shows results for magnetic field strengths up to 100 G which, for this line, is of the order of 10 times the Hanle critical field. The formation height for the core of the line, in the FALC model and for an LOS with $\mu = 0.1$, is around 1065 km, where the Doppler width is $\Delta\nu_D \simeq 7.9 \cdot 10^9$ Hz, corresponding to $\Delta\lambda = 44$ mÅ. For a field strength of 100 G the Larmor frequency is $\nu_L \simeq 1.3 \cdot 10^8$ Hz, so it is well within the regime of validity for the weak field approximation.

Indeed, the Q/I obtained at the line core is identical for both calculations up to 50 G, and for 100 G there is a very small discrepancy due to a contribution from the Zeeman effect. But in the wings, when the weak field approximation is considered, the Q/I amplitude is found to decrease as the magnetic field increases, and it is sensitive even to field strengths as weak as 5 G. Such magnetic sensitivity is actually a numerical artifact produced because the frequency shifts are neglected in the emission profiles, and thus the Hanle depolarization factor is no longer canceled by the magnetic field dependence in the wings of the profiles. A detailed proof of this effect can be found in Sect. 10.4 of LL04, and it can easily be applied to the redistribution matrix formalism discussed in this work. Thus, it is important to bear in mind that, although the weak field approximation is valid in the line core as long as the frequency shifts due to the Zeeman effect are much smaller than the Dopper width, one must be cautious when using such approximation to consider the effects of the magnetic field when there are extended polarization signals in the wings - as often occurs in strong resonance lines affected by PRD phenomena.

Going back to the photospheric Sr I 4607 Å line, we now consider horizontal magnetic fields with $\chi_B = 90°$, i.e., perpendicular to the LOS, and larger field strengths. In Fig. 4.3 calculations are presented for magnetic fields up to 1500 G, comparing the case in which the Zeeman effect is fully accounted for to the results obtained in the weak field limit. The deviations between the Q/I found in the two calculations begin to be apparent beyond a strength of 200 G. As the splitting between the magnetic sublevels increases, the π and σ components of the transition become increasingly separate in the emission and absorption profiles, leading to the familiar Zeeman profile. The Zeeman effect is also responsible for a clear broadening of the spectral line's Stokes I profile. By neglecting the Zeeman effect in the absorption and emission profiles, one can also see that the Hanle effect also has a minor impact on the emergent intensity.

We now analyze the impact of the magnetic field under the weak field approximation, through the Hanle effect, for various inclinations of the emergent radiation. Depending on the LOS, one may find that Q/I changes its sign as the magnetic field increases, as we found for the Sr I line in Fig. 4.1, which is much more obvious for smaller inclinations of the emergent radiation, such as for an LOS with $\mu = 0.5$. Another, often undiscussed, consequence of the Hanle effect can be seen in Fig. 4.4, where the center-to-limb variation (CLV) of the Stokes I and Q/I profiles at line-center ($\lambda = 4607.33$ Å) are shown in the $\mu = [0.1, 1]$ range. The various

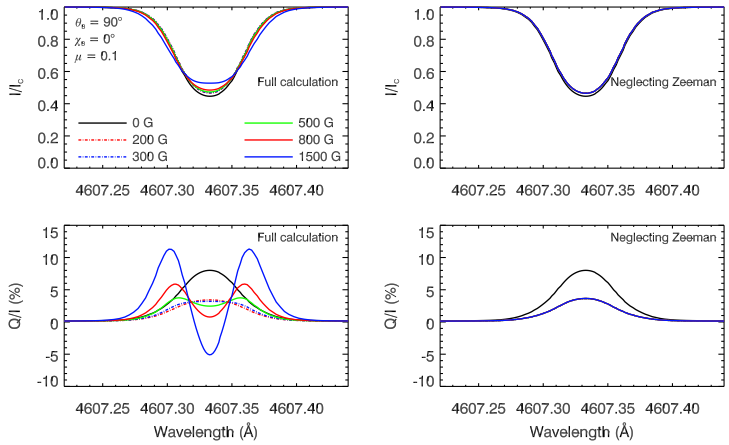

FIGURE 4.3— Stokes I (top row) and Q/I (bottom row) profiles for Sr I 4607 Å. The calculations have been performed in the presence of a horizontal ($\theta_B = 90°$) magnetic field with an azimuth of $\chi_B = 90°$, both when considering the Zeeman splitting in the absorption and emission profiles (left column) and when neglecting it (right column). Field strengths of 0 G (black solid curves), 200 G (red dashed-dotted curves), 300 G (blue dashed-dotted curves), 500 G (green solid curves), 800 G (red solid curves), and 1500 G (blue solid curves) have been considered. The FAL-C atmospheric model has been used for the calculations. We consider the radiation emerging at an LOS with $\mu = 0.1$. The reference direction for positive Stokes Q has been taken parallel to the limb.

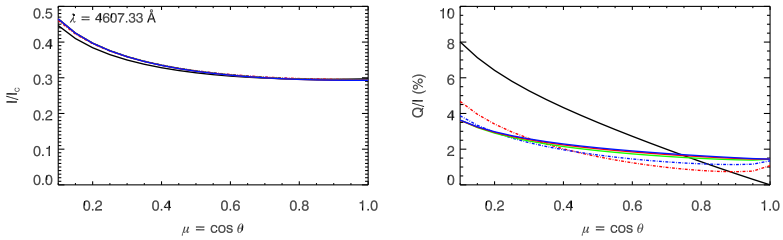

FIGURE 4.4— Center-to-limb variation (CLV) for the line-center Stokes I (left panel) and Stokes Q/I (right panel) for Sr I 4607 Å. The calculations have been performed in the presence of a horizontal magnetic field with azimuth $\chi_B = 90°$ and neglecting Zeeman splitting. Magnetic field strengths of 0 G (black solid curves), 10 G (red dashed-dotted curves), 20 G (blue dashed-dotted curves), 50 G (green solid curves), 100 G (red dashed-dotted curves) and 200 G (blue dashed-dotted curves) have been considered. The FAL-C atmospheric model has been used for the calculations. The reference direction for positive Stokes Q has been taken parallel to the limb.

curves represent the calculations, performed under the weak field approximation, in the presence of horizontal and transverse ($\theta_B = 90^\circ$ and $\chi_B = 90^\circ$) magnetic fields, with strengths ranging from 0 to 200 G, for which we have established that Zeeman splitting can be safely neglected for this line. For LOS with μ between 0.3 and 0.8 it is especially clear that, as the magnetic field strength increases, the Q/I signal begins to decrease until, at field strengths of the order of the Hanle critical field, this trend is inverted and Q/I begins to increase until Hanle saturation is reached.

The aforementioned behavior is a direct consequence of the modification of scattering polarization due to the magnetic field, as it relaxes coherences between the various M-levels in the magnetic reference frame. A magnetic field that is perpendicular to the symmetry axis of the radiation field modifies the scattered radiation in such a way that, for 90° scattering, the linear polarization fraction always decreases as the field strength increases until Hanle saturation is reached. On the other hand, the linear polarization fraction increases monotonically due to the Hanle effect in the forward scattering case, i.e., for an LOS of $\mu = 1$. The emergent intensity is also found to be sensitive to the magnetic field, so that the Hanle effect at saturation causes a slight decrease for inclinations close to disk center, and instead a slight increase close to the limb.

Although the impact of the Hanle effect field on the polarization of the emergent spectral line radiation is well-understood, and its dependence on the direction of the scattered radiation has already been described in multiple occasions (e.g., Landi Degl'Innocenti 1983, Stenflo 1994, Bommier 1997b, Trujillo Bueno 2001, LL04), it is often assumed that the Hanle sensitivity for the radiation emerging close to the limb is qualitatively the same as the one occurring for 90° scattering. However, for smaller inclinations of the emergent radiation one can find, as the magnetic field strength increases, a change in sign for the emergent Q/I (see the Hanle diagram in Trujillo Bueno et al. 2012), or a relative extremum for Q/I before reaching the Hanle saturation.

In order to emphasize that such behaviors occur even for LOS with relatively small μ, it is instructive to analytically study the magnetic sensitivity of the scattered radiation. For simplicity, let us consider the CRD limit case, in which all scattering processes are described via the $\mathcal{R}_{\rm III}$ redistribution matrix, but neglecting any depolarizing effect produced by collisions. The line part of the emission coefficient, as shown in Eq. (2.119) in terms of the source function's multipolar components, is given by

$$\varepsilon_i(\nu, \vec{\Omega}) = k_L\, \phi(\nu_0 - \nu) \sum_{KQ''} \mathcal{T}^K_{Q''}(i, \vec{\Omega}) S^K_{Q''}\,. \tag{4.4}$$

If we assume that there exists a reference frame for which the radiation field is cylindrically symmetric around the total angular momentum's quantization axis Z, i.e., only J^0_0 and J^2_0 are nonzero, then in such reference frame the only nonzero

components of the source function are

$$S_0^0 = \tilde{J}_0^0\,,$$
$$S_{Q''}^2 = \sum_{Q=-2}^{2} \frac{1}{1+\mathrm{i}\,H_u Q} W_K(J_\ell, J_u)\,\tilde{J}_0^2\,\mathcal{D}^K_{Q0}(R_B)\mathcal{D}^K_{QQ''}(R_B)^*\,, \tag{4.5a}$$

where the rotation matrices are defined in Eq. (2.53) and the rotation that leaves the system in the new reference frame is $R_B = (-\gamma_B, -\theta_B, -\chi_B)$. As in Eq. (2.49), we take the parameter $H_u = 2\pi\nu_L g_u/A_{u\ell}$ to quantify the efficiency of the Hanle effect. We define the frequency-averaged radiation field tensor as

$$\tilde{J}^K_Q = \int J^K_Q(\nu')\,\phi(\nu_0-\nu')\,\mathrm{d}\nu'\,, \tag{4.6}$$

where the radiation field tensor $J^K_Q(\nu)$ has been defined in Eq. (2.23). We now consider two specific cases, one (A) in which the magnetic field is horizontal with azimuth $\chi_B = 0^\circ$ and another (B) in which it is also horizontal but with $\chi_B = 90^\circ$. We recall that the reference system has been taken so that the LOS is contained in the XZ plane (see Fig. 3.1), i.e., $\chi = 0^\circ$, considering the radiation field's symmetry axis to be along the Z axis. Taking the angle defining the direction for positive Stokes Q to be along the Y axis, the relevant polarization tensors (e.g., LL04) are

$\mathcal{T}^2_Q(i,\vec{\Omega})$	$i=0$	$i=1$	$i=2$
$Q=-2$	$\frac{\sqrt{3}}{4}\sin^2\theta$	$\frac{\sqrt{3}}{4}(1+\cos^2\theta)$	$-\mathrm{i}\frac{\sqrt{3}}{2}\cos\theta$
$Q=-1$	$\frac{\sqrt{3}}{2}\sin\theta\cos\theta$	$-\frac{\sqrt{3}}{2}\sin\theta\cos\theta$	$\mathrm{i}\frac{\sqrt{3}}{2}\sin\theta$
$Q=0$	$\frac{\sqrt{2}}{4}(3\cos^2\theta-1)$	$\frac{3\sqrt{2}}{4}\sin^2\theta$	0
$Q=1$	$-\frac{\sqrt{3}}{2}\sin\theta\cos\theta$	$\frac{\sqrt{3}}{2}\sin\theta\cos\theta$	$\mathrm{i}\frac{\sqrt{3}}{2}\sin\theta$
$Q=2$	$\frac{\sqrt{3}}{4}\sin^2\theta$	$\frac{\sqrt{3}}{4}(1+\cos^2\theta)$	$\mathrm{i}\frac{\sqrt{3}}{2}\cos\theta$

and $\mathcal{T}^0_0(i,\vec{\Omega}) = \delta_{i0}$.

For case (A), where $\theta_B = 90^\circ$ and $\chi_B = 0^\circ$

$$S_0^2 = W_K(J_\ell, J_u)\,\tilde{J}_0^2\,\frac{1}{4}\Big(1+3\frac{1}{1+4{H_u}^2}\Big)\,, \tag{4.7a}$$
$$S_1^2 = -\mathrm{i}\,W_K(J_\ell, J_u)\,\tilde{J}_0^2\,\frac{\sqrt{6}}{8}\frac{4H_u}{1+4{H_u}^2} = S^2_{-1}\,, \tag{4.7b}$$
$$S_2^2 = W_K(J_\ell, J_u)\,\tilde{J}_0^2\,\frac{\sqrt{6}}{8}\Big(\frac{1}{1+4{H_u}^2}\Big) = S^2_{-2}\,. \tag{4.7c}$$

So in this case the expressions for the emissivities for Stokes I, Q, and U are

$$\varepsilon_I(\nu,\vec{\Omega}) = k_L\,\phi(\nu_0-\nu)\Bigg\{\tilde{J}^0_0 + W_K(J_\ell,J_u)\tilde{J}^2_0\,\frac{\sqrt{2}}{16} \times\left[\left(1+3\frac{1}{1+4{H_u}^2}\right)\left(3\cos^2\theta-1\right)+3\left(\frac{1}{1+4{H_u}^2}-1\right)\sin^2\theta\right]\Bigg\}, \tag{4.8a}$$

$$\varepsilon_Q(\nu,\vec{\Omega}) = k_L\,\phi(\nu_0-\nu)W_K(J_\ell,J_u)\tilde{J}^2_0\,\frac{\sqrt{2}}{16} \times\left[3\left(1+3\frac{1}{1+4{H_u}^2}\right)\sin^2\theta+3\left(\frac{1}{1+4{H_u}^2}-1\right)\left(1+\cos^2\theta\right)\right], \tag{4.8b}$$

$$\varepsilon_U(\nu,\vec{\Omega}) = k_L\,\phi(\nu_0-\nu)W_K(J_\ell,J_u)\,\tilde{J}^2_0\,\frac{3\sqrt{2}}{2}\frac{H_u}{1+4{H_u}^2}\,. \tag{4.8c}$$

For case (B), where $\theta_B = 90^\circ$ and $\chi_B = 90^\circ$, the $S^2_{Q''}$ components become

$$S^2_0 = W_K(J_\ell,J_u)\tilde{J}^2_0\frac{1}{4}\left(1+3\frac{1}{1+4{H_u}^2}\right), \tag{4.9a}$$

$$S^2_1 = -W_K(J_\ell,J_u)\tilde{J}^2_0\frac{\sqrt{6}}{8}\left(\frac{4H_u}{1+4{H_u}^2}\right) = -S^2_{-1}\,, \tag{4.9b}$$

$$S^2_2 = -W_K(J_\ell,J_u)\tilde{J}^2_0\frac{\sqrt{6}}{8}\left(\frac{1}{1+4{H_u}^2}\right) = S^2_{-2}\,. \tag{4.9c}$$

Therefore,

$$\varepsilon_I(\nu,\vec{\Omega}) = k_L\,\phi(\nu_0-\nu)\Bigg\{\tilde{J}^0_0 + W_K(J_\ell,J_u)\tilde{J}^2_0\frac{\sqrt{2}}{16} \times\left[\left(1+3\frac{1}{1+4{H_u}^2}\right)\left(3\cos^2\theta-1\right)+6\frac{4H_u}{1+4{H_u}^2}\cos\theta\sin\theta -3\left(\frac{1}{1+4{H_u}^2}-1\right)\sin^2\theta\right]\Bigg\}, \tag{4.10a}$$

$$\varepsilon_Q(\nu,\vec{\Omega}) = k_L\,\phi(\nu_0-\nu)W_K(J_\ell,J_u)\tilde{J}^2_0\frac{\sqrt{2}}{16} \times\left[3\left(1+3\frac{1}{1+4{H_u}^2}\right)\sin^2\theta-6\frac{4H_u}{1+4{H_u}^2}\cos\theta\sin\theta -3\left(\frac{1}{1+4{H_u}^2}-1\right)\left(1+\cos^2\theta\right)\right], \tag{4.10b}$$

$$\varepsilon_U(\nu,\vec{\Omega}) = 0\,. \tag{4.10c}$$

In Figs. 4.5 and 4.6 the Stokes components of the emissivity at line center are shown as a function of the magnetic field strength (proportional to H_u) for various

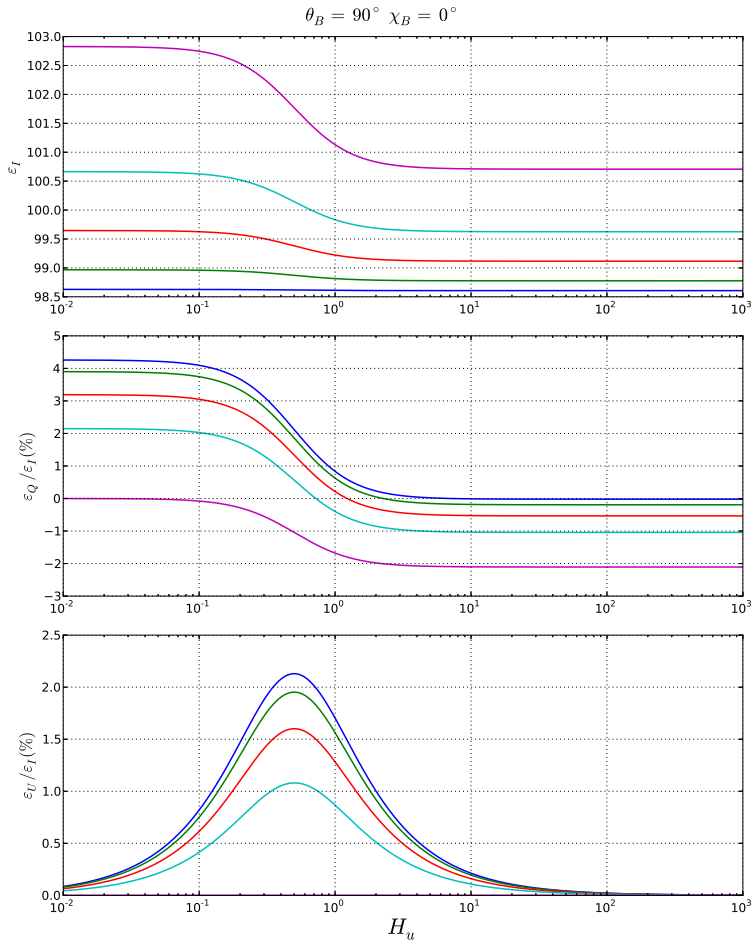

FIGURE 4.5— Line-center emissivity in intensity (top, arbitrary units), $\varepsilon_Q/\varepsilon_I$ (middle) and $\varepsilon_U/\varepsilon_I$ (bottom) for a horizontal magnetic field with $\chi_B = 0°$, as a function of H_u (see Eqs. (4.8)). Each of the curves represents a different inclination of the direction of the emission with respect to the radiation field's symmetry axis, including $\mu = 0.1$ (blue curve), $\mu = 0.3$ (green curve), $\mu = 0.5$ (red curve), $\mu = 0.7$ (cyan curve) and $\mu = 1$ (magenta curve).

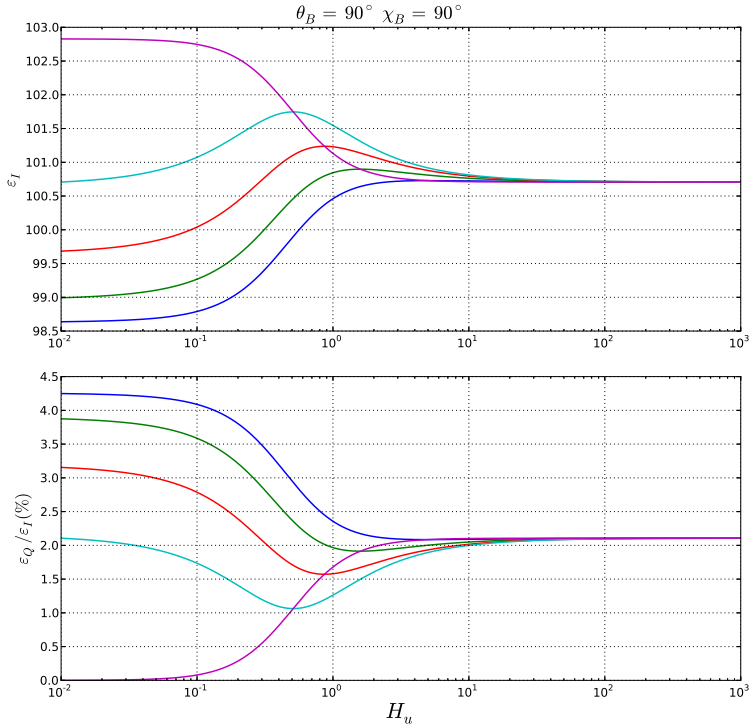

FIGURE 4.6— Line-center emissivity in intensity (top, arbitrary units) and $\varepsilon_Q/\varepsilon_I$ (bottom) for a horizontal magnetic field with $\chi_B = 90^\circ$, as a function of H_u (see Eqs. (4.10)). ε_U is zero independently of field strength for this geometry, and therefore it is not shown. Each of the curves represents a different inclination of the direction of emission with respect to the radiation field's symmetry axis, including $\mu = 0.1$ (blue curve), $\mu = 0.3$ (green curve), $\mu = 0.5$ (red curve), $\mu = 0.7$ (cyan curve) and $\mu = 1$ (magenta curve).

inclinations of the scattered radiation with respect to the symmetry axis of the radiation field. Figure 4.5 shows the dependence of the emissivities on H_u in the presence of a magnetic field oriented along the X-axis, as described by Eq. (4.8). Figure 4.6 shows the dependence on the magnetic field strength given by Eq. (4.10), which corresponds to the case of a horizontal magnetic field with $\chi_B = 90^\circ$, i.e., oriented along the Y-axis. The main object of this study is the magnetic dependence of the linear polarization fraction, and so arbitrary units have been taken. We have chosen the values $\phi(0) = k_L = W_K(J_\ell, J_u) = 1$ and $\tilde{J}^0_0 = 100$ and $\tilde{J}^2_0 = 4$. Of course, only the local values of emissivity are considered in such expressions, and transfer

effects are not accounted for.

In case (A), we note that $\varepsilon_Q/\varepsilon_I$ is positive when the inclination of the emitted radiation with respect to the symmetry axis of the radiation field, or the Z-axis, is large, as is the case for $\mu = \cos\theta = 0.1$, and it decreases considerably as the magnetic field strength approaches the Hanle critical field, reaching a negative, although small, value at saturation. On the other hand, in the forward scattering case it is zero in the absence of a magnetic field but becomes increasingly negative as this magnetic field increases. This is consistent with what we have discussed for Fig. 4.1. For intermediate inclinations, the $\varepsilon_Q/\varepsilon_I$ is significant in the absence of magnetic field and, when the field reaches saturation, it also has a considerable amplitude, although with the opposite sign. The intensity of the scattered radiation does not change much in relative terms when the radiation anisotropy is small, such as in the case presented here. Nevertheless, it is interesting to note that the influence of the Hanle effect on intensity is largest in the forward scattering case for this geometry while, for an inclination of $\mu = 0.1$, the emitted intensity is practically insensitive to the Hanle effect. For the magnetic field considered in this case, Hanle rotation gives rise to an $\varepsilon_U/\varepsilon_I$ which, being zero in the absence of a magnetic field, increases as H_u approaches 1, and then decreases as the magnetic field continues to increase. Its amplitude maximizes for 90° scattering, which again coincides with the previous discussion concerning Fig. 4.1.

In case (B), in which the magnetic field is horizontal and perpendicular to the scattering direction, the Hanle effect does not produce any rotation of the plane of polarization for the emergent radiation, so ε_U is always zero. Although $\varepsilon_Q/\varepsilon_I$ does not change sign for a magnetic field with such orientation, for inclinations such as $\mu = 0.5$ or 0.7, we find that small magnetic fields cause the polarization fraction of the emitted radiation to decrease until, around field strengths such that H_u approaches 1, this trend is inverted and the polarization fraction instead starts to increase until saturation is reached. For such inclinations, $\varepsilon_Q/\varepsilon_I$ continues to change perceptibly for greater field strengths than in case (A), up to $H_u \simeq 20$. As for ε_I, we see that for inclinations of the emitted radiation close to the forward scattering case ($\mu = 1$), it is smaller at Hanle saturation than in the absence of magnetic field. For larger inclinations, however, the intensity instead increases with the magnetic field. These findings are consistent with the discussion on the CLV of the calculated profiles shown in Fig. 4.4.

4.3 Scattering polarization in the presence of micro-structured fields

In previous sections we have considered the situation where the orientation of the magnetic field is fixed along a specific direction at each spatial grid point, which we will hereafter refer to the deterministic magnetic field case. We now study the case in which the magnetic field's orientation changes at scales smaller than the line photon's mean free path, i.e., the case of a micro-structured magnetic field. The expressions for the radiative transfer coefficients in this case are shown in Sect. 2.6. In analogy to what was done in the previous section, here we present RT calculations,

for the same two spectral lines - namely Sr I 4607 Å and Sr II 4078 Å - in which micro-structured fields of increasing strength have been included. In Fig. 4.7, the

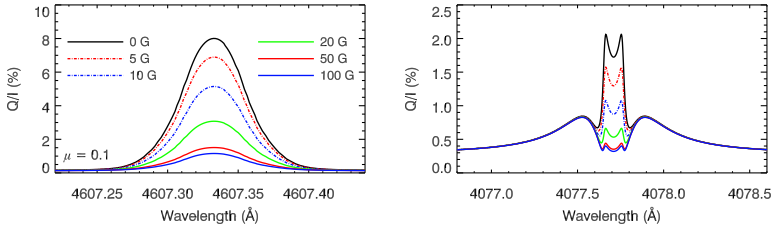

FIGURE 4.7— Stokes Q/I profiles for the Sr I line at 4607 Å (left panel) and for the Sr II line at 4078 Å (right panel). The calculations have been performed in the presence of a micro-structured and isotropic magnetic field. The colored curves represent the same field strengths as in Fig. 4.1. The FAL-C atmospheric model has been used for the calculations. We consider the radiation emerging at an LOS with $\mu = 0.1$. The reference direction for positive Stokes Q is taken parallel to the limb.

linear polarization profile of the radiation emerging at an LOS with $\mu = 0.1$ is shown for such lines, in the presence of a micro-structured and isotropic magnetic field. The colored curves presented in both figures correspond to the same field strengths, although the Hanle critical field of the Sr II 4078 Å line is smaller by about a factor 2; therefore its line core polarization decreases more noticeably for weaker fields.

Due the spherical symmetry of the magnetic field under consideration, the Hanle effect produces no net rotation of the plane of linear polarization, and the longitudinal components of the magnetic fields, which would individually give rise to circular polarization signals via the Zeeman effect, cancel each other out. Therefore, neither Stokes U nor V are produced in this case, for any LOS. For Sr II 4078 Å, we once again note that the Hanle effect only operates in the line core, while the wings are insensitive to the magnetic field.

It is also interesting to note that, especially for the Sr I line at 4607 Å, the line-core value for Q/I at saturation is not 1/5 of its nonmagnetic value, as discussed by Stenflo (1982) and Landi Degl'Innocenti (1985), but is in fact significantly smaller. The explanation for this is related to the radiative transfer effects occuring in optically thick media.

In order to illustrate this, we have first considered two optically thin slabs whose atmospheric parameters are taken from the FAL-C model, at heights of 350 km and 250 km above the model's visible surface, which correspond to the line-core formation height of Sr I 4607 Å for LOS of $\mu = 0.1$ and $\mu = 0.5$, respectively. The $\varepsilon_Q/\varepsilon_I$ ratio has been calculated in the two slab models, considering LOS with $\mu = 0.1$ and $\mu = 0.5$, respectively, both in the absence of a magnetic field and in the presence of a micro-structured and isotropic magnetic field with $B = 400$ G, for which Hanle saturation is reached. Such calculations, obtained under the weak field

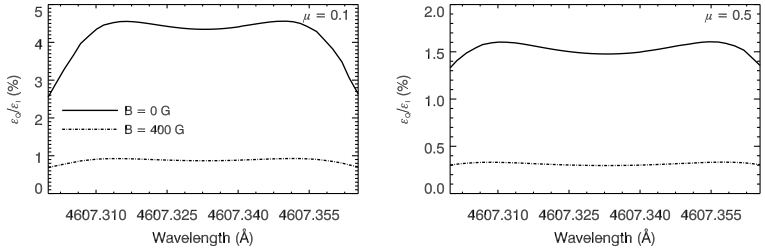

FIGURE 4.8— $\varepsilon_Q/\varepsilon_I$ for the Sr I 4607 Å line comparing calculations in the absence of a magnetic field (solid curves) are compared to calculations in the presence of a 400 G micro-structured and isotropic magnetic field, under the weak field approximation (dash-dotted curves). The calculations consider an optically thin slab whose atmospheric parameters are those of the FAL-C model, at 350 km above the model's visible surface when a LOS with $\mu = 0.1$ is taken (left panel), and at 250 km when $\mu = 0.5$ (right panel), which correspond to the height where the line-center $\tau(\mu) = 1$. The reference direction for positive Stokes Q is taken parallel to the limb.

approximation, are shown for the spectral region corresponding to the line core in Fig. 4.8. Indeed, the ratio between the $\varepsilon_Q/\varepsilon_I$ obtained at Hanle saturation over the $\varepsilon_Q/\varepsilon_I$ obtained in the unmagnetized case approaches the expected 1/5 value. We note that small deviations from this theoretical value remain due to the fact that, not only does ε_Q decrease due to the Hanle effect, but ε_I at line center experiences a slight increase. Moreover, we note that the continuum contribution, which is of course insensitive to the Hanle effect, is also accounted for. Although the deviation from the 1/5 theoretical value due to such effects is small, the overall deviation can be much greater when radiative transfer effects are important, as occurs in the optically thick plasma of the solar atmosphere, in regions where conditions are far from LTE.

In Fig. 4.9, such radiative transfer effects are considered by showing $\varepsilon_Q/\varepsilon_I$ for an LOS with $\mu = 0.1$, both after having obtained the self-consistent solution with the HZ code, and at the first iteration. The initial estimate for the radiation field tensor has been taken from the self-consistent solution of the non-LTE calculation for intensity only, obtained with the RH code of Uitenbroek (2001). The results are shown at line-center, in terms of optical depth (for the same LOS), which is taken to be zero at the atmosphere's upper boundary. The calculations have been performed accounting for PRD effects and, for simplicity, the weak field approximation has been considered. If we consider the ratio of the $\varepsilon_Q/\varepsilon_I$ obtained for a 400 G micro-structured and isotropic field over the one obtained in the absence of a magnetic field, obtained at the first iteration, we find that it is indeed close to 1/5; such ratio is however significantly smaller when the self-consistent solution has been reached.

As we have noted, the calculations are initialized using the radiation field tensor obtained from the RH code, which does not account for the polarization induced by scattering of anisotropic radiation. In the HZ code, such effects are included in

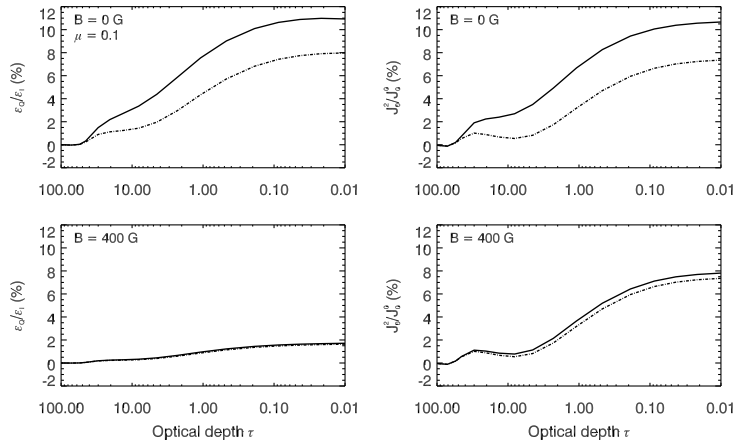

FIGURE 4.9— Line-center $\varepsilon_Q/\varepsilon_I$ (left column) for radiation emitted at an LOS with $\mu = 0.1$ and J^2_0/J^0_0 (right column) in terms of the line-center optical depth for this inclination, calculated for the Sr I 4607 Å line. Their values at the first iteration (dash-dotted curves) are compared to the values when the self-consistent solution has been reached (solid curves). Such calculations are performed in the absence of a magnetic field (top row), and in the presence of a 400 G micro-structured and isotropic magnetic field, under the weak field approximation (bottom row). The reference direction for positive Q is taken parallel to the limb. The line-center wavelength considered is $\lambda = 4607.33$ Å.

a rigorous manner, and we find that they play an important role in the transfer process. In the absence of a magnetic field, such scattering polarization contributes to the J^2_0 component of the radiation field tensor. We recall that J^2_0 depends on Stokes I, Q, and U, as can be seen from its expression

$$J^2_0(\nu) = \oint \frac{\mathrm{d}\vec{\Omega}}{4\pi}\Big[\mathcal{T}^2_0(0,\vec{\Omega})\, I(\nu,\vec{\Omega}) + \mathcal{T}^2_0(1,\vec{\Omega})\, Q(\nu,\vec{\Omega}) + \mathcal{T}^2_0(2,\vec{\Omega})\, U(\nu,\vec{\Omega})\Big]\,. \quad (4.11)$$

Therefore, the J^2_0 obtained in the self-consistent solution is considerably larger when the joint action of transfer effects and scattering polarization is accounted for. A micro-structured isotropic magnetic field, strong enough that Hanle saturation is reached, leads to a significant reduction of the polarization fraction of scattered radiation, which makes the resulting J^2_0 noticeably smaller than the one obtained in the absence of a magnetic field.

Indeed, the J^2_0/J^0_0 ratio obtained in the self-consistent solution of the HZ code, represented by the solid curves in the right panels of Fig. 4.9 are much closer to the values obtained at the first iteration (dash-dotted curves) when a magnetic field is present than when it is absent. In contrast, the J^2_0/J^0_0 found at the first iteration both with and without a magnetic field coincide very well. Thus, when non-LTE

radiative transfer effects are accounted for, the decrease of the J^2_Q component of the pumping radiation field due to the Hanle effect cause the emergent Q/I at line center to be considerably smaller than 1/5 of the Q/I obtained in the absence of a magnetic field.

We note that the deviation from this theoretical ratio is not as great when depolarizing collisions are included since, if atomic polarization is collisionally suppressed, then the contribution of scattering polarization to J^2_0 is not as significant, even in the absence of a magnetic field. In the case of Sr II 4078 Å, the joint action of scattering polarization and the transfer of polarized radiation still plays a role, but it is not as obvious as it was for Sr I 4607 Å , because the line-center radiation anisotropy is considerably smaller around the formation height at its core.

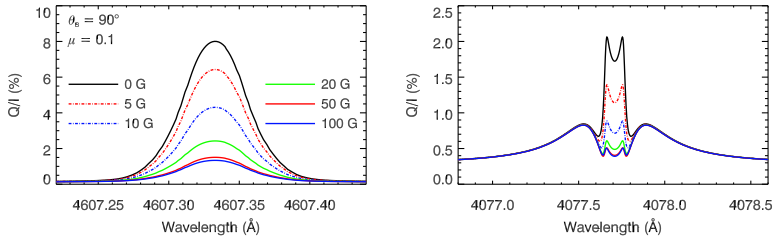

FIGURE 4.10— Stokes Q/I profiles for the Sr I line at 4607 Å (left panel), and for the Sr II line at 4078 Å (right panel). The calculations have been performed in the presence of a micro-structured magnetic field with inclination $\chi_B = 90°$ and a randomly-changing azimuth. The colored curves represent the same field strengths as in Fig. 4.1. The FAL-C atmospheric model has been used for the calculations. We consider the radiation emerging at an LOS with $\mu = 0.1$. The reference direction for positive Stokes Q is taken parallel to the limb.

In Fig. 4.10 calculations are shown in the presence of a horizontal magnetic field whose azimuth changes randomly at small scales. It can be seen, through symmetry considerations analogous to the ones used in the previous case, that no Stokes U nor V is produced in this case, independently of the LOS one considers. However, we note that in this case the linear polarization produced by the magnetic field's transverse components does not necessarily cancel, so considerable Zeeman signals in linear polarization would be produced for strong magnetic fields. For the weaker magnetic fields shown in the figure, the magnetic sensitivity for Q/I is exclusively due to the Hanle effect. Although, for magnetic fields strengths that correspond to fractions of the Hanle critical field, the Hanle depolarization is more efficient than in the isotropic case, the Q/I line-core amplitude at Hanle saturation is instead larger. This is in agreement with the discussion by Stenflo (1982). Also in this case, the Q/I amplitude is significantly lower than the predicted 1/4 of the nonmagnetic case, for the same reason.

In Fig. 4.11, calculations are presented for a magnetic field whose azimuth also changes randomly at small scales, but whose inclination is fixed at $\theta_B = 30°$ instead.

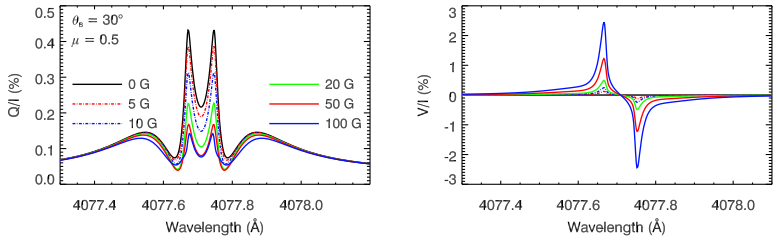

FIGURE 4.11— Stokes Q/I (left) and V/I (right) profiles for the Sr II line at 4078 Å. The calculations have been performed in the presence of a micro-structured magnetic field with a fixed inclination $\theta_B = 30^\circ$ and a randomly-changing azimuth. The colored curves represent the same field strengths as in Fig. 4.1. The FAL-C atmospheric model has been used for the calculations. We consider the radiation emerging at an LOS with $\mu = 0.5$. The reference direction for positive Stokes Q is taken parallel to the limb.

A narrower spectral range is shown for this figure, in order to better illustrate the magnetic sensitivity in the line core and near wings. The distribution of magnetic field orientations and the radiation field are symmetric around the same axis; therefore the Hanle effect does not not produce any net rotation of the plane of linear polarization in this case either, and so U is again zero. Since the efficiency of the Hanle effect depends on the inclination of the magnetic field with respect to the symmetry axis of the radiation field, and such inclination is smaller when considering this magnetic field configuration than for the previous case, the depolarization produced by the Hanle effect is less effective. However, in this case the longitudinal components of the small-scale field orientations do not perfectly cancel each other, and so the Zeeman effect may give rise to circular polarization signals. This is better illustrated by taking a LOS of $\mu = 0.5$, which corresponds to $\theta = 60^\circ$, as is shown in the figure.

4.4 Strong isotropic magnetic fields

Up to now, we have studied relatively weak micro-structured magnetic fields, at most around 10 times stronger than the Hanle critical field. In this section we consider the case of stronger micro-structured magnetic fields, for which the splitting of Zeeman components is apparent also in the intensity profile.

Let us consider the case in which a spectral line forms in a spatial region of the medium where the elastic collision rate is large enough that any correlation between the incoming and scattered photons is completely lost, so that CRD occurs in scattering. Such collisions also have the effect of completely relaxing atomic level polarization. We have imposed this limit in our calculations by artificially forcing both the elastic collision rate Γ_E and the K-multipole components of the depolarizing collision rate other than $D^{(0)}$ to be very large.

In Fig. 4.12, such calculations are presented for Sr I 4607 Å - a transition with

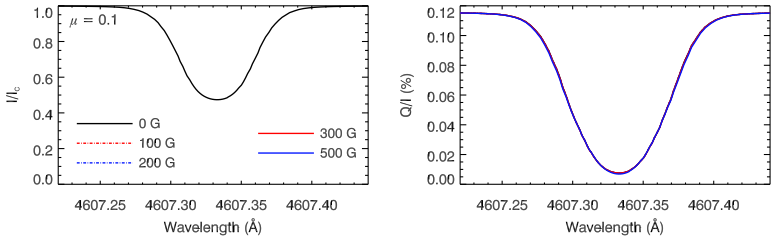

FIGURE 4.12— Intensity (left) and Stokes Q/I (right) profiles for the Sr I line at 4607 Å.The calculations have been performed in the presence of a micro-turbulent and isotropic magnetic field, and artificially large elastic collisional rates and K-multipole depolarizing collisional rates have been taken, so that the CRD limit is obtained and atomic level polarization is negligible. Magnetic field strengths of 0 G (black solid curves), 100 G (red dashed-dotted curves), 200 G (blue dased-dotted curves), 300 G (red solid cuves) and 500 G (blue solid curves) have been considered. The FAL-C atmospheric model has been used for the calculations. We consider the radiation emerging at an LOS with $\mu = 0.1$. The reference direction for positive Stokes Q is taken parallel to the limb.

$J_u = 1$ and $J_\ell = 0$ - in the presence of micro-structured isotropic magnetic fields of various strengths, up to 500 G. Elastic collisions completely relax coherences between magnetic sublevels and redistribute their populations, effectively eliminating any imbalance between them. At wavelengths corresponding to the line core, the Q/I signal is well below the continuum level, since the line opacity is large at such frequencies and, given that $D^{(K)} \gg 1$, the radiation scattered through line processes is unpolarized. As a result, the emergent radiation is depolarized with respect to the continuum in this spectral region (see del Pino Alemán et al. 2014). Again, given that the orientations of the magnetic fields are isotropically distributed at small scales, the Zeeman polarization signals due to magnetic fields with different orientations cancel each other, so no net polarization is produced due to the Zeeman effect, even for field strengths of 500 G.

In Fig. 4.13, the same situation has been considered for stronger fields. Here, as expected, the signatures of the Zeeman effect are clear in the intensity profile. In the Q/I profiles, aside from the previously mentioned depolarization of the continuum which is still appreciable, a negative signal is produced due to the effect of the magnetic field. We have checked that such magnetic sensitivity is not merely a consequence of the changes in the line absorption coefficient due to the Zeeman splitting, but also of the fact that a nonzero contribution to the line emissivity in Stokes Q arises. According to the symmetry arguments we have discussed, one might not, *a priori*, expect the line emissivity to be polarized. However, we point out that the symmetry of the problem is broken because the radiation field is anisotropic. Taking the expression for the emissivity in the presence of a micro-structured and isotropic magnetic field, as shown in Eq. (2.82), the nonzero components of frequency-dependent part of the $\mathcal{R}_{\rm III}$ redistribution matrix, when very

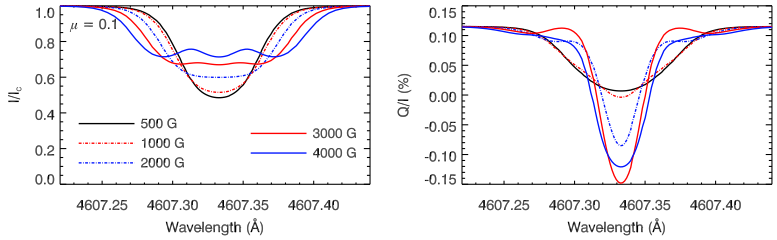

FIGURE 4.13— Intensity (left) and Stokes Q/I (right) profiles for the Sr I line at 4607 Å. The calculations have been performed in the presence of a micro-structured and isotropic magnetic field, and artificially large elastic collisional rates and K-multipole depolarizing collisional rates have been taken, so that the CRD limit is obtained and atomic level polarization is negligible. Magnetic field strengths of 500 G (black curves), 1000 G (red dashed-dotted curves), 2000 G (blue dashed-dotted curves), 3000 G (red solid cuves) and 4000 G (blue solid curves) have been considered. The FAL-C atmospheric model has been used for the calculations. We consider the radiation emerging at an LOS with $\mu = 0.1$. The reference direction for positive Stokes Q is taken parallel to the limb.

large elastic and depolarizing collisional rates are considered, are

$$\left[R_{\rm III}\right]^{KK}_{Q'} = \frac{\Gamma_R}{\Gamma_R+\Gamma_I}\,\delta_{Q'0}\,\Phi_0^{0,K}(J_\ell,J_u;\nu)\,\Phi_0^{0,K}(J_\ell,J_u;\nu')\,, \tag{4.12}$$

and thus the line emission coefficient becomes

$$\varepsilon_i^\ell(\nu,\vec{\Omega}) = \frac{k_L}{1+\epsilon'}\left[\sum_{KQ}\frac{1}{2K+1}\mathcal{T}_Q^K(i,\vec{\Omega})\Phi_0^{0,K}(J_\ell,J_u;\nu)(-1)^Q \right.$$
$$\left. \times \int J^K_{-Q}(\nu')\Phi_0^{0,K}(J_\ell,J_u,\nu')\mathrm{d}\nu' \;+\epsilon'\,\Phi_0^{0,0}(J_\ell,J_u,\nu)B_{\nu_0}(T)\,\delta_{i,0}\right]. \tag{4.13}$$

If the radiation field is spectrally flat, then it can be taken out of the integral in the previous expression. Since (see appendix 13 of LL04)

$$\int \Phi_Q^{K,K'}(J_\ell,J_u,\nu)\,\mathrm{d}\nu = \delta_{K,K'}\,w^{(K)}_{J_uJ_\ell}\,, \tag{4.14}$$

in this case only the J^0_0 component of the radiation field tensor contributes to emissivity, and so

$$\varepsilon_i^\ell(\nu,\vec{\Omega}) = \frac{k_L}{1+\epsilon'}\Phi_0^{0,0}(J_\ell,J_u;\nu)\Big(J^0_0(\nu_0)+\epsilon' B_{\nu_0}(T)\Big)\delta_{i,0}\,, \tag{4.15}$$

which is obviously unpolarized. Likewise, if the Zeeman splitting is negligible with respect to the Doppler width, and so the only nonzero generalized profile is $\Phi_0^{0,0}(J_\ell,J_u,\nu)$, then the components of the radiation field tensor other than J^0_0 do

not contribute to the emissivity, independently of their spectral structure. Therefore, even if collisions completely destroy atomic level polarization, the radiation scattered in the presence of a micro-turbulent isotropic magnetic field can still be polarized if (a) the radiation field breaks the spherical symmetry of the problem, (b) it has some spectral structure, and (c) the magnetic field strength is sufficient for the separation between the different Zeeman components to be comparable to the Doppler width.

This physical situation can be described more intuitively in the following manner. Given that the magnetic field relaxes all coherence between magnetic sublevels, the only nonzero density matrix elements are $\rho_{\alpha_u J_u}(M, M)$, which are therefore sufficient to fully characterize the state of all atomic levels. This is commonly known as the strong field regime, which require the Zeeman splitting to be much larger than the line's natural width (see LL04). For simplicity, we consider a normal Zeeman triplet with $J_u = 1$ and $J_\ell = 0$, for which the Landé factor of the upper level is $g_u = 1$. The population of the upper level per unit volume is given by

$$\mathcal{N}_u = \mathcal{N}\left[\rho_{\alpha_u J_u}(1,1) + \rho_{\alpha_u J_u}(0,0) + \rho_{\alpha_u J_u}(-1,-1)\right], \tag{4.16}$$

where $\mathcal{N}$ is the total number density of atoms, and $\rho_{\alpha_u J_u}(M, M)$ are the upper level's density matrix elements. We point out that, by definition, elastic collisions do not modify the population of any given atomic J-level, and can only affect the relative populations of magnetic sublevels and their coherence. Therefore, even when the elastic collisional rate and depolarizing collisional rates are taken to be very large, the population of the upper level $\mathcal{N}_u$ remains the same as in the absence of such collisions. Neglecting the depolarizing effects of collisions, for a normal Zeeman triplet, the density matrix elements of the upper level that are non-zero are given by (see Eq. (10.46) LL04)

$$\rho_{\alpha_u J_u}(M_u, M_u) = 3\,\frac{\mathcal{N}_\ell}{\mathcal{N}}\,\frac{c^2}{2h\nu_0^3} J_{-M_u,-M_u}\,, \tag{4.17}$$

where $\mathcal{N}_\ell$ is the lower level population per unit volume, and we have defined

$$J_{M_u,M_u} = \oint \frac{\mathrm{d}\vec{\Omega}'_B}{4\pi} \sum_{j=0}^{3} \mathcal{T}_{M_u,M_u}(j, \vec{\Omega}'_B) \int \mathrm{d}\nu'\, \phi_{M_u}(\nu')\, I_j(\nu', \vec{\Omega}'_B)\,, \tag{4.18}$$

where $\vec{\Omega}'_B$ is the angle between the direction of propagation of the radiation and the orientation of the magnetic field, the $\mathcal{T}_{M_u,M_u}(i, \vec{\Omega})$ are defined in LL04, and the profiles ϕ_{M_u} are given by

$$\phi_{M_u} = \phi(\nu_{-M_u,0} - \nu)\,. \tag{4.19}$$

If we assume the radiation field to be unpolarized, and we define the line-integrated intensity for each magnetic component as

$$J_{M_u}(\vec{\Omega}) = \int \mathrm{d}\nu'\, \phi_{M_u}(\nu)\, I_0(\nu', \vec{\Omega})\,, \tag{4.20}$$

then the quantities defined in Eq. (4.18) are given by (see Table 5.3 of LL04)

$$J_{\pm1,\pm1} = \frac{1}{4}\oint \frac{\mathrm{d}\vec{\Omega}'_B}{4\pi}(1+\cos^2\theta'_B)\,J_{\pm1}(\vec{\Omega}'_B)\,, \tag{4.21a}$$

$$J_{0,0} = \frac{1}{2}\oint \frac{\mathrm{d}\vec{\Omega}'_B}{4\pi}\sin^2\theta'_B\,J_0(\vec{\Omega}'_B)\,. \tag{4.21b}$$

For simplicity, the radiation field is assumed to be anisotropic, with its symmetry axis parallel to the local vertical, and with a small angular spread $\Delta\Omega'$ such that, within the cone it defines, the line-integrated intensity is independent of direction. Then

$$\oint \frac{\mathrm{d}\vec{\Omega}'_B}{4\pi}\big(1+\cos^2\theta'_B\big)J_{\pm1}(\vec{\Omega}) = \big(1+\cos^2\theta_B\big)\,J_{\pm1}\,\frac{\Delta\Omega'}{4\pi}\,, \tag{4.22a}$$

$$\oint \frac{\mathrm{d}\vec{\Omega}'_B}{4\pi}\sin^2\theta'_B J_0(\vec{\Omega}) = \sin^2\theta_B\,J_0\,\frac{\Delta\Omega'}{4\pi}\,, \tag{4.22b}$$

where θ_B is the inclination between the magnetic field and the local vertical, and χ_B is its azimuth. In this case, the upper level's population, illuminated by such a radiation field, is given by

$$\mathcal{N}_u = \frac{3}{2}\mathcal{N}_\ell\frac{c^2}{2h\nu_0^3}\Big[J_0\sin^2\theta_B + \frac{J_{-1}+J_1}{2}\big(1+\cos^2\theta_B\big)\Big]\frac{\Delta\Omega'}{4\pi}\,. \tag{4.23}$$

From the previous expression, it is clear that, if the incident radiation field has some spectral structure, the population of the upper level is sensitive to its relative inclination with respect to the magnetic field.

Let us consider the geometry shown in Fig. 4.14, in which α is the angle between the direction of emission (i.e., the LOS) and the orientation of the magnetic field, while β is the angle between the plane defined by the LOS and the local vertical and the plane defined by the LOS and the orientation of the magnetic field[1].

Bearing in mind that elastic collisions cause all magnetic sublevels to be equally populated, the emissivities become (see Eq. (10.48) of LL04)

$$\varepsilon_I(\nu,\vec{\Omega}) = \frac{h\nu}{4\pi}A_{u\ell}\,\mathcal{N}_u\frac{1}{2}\left[\phi_0(\nu)\sin^2\alpha + \frac{\phi_1(\nu)+\phi_{-1}(\nu)}{2}(1+\cos^2\alpha)\right] \tag{4.24a}$$

$$\varepsilon_Q(\nu,\vec{\Omega}) = \frac{h\nu}{4\pi}A_{u\ell}\,\mathcal{N}_u\frac{1}{2}\left[\phi_0(\nu) - \frac{\phi_1(\nu)+\phi_{-1}(\nu)}{2}\right]\sin^2\alpha\cos(2\beta) \tag{4.24b}$$

$$\varepsilon_U(\nu,\vec{\Omega}) = \frac{h\nu}{4\pi}A_{u\ell}\,\mathcal{N}_u\frac{1}{2}\left[\phi_0(\nu) - \frac{\phi_1(\nu)+\phi_{-1}(\nu)}{2}\right]\sin^2\alpha\sin(2\beta) \tag{4.24c}$$

$$\varepsilon_V(\nu,\vec{\Omega}) = \frac{h\nu}{4\pi}A_{u\ell}\,\mathcal{N}_u\frac{1}{2}\Big[\phi_1(\nu) - \phi_{-1}(\nu)\Big]\cos\alpha \tag{4.24d}$$

[1]Note that α and β represent the same angles as θ'_B and χ'_B, respectively, which were used in the integration to obtain the J_{M_u,M_u} radiation field tensors.

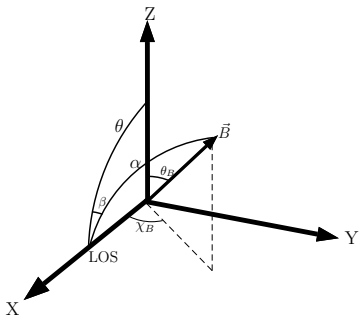

FIGURE 4.14— Geometry for the case in which the radiation is propagating along the Z-axis (i.e., the local vertical), with the magnetic field oriented with inclination θ_B with respect to the local vertical, while the its azimuth χ_B is the angle between the X-axis and the projection of the mangetic field's orientation $\vec{B}$ on the XY plane. Analogously, θ is the inclination of the LOS, which here is taken to be 90°, while its azimuth χ is taken to be zero. α represents the angle between the direction of the LOS and $\vec{B}$, while β is the angle between the plane defined by the local vertical and the LOS, and the plane defined by the LOS and $\vec{B}$, respectively.

where the reference direction for positive Stokes Q has been taken parallel to the Y axis. Considering a $\theta = 90°$ scattering geometry, the following spherical trigonometry formulae (see Smart 1960) can be used

$$\cos\alpha = \sin\theta_B \cos\chi_B\,, \quad \sin\alpha\sin\beta = \sin\theta_B \sin\chi_B\,, \quad \sin\alpha\cos\beta = \cos\theta_B\,,$$
$$\sin^2\alpha\cos(2\beta) = \cos^2\theta_B - \sin^2\theta_B\sin^2\chi_B\,, \quad \sin^2\alpha\sin(2\beta) = 2\sin\theta_B\cos\theta_B\sin\chi_B\,.$$

In this case, considering that the magnetic field's orientations have an isotropic distribution over scales smaller than the line photon's mean free path, and that $\mathcal{N}_u$ is independent of χ_B, then the average over azimuth

$$\langle\varepsilon_I\rangle_{\chi_B}(\nu,\vec{\Omega}) = \frac{h\nu}{4\pi}A_{u\ell}\mathcal{N}_u\frac{1}{2}\Big[\phi_0(\nu)\Big(1-\frac{\sin^2\theta_B}{2}\Big)+\frac{\phi_1(\nu)+\phi_{-1}(\nu)}{2} \times\Big(1+\frac{\sin^2\theta_B}{2}\Big)\Big]\,, \tag{4.25a}$$

$$\langle\varepsilon_Q\rangle_{\chi_B}(\nu,\vec{\Omega}) = \frac{h\nu}{4\pi}A_{u\ell}\mathcal{N}_u\frac{1}{2}\Big[\phi_0(\nu)-\frac{\phi_1(\nu)+\phi_{-1}(\nu)}{2}\Big] \times\Big(\cos^2\theta_B-\frac{\sin^2\theta_B}{2}\Big)\,, \tag{4.25b}$$

$$\langle\varepsilon_U\rangle_{\chi_B}(\nu,\vec{\Omega}) = \langle\varepsilon_V\rangle_{\chi_B}(\nu,\vec{\Omega}) = 0\,. \tag{4.25c}$$

Clearly, the population $\mathcal{N}_u$ does have a dependence on θ_B. Using the averages

$$\langle \sin^2\theta_B \rangle_{\theta_B} = \frac{2}{3}\,,\ \ \langle \cos^2\theta_B \rangle_{\theta_B} = \frac{1}{3}\,,\ \ \langle \sin^4\theta_B \rangle_{\theta_B} = \frac{8}{15}\,,$$
$$\langle \sin^2\theta_B \cos^2\theta_B \rangle_{\theta_B} = \frac{4}{15}\,,\ \ \langle \cos^4\theta_B \rangle = \frac{1}{5}\,,$$

the emissivity in Stokes I and Q become

$$\langle \varepsilon_I \rangle_{\theta_B,\chi_B}(\nu,\vec{\Omega}) = \frac{3}{4}\frac{h\nu}{4\pi}\frac{c^2}{2h\nu_0^3}\,A_{u\ell}\frac{\Delta\Omega'}{4\pi}\frac{1}{15}\left[6J_0\,\phi_0(\nu) + 14J_0\left(\frac{\phi_1(\nu)+\phi_{-1}(\nu)}{2}\right)\right.$$
$$\left. + 13\left(\frac{J_1+J_{-1}}{2}\right)\phi_0(\nu) + 27\left(\frac{J_1+J_{-1}}{2}\right)\left(\frac{\phi_1(\nu)+\phi_{-1}(\nu)}{2}\right)\right]\,; \quad (4.26a)$$

$$\langle \varepsilon_Q \rangle_{\theta_B,\chi_B}(\nu,\vec{\Omega}) = \frac{3}{4}\frac{h\nu}{4\pi}\frac{c^2}{2h\nu_0^3}\,A_{u\ell}\frac{\Delta\Omega'}{4\pi}\frac{2}{15}\left(\frac{J_1+J_{-1}}{2} - J_0\right)$$
$$\times\left(\phi_0(\nu) - \frac{\phi_1(\nu)+\phi_{-1}(\nu)}{2}\right). \quad (4.26b)$$

We remind the reader that this final expression is valid when the radiation field has axial symmetry around the local vertical, and a small angular spread $\Delta\Omega'$. From this expression, it can be clearly seen that, if the spectrum is flat ($J_1 = J_0 = J_{-1}$) then the emissivity in Q will be zero. For weak magnetic fields such that $\phi_1(\nu) \simeq \phi_0(\nu) \simeq \phi_{-1}(\nu)$, the emitted radiation will not be significantly polarized either. Lastly, if the radiation field is completely isotropic, $\mathcal{N}_u$ will of course have no dependence on either θ_B nor χ_B, and so $\langle \varepsilon_Q \rangle_{\theta_B,\chi_B}(\nu,\vec{\Omega}) = 0$. This illustrates that, linear polarization can be produced in the presence of a strong isotropic micro-structured magnetic field, provided that the incoming radiation field is anisotropic, and spectrally structured. We note that the expressions can be more complicated for inclinations other than $\theta = 90°$, for which the following, more general, spherical trigonometry relations must be taken

$$\cos\alpha = \cos\theta\cos\theta_B + \sin\theta\sin\theta_B\cos\chi_B\,,$$
$$\sin\alpha\sin\beta = \sin\theta_B\sin\chi_B\,,$$
$$\sin\alpha\cos\beta = \sin\theta\cos\theta_B - \cos\theta\sin\theta_B\cos\theta_B\,,$$
$$\sin^2\alpha\cos(2\beta) = (\sin\theta\cos\theta_B - \cos\theta\sin\theta_B\cos\theta_B)^2 - \sin^2\theta_B\sin^2\chi_B\,,$$
$$\sin^2\alpha\sin(2\beta) = 2\sin\theta_B\sin\chi_B(\sin\theta\cos\theta_B - \cos\theta\sin\theta_B\cos\theta_B)\,.$$

In Fig. 4.15 we present the same calculation as in Fig. 4.13, using the collisional depolarizing rates shown in Faurobert-Scholl (1993), so PRD effects are taken into account in the scattering process. In this case, a considerable fraction of the scattering processes are unperturbed by collisions, which allows for frequency coherence in such processes, as described by the $\mathcal{R}_{\rm II}$ redistribution matrix. Moreover, the collisions are not efficient enough for all atomic level polarization to be destroyed, and as a result the fractional polarization of the scattered radiation increases substantially, as compared to the previous case. The polarization fraction obtained for a

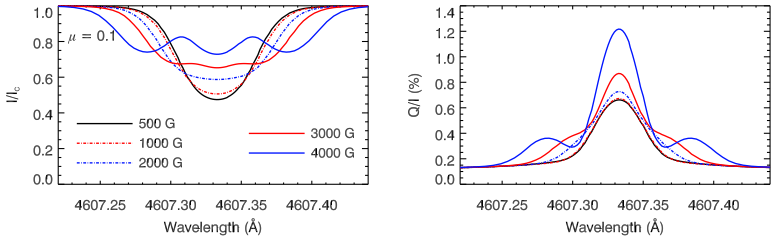

FIGURE 4.15— Intensity (left) and Stokes Q/I (right) profiles for the Sr I line at 4607 Å. The calculations have been performed in the presence of a micro-structured and isotropic magnetic field, and taking the elastic collisional rates presented in Faurobert-Scholl (1993) and the K-multipole depolarizing collisional rates $D^{(K)} = 1/2\,\Gamma_E$ for $K \neq 0$. The colored curves represent the same field strengths as in Fig. 4.13. The FAL-C atmospheric model has been used for the calculations. We consider the radiation emerging at an LOS with $\mu = 0.1$. The reference direction for positive Stokes Q is taken parallel to the limb.

500 G isotropic field is again produced mainly by scattering polarization and the Hanle effect. For stronger fields, the Zeeman effect begins to be important through the mechanism discussed in this section, and the absolute increase in Q/I is much greater in this case, in which atomic level polarization and PRD effects are involved.

It is worth noting that, although anisotropic and spectrally structured radiation fields are commonplace in the solar atmosphere, we do not expect micro-structured and isotropic magnetic fields with strengths of the order of kG to be present. Thus, the conditions we have discussed in this section do not occur in the solar atmosphere, and in consequence their implications are mainly of academic interest.

4.5 Are the CRD and weak field approximations suitable for the Sr I 4607 Å line ?

The fact that most of the quiet solar photosphere is filled by unresolved, turbulent fields is suggested both by strong theoretical arguments and observational evidence. Given that the polarities of such magnetic fields change over very small scales, the signatures produced by the Zeeman effect are difficult to detect.

Stenflo (1982) pointed out that the depolarization due to the Hanle effect could be useful to detect such turbulent fields, and estimated a lower limit of 10 G, assuming their distribution of orientations to be isotropic. An upper limit of 100 G had been found from line-broadening arguments using Fe I lines (see Stenflo & Lindegren 1977). Trujillo Bueno et al. (2004) presented 3D RT calculations for the Sr I 4607 Å line considering the impact of a volume-filling micro-turbulent magnetic field of constant strength, and found that a field of 60 G gave the best fit to the CLV of observed line-center Q/I signals. They also considered the case in which, instead, the magnetic field strength follows the probability distribution function $f(B) = \mathrm{e}^{-B/B_0}/B_0$, and found that an average field of $B_0 = 130$ G gave the best

agreement with observations.

Such calculations were performed by assuming the CRD and the weak field approximations. Here we relax such approximations in order to analyze whether the error incurred by taking such assumptions is significant. Since the HZ code considers a one-dimensional model atmosphere, atmospheric motions cannot be properly accounted for in the calculations and, therefore, their effects must be artificially included. Small-scale motions have been introduced as a micro-turbulent velocity which contributes to the distribution of atomic velocities as described in Eq. (2.70); on the other hand, large-scale turbulent motions (hereafter macro-turbulent motions) $v_{\rm mac}$ must be taken into account by smearing the emergent Stokes profiles after they have been synthesized, by convolving a Gaussian

$$I_{{\rm sm},i}(\nu) = \frac{1}{\sqrt{\pi}\Delta\nu_{\rm mac}} \int {\rm d}\nu'\, I_i(\nu') \exp\left[-\left(\frac{\nu-\nu'}{\Delta\nu_{\rm mac}}\right)^2\right], \tag{4.27}$$

with $\Delta\nu_{\rm mac} = \nu_0\, v_{\rm mac}/c$. In Fig. 4.16 the results of calculations for Sr I 4607 Å

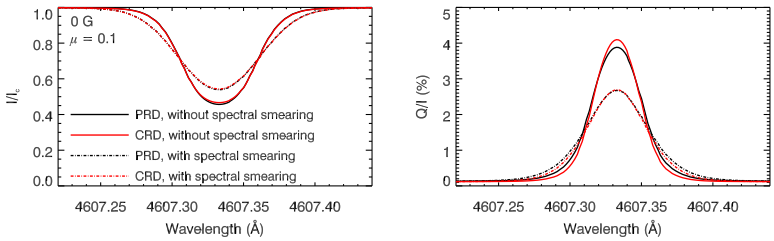

FIGURE 4.16— Intensity (left) and Stokes Q/I (right) profiles for the Sr I 4607 Å line. The results before spectral smearing due to macro-turbulent velocities (solid curves) and after them (dash-dotted curves) are presented. Both the calculations considering PRD effects (black curves) and those in the CRD limit (red curves) are shown. The FAL-C atmospheric model has been used for the calculations. We consider the radiation emerging at an LOS with $\mu = 0.1$. The reference direction for positive Stokes Q is taken parallel to the limb.

are presented in the absence of a magnetic field, for an LOS with $\mu = 0.1$. In this case the collisional rates shown in Eq. (3.4) have been used, and the results - both for calculations considering PRD and in the CRD limit - are shown before and after the convolution, performed as described in Eq. (4.27). We have used the $v_{\rm mac}$ that was obtained by Gurtovenko & Kostyk (1989) by fitting intensity calculations of Sr I 4607 Å to observations of the quiet Sun for various LOS. When such smearing is applied, both the intensity and Q/I profiles are broadened and, as a result, the differences found at line-center between both calculations become noticeably smaller, also in relative terms. In Fig. 4.17, the CLVs of the line-center Q/I, are shown after the profiles have been convolved as described in Eq. (4.16). Rather than considering a continuous distribution of strengths, micro-structured magnetic fields of a fixed strength of 0, 50, 100, and 200 G have been considered.

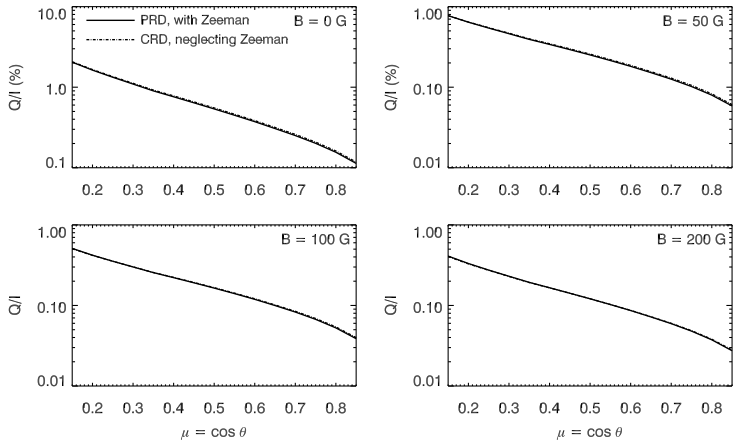

FIGURE 4.17— CLV for the line-center Q/I of Sr I 4607 Å,after smearing the line profiles in order to account for large scale random motions in the solar atmosphere. Calculations have been performed in the presence of a micro-structured and isotropic magnetic field, comparing the results obtained when accounting for PRD effects and Zeeman splitting in the absorption and emission profiles (solid curves) to those obtained in the CRD limit under the weak field approximation (dash-dotted curves). Field strengths of 0 G (top left panel), 50 G (top right panel), 100 G (bottom left panel), and 200 G (bottom right panel) have been considered. The FAL-C atmospheric model has been used for the calculations. The direction for positive Stokes Q is taken parallel to the limb.

The magnetic field is assumed to also have a constant strength at all grid points. The results obtained in the CRD limit under the weak field approximation (plotted with dashed-dotted curves), are comparted to those obtained when relaxing such approximations (solid curves). Even for field strengths of 200 G, the differences in the line-center polarization between the two calculations are found to be very small when the effects of the atmosphere's large-scale turbulent motions are accounted for. Thus, we conclude that both PRD effects and Zeeman splitting can be safely neglected when fitting observations with calculations in which such field strengths and geometries are assumed, as was done by Trujillo Bueno et al. (2004).

4.6 The effect of coherent scattering on circular polarization

Up until now, the main focus of this chapter has been on the intensity and linear polarization of spectral lines, when PRD is accounted for in scattering, and in the presence of magnetic fields of arbitrary strength. In this section, we study the circular polarization profiles signatures produced when scattering is essentially coherent.

Since the 1950s (see Babcock 1953), the magnetograph has been an extensively used instrument in the investigation of solar magnetism. The signal produced by a

magnetograph can easily be related to the longitudinal component of the magnetic field, since the circular polarization signal produced by the Zeeman effect is given by (see LL04)

$$V(\lambda) = -\Delta\lambda_B\,\bar{g}\,\cos\alpha\frac{\partial I(\lambda)}{\partial\lambda}\,, \tag{4.28}$$

where α is the angle between the LOS and the magnetic field, $\Delta\lambda_B$ is the Zeeman splitting, and $\bar{g}$ is the line's effective Landé factor (see LL04). This expression is commonly known as the magnetograph formula.

Asymmetries in circular polarization profiles have often been reported in the presence of large-scale velocities with vertical gradients of the magnetic field (e.g., Sánchez Almeida et al. 1988, Martínez Pillet et al. 1990, or Viticchié & Sánchez Almeida 2011). Other interesting structures in the V/I profiles can be produced by the alignment-to-orientation conversion mechanism (see Kemp et al. 1984), and by the anomalous dispersion terms induced by strong magnetic fields. But the former cannot be accounted for in a two-level atom, and anomalous dispersion does not have a significant impact in the line core in the presence of magnetic fields for which $\Delta\lambda_B \ll \Delta\lambda_D$. The spectral structure of the radiation field, however, can produce characteristic circular polarization signals in the presence of weaker magnetic fields.

The radiation emerging at frequencies corresponding to the near wings of the Mg II k line, as well as in the line core, originates high in the atmosphere, where the density of collisional perturbers is very low, and so the coherence fraction is large. In Fig. 4.18 the Stokes I and V/I profiles are presented, as calculated using the HZ code, which, as discussed in Chapter 2, accounts for the joint action of scattering polarization and the magnetic field through both the Hanle and Zeeman effects. The calculations accounting for PRD and in the CRD limit are compared, in the presence of an almost longitudinal, horizontal magnetic field, and considering an LOS with $\mu = 0.1$. The circular polarization profiles obtained from the full RT calculation in the four Stokes parameters are also compared to the ones obtained from the resulting intensity profile using the magnetograph formula.

When considering the CRD limit, the V/I profiles obtained from the full RT calculation coincide very well with those found considering the magnetograph formula, as can be seen in the left panel of Fig. 4.18. On the other hand, discrepancies are found when the frequency coherence is accounted for in scattering events, as shown in the right panel of the previous figure. In the line core, the V/I profile obtained from the full RT calculation and the one obtained using the magnetograph formula coincide very well. However, when PRD effects are taken into account, one finds very conspicuous lobes in the wings whose sign is opposite to that of the central peaks in the line core and whose amplitude is overestimated by the magnetograph formula. The origin of such lobes can be understood from the terms in the RT equation for Stokes V, shown in Eq. (2.1). The η_V coefficients are unchanged with respect to the ones obtained in the CRD limit. However, when PRD effects are taken into account, ε_V presents more extended wings so, outside the Doppler core, its contribution to the RT equation around the spatial region where the wings form is more important

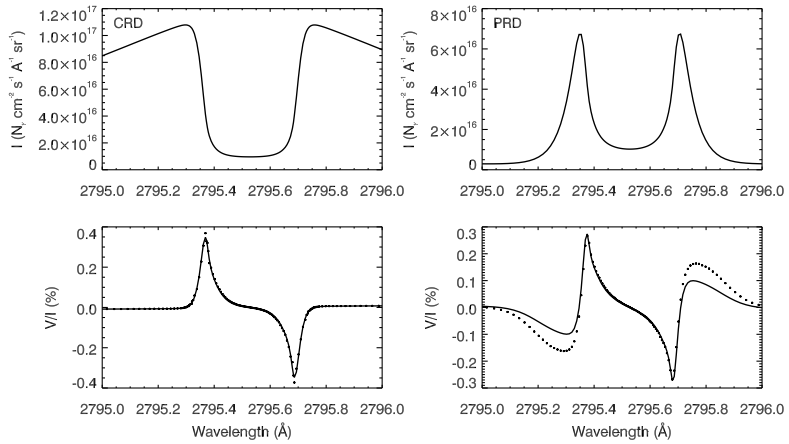

FIGURE 4.18— Stokes I (top row) and V/I (bottom row) profiles for the Mg II k line (solid curves). Such calculations have been performed in the presence of a quasi-longitudinal ($\theta_B = 90°$ and $\chi_B = 0°$) magnetic field of 20 G. The V/I profiles obtained from the calculated intensity using the magnetograph formula in Eq. (4.28) are represented by small crosses. The results are presented both for calculations in the CRD limit (left column) and accounting for PRD effects (right column). The FAL-C atmospheric model has been used for the calculation. We consider the radiation emerging at an LOS with $\mu = 0.1$. Stokes V is defined as positive for right-handed (clockwise) circular polarization.

than the competing terms, which explains the difference in sign found between the wing lobes and the core peaks.

We have checked that the amplitudes of both the central peaks and the lateral lobes increase linearly with the strength of a longitudinal magnetic field, which is an indication that, ultimately, Zeeman splitting is responsible for both of these features. Furthermore, they are both qualitatively reproduced by the magnetograph formula. Indeed, this implies that, for very strong lines that form high in the solar atmosphere, such as the Mg II k line, the same transfer effects that produce very sharp emission peaks around line center in the intensity profile are also responsible for the wing lobes in V/I. Nevertheless, the fact that the amplitude of such lobes obtained in the full RT calculation are smaller than when considering the magnetograph formula leads us to suggest that effects that are neglected by such formula (e.g., quantum interferences between M-levels of the same atomic level) may play a role in the wings of ε_V.

The circular polarization produced by the Zeeman effect breaks the axial symmetry of the radiation field, and we have found that this has a non-neglible impact on the circular polarization of the emergent radiation. In Fig. 4.19, the V/I profiles obtained from the self-consistent solution of the RT calculation are compared to the

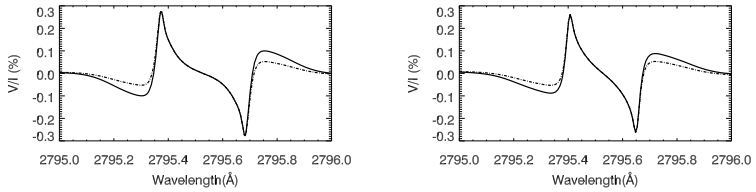

FIGURE 4.19— Stokes V/I profiles for the Mg II k line. Two geometries have been considered; for an LOS with $\mu = 0.1$ in in the presence of a quasi-longitudinal ($\theta_B = 90°$ and $\chi_B = 0°$) magnetic field of 20 G (left panel), and for an LOS with $\mu = 1$ in the presence of a vertical 20 G magnetic field (right panel). In both cases, the full calculation (solid curves), is compared to a calculation in which the J^1_Q components of the radiation field tensor have been artificially neglected (dash-dotted curves). The FAL-C atmospheric model has been used for the calculation. Stokes V is defined as positive for right-handed (clockwise) circular polarization.

result of calculations in which, at every iteration, the J^1_Q components of the radiation field tensor have been artificially set to zero when solving the RT problem. We point out that the latter is an approximation, and it can lead to inconsistencies if the values if the J^1_Q components are comparable in magnitude to J^0_0. The J^1_Q components are related to the axial asymmetry of the radiation field, they are sensitive to the circular polarization of the radiation field, and they contribute to the line ε_V. It can clearly be seen in the figure that the amplitudes of the wing lobes are affected by such components of the radiation field tensor. This sensitivity can be found both in the presence of a horizontal magnetic field, for $\mu = 0.1$, and in the presence of a vertical field, for $\mu = 1$, which is again an indication that the Zeeman effect due to a longitudinal magnetic field - rather than the Hanle effect - produces the circular polarization which gives rise to J^1_Q.

On the other hand, the circular polarization of the emergent radiation in the line core is not affected by the inclusion of such components of the radiation field tensor in the calculation. This can be explained by the fact that such components are very small around line center in the atmospheric regions where the line core peaks in V/I form, and present an antisymmetric structure around the wavelengths which correspond to the V/I peaks. This is illustrated in the left panel of Fig. 4.20, in which the real part of J^1_1, which is the only nonzero J^1_Q component which is produced in the presence of a horizontal magnetic field with $\chi_B = 0°$, i.e., is shown at a height of 2110 km, which corresponds to the region where $\tau = 1$ for a LOS with $\mu = 0.1$ at the line core wavelength $\lambda = 2795.38$ Å. Due to its spectral structure, when Doppler redistribution is considered, the contributions from J^1_Q to ε_V in the around the wavelengths corresponding to the central peaks is very small. The right panel of the figure shows the wavelength dependence of real part of J^1_1 at a height of 1180 km, which corresponds to the $\tau = 1$ region for $\mu = 0.1$ at wavelength $\lambda = 2795.30$ Å, for which the amplitude of the blue V/I lobe is maximum in this spatial region.

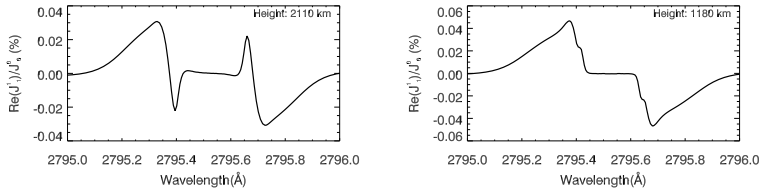

FIGURE 4.20— Real part of J^1_1 over J^0_0, with respect to wavelength, obtained in the self-consistent solution of the the HZ code for the Mg II k line. The calculation has been performed in the presence of a 20 G horizontal magnetic field with $\chi_B = 0°$. The FAL-C atmospheric model has been used for the calculation. In the left panel, it is shown at a height of 2110 km, where the line core peaks in V/I form for an LOS with $\mu = 1$, while in the right panel it is shown deeper in the atmosphere, for a height of 1180 km, where the wing lobes from for the same LOS.

$\mathrm{Re}\{J^1_1/J^0_0\}$ presents a spectral structure with extended wings, which explains why the wing lobes are sensitive to its contribution.

4.7 Conclusions

In this chapter we have presented RT calculations in which we have focused on the effects of the magnetic field, and in particular on its impact on scattering polarization.

Calculations accounting for PRD effects show that the weak field approximation yields reliable results for the linear polarization profiles in the line core, provided that the magnetic field are weak enough that the Zeeman splitting is much smaller than the Doppler width. However, in lines for which PRD effects produce extended wing profiles, such as Sr II 4078 Å, an artificial magnetic sensitivity is encountered in the wings of the linear polarization profiles, even for relatively weak fields which are within the range of validity of the approximation. Thus, caution must be exercised when considering the weak field approximation, especially when modeling the polarization of strong resonance lines which are sensitive to PRD phenomena.

The Hanle effect produced signatures in the line core polarization for LOS with inclinations between $\theta = 0°$ and $\theta = 90°$, such as the change of sign or the appearance of a relative extremum in Q/I, as the magnetic field strength increases. Given that, in the past, little attention has been paid to such behavior, we have provided a justification for them by considering the analytical expressions of the emission coefficients as a function of the magnetic field strength and the direction of emission, under the weak field approximation.

When considering strong micro-structured isotropic magnetic fields we find that, even when atomic polarization is completely relaxed by collisions, the emergent radiation can be polarized provided that the incident radiation field (a) breaks the spherical symmetry of the problem and (b) is spectrally structured, and (c) the

Zeeman splitting is of the order of the Doppler width or larger.

Trujillo Bueno et al. (2004) confronted observations of the CLV of the Sr I 4607 Å line's Q/I to 3D RT calculations, assuming the magnetic field to be microturbulent and isotropic, in order to infer the strength of the unresolved photospheric magnetic field. In such calculations, the CRD limit and the weak field approximation were taken. In order to evaluate the error incurred by taking such approximations, calculations both accounting for and relaxing them have been compared. After including a spectral smearing, in order to mimic the effects of large-scale turbulent velocities when performing calculations in a static one-dimensional atmosphere, the differences in the calculated line-center Q/I are found to be minimal, even when considering isotropic magnetic fields of 200 G.

The chapter concludes with a discussion on the emergent circular polarization profile of the Mg II k line, in which lateral lobes whose sign is the opposite of the line core peaks are produced when the frequency coherence of scattering is taken into account. The fact that such lobes are qualitatively reproduced using the magnetograph formula indicates that they are produced by the same transfer processes that give rise to the sharp emission peaks in the core of the intensity profile, together with the longitudinal Zeeman effect. Nevertheless, they are overestimated by the magnetograph formula, which suggests that other physical mechanisms, such as quantum interferences between M-levels of the same level, has a noticeable effect on them. Furthermore, the modification of the radiation field due to the production of circular polarization, illustrated by the appearance of J^1_Q components of the radiation field tensor, is also found to impact the amplitude of the V/I lobes of the emerging radiation.

5

The impact of magneto-optical effects on the line wing polarization

We investigate the influence of magneto-optical effects on the linear polarization of strong resonance lines in which PRD plays a significant role in the scattering processes, pointing out the relevance of the ρ_V terms that couple Stokes Q and U of the Stokes-vector transfer equation. The magnetic sensitivity of the wings of the linear polarization profiles, caused by such anomalous dispersion terms, is analyzed in depth for the Mg II k and Ca I 4227 Å spectral lines. The fact that the rotation of the radiation's plane of linear polarization can produce a modification of its linear polarization fraction is also studied in detail. A discussion is provided on the diagnostic potential of the linear polarization signatures produced by magneto-optical effects in the linear polarization wings of strong resonance lines.

5.1 Introduction

In the previous chapter, we have discussed in depth how magnetic fields of various strengths and configurations influence the generation and transfer of polarized radiation, focusing especially on how they affect the line scattering emissivity, as described through the redistribution matrices. On the other hand, we have paid little attention to the selective absorption of certain polarization states from the radiation that propagates through the atmosphere, or the coupling of different polarization states. Such processes are described by the off-diagonal elements of the propagation matrix. When relatively weak magnetic field strengths are considered, it is common to use the weak field approximation discussed in Sect. 4.2 (e.g., Anusha et al. 2011, Bommier 1997b), under which the propagation matrix is diagonal if lower level polarization is neglected. Another common approach is the last scattering approximation (e.g., Sampoorna et al. 2009), which neglects radiative transfer effects when calculating the emergent radiation's Stokes profiles.

In this work we refer to the anomalous dispersion effects induced by the presence

of a magnetic field as magneto-optical (MO) effects. When considering a two-level atom with an unpolarized lower level, as is the case in this thesis, anomalous dispersion is caused exclusively by the Zeeman effect. In this chapter we study the influence of MO effects on the polarization of the emergent spectral line radiation, especially through the rotation of the plane of linear polarization as it travels through the material, due to the component of magnetic field vector that is longitudinal to the direction of propagation. Such fields induce a shift in the energies of the different magnetic sublevels which, for a direction of propagation parallel to the magnetic field, due to which the propagation velocities of right-handed and left-handed circularly polarizated radiation in the medium differ (e.g., Portis 1978). Since linearly polarizated states of radiation are a quantum superposition of two circularly polarized states of opposite handedness, the phase-shift introduced as the radiation propagates through the medium causes the plane of linear polarization to be rotated. This effect is quantified by the ρ_V element of the propagation matrix, and throughout this chapter we will equivalently refer to it as Faraday rotation.

Faraday rotation has been extensively used to determine the magnetic field in interstellar media (e.g., Longair 1992), and has also been used to estimate the electron density and magnetic field distribution in the solar corona (Mancuso & Spangler 2000) by studying the rotation of the linear polarization of transmitted radio waves. Its effects are also known to be significant in solar regions where the magnetic field is strong, e.g., in sunspots (see Landi Degl'Innocenti 1979, also Makita 1986).

In the following sections, we present calculations using the HZ code discussed in previous chapters to show that, when partial frequency redistribution effects produce broad linearly polarized wings, the linear polarization in the wings of strong resonance lines is sensitive to the magnetic field via such effects - even for magnetic fields with strengths comparable to the critical field for the onset of the Hanle effect.

5.2 The magnetic sensitivity of the wings of the Mg II k line for an LOS with $\mu = 0.1$

We now consider situations in which an LOS close to the limb is considered, namely with $\mu = 0.1$. We consider applications to the Mg II k line, whose core forms high in the solar chromosphere, close to the transition region, and presents a very broad absorption profile in intensity, with two emission peaks (k_{2V} and k_{2R}) around line center (k_3). Furthermore, its Q/I presents very extended lobes in the wings with large amplitudes. For the first application, a vertical magnetic field is considered, and the four Stokes profiles of the emergent radiation are shown in Fig. 5.1. Magnetic fields between 0 and 100 G are considered, for which there is no appreciable impact on the emergent intensity. We note that we are considering the spectral region between the k_{1V} and k_{1R} (see the top panel of the figure), where this spectral line can be suitably modeled by considering a two-level atom. As expected, the magnetic field produces a signal in Stokes V/I, whose amplitude scales linearly with the magnetic field strength. This is a consequence of the Zeeman effect, given that the magnetic field has a non-negligible component along the LOS (see Sect. 4.6 for a discussion

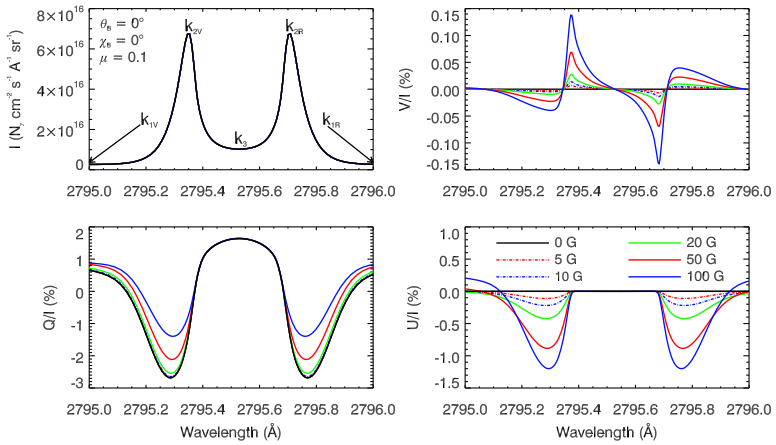

FIGURE 5.1— Intensity (top left panel), Stokes V/I (top right panel), Stokes Q/I (bottom left panel), and Stokes U/I (bottom right panel) profiles for the Mg II k line. For the remainder of this chapter, calculations are performed using the HZ code, unless otherwise specified. Calculations have been performed in the presence of a vertical magnetic field. Field strengths of 0 G (black solid curves), 5 G (red dashed-dotted curves), 10 G (blue dashed-dotted curves), 20 G (green solid curves), 50 G (red solid curves) and 100 G (blue solid curves) have been considered. The FAL-C atmospheric model has been taken for these calculations. We consider the radiation emerging at an LOS with $\mu = 0.1$. The reference direction for positive Stokes Q has been taken parallel to the limb.

on the circular polarization profiles in the Mg II k line). In the line core region the magnetic field has no impact on the linear polarization signals, given that it is parallel to the symmetry axis of the radiation field, and so, for a two-level atom, the Hanle effect cannot operate. On the other hand, we observe that, beyond the Doppler core, there is a clear magnetic sensitivity; as the magnetic field increases, a reduction of the Q/I amplitude is apparent, while a U/I signal appears and becomes larger with the magnetic field.

In order to better study this magnetic sensitivity in the wings, we now consider a horizontal magnetic field with $\chi_B = 0°$, which is almost parallel to the LOS we are considering here. In Fig. 5.2, the Stokes Q/I, U/I and V/I profiles are shown, calculated using the HZ code, for the same range of field strengths as for Fig. 5.1.

In the core of the line the typical signatures of the Hanle effect can be easily seen; Stokes Q/I, produced by scattering polarization, presents its largest amplitude in the absence of magnetic field and, as the magnetic field increases, the Q/I line core signal becomes smaller. For this geometry, it approaches zero at Hanle saturation. The Hanle rotation also causes the appearance of Stokes U/I in the core which, after reaching a maximum value, decreases as the magnetic field continues increasing and

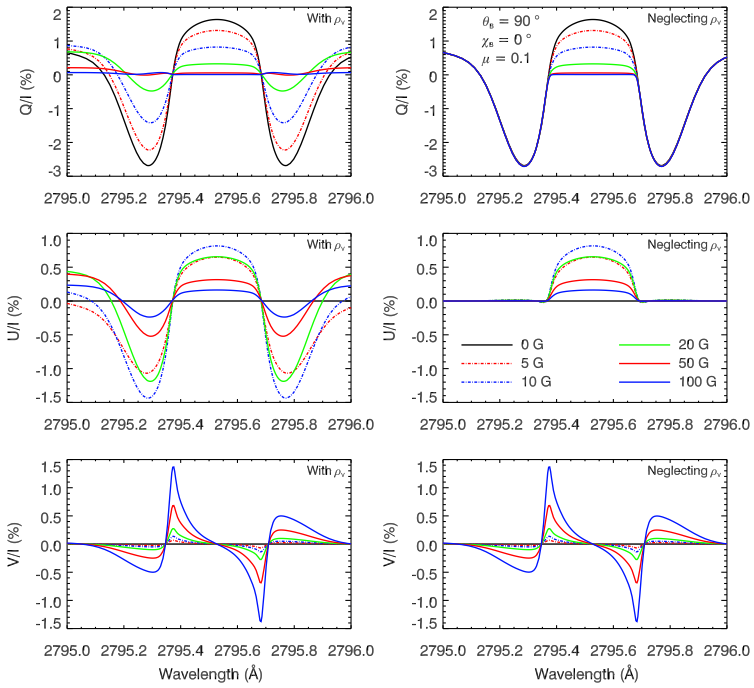

FIGURE 5.2— Stokes Q/I (top row), Stokes U/I (middle row), and Stokes V/I (bottom row) profiles for the Mg II k line. Calculations have been performed in the presence of a horizontal magnetic field with an azimuth of $\chi_B = 0°$, both considering the full propagation matrix in the RT equation (left column) and artificially neglecting the impact of the ρ_V anomalous dispersion term (right column). The colored curves represent the same field strengths as in Fig. 5.1. The FAL-C atmospheric model has been taken for these calculations. We consider the radiation emerging at an LOS with $\mu = 0.1$. The reference direction for positive Stokes Q has been taken parallel to the limb.

also approaches zero. This is consistent with the discussion presented in Sect. 4.2. In this case the amplitude of the V/I signal is larger than when the magnetic field was vertical, since in this case the projection of the mangetic field vector onto the LOS is much greater.

In the left column of the figure, a magnetic sensitivity in the wings of the linear polarization profiles is apparent, and it is in fact even greater than the sensitivity found when the magnetic field was vertical. Again, such signatures cannot be caused by the Hanle effect since, as discussed in Sect. 4.2, it does not operate outside the line

core. We compare these full RT calculations with those in which the ρ_V coefficients of the propagation matrix have been neglected when solving the RT equation. In the line core, the resulting polarization profiles, which are shown in the right column of Fig. 5.2, are identical to the ones obtained when ρ_V is taken into account. In the wings, however, no change is found in Q/I and U/I when the impact of such MO terms is neglected, indicating that it is the physical mechanism that gives rises to such magnetic sensitivity. From Eq. (2.1) we see that the RT equations for Stokes Q and U are

$$\frac{\mathrm{d}}{\mathrm{d}s}Q = \varepsilon_Q - \eta_I Q - \rho_V U + \rho_U V - \eta_Q I\,;$$
$$\frac{\mathrm{d}}{\mathrm{d}s}U = \varepsilon_U - \eta_I U + \rho_V Q - \rho_Q V - \eta_U I\,. \tag{5.1a}$$

We also note that, in the RT equation for Stokes V, the ρ_V term does not appear, and thus its profile is unchanged when ρ_V is artificially eliminated in the formal solution. For weak fields, a commonly-used approximation is to neglect the last three terms on the right hand side of these equations, based on the assumption that $Q, U, V \ll I$ and that $\eta_X, \rho_X \ll \eta_I$, for $X = (Q, U, V)$. Although this is indeed the case in the line core, the line coefficients of certain off-diagonal elements of the propagation matrix may be significant when compared to the absorption coefficient η_I at wing frequencies, even for relatively weak fields.

In Fig. 5.3, the ratios of such coefficients over η_I are shown at a height of 1180 km above the $\tau_{5000} = 1$ surface, which is within the formation region of the near-wing radiation at 250 mÅ, for an LOS with $\mu = 0.1$. Since the reference direction for positive Stokes Q is taken parallel to the limb, the η_U and ρ_U coefficients are zero for a horizontal magnetic field with $\chi_B = 0°$, and therefore they are not shown in this case. Independently of the choice of the reference direction for positive Q, and of χ_B, the coefficients η_Q, η_U, ρ_Q, and ρ_U are small enough to be neglected even for a field strength of 100 G. On the other hand, η_V and ρ_V can play a critical role on the emergent polarization profiles. Indeed, it was already discussed in Sect. 4.6 that, also when considering the Mg II k line, η_V plays an important role in the shape of the central peaks in circular polarization. Outside the line core, $\eta_V(\nu)/\eta_I(\nu)$ quickly falls to zero, but $\rho_V(\nu)$ is of the same order of magnitude as $\eta_I(\nu)$, even for fields as weak as 20 G. Therefore, at wing frequencies, its role cannot be neglected in the transfer equation. Thus, in the presence of relatively weak fields, it is a very good approximation to write the RT equations for Stokes Q and U as

$$\frac{\mathrm{d}}{\mathrm{d}s}Q \simeq \varepsilon_Q - \eta_I Q - \rho_V U\,; \tag{5.2a}$$
$$\frac{\mathrm{d}}{\mathrm{d}s}U \simeq \varepsilon_U - \eta_I U + \rho_V Q\,. \tag{5.2b}$$

The effect of ρ_V on the radiation propagating through the medium is to couple the Stokes Q and U parameters, i.e., to rotate its plane of linear polarization. Therefore, unless some other mechanism, such as coherent scattering, produces a substantial

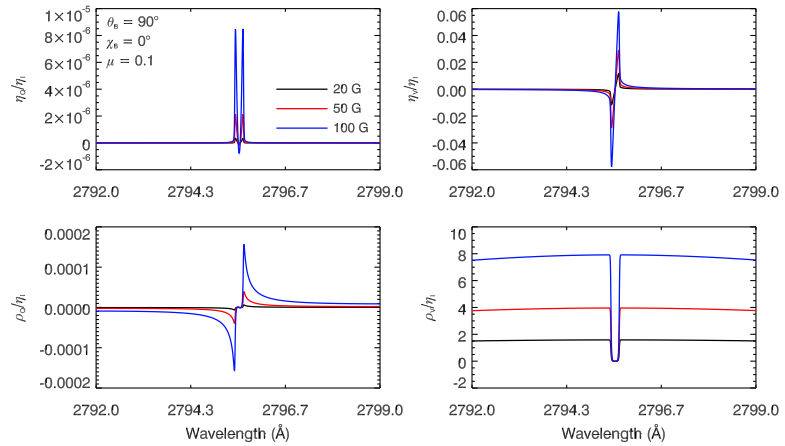

FIGURE 5.3— Plot of the η_Q/η_I (top left), η_V/η_I (top right), ρ_Q/η_I (bottom left) and ρ_V/η_I (bottom right) ratios as a function of wavelength, obtained for an LOS with $\mu = 0.1$ at a height of 1180 km in the FAL-C atmospheric model, and in the presence of a horizontal magnetic field with $\chi_B = 0°$. The η_U and ρ_U coefficients are zero for this geometry, and therefore are not included in this figure. Magnetic field strengths of 20 G (black curves), 50 G (red curves) and 100 G (blue curves) have been considered. The reference direction for positive Stokes Q is taken parallel to the limb.

amount of linear polarization in the wings, ρ_V will have no appreciable effect, independently of the strength of the magnetic field. For this reason, when considering spectral lines that do not present extended wing polarization profiles, it is generally not necessary to account for its effects for weak magnetic fields.

The reason why the ρ_V/η_I ratio is large outside the line core is ultimately related to the behavior of the Voigt and associated dispersion profiles beyond the dispersion profile's local extrema, and to the specific linear combinations of these profiles that define the aforementioned RT coefficients (see Eq. (2.12), and the definition of the generalized profiles in Eqs. (2.14) and (2.15)).

This relation can be seen from the expressions of the line contributions elements of the propagation matrix, which are shown in Eq. (2.12) for a two-level atom with an unpolarized lower level. When considering a reference frame in which the quantization axis of total angular momentum is parallel to the magnetic field, we have

$$\eta_I^\ell(\nu,\vec{\Omega}) = k_L\Big(\Phi_0^{0,0}(J_\ell,J_u;\nu)\mathcal{T}_0^0(0,\vec{\Omega}) + \Phi_0^{0,2}(J_\ell,J_u;\nu)\mathcal{T}_0^2(0,\vec{\Omega})\Big)\,, \tag{5.3a}$$

$$\rho_V(\nu,\vec{\Omega}) = k_L\Psi_0^{0,1}(J_\ell,J_u;\nu)\mathcal{T}_0^1(3,\vec{\Omega})\,. \tag{5.3b}$$

The ℓ label has been dropped for ρ_V since it has no continuum contribution (see LL04). The $\mathcal{T}_0^1(3,\vec{\Omega})$ is proportional to $\cos\theta$ (e.g., LL04), so it is clear that ρ_V

depends on the angle between the LOS and the magnetic field vector. This is why, for a LOS with $\mu = 0.1$, a vertical magnetic field (see Fig. 5.1) does not modify Q/I and U/I due to ρ_V as much as a horizontal magnetic field with azimuth $\chi_B = 0°$ (see Fig. 5.2).

Assuming $J_u = 1$ and $J_\ell = 0$ for simplicity, the components of the generalized profiles can be written as follows (see LL04)

$$\begin{aligned}
\Phi_0^{0,0}(0,1,\nu) &= \frac{1}{3}\Big[\phi_1 + \phi_0 + \phi_{-1}\Big], & \Psi_0^{0,0}(0,1,\nu) &= \frac{1}{3}\Big[\psi_1 + \psi_0 + \psi_{-1}\Big], \\
\Phi_0^{0,1}(0,1,\nu) &= \frac{1}{\sqrt{6}}\Big[\phi_1 - \phi_{-1}\Big], & \Psi_0^{0,1}(0,1,\nu) &= \frac{1}{\sqrt{6}}\Big[\psi_1 - \psi_{-1}\Big], \\
\Phi_0^{0,2}(0,1,\nu) &= \frac{1}{3\sqrt{2}}\Big[\phi_1 - 2\,\phi_0 + \phi_{-1}\Big], & \Psi_0^{0,2}(0,1,\nu) &= \frac{1}{3\sqrt{2}}\Big[\psi_1 - 2\,\psi_0 + \psi_{-1}\Big],
\end{aligned} \tag{5.4}$$

where, in the observer's frame,

$$\begin{aligned}
\phi_q &= \frac{1}{\sqrt{\pi}\Delta\nu_D} H(x - q\Delta x, a)\,; \\
\psi_q &= \frac{1}{\sqrt{\pi}\Delta\nu_D} L(x - q\Delta x, a)\,,
\end{aligned}$$

where $a = \Gamma/4\pi\Delta\nu_D$ is the damping parameter, Γ is the line broadening parameter in s^{-1}, $x = (\nu_0 - \nu)/\Delta\nu_D$ is the reduced frequency, and $\Delta x = \nu_L/\Delta\nu_D$ is the frequency shift due to Zeeman splitting, in units of Doppler widths. The ratios of the generalized profiles over $\Phi_0^{0,0}(0,1,x)$, and their frequency dependences, are shown in Fig. 5.4. When the condition $(a^2 + x^2) \gg 1$ is verified, as is the case in the line wings, we can use the asymptotic expansion for the Voigt profile and its associated dispersion profile (see Eq. (5.57) of LL04)

$$\begin{aligned}
H(x,a) &\sim \frac{1}{\sqrt{\pi}} \frac{a}{a^2 + x^2}\left[1 + \frac{1}{2}\frac{3x^2 - a^2}{(a^2 + x^2)^2} + \cdots\right]; \\
L(x,a) &\sim \frac{1}{\sqrt{\pi}} \frac{x}{a^2 + x^2}\left[1 + \frac{1}{2}\frac{x^2 - 3a^2}{(a^2 + x^2)^2} + \cdots\right].
\end{aligned} \tag{5.5}$$

In the far wings it is sufficient to take only the first order. The ratios of $\Phi_0^{0,1}(0,1,x)$, $\Phi_0^{0,2}(0,1,x)$, and $\Psi_0^{0,2}(0,1,x)$ over $\Phi_0^{0,0}(0,1,x)$ all quickly go to zero far from the core, while $\Psi_0^{0,1}(0,1,x)/\Phi_0^{0,0}(0,1,x)$ takes a constant value. We also observe that

$$\lim_{x\to\infty} \Psi_0^{0,0}(0,1,x)/\Phi_0^{0,0}(0,1,x) \to \infty,$$

but the $\Psi_0^{0,0}(0,1,x)$ generalized dispersion profile is not involved in any of the coefficients for the propagation matrix. Using the asymptotic expansion, the generalized

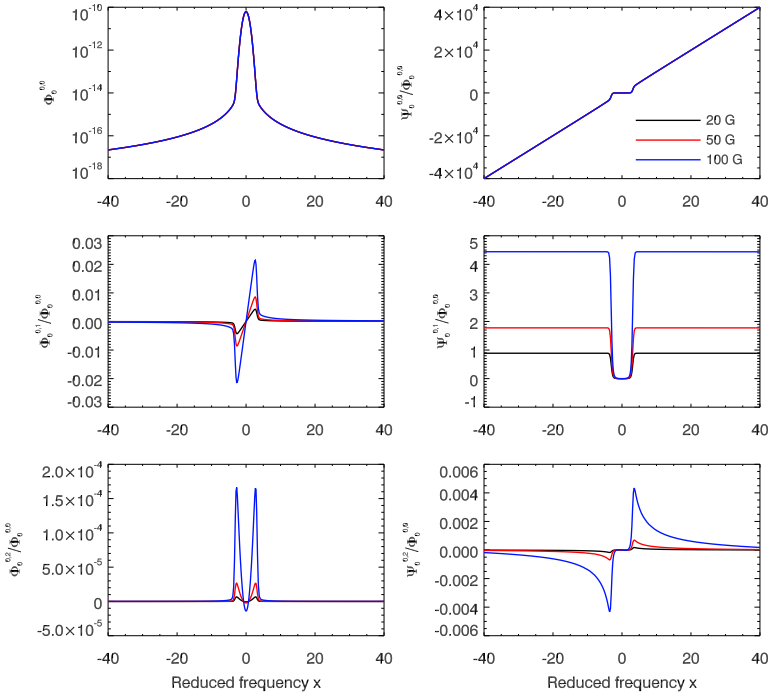

FIGURE 5.4— Plot of the variation with reduced frequency for the $\Phi_0^{0,0}(0,1,x)$ generalized profile (top left), and for the ratios of $\Phi_0^{0,1}(0,1,x)$ (top center), $\Phi_0^{0,1}(0,1,x)$ (top right), $\Psi_0^{0,0}(0,1,x)$ (bottom left), $\Psi_0^{0,1}(0,1,x)$ (center left) and $\Phi_0^{0,2}(0,1,x)$ (bottom right) over $\Phi_0^{0,0}(0,1,x)$. The generalized profiles are obtained using the asymptotic expansion of the Voigt and associated dispersion profiles, assuming a damping constant of $a = 10^{-3}$ and splittings of $\Delta x = a$ (black curve), $\Delta x = 2a$ (red curve), and $\Delta x = 5a$ (blue curve).

profiles, and generalized dispersion profiles, can be written as

$$\begin{aligned}
\Phi_0^{0,0}(0,1,x) &\sim \frac{1}{\sqrt{\pi}}\frac{a}{x^2} & \Psi_0^{0,0}(0,1,x) &\sim \frac{1}{\sqrt{\pi}}\frac{1}{x}\\
\Phi_0^{0,1}(0,1,x) &\sim \frac{1}{\sqrt{\pi}}\frac{4}{\sqrt{6}}\frac{a\Delta x}{x^3} & \Psi_0^{0,1}(0,1,x) &\sim \frac{1}{\sqrt{\pi}}\frac{2}{\sqrt{6}}\frac{\Delta x}{x^2}\\
\Phi_0^{0,2}(0,1,x) &\sim \frac{1}{\sqrt{\pi}}\frac{2}{\sqrt{2}}\frac{a\Delta x^2}{x^4} & \Psi_0^{0,2}(0,1,x) &\sim \frac{1}{\sqrt{\pi}}\frac{2}{3\sqrt{2}}\frac{\Delta x^2}{x^3}\,.
\end{aligned} \tag{5.6}$$

Given that, away from the line core, $\Phi_0^{0,2}(0,1,x)$ falls to zero much faster than

$\Phi_0^{0,0}(0,1,x)$, the former can be neglected in the expression for η_I^ℓ and so

$$\frac{\rho_V}{\eta_I^\ell} \sim \frac{\Psi_0^{0,1}(0,1,x)}{\Phi_0^{0,0}(0,1,x)} = \frac{2}{\sqrt{6}}\frac{\Delta x}{a} = \frac{4\sqrt{6}\pi}{3}\frac{\nu_L}{\Gamma}\,. \tag{5.7}$$

As can also be seen in Fig. 5.4, this ratio grows linearly with the Larmor frequency and, furthermore, it is independent of the Doppler width. Thus, the ρ_V/η_I ratio scales with the same parameters that characterize the efficiency of the Hanle effect (see Eq. (2.49) for the collisionless case), which explains why both effects begin to significantly affect the line polarization profiles at similar field strengths. Note, however, that (a) Faraday rotation modifies the radiation as it propagates through the medium, while instead the Hanle effect operates on local scattering processes and furthermore that (b) the rotation of the linear polarization angle scales differently with the magnetic field and has a different geometrical dependence for the two effects. Therefore, one should not expect the magnetic sensitivity of the polarization profiles to be exactly the same in the wings and the core.

Note finally that, unlike the $\Psi_0^{0,1}/\Phi_0^{0,0}$ ratio shown in Fig. 5.4, the ρ_V/η_I ratio is not independent of wavelength in the far wings, but rather it slowly decreases, as can be seen in Fig 5.3. This is because the continuum contribution to the absorption coefficient is also included. Outside the line core, as one goes further into the wings, both η_I^ℓ and ρ_V decrease at the same rate, while η_I^c remains essentially constant.

Furthermore, we reiterate that the MO terms of the propagation matrix can only have an impact on the wings of the polarization profiles of the emergent radiation if polarized radiation is produced by some other physical mechanism, such line scattering processes in which PRD effects are important.

5.3 The magnetic sensitivity of the Mg II k line for an LOS with $\mu = 1$

We now consider the forward scattering case, i.e., the case in which the LOS coincides with the symmetry axis of the radiation field which, in this work, is parallel to the local vertical. Bearing in mind that ρ_V operates when the mangetic field has a longitudinal component along the direction of propagation of the radiation, we study the magnetic field orientations for which MO effects can impact the polarization signals of the emergent radiation.

When considering an LOS along the local vertical, i.e., one with $\mu = 1$, a circular polarization signal is found, ultimately produced by the Zeeman effect (see the left panel of Fig. 4.19). In the line core, no signal is produced in either Stokes Q/I or U/I, since the magnetic field is parallel to the symmetry axis of the radiation field and therefore the Hanle effect cannot operate (for a two-level atom). Moreover, the Zeeman effect produces absolutely no linearly polarized signal, given that the magnetic field has no transverse component with respect to the LOS. We note that, for this geometry, ρ_V can be considerable, since the magnetic field is parallel to the LOS. However, the radiation is emitted along the local vertical due to scattering

processes is not linearly polarized, and so ρ_V is inoperative in modifying it. As a result, both Q/I and U/I are zero at all frequencies, independently of the magnetic field strength, and so the corresponding figures are not shown.

In Fig. 5.5 we show the Q/I profile, in the presence of a 20 G horizontal magnetic

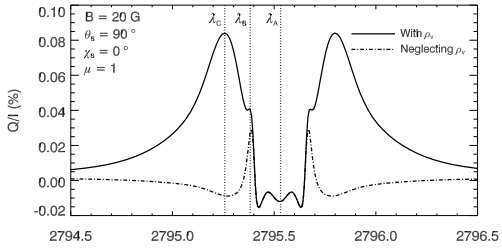

FIGURE 5.5— Stokes Q/I profile for the Mg II k line. The calculations have been performed in the FAL-C atmospheric model, including a horizontal magnetic field with $\chi_B = 0^\circ$, and a field strength of 20 G, both considering the full propagation matrix in the RT equation (solid curve) and artificially neglecting the impact of the ρ_V anomalous dispersion term (dashed-dotted curve). The vertical dotted lines indicate the air wavelengths $\lambda_A = 2795.53$ Å, $\lambda_B = 2795.38$ Å, $\lambda_C = 2795.26$ Å. The radiation emerging at an LOS with $\mu = 1$, i.e., the forward scattering case, has been considered. The reference direction for positive Stokes Q has been taken perpendicular to the direction of the magnetic field.

field with azimuth $\chi_B = 0^\circ$, for an LOS with $\mu = 1$. The result obtained when the ρ_V term is included in the RT calculation is compared to the result found when such term is neglected. For our selection of the reference direction of Stokes Q, the U/I profile is zero at all frequencies and, given that the magnetic field is perpendicular to the LOS considered here, the Zeeman effect does not give rise to circularly polarized radiation. Therefore, the U/I and V/I profiles are not shown.

For the line center wavelength $\lambda_A = 2795.53$ Å, one can find a small Q/I signal due to the Hanle effect in forward scattering, since the magnetic field breaks the axial symmetry of the problem. In the Doppler core, for the considered magnetic field strength, the emergent polarization in this spectral region is unaffected by inclusion of ρ_V in the calculation. On the other hand, when the calculation accounts for such MO effects, polarization signals appear in the line wings, as can be seen for wavelength $\lambda_C = 2795.26$ Å, where the amplitude of the Q/I wings is maximal. Closer to the line center, e.g., for wavelength $\lambda_B = 2795.38$ Å, some deviation can also be found between the Q/I obtained in the two calculations.

As can be seen from Eq. 5.3, ρ_V is zero when the magnetic field is perpendicular to the line of sight, so one may not, in principle, expect Faraday rotation to have any impact whatsoever. The sensitivity to ρ_V in this geometry can be explained by the fact that ε_Q is affected by the pumping radiation arriving from all direc-

tions, including those upon which the magnetic field has a significant projection. The linear polarization angle of the radiation propagating in such directions is, of course, modified by Faraday rotation, thereby modifying the radiation field. In other words, the magnetic field breaks the axial symmetry of the radiation field, which in the wing regions mainly impacts its linear polarization through ρ_V/η_I. Because of this symmetry breaking, the radiation scattered along the local vertical is linearly polarized.

In order to understand this better, we now study the impact of the magnetic field on the scattering emissivity in terms of the radiation field tensors (see Eq. (2.23)). In Fig. 5.6, all non-zero components of J^K_Q with $K = 2$ are shown, normalized to J^0_0,

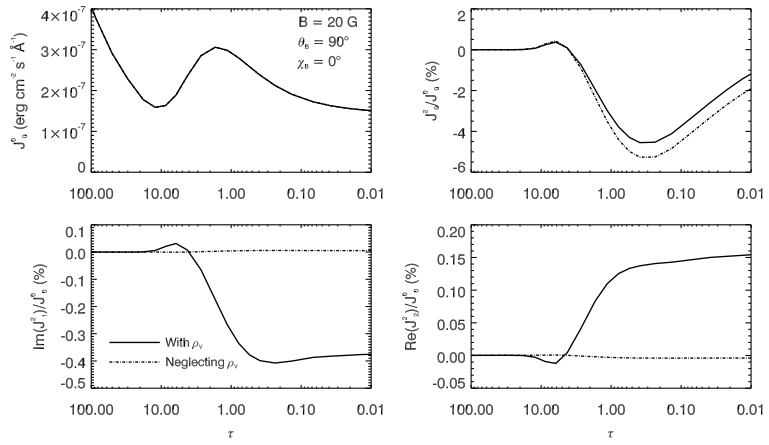

FIGURE 5.6— J^0_0 (upper left panel), J^2_0/J^0_0 (upper right panel), $\mathrm{Im}\{J^2_1\}/J^0_0$ (lower left panel), and $\mathrm{Re}\{J^2_2\}/J^0_0$ (lower right panel) ratios at wing wavelength λ_C, obtained from the self-consistent solution of the HZ code for the Mg II k line, taking into account the full propagation matrix (solid curves) and neglecting the ρ_V terms (dashed-dotted curves). Such quantities are given as functions of the optical depth for a LOS with $\mu = 1$, and at wavelength λ_C. The calculation has been performed in the presence of a horizontal magnetic field with $\chi_B = 0°$ and a field strength of 20 G. The FAL-C atmospheric model has been used for the calculation.

for the radiation at wavelength $\lambda_C = 2795.26$ Å (see Fig. 5.5), obtained in the self-consistent solution of the RT problem in the presence of a 20 G horizontal magnetic field with an azimuth of $\chi_B = 0°$. When the coupling between Stokes Q and U produced by ρ_V is accounted for in the RT equation, J^2_0 is found to decrease in absolute value at the wing frequencies, compared to the case in which such coupling is neglected. On the other hand, the ratios of the imaginary part of J^2_1 and of the real part of J^2_2 over J^0_0, which are related to the breaking of the radiation field's axial symmetry, reach values larger than 0.1% when ρ_V is included in the calculation.

When such MO effects are neglected, such radiation field tensor components are rather insignificant. In Fig. 5.7, the $\varepsilon_Q/\varepsilon_I$ ratios are shown for LOS with $\mu = 0.1$

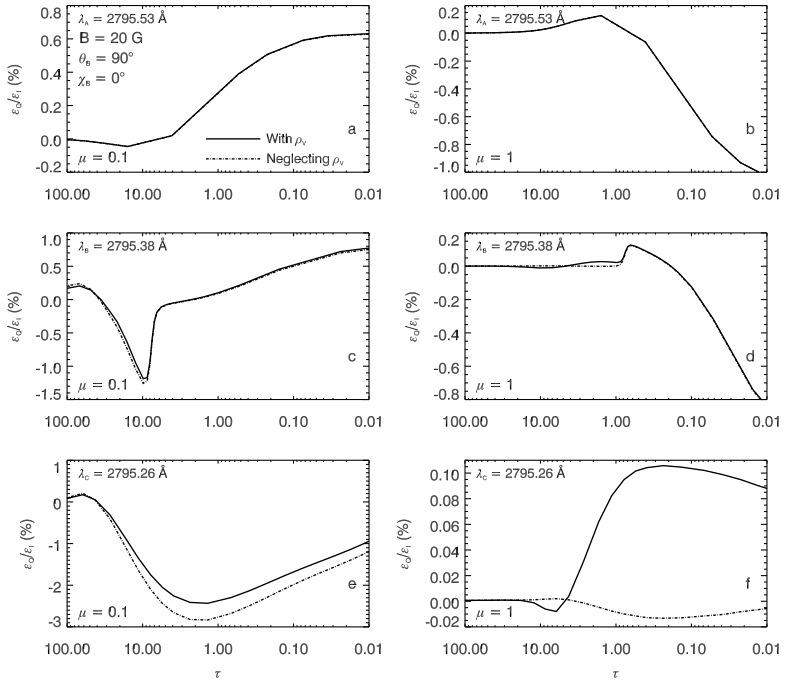

FIGURE 5.7— $\varepsilon_Q/\varepsilon_I$ for the Mg II k line, obtained from the self-consistent solution of the HZ code, both considering the full propagation matrix (solid curves) and neglecting the ρ_V terms (dashed-dotted lines). The calculations have been performed in the presence of a horizontal magnetic field with $\chi_B = 0°$ and a field strength of 20 G. The results for wavelengths λ_A (top row), λ_B (middle row), and λ_C (bottom row) are shown for LOS with $\mu = 0.1$ (left column) and $\mu = 1$ (right colum), with respect to their corresponding optical depths. The reference direction for positive Stokes Q is parallel to the limb for $\mu = 0.1$, and perpendicular to the direction of the magnetic field for $\mu = 1$.

and $\mu = 1$, also in the presence of a 20 G horizontal field with an azimuth of $\chi_B = 0°$, for the three illustrative wavelengths discussed in this section. At wing wavelength λ_C, the emitted polarization fraction for the LOS with $\mu = 0.1$ is found to decrease in absolute value when the effects of Faraday rotation are included (see panel e of the figure). In the forward scattering case, for the same wavelength, the amplitude of $\varepsilon_Q/\varepsilon_I$ increases significantly when the effects of ρ_V are accounted for (see panel f of the figure), and its dependence on optical depth is reminiscent of the one found

for $\mathrm{Re}\{J^2_2\}/J^0_0$, shown in Fig. 5.6.

On the other hand, there is no change in $\varepsilon_Q/\varepsilon_I$ at the line center wavelength λ_A when such MO effects are neglected (see panels a and b of Fig. 5.7), as expected from the fact that ρ_V/η_I is very small in the line core for the 20 G magnetic field considered here. This agrees with the results which were obtained for the emergent Q/I profiles shown in Figs. 5.2 and 5.5. In the intermediate frequency λ_B, the impact of ρ_V on the emissivity is considerably smaller than for the wavelength λ_C (see panels c and d of Fig. 5.7). This is a consequence of (a) the fact that the ρ_V/η_I ratio is smaller at this frequency at the formation height of the wings and (b) that, due to Doppler redistribution, the contribution from the line-core radiation field, which is essentially insensitive to Faraday rotation, is much greater at this wavelength.

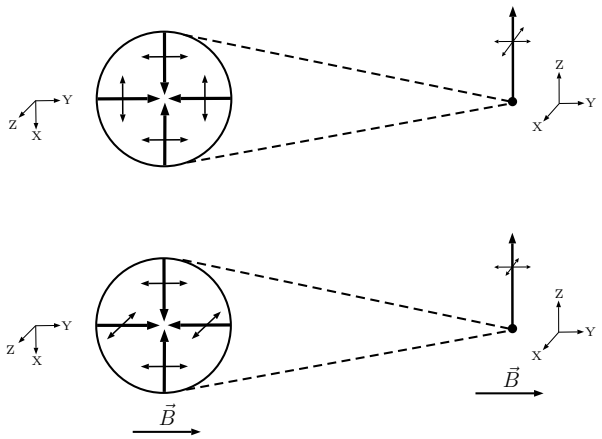

FIGURE 5.8— Schematic representation of the impact of MO effects, produced by a horizontal magnetic field, on the radiation that is scattered in the vertical direction. For the sake of simplicity, we consider an atom illuminated by radiation propagating in the XY plane, with a given degree of linear polarization. In the absence of a magnetic field (top panel), the radiation field is perfectly axially symmetric and the radiation that is scattered in the vertical (Z) direction is unpolarized. However, when a magnetic field parallel to the X axis is included (bottom panel), it produces a rotation of the plane of polarization of the radiation propagating in directions along which its longitudinal component is non-zero. Because of this modification of the radiation field, the radiation that is scattered in the Z direction becomes linearly polarized.

The sensitivity of the wings of the linear polarization profiles to MO effects in the forward scattering case, in the presence of a horizontal magnetic field, is further illustrated in Fig. 5.8. For didactic purposes, we assume that the radiation only propagates in the XY plane. We also consider that - in the absence of a magnetic field - its linear polarization is contained in the same plane, i.e., the electric field does not oscillate parallel to the Z-axis. Although the radiation propagating in a given

direction in the XY plane is linearly polarized, again in the absence of a magnetic field, the radiation field is perfectly symmetric around the Z axis, and the radiation scattered along this direction is not polarized.

Consider now the case in which a magnetic field along the Y axis is present and induces Faraday rotation. The radiation propagating in directions that are perpendicular to the magnetic field, i.e., along the X axis, will not be affected. On the other hand, those propagating in directions along which the magnetic field has a significant longitudinal component will experience a rotation of their plane of linear polarization, causing the axial symmetry of the pumping radiation field to be broken. Because of this, the presence of a horizontal magnetic field causes the radiation that is scattered in the direction parallel to the local vertical to be polarized, despite the fact that Faraday rotation does not operate in this direction.

5.4 The impact of MO effects on the Ca I 4227 Å line

Wing linear polarization signatures of MO effects are not found exclusively in spectral lines whose wings form in the chromosphere, such as the Mg II k line. Indeed, the core of the Ca I 4227 Å line forms much lower in the solar atmosphere, around 1000 km, and the radiation emerging at frequencies corresponding to the near wing originates in the photosphere but, as can be seen in Fig. 5.9, such anomalous dispersion effects have a sizable impact also for the linear polarization profiles of this line. For a near-limb LOS, such as the one with $\mu = 0.1$, the influence of ρ_V gives rise to a magnetic sensitivity in the wings of both Q/I and U/I. As the magnetic field becomes stronger, the impact of Faraday rotation can be found at frequencies increasingly further from the line core as the ρ_V - which scales with Zeeman splitting - becomes significant with respect to η_I at such frequencies, when taking the continuum opacity into account.

It is important to note that a magnetic field whose orientation is constant over the whole atmosphere - and is almost longitudinal to the LOS - has been considered. For this geometry, the ρ_V coefficient is large for the direction corresponding to the LOS and it has the same sign at all spatial heights. Thus, it is especially advantageous for the modification of the linear polarization of the emergent radiation. This contrasts with the situation we considered in the left panel of Fig. 4.10, in which the emergent Q/I is shown for Sr II 4078 Å, in the presence of a horizontal magnetic field whose azimuth changes at scales smaller than the line photon's mean free path, there is no magnetic sensitivity in the wings since the longitudinal components of the magnetic field cancel each other (this was expected from Eq. (2.83)). In Fig 4.11, a microstructured magnetic field with a fixed inclination and a randomly changing azimuth was also considered, but with an inclination of $\theta_B = 30°$. In this case such components do not cancel perfectly, so the emergent wing polarization is still sensitive to ρ_V, although its effect is by no means as great as in the geometry presented in Fig. 5.9.

We consider the interesting case in which a deterministic magnetic field changes its orientation with height. In Fig. 5.10 we compare the case in which a horizontal

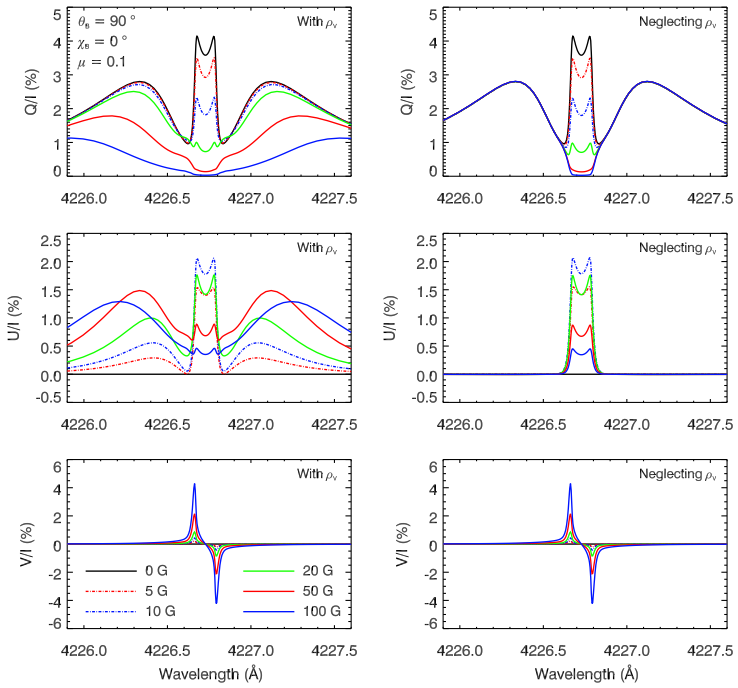

FIGURE 5.9— Stokes Q/I (top row), U/I (middle row), and V/I (bottom row) profiles for the Ca I 4227 Å line. The calculations have been performed in the presence of a horizontal magnetic field with azimuth $\chi_B = 0°$, both by considering the full propagation matrix in the RT equation (left column) and by artificially setting the ρ_V anomalous dispersion coefficient to zero (right column). The colored curves represent the same field strengths as in Fig. 5.1. The FAL-C atmospheric model has been used for the calculation. We consider the radiation emerging at an LOS with $\mu = 0.1$. The reference direction for positive Stokes Q has been taken parallel to the limb.

magnetic field with $\chi_B = 0°$ is present at all spatial points of the FAL-C plane-parallel atmosphere to the case in which, around the formation region for the line core and above, the magnetic field is also horizontal with $\chi_B = 0°$, but at lower atmospheric heights (below 700 km) the magnetic field is also horizontal but is oriented along in the opposite direction, i.e., its azimuth is $\chi_B = 180°$. Thus, around the spatial region where the wings originate, the sign of ρ_V in one case is opposite to that of the other. In both cases the magnetic field has a strength of 20 G at all spatial points. As can be seen from the figure, in both cases the Q/I wing signal decreases by the same amount, independently of the sign of ρ_V. On the

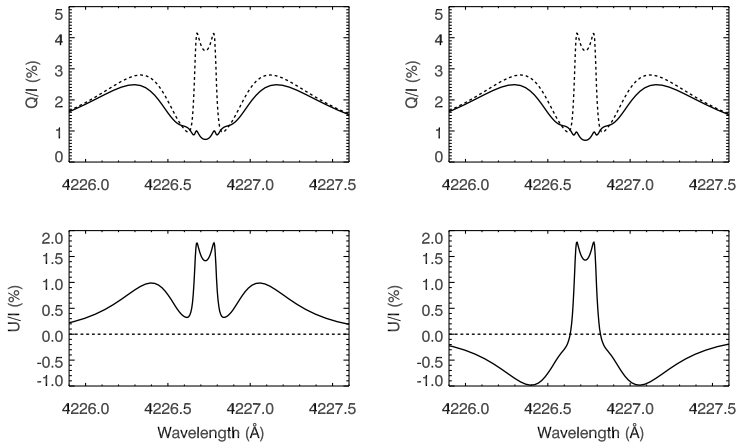

FIGURE 5.10— Stokes Q/I (top row) and U/I (bottom row) profiles for the Ca I 4227 Å line. The results of the calculation (solid curves) performed in the presence of a 20 G horizontal ($\theta_B = 90°$) magnetic field with an azimuth of $\chi_B = 0°$ at all spatial points in the atmosphere (left column) are compared to those obtained from a calculation in which a 20 G horizontal magnetic field with azimuth $\chi_B = 0$ is present at atmospheric heights of 700 km and above, while at lower heights the magnetic field is also horizontal with a 20 G field strength, but its azimuth is $\chi_B = 180°$ (right colum). The dashed curves represent calculations in the absence of a magnetic field. The FAL-C atmospheric model has been used for the calculation. We consider the radiation emerging at an LOS with $\mu = 0.1$. The reference direction for positive Stokes Q has been taken parallel to the limb.

other hand, the U/I wing signals produced by Faraday rotation are sensitive to the orientation of the magnetic field, and their signs change between the two cases. This can easily be seen from the transfer equations for Q and U in Eq. (5.2), in which the only non-zero coefficients of the propagation matrix are η_I and ρ_V, and we assume for simplicity that $\varepsilon_U = 0$. The Q/I and U/I profiles obtained in the line core for both cases coincide, since the magnetic field does not change around its formation region.

Bianda et al. (2003) performed observations close to the limb for the Ca I line at 4227 Å, in which they found a considerable variation in the line wings of Q/I along the slit, and Stokes U/I signals were also produced, which likewise presented a significant spatial variation. Given that, as discussed in Sect. 4.2, the Hanle effect should not, in principle, modify the wing polarization, both these authors and others (see Sampoorna et al. 2009) suggested alternative explanations for such behavior in the wing polarization, both magnetic and non-magnetic in origin.

One of the explanations they offered was that the Hanle effect may operate outside of the line core due to the influence of elastic collisions. However, when

performing last scattering calculations, Sampoorna et al. (2009) were able to find only a very small magnetic sensitivity in the wings despite searching over a large parameter space for collisional rates and magnetic field strengths. As noted in Sect. 3.6, for lines with extended polarization signals in the wings - such as Sr II 4078 Å and Ca I 4227 Å - the wing polarization signals are mainly produced by coherent scattering processes, even if the branching ratio for $\mathcal{R}_{\rm II}$ is comparatively small around the wing formation region. It can be seen, both from the expression of $\mathcal{R}_{\rm II}$ (e.g., in the atomic rest frame as shown in Eq. 2.44) and from time-uncertainty arguments, that the contribution to the wing emissivity due to coherent scattering is insensitive to the Hanle effect. The authors also suggested that the presence of horizontal inhomogeneities in the solar atmosphere could produce the observed spatial variation in the wing polarization.

Although we cannot exclude that the latter could play a relevant role, we submit that - as can be seen from Fig. 5.9 - a magnetic sensitivity in the line wings can be produced by MO effects, namely through Faraday rotation. In particular, it is very encouraging that our modeling allows us to find opposite signs in the U/I found in the line core (due to the Hanle effect) and in the wings (due to ρ_V) shown in Fig. 5.10, which qualitatively reproduces the behavior presented in Fig. 3 of Bianda et al. (2003) for an LOS with $\mu = 0.31$.

We also note that the signatures produced indirectly by Faraday rotation, i.e., those produced due to a magnetic field that is perpendicular to the LOS through the impact of ρ_V on the pumping radiation field, do not significantly contribute to the polarization signals of the Ca I 4227 Å line in forward scattering, unlike what we have found for the Mg II k line. Indeed, in the top left panel of Fig. 5.11 it can be seen that, even for a magnetic field strength of 100 G, the signatures produced by the coupling of Stokes Q and U in the RT equation due to such MO effects are very small. Thus, when considering the forward scattering signals in the Ca I 4227 Å line, disentangling the magnetic origin of the wing linear polarization from the atmosphere's thermodynamical properties would be a very challenging task, even without considering the spectral smearing of the measured signals due to the finite spectral resolution of any instrument.

The reduced sensitivity of this line to such MO effects for $\mu = 1$ and $\theta_B = 90°$ can be explained by the conditions of the atmospheric region where this line forms. At this wavelength, the J^2_0 component of the radiation field tensor is negligible, compared to the J^0_0 component, in the spatial region where the radiation at wavelength λ_W emerging at an LOS with $\mu = 1$ originates. This can be seen in the top right panel of Fig. 5.11. Thus, at such atmospheric heights, also the linear polarization fraction, defined as

$$P_L = \frac{\sqrt{Q^2 + U^2}}{I}\,, \tag{5.8}$$

is essentially zero for the radiation propagating in any direction, also those in which the magnetic field has a significant longitundinal component. This can be seen in the bottom right panel of the figure, where the height where $\tau = 1$ for an LOS

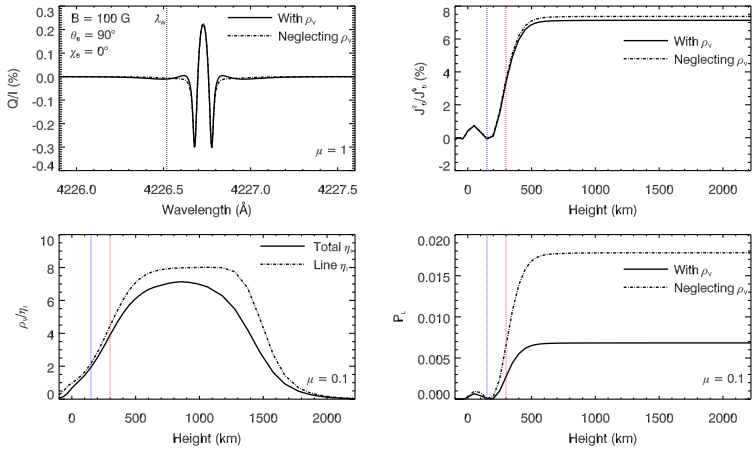

FIGURE 5.11— This figure shows the results of calculations considering the FAL-C semi-empirical atmospheric model, for the Ca I 4227 Å line and in the presence of a 100 G horizontal magnetic field with azimuth $\chi_B = 0°$. The vertical dotted lines indicate the height where $\tau = 1$ for the wavelength $\lambda_W = 4226.52$ Å, for LOS with $\mu = 0.1$ (red) and $\mu = 1$ (blue). Top left panel: Stokes Q/I profiles, both considering the full propagation matrix (solid curve), and artificially setting the ρ_V anomalous dispersion coefficient to zero (dashed-dotted curve). The radiation emerging at an LOS with $\mu = 1$ has been considered, and the direction for positive Stokes Q has been taken perpendicular to the direction of the magnetic field. The vertical dotted line corresponds to wavelength $\lambda_W = 4226.52$ Å. Top right panel: J^2_0/J^0_0 ratio, as a function of atmospheric height at wavelength λ_W. The calculations have been performed both when accounting for the ρ_V term in the RT equation (solid curve) and neglecting it (dash-dotted curve) at wing wavelength λ_W. Bottom left panel: ρ_V/η_I ratio, as a function of atmospheric height at wavelength λ_W, for an LOS with $\mu = 0.1$ and $\chi = 0°$, both neglecting the continuum contribution to η_I (dash-dotted curve) and taking it into account (solid curve). The direction for positive Stokes Q has been taken perpendicular to the direction of the magnetic field. Bottom right panel: Linear polarization fraction, P_L, as a function of atmospheric height at wavelength λ_W. The calculations have been performed both accounting for the ρ_V term in the RT equation (solid curve) and neglecting it (dash-dotted curve). The direction with $\mu = 0.1$ and $\chi = 0°$ has been considered.

with $\mu = 1$ at the λ_W wavelength is indicated by the blue dotted line. Given that the radiation has such a small linear polarization fraction, ρ_V cannot impact the radiation field in any meaningful way. Thus, the radiation scattered at such spectral and spatial regions along the local vertical remains essentially unpolarized, when a horizontal magnetic field is present.

It is also worth noting that the ρ_V/η_I ratio at these spatial regions is suppressed, in comparison to the ratio found at higher altitudes, as shown in the bottom left panel of Fig. 5.11. The reason for this is mainly related to the larger collisional rates in photospheric regions, due to which the total line broadening parameter Γ is also larger. As shown in Eq. (5.7), this causes a significant decrease in the ra-

tio at photospheric heights, which further reduces their effectiveness in modifying the wing polarization signals. At higher layers in the solar atmosphere, where the collisional rates are smaller, we note that the continuum opacity represents a significant contribution to the total absorption coefficient for the wing wavelengths we are considering.

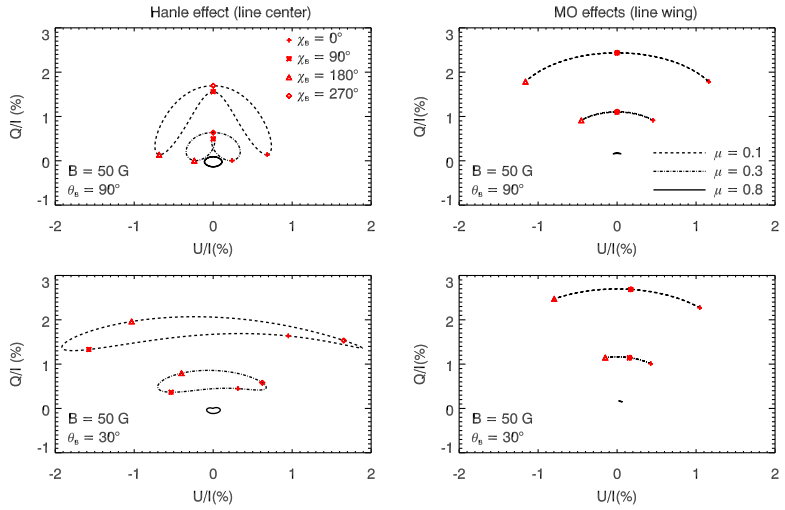

FIGURE 5.12— Linear polarization of the emergent radiation in the Ca I line at 4227 Å. Results are shown on the Q/I-U/I plane, at line center (left column), and at the wavelengths corresponding the the Q/I blue wing maximum (right column). Calculations have been performed in the presence of magnetic fields with $B = 50$ G, and inclinations $\theta_B = 90°$ (top row) and $\theta_B = 30°$ (bottom row), for a range of azimuths between 0° and 360°, in 5° increments. LOS with $\mu = 0.1$ (dashed curve), $\mu = 0.3$ (dashed-dotted curves), and $\mu = 0.8$ (solid curves) have been considered. The reference direction for positive Stokes Q has been taken parallel to the limb.

In order to further illustrate the fact that the efficiency of the MO effects in modifying the wing polarization depends on the longitudinal component of the magnetic field, we compare the linear polarization signals obtained in the presence of magnetic fields with various azimuths. The closed curves show in Fig. 5.12 represent the variation in the Q/I-U/I plane of the linear polarization of the emergent radiation, calculated in the presence of magnetic fields with constant stength and inclination, while azimuths in the $\chi_B = [0°, 360°]$ range are considered. Although the Hanle critical field is approximately 25 G for this line, the magnetic sensitivity of the line wings due to ρ_V is smaller, given that such wings originate in deeper layers where the collisional rates are higher than in the line core. Thus, such diagrams are shown for field strength of 50 G and inclination $\theta_B = 90°$ (top row) and $\theta_B = 30°$ (bottom

row), while the azimuth changes in 5° increments. Two wavelengths have been considered, one corresponding to the line center (left column), where the Hanle effect operates, and another corresponding to the Q/I maximum in the blue wing (right column), which depends on the LOS. We have already shown that the magnetic sensitivity of the latter depends on the MO effects.

When considering a horizontal magnetic field, we point out that for azimuths $\chi_B = 90°$ and $\chi_B = 270°$, in which the magnetic field is perpedicular to the LOS, no U/I is produced either in the line wing, since ρ_V does not operate, nor in line center, since the Hanle effect does not induce any rotation of the plane of polarization in such geometries. However, we observe that at line center the Q/I values differ for the two aforementioned azimuths because we are considering LOS other than $\mu = 0$ or $\mu = 1$ (e.g., Trujillo Bueno 2001). When horizontal magnetic fields are considered, the diagrams shown in Fig. 5.12 are symmetric with respect to $U/I = 0$, both at line center and for the wavelength corresponding to the Q/I maximum. This is because the rotation of the plane of polarization, both due to the Hanle effect and to the MO effects, is produced by the component of the magnetic field that is parallel to the LOS. For a horizontal magnetic field with azimuth χ_B, its component along the LOS is opposite to that of a magnetic field with $\chi_B + 180°$. This has interesting observational implications; the radiation reaching the observer from a spatially unresolved region in which various horizontal magnetic fields are present, such that their azimuths are equally distributed in any direction, the U/I signals will be cancelled out, for any LOS, both in the line and the wings. It is well known that in the line center, the Hanle effect still leads to a net decrease in Q/I with respect to the unmagnetized case (for LOS close to the limb) if unresolved magnetic fields are present in such configuration. Here we also point out that the MO effects would lead to a similar depolarization in line wings of Q/I, provided that the magnetic fields are structured at scales larger than the mean free path of the line's photons, and so the field-averaged $\langle \rho_V \rangle$ is non-zero.

When considering a magnetic field with inclination $\theta_B = 30°$, the situation is clearly different. The Q/I-U/I diagrams are not symmetric around $U/I = 0$, since the longitudinal components of the magnetic fields with different azimuths are not symmetrically distributed around LOS other than $\mu = 0$ and $\mu = 1$. Thus, if the radiation reaches the observer from a spatially unresolved region with magnetic fields of inclination $\theta_B = 30°$ and equally distributed azimuths, a remaining non-zero U/I signal will be appreciable, as well as a modification of Q/I with respect to the unmagnetized case. Of course, the aforementioned asymmetry around $U/I = 0$ is not specific to fields with inclination $\theta_B = 30°$, but rather can be found for inclinations other than $\theta_B = 0°$, 90°, and 180°.

5.5 The change in polarization fraction produced by Faraday rotation

In the previous sections, the reader may have noticed that, as the magnetic field strength increases, both the Stokes Q/I and U/I amplitudes begin to decrease,

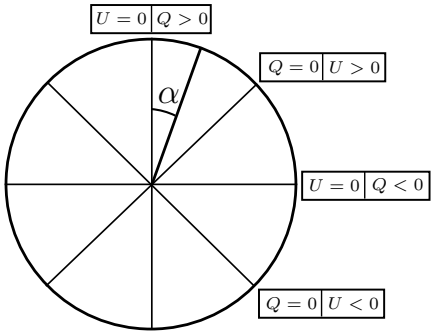

FIGURE 5.13— Representation of the linear polarization angle α, defined in the interval between 0° and 180° such that $\alpha = 0^\circ$ when $Q > 0$ and $U = 0$.

so that the overall linear polarization fraction diminishes. This occurs in the line core, as expected from the effects of Hanle depolarization and, interestingly, it also occurs in the line wings, whose polarization signals are sensitive to the magnetic field because of Faraday rotation. Therefore, it is illuminating to study the magnetic dependence of the linear polarization profiles not just in terms of Q/I and U/I, but also through the linear polarization fraction, defined in Eq. (5.8) and the polarization angle (see Fig.5.13), which is defined in the interval between 0° and 180° as

$$\alpha = \frac{1}{2}\tan^{-1}\left(\frac{U}{Q}\right) + \alpha_0\,, \tag{5.9}$$

with

$$\alpha_0 = \begin{cases} 0^\circ\,, & \text{if } P_Q > 0 \text{ and } P_U \geq 0 \\ 180^\circ\,, & \text{if } P_Q > 0 \text{ and } P_U < 0 \\ 90^\circ\,, & \text{if } P_Q < 0\,, \end{cases} \tag{5.10}$$

so that $\alpha = 0^\circ$ when $Q > 0$ and $U = 0$. In the case in which $P_Q = 0$, $\alpha = 45^\circ$ if $P_U > 0$ and $\alpha = 135^\circ$ if $P_U < 0$, while if $P_Q = P_U = 0$ the polarization angle is of course undefined.

In Fig. 5.14, both P_L and α are plotted as a function of wavelength, for the Ca I 4227 Å line, for a LOS with $\mu = 0.1$. A horizontal magnetic field with an azimuth of $\chi_B = 0^\circ$ has been considered, which is almost longitudinal to the LOS. In the figure, a comparison is shown between the results obtained when the ρ_V term is taken into account (left column) and when it is neglected. In both cases, the same behavior is found in the line core, namely that the polarization fraction is found to decrease monotonically with the magnetic field strength, while the polarization angle α increases monotonically, although it remains below 45°. This was expected, since this magnetic sensitivity is produced by the Hanle effect which, in this geometry, produces a reduction in the linear polarization fraction of the scattered radiation and a

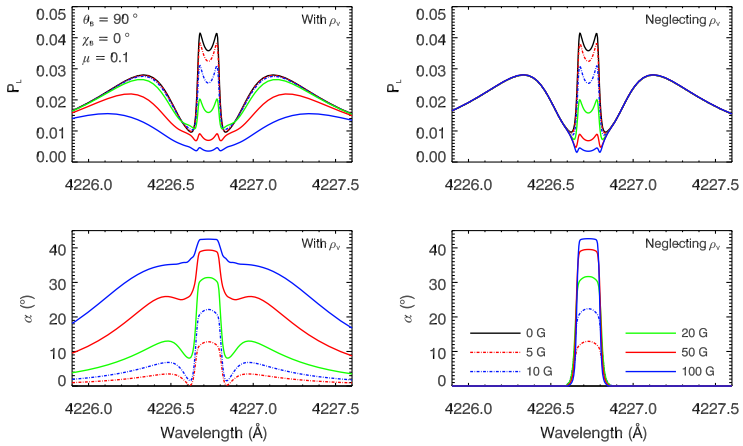

FIGURE 5.14— Polarization fraction P_L (left column), and polarization angle α (right column) for the Ca I 4227 Å line. The calculations have been performed in the presence of a horizontal magnetic field, by neglecting the ρ_V term in the RT equation (top row), accounting for the full propagation matrix (middle row) and taking the weak field approximation, i.e., neglecting the Zeeman splitting in the absorption and emission profiles of all RT coefficients (bottom row). Magnetic field strengths of 0 G (black solid curves), 5 G (red dashed-dotted curves), 10 G (blue dashed-dotted curves), 20 G (green solid curves), 50 G (red solid curves) and 100 G (blue solid curves) have been considered. The FAL-C atmospheric model has been used for the calculation. We consider the radiation emerging at an LOS with $\mu = 0.1$. The reference direction for positive Stokes Q is taken parallel to the limb.

rotation of its plane of polarization. On the other hand, it has already been established in previous sections that the magnetic dependence of the linear polarization in the wings is a consequence of Faraday rotation. Indeed, when ρ_V is neglected in the calculation, as shown in the right column of the figure, P_L and α are insensitive to the field strength in the wing region. When it is accounted for, one finds not only a montonic increase with magnetic field of the linear polarization angle in the wings, but also a decrease in the polarization fraction.

Indeed, the fact that Faraday rotation, whose effect is to modify the linear polarization angle of the radiation traveling through the material, also gives rise to a sizable decrease of its linear polarization fraction is an interesting aspect that merits some attention. To study this effect in greater depth, we will use the evolution operator formalism we have discussed in Sect. 2.6.1, introduced by Landi Degl'Innocenti & Landi Degl'Innocenti (1985). We remind the reader that, by definition, the evolution operator $\hat{O}(s, s')$ is a 4×4 matrix which, when applied to a Stokes vector at point s' of the ray path, yields the Stokes vector at point s (with $s \geq s'$)

$$\vec{I}(s) = \hat{O}(s, s')\vec{I}(s') \,. \tag{5.11}$$

In this expression, the contribution to the Stokes vector at point s due to the radiation emitted between points s' and s has been neglected. Since we are studying the effects of Faraday rotation, we will consider the specific case in which only the η_I and ρ_V coefficients of the propagation matrix are non-zero, and in this case the evolution operator takes the form shown in Eq. (2.105). Thus, when solving the transfer equation, the Stokes parameters at point s become

$$I(s) = \mathrm{e}^{-H_I}\, I(s')\,, \text{ and } V(s) = \mathrm{e}^{-H_I}\, V(s')\,, \tag{5.12a}$$

$$Q(s) = \mathrm{e}^{-H_I}\Big[Q(s')\cos R_V - U(s')\sin R_V\Big]\,, \tag{5.12b}$$

$$U(s) = \mathrm{e}^{-H_I}\Big[Q(s')\sin R_V + U(s')\cos R_V\Big]\,, \tag{5.12c}$$

where H_I and R_V are given in Eq. (2.106). Using such relations, it is trivial to find that

$$P_L(s) = \frac{\sqrt{Q(s)^2+U(s)^2}}{I(s)} = \frac{\sqrt{Q(s')^2+U(s')^2}}{I(s')} = P_L(s')\,. \tag{5.13}$$

Therefore (see Eq. 5.8), the radiation propagating through a medium whose RT coefficients are constrained as described above conserves its linear polarization fraction independently of the ρ_V/η_I ratio, and thus independently of the magnetic field strength and orientation. This is a good approximation for weakly emitting but magnetized materials, such as interestellar media. However, for the regions of the solar atmosphere considered in this work, the contribution from the emission coefficient cannot be neglected. When the emissivity of the material is accounted for, the non-homogenous solution of the RT equation is required, as shown in Eq. (2.96). If, for simplicity, we assume that there is no radiation reaching point s' in the direction of propagation, the Stokes vector of the radiation emerging from the slab is

$$\vec{I}(s) = \int_{s'}^{s} \hat{O}(s,s'')\,\vec{\varepsilon}(s'')\,\mathrm{d}s''\,. \tag{5.14}$$

We further simplify the problem by assuming that η_I, ρ_V and the four Stokes components of $\vec{\varepsilon}$ are constant along the medium. In this case

$$H_I = (s-s')\,\eta_I\,, \quad R_V = (s-s')\,\rho_V\,, \tag{5.15}$$

and Eq. (5.14) becomes

$$\vec{I}(s) = \int_{s'}^{s} \mathrm{e}^{-(s-s')\,\eta_I} \times \begin{pmatrix} 1 & 0 & 0 & 0 \\ 0 & \cos\big[(s-s'')\,\rho_V\big] & -\sin\big[(s-s'')\,\rho_V\big] & 0 \\ 0 & \sin\big[(s-s'')\,\rho_V\big] & \cos\big[(s-s'')\,\rho_V\big] & 0 \\ 0 & 0 & 0 & 1 \end{pmatrix} \begin{pmatrix} \varepsilon_I \\ \varepsilon_Q \\ \varepsilon_U \\ \varepsilon_V \end{pmatrix} \mathrm{d}s''\,. \tag{5.16}$$

The following definite integrals appear in the previous expression

$$T_1 = \int_{s'}^{s} \mathrm{e}^{-(s-s'')\,\eta_I}\,\mathrm{d}s'' = \frac{1}{\eta_I}\big(1-\mathrm{e}^{-(s-s')\,\eta_I}\big)\,, \tag{5.17a}$$

$$\begin{aligned} T_2 &= \int_{s'}^{s} \mathrm{e}^{-(s-s'')\,\eta_I}\cos\big[(s-s'')\rho_V\big]\,\mathrm{d}s'' \\ &= \frac{1}{\eta_I^2+\rho_V^2}\Big\{\eta_I - \mathrm{e}^{-(s-s')\,\eta_I}\Big(\eta_I\cos\big[(s-s')\,\rho_V\big] - \rho_V\sin\big[(s-s')\,\rho_V\big]\Big)\Big\}\,, \end{aligned} \tag{5.17b}$$

$$\begin{aligned} T_3 &= \int_{s'}^{s} \mathrm{e}^{-(s-s'')\,\eta_I}\sin\big[(s-s'')\rho_V\big]\,\mathrm{d}s'' \\ &= \frac{1}{\eta_I^2+\rho_V^2}\Big\{\rho_V - \mathrm{e}^{-(s-s')\,\eta_I}\Big(\eta_I\sin\big[(s-s')\,\rho_V\big] + \rho_V\cos\big[(s-s')\,\rho_V\big]\Big)\Big\}\,. \end{aligned} \tag{5.17c}$$

So the Stokes parameters for the radiation emerging from the material are

$$I(s) = T_1\,\varepsilon_I\,, \tag{5.18a}$$

$$Q(s) = T_2\,\varepsilon_Q - T_3\,\varepsilon_U\,, \tag{5.18b}$$

$$U(s) = T_3\,\varepsilon_Q + T_2\,\varepsilon_U\,, \tag{5.18c}$$

$$V(s) = T_1\,\varepsilon_V\,. \tag{5.18d}$$

The linear polarization fraction of the radiation emerging from the slab is thus

$$P_L = \sqrt{\frac{T_2^2+T_3^2}{T_1^2}}\,\sqrt{\frac{\varepsilon_Q^2+\varepsilon_U^2}{\varepsilon_I^2}}\,, \tag{5.19}$$

where

$$\frac{T_2^2+T_3^2}{T_1^2} = \frac{1-2\mathrm{e}^{-(s-s')\,\eta_I}\cos\big[(s-s')\rho_V\big]+\mathrm{e}^{-2(s-s')\,\eta_I}}{1-2\mathrm{e}^{-(s-s')\,\eta_I}+\mathrm{e}^{-2(s-s')\,\eta_I}}\,. \tag{5.20}$$

From the last two expressions the following conclusions are obvious. If the radiation emitted by the material is unpolarized (or indeed, $\varepsilon_Q = \varepsilon_U = 0$), the linear polarization fraction of the emergent radiation will be zero, independently of the values of $\Delta s = (s-s')$, η_I, and ρ_V. In the absence of ρ_V, the linear polarization fraction will depend only of the emissivities, but not on η_I or Δs. When ρ_V is non-zero, the resulting polarization fraction will not depend on its sign.

In Fig. 5.15, the $\sqrt{(T_2^2+T_3^2)/T_1^2}$ factor is plotted as a function of ρ_V/η_I. Recall that this factor, which is unity in the absence of a magnetic field, indicates the change in the linear polarization fraction of the emitted radiation. The various curves in the figure represent different Δs values for this slab and, since η_I has been taken equal to unity, they are a measure of different optical thicknesses ranging from 0.05 to 1. Of course, the smaller the optical thickness of the atmospheric region under consideration, the larger the ρ_V must be in order to significantly reduce the polarization fraction. The dependence of P_L on ρ_V can be understood as follows.

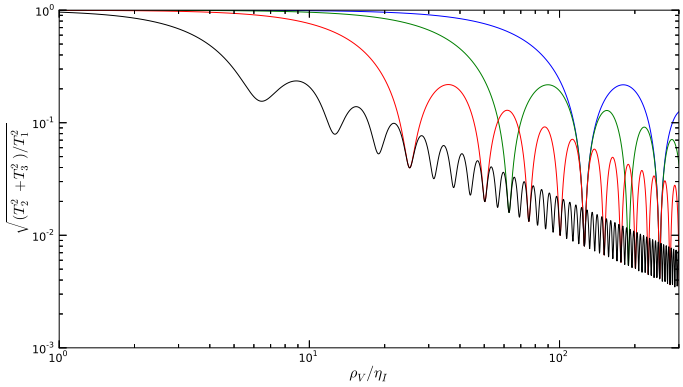

FIGURE 5.15— $\sqrt{(T_2^2+T_3^2)/T_1^2}$ factor (see Eq. (5.20)) as a function of ρ_V/η_I. The various curves correspond to different optical depths, including $\Delta\tau = 1$ (black curve), $\Delta\tau = 0.25$ (red curve), $\Delta\tau = 0.1$ (green curve), and $\Delta\tau = 0.05$ (blue curve).

The effect of Faraday rotation on a linearly polarized radiation beam depends on the strength of the magnetic field and on the distance it travels through the magnetized material. Assuming that the radiation is emitted from all spatial points with the same linear polarization angle, the radiation emitted from each point is attenuated and its polarization angle is modified by a different amount, according to their optical distance from the boundary of the slab. Thus, the radiation which emerges from the material, which receives contributions from all spatial points inside, generally experiences a net reduction of its linear polarization fraction.

As can be seen in Fig. 5.15, the linear polarization fraction of the radiation emerging from the slab tends to decrease with ρ_V, although it is interesting to note that, for particular values of ρ_V/η_I, the rotation of the plane of linear polarization is particularly efficient in reducing the linear polarization fraction of the emergent radiation. Thus, in Fig. 5.15 one finds an oscillatory behavior in terms of ρ_V/η_I superimposed on the general decreasing trend. We remind the reader that the proof presented here is only intended to illustrate that ρ_V can modify the radiation's linear polarization fraction in self-emitting materials. Clearly, the situation is more complicated if the radiation entering the lower boundary is significant, or if the RT coefficients are not constant over all spatial points in the material.

As we have discussed, this reduction of the linear polarization fraction due to Faraday rotation has a concrete, physical, explanation. On the other hand, a modification of P_L can also be artificially produced by the constraints imposed by certain formal solvers. In particular, this may occur when formal solvers of the DELO family such as DELOPAR or BESSER (see Sect 2.6.1) are used, as is the case for most of

the calculations presented in this thesis. These formal solvers make the assumption that, between two adjacent spatial grid points, the $\hat{K}'\vec{I}$ product in the RT equation varies linearly. We remind the reader that $\hat{K}'$ contains the off-diagonal terms of the propagation matrix, normalized to η_I. Let us consider, for simplicity, a non-emitting medium. From Eq. (2.94), we derive the following expression for a monochromatic and unidirectional ray, transmitted from an upwind point M into point O

$$I_{O,i} = \sum_j \left[\mathbb{1} + {\Psi'}_O {K'}_O\right]^{-1}_{ij} {I'}_{M,j} \,, \tag{5.21}$$

where i and j are the Stokes components, and

$$ {I'}_{M,j} = \sum_k \left[\mathrm{e}^{-\Delta\tau_M}\mathbb{1} - {\Psi'}_M {K'}_M\right]_{jk} I_{M,k} \,, \tag{5.22}$$

where the ${\Psi'}_O$ and ${\Psi'}_M$ factors, related to the optical distance between points M and O, are defined in Eqs. (2.90c). $\Delta\tau_M$ is the optical distance between grid points M and O (see Sect. 2.6.1). Note that this expression is valid for all formal solvers of the DELO family. Assuming again that only η_I and ρ_V are non-zero, the matrices, whose components appear in the previous expressions, can be written as

$$\left[\mathbb{1} + {\Psi'}_O {K'}_O\right]^{-1} = \begin{pmatrix} 1 & 0 & 0 & 0 \\ 0 & \frac{1}{A^2+1} & -\frac{A}{A^2+1} & 0 \\ 0 & \frac{A}{A^2+1} & \frac{1}{A^2+1} & 0 \\ 0 & 0 & 0 & 1 \end{pmatrix} ; \tag{5.23a}$$

$$\left[\mathrm{e}^{-\Delta\tau_M}\mathbb{1} - {\Psi'}_M {K'}_M\right] = \begin{pmatrix} \mathrm{e}^{-\Delta\tau_M} & 0 & 0 & 0 \\ 0 & \mathrm{e}^{-\Delta\tau_M} & -B & 0 \\ 0 & B & \mathrm{e}^{-\Delta\tau_M} & 0 \\ 0 & 0 & 0 & \mathrm{e}^{-\Delta\tau_M} \end{pmatrix} , \tag{5.23b}$$

where $A = {\Psi'}_O\, \rho_V(O)/\eta_I(O)$ and $B = {\Psi'}_M\, \rho_V(M)/\eta_I(M)$. Given that in this case both I and V are decoupled from all other Stokes parameters,

$$\begin{aligned} I_O &= \mathrm{e}^{-\Delta\tau_M} I_M \,; \\ V_O &= \mathrm{e}^{-\Delta\tau_M} V_M \,. \end{aligned} \tag{5.24}$$

On the other hand, the matrices in Eq. (5.23b) are block diagonal for Stokes Q and U. From Eq. (5.21)

$$\begin{aligned} Q_O &= \frac{1}{1+A^2}\left({Q'}_M - A\, {U'}_M\right) ; \\ U_O &= \frac{1}{1+A^2}\left({U'}_M + A\, {Q'}_M\right) , \end{aligned} \tag{5.25}$$

and

$$\begin{aligned} {Q'}_M &= \mathrm{e}^{-\Delta\tau_M} Q_M - B\, U_M \,; \\ {U'}_M &= \mathrm{e}^{-\Delta\tau_M} U_M + B\, Q_M \,. \end{aligned} \tag{5.26}$$

Thus the Stokes Q and U parameters obtained at point O using a DELO formal solver, due to the radiation transmitted from point M, can be written as

$$Q_O = \frac{1}{1+A^2}\Big((\mathrm{e}^{-\Delta\tau_M} - AB)Q_M - \big(B + A\mathrm{e}^{-\Delta\tau_M}\big)U_M\Big) \tag{5.27a}$$

$$U_O = \frac{1}{1+A^2}\Big((\mathrm{e}^{-\Delta\tau_M} - AB)U_M + \big(B + A\mathrm{e}^{-\Delta\tau_M}\big)Q_M\Big)\,. \tag{5.27b}$$

From here it is straightforward to find

$$Q_O^2 + U_O^2 = \frac{1}{1+A^2}\big(Q_M^2 + U_M^2\big)\big(\mathrm{e}^{-2\Delta\tau_M} + B^2\big)\,. \tag{5.28}$$

Thus, the linear polarization fraction is

$$P_L(O) = \sqrt{\frac{Q_O^2 + U_O^2}{I_O^2}} = \sqrt{\frac{1 + B^2\,\mathrm{e}^{2\Delta\tau_M}}{1+A^2}}\,P_L(M)\,. \tag{5.29}$$

If ρ_V is zero (and therefore $A = B = 0$), the polarization fraction of the radiation transmitted between points M and O is conserved, independently of the optical distance between the two points. However, if ρ_V is non-zero, the use of a DELO formal solver introduces an artificial modification of the polarization fraction.

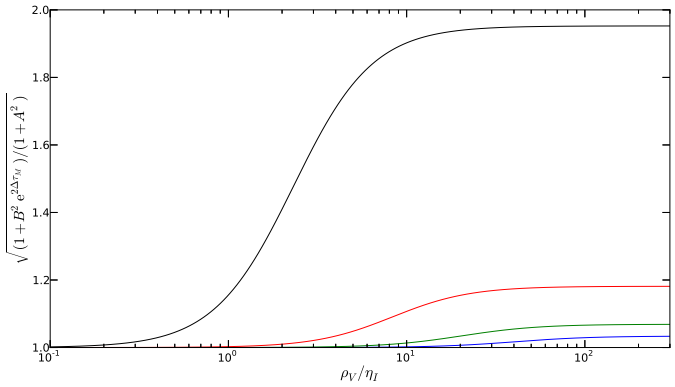

FIGURE 5.16— The $\sqrt{\frac{1+B^2\mathrm{e}^{2\Delta\tau_M}}{1+A^2}}$ factor (see Eq. (5.29)), corresponding to the $P_L(O)$ over $P_L(M)$ ratio, as a function of ρ_V/η_I. This factor refers to the radiation transmitted through a non-emitting material, considering a DELO formal solver, for which η_I and ρ_V coefficients of the propagation matrix are constant between points O and M. The colored curves indicate various optical distances between the grid points, including $\Delta\tau_M = 1$ (black curve), $\Delta\tau_M = 0.25$ (red curve), $\Delta\tau_M = 0.1$ (green curve), and $\Delta\tau_M = 0.05$ (blue curve).

In Fig. 5.16 the change of the polarization fraction between points M and O introduced by the formal solver, as found in the factor on the rhs of Eq. (5.29), is presented as a function of ρ_V/η_I. Various optical distances between points M and O have been considered, ranging from $\Delta\tau_M = 0.05$ to $\Delta\tau_M = 1$. We point out that ρ_V and η_I are both assumed to be constant between points M and O. As can be seen from Eq. (5.29), if the optical distance between the two points is larger, changes between $P_L(O)$ and $P_L(M)$ are obtained for smaller values of ρ_V/η_I. From Fig. 5.16, it can be seen that the $P_L(O)/P_L(M)$ ratio reaches an asymptotic value which depends on the optical depth, and which increases for larger $\Delta\tau_M$.

It is important to note that the overall error introduced by such formal solvers can be greatly reduced by subdividing the spatial grid. For a given optical distance $\Delta\tau_M$

$$\frac{P_L(O)}{P_L(M)} = \sqrt{\frac{1 + B(\tau_M)^2\, \mathrm{e}^{2\Delta\tau_M}}{1 + A(\tau_M)^2}}\,.$$

If the interval is subdivided into n intervals which are equally spaced in optical depth, the ratio between the polarization fraction in the same two points becomes

$$\frac{P_L(O)}{P_L(M)} = \left(\sqrt{\frac{1 + B(\tau_M/n)^2\, \mathrm{e}^{2\Delta\tau_M/n}}{1 + A(\tau_M/n)^2}}\right)^n\,. \tag{5.30}$$

As an example, if the optical distance between the two points is $\Delta\tau_M = 1$ and $\rho_V/\eta_I = 10$, the ratio of $P_L(O)$ over $P_L(M)$ is 1.90. If instead the interval is divided into 4 subintervals of $\Delta\tau_M = 0.25$, the ratio becomes 1.50, and when considering 20 subintervals of $\Delta\tau_M = 0.05$ the ratio instead becomes 1.04. However, we note that for greater values of ρ_V/η_I an extremely fine grid will be necessary to significantly reduce such error. Nevertheless, when ρ_V/η_I is large enough for the change in P_L to be significant for a grid with reasonable spacing, we expect the reduction of the polarization fraction due to MO effects in a material which emits polarized radiation (see Fig. 5.15) to have a far greater impact, by various orders of magnitude. Furthermore, we have performed numerical tests for the Ca I 4227 Å and Mg II k lines to check that furhter refining the spatial grid does not lead to substantial changes in the Q/I and U/I wing signals in the emergent radation for horizontal magnetic fields as strong as 200 G.

5.6 Conclusions

In the previous chapter, the impact of the magnetic field on the scattering emissivity was studied, taking both the Hanle and Zeeman effects into account. In this chapter, we have instead focused on the theoretical discovery that, in resonance lines for which PRD effects produce broad Q/I profiles with considerable amplitudes in the wings, the $\rho_V\, U$ and $\rho_V\, Q$ terms of the RT equations for Stokes Q and U, respectively, give rise to a substantial magnetic sensitivity in the wings signals of both Q/I and U/I. If the lower level is unpolarized, such terms are non-zero only in the presence of a

magnetic field, and we refer to them as MO effects. For the magnetic fields strengths typically found in the quiet Sun, their influence has been commonly neglected in the past. While the aformentioned terms of the RT equation are indeed negligible in the Doppler core, in the wings the ρ_V term becomes comparable to the absorption coefficient for field strengths of the order of the Hanle critical field.

It was already known that the linear and circular polarization signatures of strong chromospheric spectral lines such as Ca I 4227 Å and Mg II k are influenced by the magnetic fields with strengths typical of the quiet Sun through both (a) the familiar Zeeman effect, which produces measureable circular polarization signals in the presence of spatially resolved magnetic fields that are longitudinal to the LOS, and (b) the Hanle effect, which gives rise to a magnetic sensitivity in the core of the linear polarization profiles, even in the presence of fields that are tangled at scales below the line photon's mean free path. Moreover, through (c) the joint action of PRD and MO effects, U/I signals are produced in the line wings, and both Q/I and U/I become sensitive to the impact of the magnetic field. We point out that the observable U/I wing signals produced by such effects may be masked if magnetic fields with mixed polarities are present in spatially unresolved regions that contribute significantly to the emergent radiation. On the other hand, signatures of such MO effects will still be appreciable in Q/I if the magnetic field is structured at scales larger than the mean free path of the line's photons. This novel physical mechanism expands the diagnostic potential of spectral lines in quiet solar regions, providing a tool to study the magnetic activity in the spatial regions where the line wings originate.

The success of the Chromospheric Lyman-Alpha Spectro-Polarimeter (CLASP), a sounding rocket experiment which was launched in September of 2015 in order to measure the Q/I and U/I profiles of the hydrogen Lyman-α line in quiet regions of the solar disk (Kano et al. 2012), motivated the CLASP international team to propose a second mission. Its goal is to measure the four Stokes profiles in the spectral range comprised between 2794.5 Å and 2803.5 Å which includes the Mg II h & k lines, as well as some subordinate lines of Mg II. In order to suitably model the h & k lines, which share the same lower level (the ground level of Mg II), PRD effects in scattering, which produce very extended linear polarization profiles, must be accounted for. Although the Mg II h & k lines are separated by 6 Å, quantum interferences between their upper levels (J-state interference) substantially affect their wing linear polarization signals (see Belluzzi & Trujillo Bueno 2012). Our findings suggest that such signals are also sensitive to the aforementioned MO effects (see Alsina Ballester et al. 2016). Indeed, based on the formulation of Casini et al. (2014) for the $\mathcal{R}_{\rm II}$ matrix considering a multiterm atom, del Pino Alemán et al. (2016) also recently studied such a magnetic sensitivity across the Mg II h and k lines.

Motivated by the interesting spectropolarimetric observations of the Ca I 4227 Å line carried out by Bianda et al. (2003), which showed Q/I and U/I signals with large amplitudes and spatial variability in the wings, we have also performed RT

calculations for this spectral line. In particular, it is remarkable that the illustrative example we present in Fig. 5.10 is qualitatively similar to the observed profiles at an LOS with $\mu = 0.31$, shown in Fig. 3 of Bianda et al. (2003).

It is also interesting to note that, aside from a rotation of the plane of linear polarization of the emergent radation, the MO effects quantified by ρ_V (also known as Faraday rotation), may also produce an effective decrease of its linear polarization fraction. In order for this to occur, radiation must be emitted across an extended spatial region along the LOS, and the magnetic field must be structured at scales larger than the mean free path of the line's photons. Both the former and latter conditions are rather common in the solar atmosphere.

Moreover, even when the medium is non-emitting, we find that an artificial modification of the linear polarization fraction is produced when the RT equations are solved using a formal solution method of the DELO family. This modification is produced because of the constraint that the $\hat{K}'\vec{I}$ product must change linearly between two adjacent grid points. Fortunately, whenever the ρ_V/η_I ratio is large, and so a very fine spatial grid would be required to reduce this numerical error, the mechanism discussed in the previous paragraph - which is physical in origin - will have reduced the linear polarization by several orders of magnitude, provided that polarized radiation is emitted from the medium.

6

Conclusions

Solar magnetic fields leave their fingerprints on the polarization of the solar spectrum. Thus, the magnetic activity in the solar atmosphere can be explored by measuring and interpreting the four Stokes parameters of spectral lines. Until recently, the generation and transfer of spectral line polarization had generally been modeled by assuming either (a) the weak magnetic field regime, in which scattering polarization due to the anisotropic illumination of atoms, and its modification due to the Hanle effect, is accounted for, while the Zeeman effect is neglected, or (b) by taking the strong field limit, in which the spectral line radiation is polarized only due to the Zeeman effect. In this work, we have considered all such physical mechanisms together, performing radiative transfer calculations that include the joint action of scattering polarization (with PRD effects), and the magnetic field via both the Hanle and Zeeman effects. Building upon the work of Trujillo Bueno & Manso Sainz (1999) and Belluzzi & Trujillo Bueno (2014), an efficient iterative scheme suitable for the aforementioned non-LTE problem has been developed. We have used this iterative scheme, in combination with accurate formal solvers of the Stokes-vector transfer equation such as BESSER (see Štepán & Trujillo Bueno 2013), to develop a novel radiative transfer code for investigating the generation and transfer of spectral line polarization in the presence of magnetic fields of arbitrary strength, taking into account correlation effects between the frequencies of the incoming and outgoing photons in the scattering events. The theoretical framework on which this investigation is based is discussed in depth in Chapter 2.

The contributions presented in Chapter 3 can be divided as follows:

- Computational performance and other numerical aspects of the radiative transfer code. We have studied the influence of a magnetic field on the convergence rate of the calculation, focusing on the Sr II 4078 Å resonance line. We have first considered the case in which Lambda iteration is applied to all the multipolar components $\mathcal{E}^K_Q$ of the line scattering emissivity, except for $\mathcal{E}^0_0$, to which Jacobi iteration is applied. We have found this iterative scheme to be very well behaved when considering field strengths of up to a few hundred gauss,

although it deteriorates as the magnetic field strength increases further. For such stronger fields, the convergence rate can be improved if all the $\mathcal{E}^K_Q$ components, instead of only $\mathcal{E}^0_0$, are accounted for when calculating the correction to $\mathcal{E}^0_0$ at every iterative step.

- Physical aspects not directly related to the magnetic field, focusing on the unmagnetized case. Most notably, we have studied the role of elastic collisions in strong resonance lines that originate in the solar chromosphere and present linear polarization profiles that extend into the line wings. We have found a clear signature of collisionally-induced frequency redistribution in the linear polarization wings, consisting in a reduction of the polarization amplitude. On the other hand, the depolarizing effect of collisions has no appreciable effect on the polarization signals of such lines, either in the line core or in the wings.

In Chapter 4 we have focused on the impact of the magnetic field on the line scattering emissivity. For spectral lines that present extended wing linear polarization signals due to PRD effects, we have found that the weak field approximation, i.e., neglecting Zeeman shifts in the emission and absorption profiles of the radiative transfer coefficients, produces an artificial magnetic sensitivity in the wings, even when the Zeeman splitting is much smaller than the line's Doppler width. Thus, caution must be exercised when applying the weak field approximation in such spectral lines. In this chapter we have also shown that, when modeling the Q/I profile of the photospheric Sr I 4607 Å line, the error introduced by considering the CRD and weak field approximations is negligible. This is an interesting result because such approximations have been used in the past when modeling observations in order to infer the strength of unresolved magnetic fields in the quiet solar photosphere (e.g., Trujillo Bueno et al. 2004). Another interesting finding is that, even when elastic collisional rates are large enough that the CRD limit is obtained and atomic level polarization is destroyed, the scattered radiation can be polarized in the presence of a strong microturbulent and isotropic magnetic field, if the illuminating radiation field breaks the spherical symmetry and is spectrally structured. Also in this chapter, we have studied the circular polarization signals produced in resonance lines whose cores originate in the upper chromosphere, such as the Mg II k line. In addition to the familiar antisymmetric peaks found around line center in the Stokes V/I profiles, lobes of significant amplitude are found in the near wings of this line for fields stronger than 10 G, with opposite sign. Interestingly, while the near wing lobes cannot be modeled without accounting for the joint action of scattering of anisotropic radiation and PRD effects, the stronger inner wing lobes can be well fitted by applying the familiar magnetograph formula.

In Chapter 5 we have studied the influence of the magneto-optical (MO) effects on the linear polarization profiles of resonance lines for which PRD phenomena produce broad Q/I profiles with considerable amplitudes in the wings. We show that the $\rho_V\, U$ and $\rho_V\, Q$ terms of the transfer equations for Stokes Q and U, respectively, cause broad U/I signals to appear in the wings of such resonance lines, and a

magnetic sensitivity arises in the wings of both Q/I and U/I. Such sensitivity is not encountered only in the presence of the strong magnetic fields typical of active solar regions, but also for the field strengths commonly found in the quiet Sun. Indeed, for the Mg II k line, variations in the Q/I wings are significant for field strengths as low as 5 G. We also note that, although ρ_V rotates the plane of linear polarization of the radiation propagating through the medium, it can also produce a net decrease in the total linear polarization fraction if polarized radiation is emitted along an extended region where such MO effects operate.

We argue that the observable signatures produced by the MO effects explain certain features of the solar spectrum whose physical origin is currently unclear, such as the surprising U/I wing signals and the interesting spatial variation in the wings of the Q/I and U/I profiles of the Ca I 4227 Å resonance line observed by Bianda et al. (2003). Moreover, we have shown that, even in quiet solar regions, the magnetic sensitivity of the polarization signals, produced in strong resonance lines for which PRD phenomena are important, is controlled by the following mechanisms: (a) the familiar Zeeman effect, which in the presence of weak magnetic fields most notably produces circular polarization signals, provided that the magnetic field is organized at spatial scales larger than the resolution element, (b) the Hanle effect, which produces a modification of the linear polarization signal in the line core, even if the orientations of the magnetic fields are tangled at scales smaller than the mean free path of the line's photons, and (c) the joint action of PRD and MO effects in the wing linear polarization profiles. Although the latter signatures can be masked if fields with mixed polarities at sub-resolution scales are present, also in this case a net decrease in Q/I can be found, provided that the field is structured at scales larger than the mean free path of the line's photons.

The MO effects we have theoretically discovered extend the diagnostic potential of strong resonance lines with broad linearly polarized wings (e.g., Ca I 4227 Å, Sr II 4078 Å, Ca II H & K, Mg II h & k, Ly-α), since they can be used to probe the magnetic activity also in the deeper layers of the atmosphere where the wings originate. Indeed, our investigation of the sensitivity of the Mg II k line to the MO effects (see Alsina Ballester et al. 2016) complements the theoretical work of Belluzzi & Trujillo Bueno (2012), in which the linear polarization (due to scattering processes) and circular polarization (due to the Zeeman effect) profiles of the Mg II h & k lines were studied (see also del Pino Alemán et al. 2016). This serves as a further motivation for the CLASP2 sounding rocket mission (see Narukage et al. 2016) which, following the great success of CLASP1 (see Kano et al. 2017), will measure the four Stokes parameters in the spectral range that includes these two lines, and which is scheduled to launch in 2019.

The work presented in this thesis represents another step forward in the development of magnetic diagnostics based on spectropolarimetry. The forward modeling radiative transfer code developed in this thesis, which accounts for the scattering of anisotropic radiation with PRD effects, together with the MO, Hanle, and Zeeman effects, should now be used as a starting point to develop a numerical code

capable of performing inversions for observations of spectral lines in the four Stokes parameters. On the other hand, our PRD forward modeling code should be extended by relaxing the angle-averaged approximation, through which more accurate calculations could be performed, potentially revealing physical mechanisms that are obscured by such approximation. Furthermore, considering angle-dependent redistribution matrices is an important first step for extending the radiative transfer code to three-dimensional (3D) atmospheric models, which is a highly attractive prospect for the future, although one for which certain numerical difficulties remain to be addressed. Finally, the consideration of more sophisticated atomic models would allow us to suitably model a greater number of spectral lines, while providing further insights into the physics of the generation and transfer of polarized radiation. Several theoretical frameworks currently exist through which scattering polarization can be treated, accounting for PRD effects, in the presence of magnetic fields of arbitrary strength, for atomic models with many levels and transitions. Such frameworks include the theory of Casini et al. (2017), applicable to a multi-term Λ-type atom, the theory of Bommier (2017) for a two-term atom, or the heuristic metalevel theory of Landi Degl'Innocenti et al. (1997), which has already been used in the past to derive the $\mathcal{R}_{\rm II}$ redistribution matrix for a two-term atom in the unmagnetized case (see Belluzzi & Trujillo Bueno 2014). All of the avenues of investigation discussed here would pave the road for a deeper understanding of solar magnetism through the modeling of spectropolarimetric observations.

Bibliography

Abramowitz, M., & Stegun, I. A. 1972, Handbook of Mathematical Functions (New York: Dover)

Adams, T. F., Hummer, D. G., & Rybicki, G. B. 1971, J. Quant. Spectrosc. Radiat. Transfer, 11, 1365

Alsina Ballester, E., Belluzzi, L., & Trujillo Bueno, J. 2016, ApJ, 831, L15

Alsina Ballester, E., Belluzzi, L., & Trujillo Bueno, J. 2017, ApJ, 836, 6

Alsina Ballester, E., Belluzzi, L., & Trujillo Bueno, J. 2017, arXiv:1711.00372

Anstee, S. D., & O'Mara, B. J. 1995, MNRAS, 276, 859

Anusha, L. S., & Nagendra, K. N. 2011, ApJ, 738, 116

Anusha, L. S., Nagendra, K. N., Bianda, M., et al. 2011, ApJ, 737, 95

Auer, L. 2003, in Stellar Atmosphere Modeling, ed. I. Hubeny, D. Mihalas, & K. Werner, ASP Conf. Ser., Vol. 288 (San Francisco: ASP), 405

Asensio Ramos, A., & Trujillo Bueno, J. 2005, ApJ, 635, L109

Asensio Ramos, A., Trujillo Bueno, J., & Landi Degl'Innocenti, E. 2008, ApJ, 683, 542

Avrett, E. H. 1995, in Proc. 15th NSO Sac Peak Workshop, Infrared Tools for Solar Astrophysics: What's next?, ed. J. R. Kuhn & M. J. Penn (Singapore: World Scientific), 303

Barklem, P. S., & O'Mara, B. J. 1997, MNRAS, 290, 102

Babcock, H. W. 1953, ApJ, 118, 387

Baur, T. G., House, L. L., & Hull, H. K. 1980, Sol. Phys., 65, 111

Beckers, J. M. 1968, Sol. Phys., 3, 367

Bellot Rubio, L. R. 2006, in Solar Polarization 4, ed. R. Casini & B. W. Lites, ASP Conf. Ser., Vol. 358, 107

Belluzzi, L., Trujillo Bueno, J., & Landi Degl'Innocenti, E. 2007, ApJ, 666, 588

Belluzzi, L., Landi Degl'Innocenti, E., & Trujillo Bueno, J. 2009, ApJ, 705, 218

Belluzzi, L., Trujillo Bueno, J., & Štěpán, J. 2012, ApJ, 755, L2

Belluzzi, L., & Trujillo Bueno, J. 2012, ApJ, 750, L11

Belluzzi, L., & Trujillo Bueno, J. 2013, ApJ, 774, L28

Belluzzi, L., & Trujillo Bueno, J. 2014, A&A, 564, A16.

Belluzzi, L., Trujillo Bueno, J., & Landi Degl'Innocenti, E. 2015, ApJ, 814, 116

Bianda, M., Stenflo, J. O., & Solanki, S. K. 1998, A&A, 337, 565

Bianda, M., Solanki, S. K., & Stenflo, J. O. 1998, A&A, 331, 760

Bianda, M., Stenflo, J. O., & Solanki, S. K. 1999, A&A, 350, 1060

Bianda, M., Stenflo, J. O., Gandorfer, A., & Gisler, D. 2003, in Current Theoretical Models and Future High Resolution Solar Observations: Preparing for ATST, ed. A. A. Pevtsov & H. Uitenbroek, ASP Conf. Ser., Vol. 286 (San Francisco: ASP), 61

Bommier, V., & Sahal-Brechot, S. 1978, A&A, 69, 57

Bommier, V., & Landi Degl'Innocenti, E. 1996, Sol. Phys., 164, 117

Bommier, V. 1997, A&A, 328, 706

Bommier, V. 1997, A&A, 328, 726

Bommier, V., & Molodij, G. 2002, A&A, 381, 241

Bommier, V. 2017, A&A, 607, A50

Born, M., & Wolf, E. 1980, Principles of Optics Electromagnetic Theory of Propagation, Interference and Diffraction of Light (Oxford, GB: Pergamon Press)

Bray, R. J., Cram, L. E., Durrant, C., & Loughhead, R. E. 1991, Plasma Loops in the Solar Corona (Cambridge, UK: Cambridge University Press)

Casini, R., & Landi Degl'Innocenti, E. 2007, in Plasma Polarization Spectroscopy, ed. T. Fujimoto & A. Iwamae (Berlin: Springer), 247.

Casini, R., Manso Sainz, R., & Low, B. C. 2009, ApJ, 701, L43

Casini, R., Landi Degl'Innocenti, M., Manso Sainz, R., Landi Degl'Innocenti, E., & Landolfi, M. 2014, ApJ, 791, 94.

Casini, R., & Manso Sainz, R. 2016, ApJ, 833, 197

Casini, R., del Pino Alemán, T., & Manso Sainz, R. 2017, ApJ, 835, 114

Centeno, R., Socas-Navarro, H., Lites, B., et al. 2007, ApJ, 666, L137

Centeno, R., Trujillo Bueno, J., & Asensio Ramos, A. 2010, ApJ, 708, 1579

Collados, M., Lagg, A., Díaz Garcí A, J. J., et al. 2007, in The Physics of Chromospheric Plasmas, ed. P. Heinzel, I. Dorotovi, & R. J. Rutten, ASP Conf. Ser., Vol. 368 (San Francisco: ASP), 611

Collados, M., López, R., Páez, E., et al. 2012, Astronomische Nachrichten, 333, 872

Condon, E. U., & Shortley, G. H. 1935, The Theory of Atomic Spectra (Cambridge: Cambridge University Press)

Chandrasekhar, S. 1960, Radiative Transfer (New York: Dover)

Chen, P. F. 2011, Living Rev. Sol. Phys., 8, 1

Deb, C., & Derouich, M. 2014, A&A, 572, A53

de la Cruz Rodríguez, J., & Piskunov, N. 2013, ApJ, 764, 33

del Pino Alemán, T., Manso Sainz, R., & Trujillo Bueno, J. 2014, ApJ, 784, 46

del Pino Alemán, T., & Trujillo Bueno, J. 2015, ApJ, 808, L13

del Pino Alemán, T., Casini, R., & Manso Sainz, R. 2016, ApJ, 830, L24

del Pino Alemán, T., & Trujillo Bueno, J. 2017, ApJ, 838, 164

del Toro Iniesta, J. C. 2007, Introduction to Spectropolarimetry (Cambridge: Cambridge University Press)

Derouich, M., Bommier, V., Malherbe, J. M., & Landi Degl'Innocenti, E. 2006, A&A, 457, 1047

Elmore, D. F., Lites, B. W., Tomczyk, S., et al. 1992, in Polarization analysis and measurement, ed. D. H. Goldstein & R. A. Chipman, Proc. SPIE, Vol. 1746, 22

Fano, U. 1949, J. Opt. Soc. Am., 39, 859

Faurobert, M. 1987, A&A, 178, 269

Faurobert-Scholl, M. 1991, A&A, 246, 469

Faurobert-Scholl, M. 1992, A&A, 258, 521

Faurobert-Scholl, M. 1993, A&A, 268, 765.

Faurobert-Scholl, M. 1994, A&A, 285, 655

Faurobert-Scholl, M., Feautrier, N., Machefert, F., Petrovay, K., & Spielfiedel, A. 1995, A&A, 298, 289.

Faurobert-Scholl, M., Frisch, H., & Nagendra, K. N. 1997, A&A, 322, 896

Faurobert, M., Derouich, M., Bommier, V., & Arnaud, J. 2009, A&A, 493, 201

Frisch, H. 2010, A&A, 522, A41

Fontenla, J. M., Avrett, E. H., & Loeser, R. 1993, ApJ, 406, 319.

Fluri, D. M., & Stenflo, J. O. 1999, A&A, 341, 902

Gandorfer, A. 2000, The Second Solar Spectrum, Vol I: 4625 Å to 6995 Å (Zürich: vdf)

Gandorfer, A. 2002, The Second Solar Spectrum, Vol II: 3910 Å to 4630 Å (Zürich: vdf)

Gandorfer, A. 2005, The Second Solar Spectrum, Vol III: 3160 Å to 3915 Å (Zürich: vdf)

Gouttebroze, P. 1986, A&A, 160, 195

Gurtovenko, E. A., & Kostyk, R. I. 1989 (Kiev: Nauk. dumka)

Hanle, W. 1924, Z. Phys., 30, 93

Hale, G. E. 1908, ApJ, 28, 315

Hale, G. E. 1913, ApJ, 38, 27

Hale, G. E., Adams, W. S., & Seahes, F. H. 1933, Mount Wilson Observatory Annual Report, 5, 127

Ishikawa, R., Trujillo Bueno, J., Uitenbroek, H., et al. 2017, ApJ, 841, 31

Hauge, P. S. 1976, in Polarized Light: Instruments, Devices, Applications, e.d. R. M. A. Azzam & W. L. Hyde, Proc. SPIE, Vol. 88, 3

Holzreuter, R., Fluri, D. M., & Stenflo, J. O. 2005, A&A, 434, 713

Holzreuter, R., & Solanki, S. K. 2012, A&A, 547, A46

Hummer, D. G. 1962, MNRAS, 125, 21.

Ivanov, V. V. 1991, in Stellar Atmospheres: Beyond Classical Models, ed. L. Crivellari, I. Hubeny, & D. G. Hummer, Proc. NATO ASI Series, Vol. 145 (Dordrecht: Kluwer Academic Publishers), 81

Jacobi 1845, Astronomische Nachrichten, 22, 297

Janett, G., Carlin, E. S., Steiner, O., & Belluzzi, L. 2017, ApJ, 840, 107

Kano, R., Bando, T., Narukage, N., et al. 2012, in Space Telescopes and Instrumentation 2012: Ultraviolet to Gamma Ray, ed. T. Takahashi, S. S. Murray, & J. A. den Herder, Proceedings of the SPIE, Vol. 8443, 84434F

Kano, R., Trujillo Bueno, J., Winebarger, A., et al. 2017, ApJ, 839, L10

Kemp, J. C., Macek, J. H., & Nehring, F. W. 1984, ApJ, 278, 863

Keller, C. U., Aebersold, F., Egger, U., et al. 1992, LEST Foundation, Technical Report, 53

Kiepenheuer, K. O. 1953, ApJ, 117, 447

Kunasz, P. and Auer, L. H. 1988, J. Quant. Spectrosc. Radiat. Transfer, 39, 67

Landi Degl'Innocenti, E., Landi Degl'Innocenti, M. & Landolfi, M., in THEMIS Forum: Science with THEMIS, ed. N. Mein & S. Sahal-Brechot (Paris: Obs. Paris-Meudon), 59

Landi Degl'Innocenti, E. 1976, A&AS, 25, 379

Landi Degl'Innocenti, E. 1979, Sol. Phys., 63, 237

Landi Degl'Innocenti, E. 1983, Sol. Phys., 85, 3

Landi Degl'Innocenti, E. 1985, Sol. Phys., 102, 1

Landi Degl'Innocenti, E. 1987, in Numerical Radiative Transfer, ed. W. Kalkofen (Cambridge: Cambridge University Press), 265

Landi Degl'Innocenti, E. 1998, Nature, 392, 256

Landi Degl'Innocenti, E. and Landi Landi Degl'Innocenti, M. 1985, Sol. Phys., 97, 239

Landi Degl'Innocenti, E., Bommier, V., & Sahal-Brechot, S. 1990, A&A, 235, 459

Landi Degl'Innocenti, E. and Landolfi, M. 2004, Polarization in Spectral Lines (Dordrecht: Kluwer Academic Publishers)

Landi Degl'Innocenti, E. 2014, Atomic Spectroscopy and Radiative Processes, (Verlag Mailand: Springer)

Lamb, F. K. & ter Haar, D. 1971, Physics Reports, 2, 253

Leroy, J. L., Ratier, G., & Bommier, V. 1977, A&A, 54, 811

Longair, M. S. 1992, High Energy Astrophysics (Cambridge: Cambridge University Press)

Low, B. C. 2001, Journal of Geophysical Research, 106, 25141

Mackay, D. H., Karpen, J. T., Ballester, J. L., Schmieder, B., & Aulanier, G. 2010, Space Science Reviews, 151, 333

Makita, M. 1986, Sol. Phys., 103, 1

Mancuso, S., & Spangler, S. R. 2000, ApJ, 539, 480

Manso Sainz, R., & Trujillo Bueno, J. 1999, in Solar Polarization, ed. K. N. Nagendra & J. O. Stenflo (Boston: Kluwer Academic Publishers), 143

Manso Sainz, R., & Landi Degl'Innocenti, E. 2003, in Solar Polarization 3, ed. J. Trujillo Bueno & J. Sánchez Almeida, ASP Conf. Ser., Vol. 307, 425

Manso Sainz, R., & Trujillo Bueno, J. 2003, in Solar Polarization 3, ed. J. Trujillo Bueno & J. Sánchez Almeida, ASP Conf. Ser., Vol. 307, 251

Manso Sainz, R., & Trujillo Bueno, J. 2003, Physical Review Letters, 91, 111102

Manso Sainz, R., Landi Degl'Innocenti, E., & Trujillo Bueno, J. 2004, ApJ, 614, L89

Manso Sainz, R., & Trujillo Bueno, J. 2010, ApJ, 722, 1416

Manso Sainz, R., del Pino Alemán, T., & Casini, R. 2017, in Solar Polarization 8, eds. L. Belluzzi et al., ASP Conf. Ser., Vol. in press

Martínez González, M. J., Manso Sainz, R., Asensio Ramos, A., et al. 2015, ApJ, 802, 3

Martínez Pillet, V., García Lopez, R. J., del Toro Iniesta, J. C., et al. 1990, ApJ, 361, L81

Mártinez Pillet, V., Collados, M., Sánchez Almeida, J., et al. 1999, in High Resolution Solar Physics: Theory, Observations, and Techniques, ed. T. R. Rimmele, K. S. Balasubramaniam, & R. R.Radick, ASP Conf. Ser., Vol. 183, 264

Martínez-Sykora, J., De Pontieu, B., Hansteen, V. H., et al. 2017, Science, 356, 1269

Merenda, L., Trujillo Bueno, J., Landi Degl'Innocenti, E., & Collados, M. 2006, ApJ, 642, 554

Mihalas, D. 1978, Stellar Atmospheres (San Francisco: W. H. Freeman and Co.)

Milkey, R. W., & Mihalas, D. 1973, ApJ, 185, 709

Nagendra, K. N., Frisch, H., & Faurobert-Scholl, M. 1998, A&A, 332, 610

Nagendra, K. N., Paletou, F., Frisch, H., & Faurobert-Scholl, M. 1999, in Solar Polarization, ed. K. N. Nagendra & J. O. Stenflo (Boston: Kluwer Academic Publishers), 127

Nagendra, K. N., Frisch, H., & Faurobert, M. 2002, A&A, 395, 305

Narukage, N., McKenzie, D. E., Ishikawa, R., et al. 2016, in Space Telescopes and Instrumentation 2016: Ultraviolet to Gamma Ray, ed. J. A. den Herder, T. Takahashi, & M. Bautz, Proceedings of the SPIE, Vol. 9905, 990508

Olson, G. L. & Auer, L. H. and Buchler, J. R. 1986, J. Quant. Spectrosc. Radiat. Transfer, 35, 431

Orozco Suárez, D., Asensio Ramos, A., & Trujillo Bueno, J. 2014, A&A, 566, A46

Orozco Suárez, D., Asensio Ramos, A., & Trujillo Bueno, J. 2015, ApJ, 803, L18

Orrall, F. Q. 1971, in Solar Magnetic Fields, ed. R. Howard, IAU Symposium, Vol. 43 (Dordrecht: Reidel), 30

Paletou, F., & Auer, L. H. 1995, A&A, 297, 771

Paletou, F., & Faurobert-Scholl, M. 1997, A&A, 328, 343

Pershan, P. S. 1967, Journal of Applied Physics, 38, 1482

A. M. Portis 1978, Electromagnetic Fields Sources and Media (New York: John Wiley & Sons).

Povel, H. P. 1995, Optical Engineering, 34, 1870

Press, W. H., Flannery, B. P., & Teukolsky, S. A. 1986, Numerical recipes. The art of scientific computing (Cambridge: University Press)

Racah, G. 1942, Physical Review Letters, 62, 438

Reale, F. 2014, Living Rev. Sol. Phys., 11, 4

Rees, E. E., Murphy, G. A., and Durrant, C. J. 1989, ApJ, 339, 1093

Rees, D. E. and Saliba, G. J. 1982, A&A, 115, 1

Ruiz Cobo, B. 1998, Ap&SS, 263, 331

Sánchez Almeida, J., Collados, M., & del Toro Iniesta, J. C. 1988, A&A, 201, L37

Sampoorna, M., Nagendra, K. N., & Stenflo, J. O. 2008, ApJ, 679, 889

Sampoorna, M., Stenflo, J. O., Nagendra, K. N., et al. 2009, ApJ, 699, 1650.

Sampoorna, M., Trujillo Bueno, J., & Landi Degl'Innocenti, E. 2010, ApJ, 722, 1269

Sampoorna, M. 2011, ApJ, 731, 114

Sampoorna, M., Nagendra, K. N., & Stenflo, J. O. 2017, ApJ, 844, 97

Scharmer, G. B. 1981, ApJ, 249, 720

Shchukina, N., & Trujillo Bueno, J. 2011, ApJ, 731, L21

Shine, R. A., Milkey, R. W., & Mihalas, D. 1975, ApJ, 199, 724

Smart, W. M. 1960, Text-book on Spherical Astronomy, (Cambridge: Cambridge University Press)

Smitha, H. N., Sampoorna, M., Nagendra, K. N., & Stenflo, J. O. 2011, ApJ, 733, 4

Smitha, H. N., Sowmya, K., Nagendra, K. N., Sampoorna, M., & Stenflo, J. O. 2012, ApJ, 758, 112

Socas-Navarro, H., Trujillo Bueno, J., & Ruiz Cobo, B. 2000, ApJ, 530, 977

Solanki, S. K. 1993, Space Science Reviews, 63, 1

Solanki, S. K. 2003, Astron. Astrophys. Rev., 11, 153

Sowmya, K., Nagendra, K. N., Stenflo, J. O., & Sampoorna, M. 2014, ApJ, 786, 150

Sowmya, K., Nagendra, K. N., Sampoorna, M., & Stenflo, J. O. 2015, ApJ, 814, 127.

Štěpán, J., & Trujillo Bueno, J. 2010, ApJL, 711, L133

Štěpán, J., & Trujillo Bueno, J. 2016, ApJL, 826, L10

Stenflo, J. O., & Lindegren, L. 1977, A&A, 59, 367

Stenflo, J. O. 1982, Sol. Phys., 80, 209

Stenflo, J. 1994, Solar Magnetic Fields. Polarized Radiation Diagnostics (Dordrecht: Kluwer Academic Publishers)

Stenflo, J. O., & Keller, C. U. 1997, A&A, 321, 927

Stenflo, J. O. 1998, A&A, 338, 301

Stenflo, J. O., Gandorfer, A., & Keller, C. U. 2000, A&A, 355, 781

Stepan, J. & Trujillo Bueno, J. 2013, A&A, 557, 143

Sterling, A. C. 2000, Sol. Phys., 196, 79

Supriya, H. D., Smitha, H. N., Nagendra, K. N., et al. 2014, ApJ, 793, 42

Thomas, R. N. 1957, ApJ, 125, 260

Trujillo Bueno, J. and Fabiani Bendicho, P. 1995, ApJ, 455, 646

Trujillo Bueno, J., & Landi Degl'Innocenti, E. 1996, Sol. Phys., 164, 135

Trujillo Bueno, J., & Landi Degl'Innocenti, E. 1997, ApJ, 482, L183

Trujillo Bueno, J., & Manso Sainz, R. 1999, ApJ, 516, 436

Trujillo Bueno, J. 1999, in Solar Polarization, ed. K. N. Nagendra & J. O. Stenflo (Boston: Kluwer Academic Publishers), 73

Trujillo Bueno, J. 2001, in Advanced Solar Polarimetry – Theory, Observation, and Instrumentation, ed. M. Sigwarth, ASP Conf. Ser., Vol. 236 (San Francisco: ASP), 161

Trujillo Bueno, J., Collados, M., Paletou, F., & Molodij, G. 2001, in Advanced Solar Polarimetry – Theory, Observation, and Instrumentation, ed. M. Sigwarth, ASP Conf. Ser., Vol. 236 (San Francisco: ASP), 141

Trujillo Bueno, J., Landi Degl'Innocenti, E., Collados, M., Merenda, L., & Manso Sainz, R. 2002, Nature, 415, 403

Trujillo Bueno, J. 2003, in Stellar Atmosphere Modeling, ed. I. Hubeny, D. Mihalas, and K. Werner, ASP Conf. Ser., Vol. 288 (San Francisco: ASP), 551

Trujillo Bueno, J., Shchukina, N., & Asensio Ramos, A. 2004, Nature, 430, 326

Trujillo Bueno, J., Merenda, L., Centeno, R., Collados, M., & Landi Degl'Innocenti, E. 2005, ApJL, 619, L191

Trujillo Bueno, J. 2009, in Solar Polarization 5, ed. S. V. Berdyugina, K. N. Nagendra, & Renzo Ramelli, ASP Conf. Ser., Vol. 405 (San Francisco: ASP), 65

Trujillo Bueno, J., Štěpán, J., & Casini, R. 2011, ApJ, 738, L11

Trujillo Bueno, J., Štěpán, J., & Belluzzi, L. 2012, ApJ, 746, L9

Unno, W. 1956, Publ. Astron. Soc. Japan, 8, 108

Uitenbroek, H. 1989, A&A, 213, 360

Uitenbroek, H. 2001, ApJ, 557, 389

Uitenbroek, H. 2006, in Solar MHD Theory and Observations: A High Spatial Resolution Perspective, ed. J. Leibacher, R. F. Stein, & H. Uitenbroek, ASP Conf. Ser., Vol. 354 (San Franscisco: ASP), 313

van Regemorter, H. 1962, ApJ, 136, 906

Varga, R. S. 1962, Matrix Iterative Analysis (Englewood Cliffs: Prentice-Hall)

Viticchié, B., & Sánchez Almeida, J. 2011, A&A, 530, A14

Wittmann, A. 1974, Sol. Phys., 35, 11

Zaitsev, V. V., & Stepanov, A. V. 2008, Physics Uspekhi, 51, 1123